



**HAL**  
open science

**Synergic thermo- and pH-sensitive hybrid microgels with self-assembled fluorescent dyes and ultrasmall gold nanoparticles for intracellular raman sensing, photoacoustic imaging and photothermal therapy**

Yu Xiao

► **To cite this version:**

Yu Xiao. Synergic thermo- and pH-sensitive hybrid microgels with self-assembled fluorescent dyes and ultrasmall gold nanoparticles for intracellular raman sensing, photoacoustic imaging and photothermal therapy. Medicinal Chemistry. Université Paris Cité, 2022. English. NNT : 2022UNIP5039 . tel-04692188

**HAL Id: tel-04692188**

**<https://theses.hal.science/tel-04692188v1>**

Submitted on 9 Sep 2024

**HAL** is a multi-disciplinary open access archive for the deposit and dissemination of scientific research documents, whether they are published or not. The documents may come from teaching and research institutions in France or abroad, or from public or private research centers.

L'archive ouverte pluridisciplinaire **HAL**, est destinée au dépôt et à la diffusion de documents scientifiques de niveau recherche, publiés ou non, émanant des établissements d'enseignement et de recherche français ou étrangers, des laboratoires publics ou privés.

Université Paris Cité

École doctorale 563 - Médicament, Toxicologie, Chimie, Imageries

Laboratoire de Chimie et Biochimie Pharmacologiques et Toxicologiques

LCBPT UMR 8601

**Synergic Thermo- and pH-Sensitive Hybrid Microgels With Self-  
assembled Fluorescent Dyes and Ultrasmall Gold Nanoparticles For  
Intracellular Raman Sensing, Photoacoustic Imaging and Photothermal  
Therapy**

Par Yu XIAO

Thèse de doctorat de chimie biologique

Dirigée par Claire MANGENEY, Florence GAZEAU

Présentée et soutenue publiquement le 1 Juillet 2022

**Devant un jury composé de :**

Corinne CHANÉAC	Professeur	Sorbonne Université	Rapportrice
Stéphane ROUX	Professeur	Université de Franche-Comté	Rapporteur
Christine MÉNAGER	Professeur	Sorbonne Université	Examinatrice
Lénaïc LARTIGUE	Maître de Conférences	Université de Nantes	Examineur
Claire MANGENEY	Professeur	Université Paris Cité	Directrice de thèse
Florence GAZEAU	Directrice de recherche	Université Paris Cité	Co-directrice de thèse
Yun LUO	Chargée de recherche	Université Paris Cité	Invitée

---

# *Table of Content*

---

<b>Table of Content</b> .....	<b>2</b>
<b>Résumé en anglais (court)</b> .....	<b>5</b>
<b>Résumé en français (court)</b> .....	<b>7</b>
<b>Acknowledgments</b> .....	<b>9</b>
<b>List of Figures</b> .....	<b>11</b>
<b>List of Tables</b> .....	<b>15</b>
<b>Acronyms</b> .....	<b>16</b>
<b>Publications included in the thesis</b> .....	<b>19</b>
<b>Introduction</b> .....	<b>20</b>
<b>Chapter 1. Background and state-of-the-art</b> .....	<b>24</b>
1.1 Photoacoustic imaging: principles and applications for cancer imaging .....	24
1.2 Chemical nature of hybrid microgels for PA imaging .....	27
1.2.1 Polymer nano- and microgels.....	27
1.2.2 Synthesis of hybrid nano- and microgels for PAI .....	27
1.2.3 PAI contrast agents .....	29
1.3 Applications in theranostics and cancer hallmark imaging. ....	31
1.3.1 Multimodal cancer theranostics.....	31
1.3.2 Applications in cancer hallmark imaging .....	36
1.4 Conclusion on the design of microgels doped with PA contrast agents .....	41
1.5 Perspectives in the framework of this PhD.....	42
<b>Chapter 2. Smart microgels loaded with fluorescent dyes and gold nanoparticles for biomedical applications</b> .....	<b>45</b>
2.1 Introduction.....	45
2.2 Results & Discussion.....	47
2.2.1 Synthesis of smart hybrid microgels.....	47
2.2.2 Optical properties.....	52
2.2.3 Stimuli-responsive properties .....	53
2.2.4 Photothermal properties .....	61
2.2.5 Viability assay, cellular uptake, and phototoxicity in colon carcinoma cells .....	63
2.2.6 Photoacoustic spectroscopy.....	67

2.3 Materials & Methods.....	72
2.3.1 Materials.....	72
2.3.2 Synthesis of gold nanoparticles (Au NPs).....	72
2.3.3 Synthesis of oligo(ethylene glycol) methyl ether methacrylate-based microgels.....	72
2.3.4 Assembly process to yield hybrid microgels with fluorescent dyes and Au NPs.....	73
2.3.5 Characterization techniques.....	73
2.3.6 Cell culture, dark cytotoxicity and Phototoxicity.....	73
2.3.7 Cell uptake of hybrid $\mu$ Gels.....	74
2.3.8 Photothermal experiments.....	74
2.3.9 Photoacoustic spectroscopy.....	75
2.4 Conclusion.....	76

**Chapter 3. Insight into cellular uptake and intracellular degradation of hybrid microgels loaded with dyes and gold nanoparticle..... 78**

3.1 Introduction.....	78
3.2 Results & Discussion.....	78
3.2.1 TEM analysis after pH and NIR light stimulation.....	78
3.2.2 SERS-fluorescent encoded particles as dual-mode optical probes.....	80
3.2.3 Surface enhanced Raman signal of the hybrids upon cellular uptake.....	83
3.2.4 Compare fluorescence and Raman intensity change to indicate the intracellular processing of hybrids.....	83
3.2.5 Intracellular evolution of Raman signature.....	84
3.2.6 Intracellular evolution of fluorescence signal.....	86
3.2.7 Subcellular nanoscale transformations of hybrids inside the fibroblast.....	88
3.2.8 Hybrids using for photothermal therapy.....	92
3.3 Materials&Methods.....	93
3.3.1 Assemble of hybrids: Hybrid microgel preparation.....	93
3.3.2 Cell culture.....	93
3.3.3 Mid-term cytotoxicity.....	93
3.3.4 Phototoxicity.....	94
3.3.5 Transmission Electron Microscopy: characterization of hybrids.....	94
3.3.6 TEM characterization of the hybrids inside cells in function of time.....	94
3.3.6 Raman imaging.....	95
3.3.7 Fluorescence imaging.....	95

3.4 Conclusion .....	95
<b>Chapter 4. Raman reporters derived from aryl diazonium salts for SERS encoded-nanoparticles .....</b>	<b>97</b>
4.1 Introduction.....	98
4.2 Results & Discussion.....	100
4.3 Materials & Methods.....	112
4.3.1 Synthesis of aryl diazonium salts (D-COOH, D-CN and D-NO <sub>2</sub> ) .....	112
4.3.2 Synthesis of citrate-capped AuNPs.....	113
4.3.3 Spontaneous functionalization of AuNPs by aryl diazonium salts.....	113
4.3.4 Post-functionalization by AMP .....	113
4.3.5 Cellular uptake studies .....	114
4.3.6 Instrumentation .....	114
4.4 Conclusion .....	114
<b>Conclusions and perspectives .....</b>	<b>116</b>
<b>Annexes.....</b>	<b>119</b>
1. Dynamic light scattering (DLS).....	119
2. Raman spectroscopy.....	119
3. UV-Vis absorption spectroscopy .....	120
4. Fluorescence spectroscopy .....	121
5. Transmission electron microscopy (TEM).....	122
6. Alamar blue test .....	122
7. Photoacoustic Imaging (PAI).....	123
8. Photothermal therapy (PTT) .....	124
9. Résumé en français (long) .....	125
<b>Bibliography .....</b>	<b>133</b>

---

## *Résumé en anglais (court)*

---

**Title:** Synergic thermo- and pH-Sensitive hybrid microgels with self-assembled fluorescent dyes and ultrasmall gold nanoparticles for intracellular Raman sensing, photoacoustic imaging and photothermal therapy

### **Abstract:**

The design of smart hydrogel particles doped with plasmonic nanoparticles has attracted great interest in recent years due to their promising outlook in nanomedicine as therapeutic systems and bioimaging agents. Nanocomposite microgels were found particularly interesting as contrast agents for photoacoustic imaging (PAI), an emerging noninvasive and inexpensive bio-imaging modality, with promising prospects for cancer theranostics. Microgels can act as protective carriers to incorporate photoacoustic imaging contrast agents thanks to their high loading capacity, biocompatibility, and stimuli-responsive properties. Plasmonic nanoparticles (NPs) are promising candidates for PAI contrast agents due to their outstanding optical properties based on the collective oscillations of free electrons at the particle surface, resulting in so-called localized surface plasmon resonances (LSPR). However, the synthesis of hybrid materials based on microgels doped with plasmonic NPs is a challenging task with the necessity to control several features, such as particle sizes and doping levels to tailor their final properties in relation to the targeted application.

To meet this challenge, we have developed in this PhD work an innovative modular strategy to achieve the rational design of well-defined and densely filled hybrid particles. It is based on the step-by-step assembly of the different building blocks, including microgels ( $\mu$ Gels), dyes and gold nanoparticles and the tuning of nanoparticle loading within the polymer matrix through successive incubation steps, leading to densely filled microgels. A polymer matrix made of copolymers of oligo (ethylene glycol) methyl ether methacrylate and methacrylic acid was chosen to provide a polyanionic building block with swelling/deswelling response, pH- and thermo-sensitive behavior, desirable colloidal stability, and biodegradability. Three different dyes were loaded within the  $\mu$ Gels: rhodamine 6G (R6G),

methylene blue (MB) and cyanine 7.5 (Cy), resulting in microparticles with optical emission extending from the visible to the NIR range. Gold NPs (Au NPs) coated with citrates were selected as the plasmonic building blocks due to their unique optical properties. Upon light excitation of LSPR, a strong electromagnetic field enhancement is produced at the NP surface, leading to a wide range of applications in the fields of biology and chemistry, including surface enhanced Raman spectroscopy (SERS), bioimaging and sensing. In addition, Au NPs can convert the absorbed light into heat through non-radiative energy dissipation, making them valuable light-to-heat plasmonic converters for biomedical hyperthermia and PAI contrast agents. The characterization of the final hybrid networks using complementary techniques, such as UV-vis absorption, fluorescence, Raman, photoacoustic imaging, transmission electron microscopy, small angle X-ray scattering and dynamic light scattering revealed that they uniquely combine the properties of hydrogel particles, including high loading capacity and stimuli-responsive behavior, the photoluminescent properties of dyes (rhodamine 6G, methylene blue and cyanine 7.5) and the features of gold nanoparticles assembly. Once the system was characterized, the potential of the final hybrid networks for biomedical science was assessed through photothermal experiments, photoacoustic and Raman imaging as well as cell viability assays. Interestingly, pH and temperature stimuli could be used to induce the shrinkage of the smart hybrid microgels resulting in Au NPs aggregation, plasmon coupling and improved absorption in the NIR region. Therefore, the final hybrid networks not only combine the remarkable features of each component but also display synergetic properties that open promising prospects for a broad range of biomedical applications.

**Keywords:**

Gold nanoparticles, pH and temperature sensitive microgels, fluorescent dyes, photoacoustic imaging, photothermal therapy, surface enhanced Raman spectroscopy, nanomedicine, diagnosis and therapy.

---

## *Résumé en français (court)*

---

**Titre :** Microgels stimulables thermo- et pH sensibles imprégnés de sondes fluorescentes et de nanoparticules d'or pour des applications biomédicales

### **Résumé :**

Les particules d'hydrogels stimulables dopées avec des nanoparticules (NPs) plasmoniques suscitent un grand intérêt dans la communauté scientifique en raison de leurs perspectives prometteuses dans le domaine de la nanomédecine, notamment en tant qu'agents de contraste pour l'imagerie photoacoustique, une technique d'imagerie non invasive et à faible coût, offrant de grandes potentialités pour des applications théranostiques dans le cadre du cancer. Les NPs plasmoniques se comportent comme des agents de contraste d'imagerie photoacoustique en raison de leurs propriétés optiques remarquables basées sur les plasmons de surface localisés (LSP). Les microgels agissent comme des vecteurs protecteurs pour véhiculer dans l'organisme les agents de contraste. Cependant, la synthèse de ces matériaux hybrides est une tâche difficile avec la nécessité de contrôler un grand nombre de paramètres, dont la taille des NPs piégées et leur niveau de dopage afin d'ajuster les propriétés finales des matériaux.

Pour répondre à ce défi, nous avons développé dans le cadre de ce travail de thèse une approche modulable innovante permettant de réaliser la conception de particules hybrides bien définies et densément chargées en NPs. Cette approche est basée sur l'assemblage étape par étape des différentes entités, *i.e.* microgels ( $\mu$ Gels), sondes fluorescentes et NPs d'or (Au NPs) et sur l'ajustement du niveau d'imprégnation des Au NPs au sein des matrices polymères via des étapes successives d'incubation. Le choix de la matrice polymère s'est porté sur un copolymère d'oligo(éthylène glycol) méthyl éther méthacrylate et d'acide méthacrylique conduisant à la formation d'un  $\mu$ Gel polyanionique avec un comportement pH- et thermosensible, une excellente stabilité colloïdale et des propriétés de biodégradabilité. Trois types de sondes fluorescences ont été internalisées dans les  $\mu$ Gels préalablement formés : la rhodamine 6G (R6G), le bleu de méthylène (MB) et la cyanine 7.5 (Cy),

conduisant à des microparticules présentant un spectre d'émission optique s'étendant depuis le visible jusqu'au proche infrarouge. Le choix des NPs plasmoniques s'est porté sur des NPs d'or en raison de leurs propriétés optiques remarquables. L'excitation lumineuse des LSP produit une forte amplification du champ électrique local à la surface des Au NPs, offrant des perspectives sans précédent pour différentes applications, dont notamment la spectroscopie Raman exaltée de surface (SERS), la bioimagerie et le diagnostic. De plus, les Au NPs sont capables de convertir la lumière absorbée en chaleur via une dissipation d'énergie non radiative, ce qui en fait des nanosources de chaleur unique pour l'imagerie photoacoustique et le traitement des cancers par hyperthermie. La caractérisation des particules hybrides obtenues a été menée à l'aide d'un grand nombre de techniques complémentaires, incluant la spectroscopie UV-visible, la fluorescence, le Raman, l'imagerie photoacoustique, la microscopie électronique à transmission, la diffusion des rayons X aux petits angles et la diffusion dynamique de la lumière. Les résultats obtenus ont montré que les nanocomposites produits combinent (i) les propriétés des  $\mu$ Gels, telles qu'une forte capacité de charge et un caractère pH- et thermosensible, (ii) les propriétés photoluminescentes des sondes fluorescentes et les caractéristiques des Au NPs. L'intérêt de ces objets pour des applications biomédicales a ensuite été évalué en menant des expériences photo-thermiques, photo-acoustiques et de l'imagerie Raman ainsi que des tests de viabilité cellulaire. De façon intéressante, des stimuli basés sur le pH et la température ont pu être utilisés afin d'induire la rétractation des  $\mu$ Gels hybrides conduisant à l'agrégation des Au NPs au sein de la matrice polymère, ce qui s'est traduit par une augmentation de l'absorption optique dans le proche infrarouge, ouvrant ainsi des opportunités uniques dans le domaine biomédical.

### **Mots clefs :**

Nanoparticules d'or, microgels stimulables, sondes fluorescentes, imagerie photoacoustique, thérapie photothermique, spectroscopie Raman exaltée de surface, nanomédecine, diagnostic et thérapie.

---

## *Acknowledgments*

---

I want to first say “Merci beaucoup” to all the people who helped me to complete this ambitious thesis project.

I sincerely thank so much for my two supervisors Prof. Claire Mangeney and Florence Gazeau for giving me the opportunity to discover the world of biochemistry and to meet many collaborators to develop this thesis project. Thank you for allowing me to participate in many congresses which make me know the art of science of other researchers in the world! You dedicate guidance and support for my Ph.D. Their immense knowledge, rigorous academic attitude and excellence of work style have deeply infected and inspired me all the time of academics and daily life.

I would like to thank the members of the jury, Mrs. Corinne Chanéac, Mr. Stéphane Roux, Mrs. Christine Ménager, Mr. Lénaïc Lartigue for the attention devoted to the evaluation of my thesis and their constructive feedback.

I would like to thank Mrs. Yun LUO; your wise advice has been a valuable lesson. I would like to thank Mr. Philippe NIZARD, your endless help and professional advice gives me a deeper insight into the data analysis of biological experiments. I would like to thank Mrs. Delphine Onidas for your kind help with many administrative procedures when I was not familiar with communication in French. And thank you for your help with my concentration calculation data analysis.

I would like to thank all the people with whom I had the opportunity to collaborate during these four years, from near or far. Thanks to Mr. Jérôme Gateau and Mr. Théotim Lucas and for the photoacoustic part experiment and for sharing your knowledge and for your responsiveness during our email exchanges. I would like to thank to Giulio Avveduto help me with intracellular TEM and the happiness time in the office. Thank to Alba Nicolás-Boluda for your kind help and training for the photothermal experiment. I would also like to thank Mrs. Kelly Aubertin for introducing me to biological experiments and providing quality training. Thank you, Mr. Florent Carn, for the SAXS

experiment and for giving me access to Zetasizer. Thanks to collaborators Alberto Martín Molina, Manuel Quesada Pérez, and M<sup>a</sup> Del Mar Ramos Tejada far away in Spain for their contributions to the data simulation of the interactions between dyes and gels. I would like to thank Kartikey Padney for your help for my experiment and Amanda K. Andriola Silva, Sonia Becharef, Da LI, Heng Zhao for the help for the work!

Last, I gratefully acknowledge the financial support from the Chinese Science Council (Yu Xiao's PhD fellowship) and France Life Imaging (grant ANR-11-INBS-0006) partly fund for this work.

Thank you!

谢谢!

Yu XIAO

---

## *List of Figures*

---

**Figure 1.1** Illustration of theranostic agent based on hybrid microgel encapsulating imaging and therapeutic agents for cancer diagnosis and therapy.

**Figure 1.2** Illustration of the various elaboration strategies for designing hybrid nano- and microgels loaded with PAI contrast agents.

**Figure 1.3** PAI contrast agents for multi modal cancer theragnostic and cancer hallmark imaging.

**Figure 1.4** Illustration of the pH-sensing mechanism of SNARF-PAA NPs, based on PA signals.

**Figure 1.5** Representative scheme of the synthesis of G2-PAA NPs, conjugated to F3 peptide. Illustration of PALT method.

**Figure 1.6** Representative scheme of the synthesis of rSPN and mechanism of protein sulfonic acid detection.

**Figure 1.7** Illustration of ROS-sensitive hybrid nanogels. The degradation of the nanogels takes place with ROS, releasing ultra-small Au NPs and decreasing PA signal.

**Figure 2.1** Representative scheme of the combination and assembly of polyanionic microgels (mGel), cationic fluorescent dyes and negatively charged inorganic NPs (Au NPs).

**Figure 2.2** TEM images of (a,b) bare  $\mu$ Gels and (c,d) Au NPs, at different magnifications. (e) histogram of Au NP diameter measured from TEM. The Au NP size was analyzed on 100 NPs using the software ImageJ.

**Figure 2.3** (a) Chemical structure of the dyes and digital pictures of Gel@dye, prepared with initial dye concentrations  $[\text{Dye}]_0 = 50 \text{ mM}$  or  $[\text{Dye}]_0 = 250 \text{ mM}$ . (b) UV-vis spectra of the various Gel@dye samples for an optical path length of 1 cm and (c) corresponding fluorescence spectra ( $\lambda_{\text{ex}[\text{R6G}]} = 490 \text{ nm}$ ,  $\lambda_{\text{ex}[\text{MB}]} = 610 \text{ nm}$ ,  $\lambda_{\text{ex}[\text{Cy}]} = 716 \text{ nm}$ ).

**Figure 2.4** Typical TEM images of hybrid microgels obtained after incubation of bare (no dye) or Gel@dye particles with Au NPs. The number of incubation steps between the mGels and the Au NPs is specified on the left by the values of X, varying from 1 to 5.

**Figure 2.5** UV-vis spectra of aqueous solutions (pH 7.5) of Gel@dye and Gel@dye@Au<sub>(x)</sub>, at 0.01 nM for an optical path length of 1 cm, with Dye = R6G, MB or Cy prepared from  $[\text{Dye}]_0 = 50 \mu\text{M}$  or

250  $\mu\text{M}$ . Spectra were obtained before incubation with Au NPs or after 1 incubation, 3 incubation or 5 incubation cycles.

**Figure 2.6** Plots of  $D_H$  determined by DLS vs temperature (at pH 7) (a) and vs pH (at 25 °C) (b) for Gel@R6G@Au<sub>(1)</sub> (squares), Gel@MB@Au<sub>(1)</sub> (circles) and Gel@Cy@Au<sub>(1)</sub> (down triangles) hybrid microgels.

**Figure 2.7** Effect of temperature and pH stimuli upon the UV-vis spectra of Gel@dye@Au<sub>(x)</sub> samples, with dye = R6G, MB or Cy.

**Figure 2.8** TEM images at different magnifications of Gel@dye@Au<sub>(5)</sub> samples recorded initially at room temperature (RT) and pH 7.5 and then submitted to different stimuli.

**Figure 2.9** Small angle X-ray scattering (SAXS) patterns of aqueous solutions (pH = 7 or 5) of (a)  $\mu\text{Gels}$ , (b) Au NPs and (c, e, g) Gel@dye@Au<sub>(x)</sub>, with dye = R6G, MB or Cy and x = 1 or 5.

**Figure 2.10** Small angle X-ray scattering (SAXS) characterization of aqueous solutions (pH = 7 or 5) of Gel@dye@Au<sub>(x)</sub>, with dye = R6G, MB or Cy and X = 1 or 5.

**Figure 2.11** Heating properties of Gel@dye@Au<sub>(x=0, 1 or 5)</sub> suspensions at 0.04 nM exposed to a 808 nm laser at 1.1W/cm<sup>2</sup>. (a) Illustration of the experimental setup, (b) Pictures of the suspensions exposed to the laser and monitoring of the heating by an infrared camera, (c-e) Heating profile of Gel@dye@Au<sub>(x)</sub> at different pH.

**Figure 2.12** Viability of CT 26 cells tested by Alamar Blue assay after 24 h of incubation with free dyes, Gel@dye or Gel@dye@Au samples.

**Figure 2.13** Bright field and fluorescence microscopy of CT26 cells incubated for 24 h with Gel@dye@Au<sub>(1 or 5)</sub>, ([Dye]<sub>0</sub> = 50  $\mu\text{M}$ ).

**Figure 2.14** Bright field and fluorescence microscopy of CT26 cells incubated for 24 h with Gel@dye@Au<sub>(1 or 5)</sub>, ([Dye]<sub>0</sub> = 250  $\mu\text{M}$ ). After washing to remove exceeded  $\mu\text{gels}$ , CT26 cells were further incubated for t=0, 6 h and 24 h and observed by HCS CellInsight CX7.

**Figure 2.15** Phototoxicity of Gel@dye@Au<sub>(1 or 5)</sub> measured by Alamar Blue assay on CT26 cells after 10 min irradiation at 808 nm laser at 1 and 2W/cm<sup>2</sup>.

**Figure 2.16.** Photoacoustic spectra of Gel@Cy (green curves) and Gel@Cy@Au<sub>(x=1,5)</sub> at pH 7.5 (blue curves) and pH 5.5 (red curves) prepared from two different [Cy]<sub>0</sub> concentrations.

**Figure 2.17** Photostability of Gel@Cy and Gel@Cy@Au<sub>(1,5)</sub> samples prepared from (a) [Cy]<sub>0</sub>= 50  $\mu\text{M}$  and (b) [Cy]<sub>0</sub>=250  $\mu\text{M}$ . Each sample was illuminated 900 times at 780nm at 3.8 mJ.cm<sup>-2</sup>.

**Figure 3.1** (a) TEM images and size distribution of Gel@R6G@Au<sub>(5)</sub>, (b) Gel@MB@Au<sub>(5)</sub> and (c) Gel@Cy@Au<sub>(5)</sub>.

**Figure 3.2.** Fluorescence and Raman spectra of the hybrid  $\mu$ Gels at 0.04 nM: (a) Fluorescence spectra of Gel@dye and (b) Raman spectra of Gel@dye. (c) Fluorescence spectra of Gel@dye@Au<sub>(5)</sub> and (d) Raman spectra of Gel@dye@Au<sub>(5)</sub>.

**Figure 3.3** Raman images and spectra of Gel@dye@Au<sub>(5)</sub> samples at pH 7.5 and pH 5.5, recorded on dried drops (1  $\mu$ L) deposited on glass plates: (a) Gel@R6G@Au<sub>(5)</sub>, (b) Gel@MB@Au<sub>(5)</sub> and (c) Gel@Cy@Au<sub>(5)</sub>.

**Figure 3.4** The comparison of intercellular and dried drop Raman signals for Gel@MB@Au. The spectra for dried drop are baseline-corrected and peak intensity normalized.

**Figure 3.5** Raman spectrum of Gel@dye@Au after cellular uptake by fibroblast at day 1, day 4 and day 7.

**Figure 3.6** Raman imaging to monitor intracellular transformation of hybrids in fibroblast cells incubated with Gel@MB@Au.

**Figure 3.7** Cellular uptake process of Gel@MB@Au after incubation with fibroblast for 2h, 6h, 1 day, 4 day and 7 days observed by Cell Insight CX7. The proximity of Gel@MB@Au (black points) and methylene blue (red points) are marked by orange arrow.

**Figure 3.8** Degradation of Gel@MB@Au after incubation with fibroblast for 1 day, 4 day and 7 day observed by TEM.

**Figure 3.9** Mid-term cytotoxicity on fibroblast of Gel@R6G@Au, Gel@MB@Au and Gel@Cy@Au test by alamar blue at day 1 (a), day 4 (b) and day 7 (c) after exposure. (d) Heating properties of fibroblast cell pellet incubated Gel@dye@Au exposed to 808 nm laser. Cell pellet were collected in 100  $\mu$ L DMEM without Phenol red before irradiation. (e) Phototoxicity of treated fibroblast pellet at different laser irradiation power (1W and 2W/cm<sup>2</sup>) with. (f) Temperature increasing of treated fibroblast pellet with two laser irradiation power. (g) Morphology of fibroblast after exposed to 808 nm laser at 2W/cm<sup>2</sup> for 5 min and re-cultured with complete medium overnight.

**Figure 4.1** Schematic representation of the key steps for the preparation of SERS-encoded NPs using aryl diazonium salts.

**Figure 4.2** TEM images of (a) and (b) AuNPs; (c) and (d) Au@NO<sub>2</sub>@COOH@AMP; (e) and (f) Au@CN@COOH@AMP.

**Figure 4.3** Normalized extinction spectra of AuNPs, Au@CN, Au@CN@COOH and Au@CN@COOH@AMP.

**Figure 4.4** (a) Normalized extinction spectra and SERS spectra for AuNPs and Au@CN@COOH@AMP prepared in different amount of PVP.

**Figure 4.5** Extinction spectra of AuNP samples dispersed in various aqueous media.

**Figure 4.6** XPS high resolution C1s spectra of the modified nanoparticles (a) Au@NO<sub>2</sub> and Au@NO<sub>2</sub>@COOH@AMP; (b) Au@CN and Au@CN@COOH@AMP.

**Figure 4.7** Comparison between the SERS spectra of nanoprobos Au@CN and Au@NO<sub>2</sub> and the Raman spectra of the corresponding diazonium salt powders,

**Figure 4.8** Raman images and corresponding SERS spectra of Au@CN, Au@NO<sub>2</sub>, Au@CN@NO<sub>2</sub> and Au@NO<sub>2</sub>@CN, deposited as dried drops on a glass slide.

**Figure 4.9** SERS spectra of Au@CN and Au@CN@COOH recorded after different times of the functionalization reaction.

**Figure 4.10** SERS spectra of Au@NO<sub>2</sub> and Au@NO<sub>2</sub>@COOH recorded after different times of the functionalization reaction.

**Figure 4.11** SERS band intensity ratios vs time of reaction after the two-step addition of first, the Raman reporter diazonium salts (D-CN and D-NO<sub>2</sub>) and second, D-COOH.

**Figure 4.12** SERS spectra of Au@CN@COOH@AMP and Au@NO<sub>2</sub>@COOH@AMP. The Raman spectrum of AMP is used as a reference. Inset: Zoom in the spectral range 350–450 cm<sup>-1</sup>, revealing the presence of n<sub>Au-C</sub> peak.

**Figure 4.13** Bright-field optical images and Raman images of EGI-1 cells after uptake of Au@CN@COOH@AMP.

---

## *List of Tables*

---

**Table 1.1** Hybrid microgels for cancer photoacoustic imaging and theranostics.

**Table 1.2** Hybrid microgels for cancer hallmark photoacoustic imaging.

**Table 2.1** Dye and Au NPs uptake ( $Dye_{\text{uptake}}$  and  $AuNP_{\text{Suptake}}$ ) and loading efficiency into  $\mu\text{Gels}$ .

**Table 2.2** Characteristics of pristine and hybrid  $\mu\text{gels}$  at pH 7 determined from DLS and zeta potential measurements. All  $\text{Gel@Dye@Au}_{(1)}$  samples used for the Table below were prepared from  $[Dye]_0 = 50 \mu\text{M}$ , after  $x = 1$  incubation cycle with Au NPs solution ( $[Au \text{ NPs}] = 0.27 \mu\text{mol.L}^{-1}$ ).

**Table 2.3** Au NP mass concentrations in  $\text{Gel@Dye@Au}_{(x = 1 \text{ or } 5)}$  samples determined from the SAXS measurements shown in Figures 2.9 and 2.10.

**Table 2.4** Molar absorption coefficients ( $\epsilon_{\text{PA}}$ ) of  $\text{Gel@Cy}$  and  $\text{Gel@Cy@Au}_{(x = 1,5)}$  samples at  $\lambda = 800 \text{ nm}$ , calculated by dividing the PA absorption coefficients by the molar concentration of the hybrid  $\mu\text{Gels}$  ( $7 \times 10^{-11} \text{ mol.L}^{-1}$ ) used for the PA experiments.

**Table 3.1** Assignment of Raman bands of R6G, MB and Cy in  $\text{Gel@Dye@Au}_{(5)}$ , based on a literature survey.

**Table 4.1** Evolution of the average NPs diameter estimated by TEM for Au,  $\text{Au@CN@COOH@AMP}$  and  $\text{Au@NO}_2\text{@COOH@AMP}$ .

**Table 4.2** Wavelength of the plasmon band ( $\lambda_{\text{max}}$ ) observed in the extinction spectra of the different AuNP samples.

**Table 4.3** Surface chemical composition (At %) of initial AuNPs,  $\text{Au@CN}$ ,  $\text{Au@CN@COOH@AMP}$ ,  $\text{Au@NO}_2$ ,  $\text{Au@NO}_2\text{@COOH@AMP}$ .

---

## *Acronyms*

---

AMP	nucleotide adenosine 5'-monophosphate
Au NPs	gold nanoparticles
AuNCs	gold nanocages
AuNRs	gold nanorods
AuNSs	gold nanostars
AuNVs	gold nanovesicles
BHQ3	black hole quencher 3
CG	coarse-grained
CTAB	cetyltrimethylammonium bromide
Cy	cyanine 7.5
D-CN	4-cyanobenzenediazonium tetrafluoroborate
D-COOH	4-carboxybenzene diazonium tetrafluoroborate
D-NO <sub>2</sub>	4-nitrobenzenediazonium tetrafluoroborate
DPPF	poly[3-(5-(9-hexyl-9-octyl-9H-fluoren-2-yl)thiophene-2-yl)-2,5-bis(2-hexyldecyl)-6-(thiophene-2-yl)pyrrolo[3,4-c]pyrrole-1,4(2H,5H)-dione]
EDC	1-ethyl-3-(3-dimethylaminopropyl)carbodiimide
FBS	fetal bovine serum
HSA	human serum albumin
HSP70	heat Shock Protein 70
KPS	potassium persulfate
LSP	localized surface plasmon
LSPR	localized surface plasmon resonance
MAA	methacrylic acid
MB	methylene blue

MEO <sub>2</sub> MA	di(ethylene glycol) methyl ether methacrylate
mGels	microgels
MPV	multifunctional nanovesicles
NaBH <sub>4</sub>	sodium tetrahydridoborate
NaCl	tri-sodium citrate dihydrate
NHS	<i>N</i> -hydroxysuccinimide
NIR	near infrared
NPs	plasmonic nanoparticles
OEGDA	poly(ethylene glycol) diacrylate
OEGMA	poly(ethylene glycol) methyl ether methacrylate
PAA	polyacrylamide
PAI	photoacoustic imaging
PALT	PA life time
PANI	polyaniline
PCCP	poly[di(carboxylatophenoxy) phosphazene
PCPDTBT	poly[2,6-(4,4-bis(2-ethylhexyl)-4H-cyclopenta[2,1-b;3,4-b']dithiophene)-alt-4,7(2,1,3benzothiadiazole)].
PCPFTBT	poly[2,6-(4,4-bis(2-ethylhexyl)-4H-cyclopenta[2,1-b;3,4-b']dithiophene)-alt-4,7(2,1,3-benzothiadiazole)]
PDT	photodynamic therapy
PHPMA	poly (N-(2-(hydroxypropyl) methacrylamide
PNIPAM	poly(N-isopropylacrylamide)
PPY	Polypyrrole
PS	penicillin streptomycin
PTT	photothermal therapy
PVP	polyvinylpyrrolidone
R6G	rhodamine 6G
RGD	arginyl-glycyl-aspartic acid

ROS	reactive oxygen species
RT	room temperature
SERS	surface-enhanced Raman scattering
SNARF®	seminaphtharhodafluor
TEM	transmission electron microscopy
VPTT	volume phase transition temperature
XPS	X-ray photoelectron spectroscopy

---

## ***Publications included in the thesis***

---

1. **Yu Xiao**, Jérôme Gateau, Amanda K A Silva, Xiangyang Shi, Florence Gazeau, Claire Mangeney, Yun Luo. Hybrid nano- and microgels doped with photoacoustic contrast agents for cancer theranostics. *View*, **2021**; 20200176.

2. Yun Luo, **Yu Xiao**, Delphine Onidas, Laura Iannazzo , Mélanie Ethève-Quelquejeu , Aazdine Lamouri , Nordin Félidj , Samia Mahouche-Chergui , Thibault Brulé, Nathalie Gagey-Eilstein, Florence Gazeau and Claire Mangeney. Raman reporters derived from aryl diazonium salts for SERS encoded-nanoparticles. *Chem. Commun.*, **2020**, 56, 6822-6825.

3. **Yu Xiao**, Alba Nicolas Boluda, Delphine Onidas, Philippe Nizard, Florent Carn, Amanda Silva Brun, Théotim Lucas, Jérôme Gateau, Alberto M. Martin-Molina, Manuel Quesada-Pérez, Maria del Mar Ramos-Tejada, Florence Gazeau\*, Yun Luo\*, Claire Mangeney\*. Self-Assembly of Smart Microgels, Fluorescent Dyes and Gold Nanoparticles For Biomedical Applications. **2022**, *in preparation*.

4. **Yu Xiao**, Giulio Avveduto, Delphine Onidas, Philippe Nizard, Florent Carn, Théotim Lucas, Jérôme Gateau, Alberto M. Martin-Molina, Manuel Quesada-Pérez, Maria del Mar Ramos-Tejada, Florence Gazeau\*, Yun Luo\*, Claire Mangeney\*. Hybrid self-assemblies under pH and laser stimulation for enhanced Raman signal and monitoring of intracellular biodegradation. **2022**, *in preparation*.

---

## *Introduction*

---

### **Smart hybrid nanocomposites**

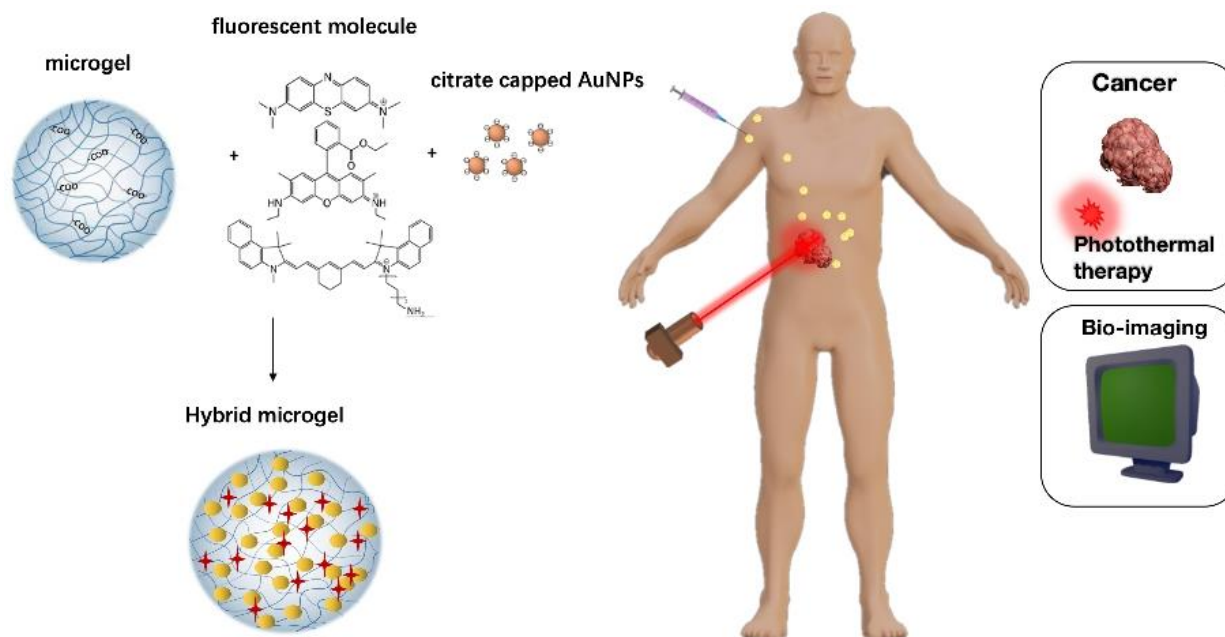
Smart hybrid nanocomposites made of hydrogel particles loaded with inorganic nanoparticles have aroused huge interest as unique multifunctional materials for nanomedicine applications, including drug delivery, therapy and imaging. Nanocomposite microgels were shown to be particularly promising as contrast agents for photoacoustic imaging (PAI), which is an emerging noninvasive and inexpensive bio-imaging modality, with promising prospects for cancer theranostics. Hybrid nano- and microgels can act as protective carriers to incorporate photoacoustic imaging contrast agents due to their high loading capacity, biocompatibility and stimuli-responsive properties. Although various kinds of PAI contrast agents have been explored, plasmonic nanoparticles (NPs) were shown to be promising candidates for PAI due to their outstanding optical properties based on localized surface plasmon (LSP). These nanoparticles display high optical absorption cross-sections, several order of magnitude larger than those of small molecular dyes. Upon LSP excitation, they provide light-to-heat conversion and thus behave as nanosources of heat. Remarkably, the absorption of nanosecond light pulses produces localized thermal expansion of the surrounding medium, resulting in the generation of ultrasound waves. This opens new opportunities, as, through the detection of the ultrasound waves, PAI can map the distribution of the nanoheaters with a sub-mm ultrasonic spatial resolution in deep tissue.

Due to these attracting features, several chemical approaches have been proposed to elaborate nanocomposite microgels embedding plasmonic NPs. They rely mainly on the in situ synthesis of the inorganic nanoparticles within the preformed polymeric particles or the ex situ synthesis of both components followed by their assembly. However, the synthesis methods developed so far present some important limitations, such as the difficulty to control the loading amount of plasmonic nanoparticles within the hydrogel matrix. Therefore, the development of a versatile strategy to achieve the elaboration of nanocomposite microgels with controlled parameters (particle size, loading efficiency) still remains a challenging task.

## Thesis project

In order to meet this challenge, this PhD work explores an innovative strategy based on the step-by-step assembly of different building blocks, *i.e.* microgels ( $\mu$ Gels), dyes and plasmonic nanoparticles, as illustrated in Scheme 1, and the tuning of nanoparticle loading within the polymer matrix through successive incubation steps. As a proof of concept, we have focused herein on the following building blocks:

- (i) For the microgel component, a pH- and thermosensitive network made of copolymers of oligo(ethylene glycol) methyl ether methacrylate and methacrylic acid was chosen;
- (ii) For the dyes, rhodamine 6G (R6G), methylene blue (MB) and cyanine 7.5 (Cy) were selected.
- (iii) Regarding the inorganic nanoparticles, citrate-coated gold nanoparticles (Au NPs) were chosen.



**Scheme 1.** Representative scheme of the self-assembly process to obtain hybrid microgels doped with both fluorescent dyes and Au NPs for photothermal therapy and bioimaging.

Each component of the final nanocomposite microgels is expected to provide valuable properties for theranostic nanomedicine, as follows:

- The gold nanoparticles and their assembly within the microgels will 1/ produce heat locally by photothermal effect, 2/ serve as photoacoustic imaging (PAI) contrast agents and 3/ enhance the Raman spectra of the dyes for surface-enhanced Raman scattering (SERS) imaging;

- The pH- and thermosensitive microgels will act as 1/ a polymer network to load the Au NPs  
2/ a retractable matrix upon heating or pH decrease, inducing the coupling of the embedded gold nanoparticles, generating an enhancement of their properties.
- The dyes (rhodamine 6G, methylene blue and cyanine 7.5) will provide optical emission extending from the visible to the NIR range.

In the first chapter of this manuscript, we introduce the basic concepts for the design of hybrid microgels in theranostics and the state-of-the-art of cancer hallmark imaging based on photoacoustic contrast agents. We give an overview of the chemical methods for the elaboration of hybrid matrices, describing the various nature of gels and PAI contrast agents and we highlight their merits and potential in relation to cancer treatment and diagnosis.

In the second chapter, we focus on the rational design of well-defined and densely filled hybrid microgels ( $\mu$ gels), using a step-by-step approach offering the possibility to finely tune the loading density of gold NPs within the polymer matrix via successive incubation steps, from one to five times. The final hybrid networks were fully characterized using complementary techniques, such as UV-vis absorption, fluorescence, Raman, small angle X-ray scattering, photoacoustic imaging, transmission electron microscopy and dynamic light scattering. Thanks to these techniques, we could investigate the pH- and thermo-responsive behavior of the pristine and hybrid microgels, their photoluminescent properties depending on the dyes loaded within the polymer matrix and the optical properties of the gold nanoparticle assembly. Once the nanocomposite platforms were fully characterized, their potential for biomedical science was assessed through photothermal experiments, photoacoustic and Raman imaging as well as cell viability and internalization assays.

In the third chapter, we have taken advantage of the dual fluorescence/Raman properties of the dyes and their enhancement or quenching by the Au NPs trapped within the microgels to investigate their biotransformation and their biodegradation in primary fibroblasts *in vitro* through dual-mode imaging. After cell internalization and ageing during up to 7 days, a strong modification of the optical signature of the  $\mu$ Gels was detected, from a SERS ON/Fluorescence OFF state to a SERS OFF/Fluorescence ON behavior, suggesting a process of disassembly with distinct fate and

relocation of Au NPs and dyes. The biotransformation was also followed by TEM, confirming the biodegradation process with the appearance of aurosomes structures after 4-7 days.

As plasmonic nanoparticles under LSPR excitation, can act both as contrast agents for PAI and Raman imaging, the nanocomposite microgels could serve as dual-modality tags for both techniques. In the fourth chapter, we focus specifically on the potential of small spherical gold NPs to bind Raman reporters for SERS bioimaging. For this, we explored a new approach for the attachment of Raman labels on the surface of Au NPs, based on aryl diazonium salts. We show that the use of aryl diazonium salt chemistry provides an easy means to obtain robust Au-C covalent links between the Raman reporters and the NPs, ensuring a high stability of the nanohybrid interface. Interestingly, this approach allows the formation of multilayers at the surface of NPs, giving access to new spectrally distinguishable SERS codes thus broadening the library of available Raman tags. Proof-of-concept Raman imaging experiments were performed on cell lines after NP uptake, highlighting the large potentials of diazonium salt chemistry to design metallic NPs-based SERS labels for Raman bioimaging. The loading of the SERS tags within the microgels studied in the previous chapters could not be studied in the framework of this PhD, due to a lack of time, but it constitutes one of the main perspectives of this work.

In the last part of the manuscript, we conclude and propose several perspectives regarding the development of more efficient/biodegradable targeted contrast agents for PAI and Raman imaging. Due to the small size, biodegradability and low toxicity of gold nanoparticles used in this work as well as the biocompatible polymer networks, these smart nanosystems should have excellent potential for clinical translation and applications as PAI/Raman agents, intracellular sensors and drug delivery system for cancer treatment.

---

## *Chapter 1. Background and state-of-the-art*

---

### **Photoacoustic active nano- and microgels for biomedical applications**

Photoacoustic imaging (PAI) is an emerging noninvasive and inexpensive bio-imaging modality, which has stimulated a wide interest in recent years for cancer theranostics. Hybrid nano- and microgels have been designed as protective carriers to incorporate PAI contrast agents due to their biocompatibility and biodegradability, high loading capacity, versatile surface chemistry and stimuli-responsive properties. These key features offer unprecedented opportunities for the design of innovative multifunctional cancer theranostic agents. This chapter focuses on the recent development of photoacoustic active nano- and microgels for biomedical applications in cancer theranostics and cancer hallmark imaging. The various chemical natures of gels and PAI contrast agents and the elaboration methods of hybrid matrices are summarized and discussed. Their applications in multimodal cancer theranostics and cancer hallmark imaging are presented, highlighting their merits and potential in treatment and diagnosis.

#### **1.1 Photoacoustic imaging: principles and applications for cancer imaging**

Imaging in medical oncology has recently experienced breakthrough with the arrival of new molecular imaging techniques devoted to the early diagnosis of cancer and to treatment monitoring. Photoacoustic imaging (PAI) has stimulated a wide interest in the medical imaging community due to its considerable capabilities for cancer physiological and molecular imaging. PAI is a hybrid imaging technique, based on the photoacoustic effect, which combines optical excitation and ultrasound detection. The PA mechanism, which was firstly observed by A. G. Bell in 1880<sup>1</sup>, is based on the local absorption of an incident non-ionizing light pulse, followed by the rapid and transient heating of the surrounding biological tissues and its thermoelastic expansion. This expansion generates ultrasound waves that originate from the optical absorbers inside the tissue and propagate outwards to the tissue surface where they can be detected and then analyzed using image reconstruction techniques to yield optical absorption maps. As a multiwave imaging

technique, PAI offers two key advantages over single-wave methods<sup>2-4</sup>. First, compared to purely optical imaging techniques, it offers large imaging depth (up to 4-5cm *in vivo*<sup>5</sup> and 11-12 cm *in vitro*) and high spatial resolution (depth-resolution ratio  $\sim 200^6$ ,  $\sim 100\mu\text{m}$  at cm depth). This is achieved thanks to the combination of the relatively high tissue penetration of near infrared<sup>7</sup> excitation (from 650 to 1700 nm) and the low scattering of the acoustic waves (in the MHz range) in tissue. Second, compared to ultrasound imaging, PAI offers a high and rich optical contrast, which enables to separate absorbing structures from the background and to distinguish absorbers based on their absorption spectra<sup>8</sup>. Endogenous absorbing molecules, such as oxy and deoxy-hemoglobin and melanin, have been efficiently used for the visualization of vessel structures, the quantification of blood oxygenation and the detection of melanoma<sup>9, 10</sup>. However, only few types of endogenous biomolecules can be exploited for intrinsic PA imaging, limiting its range of applications. To overcome these barriers and boost PA imaging specificity, many efforts have been devoted to the development of exogenous contrast agents. These materials, usually based on NIR absorbing dyes or nanomaterials, can extend the application of PAI in cancer theranostics. For example, metallic, carbon or semiconducting polymer nanoparticles (NPs), and molecular dyes (*ex.* indocyanine green, fluorescent proteins) have been reported for *in vivo* PA tumor imaging<sup>11</sup>. Nevertheless, it remains a great challenge to efficiently deliver PA contrast agent to their targets, owing to their unstable chemical properties and short circulation life-time<sup>12</sup>. To overcome these issues, biocompatible, hydrophilic and protective delivery vehicles with prolonged blood circulation lifetimes are highly desirable. Cross-linked hybrid nano- and microgels can fulfill the demands thanks to their: i) high loading capacity (*ex.* imaging agent, drugs, etc.); ii) versatility for surface modification (*ex.* by targeting molecules) and rapid response to external stimuli (*ex.* pH, temperature, etc.). These merits favor the targeting and controlled release of guest agents<sup>13</sup>, efficiently improving cancer diagnosis and therapy (**Figure 1.1**). Besides, hybrid nano- and microgels exhibit prolonged blood circulation time, which is highly suitable for theranostic agent delivery. For example, poly(N-isopropylacrylamide-co-acrylic acid) nanogels loaded with Fe<sub>3</sub>O<sub>4</sub> NPs and conjugated with Cy5.5-labeled lactoferrin, designed for targeted glioma imaging, exhibited longer blood retention time (half-life period = 5.3 h) with respect to free contrast agent (half-life period = 2.2 h) in rat models<sup>14</sup>. In another example, zwitterionic poly(phosphorylcholine) based nanogels could largely prolong the blood circulation time of anti-cancer drug (Cy5)<sup>15</sup>. 48 h after the 1<sup>st</sup> intravenous injection in BALB/c mice, more than 20 % of Cy5 injection dose could be

detected in the blood for the nanogel-Cy5 composite, whereas only less than 5% was found for free Cy5. Similar results were observed 48h after the 2<sup>nd</sup> intravenous injection. Therefore, nano- or microgels (10-200 nm) carriers have attracted lots of interests, due to their longer circulating time in blood, allowing more theranostic agents to be passively delivered and accumulate in tumor tissue after intravenous injection<sup>16</sup>.

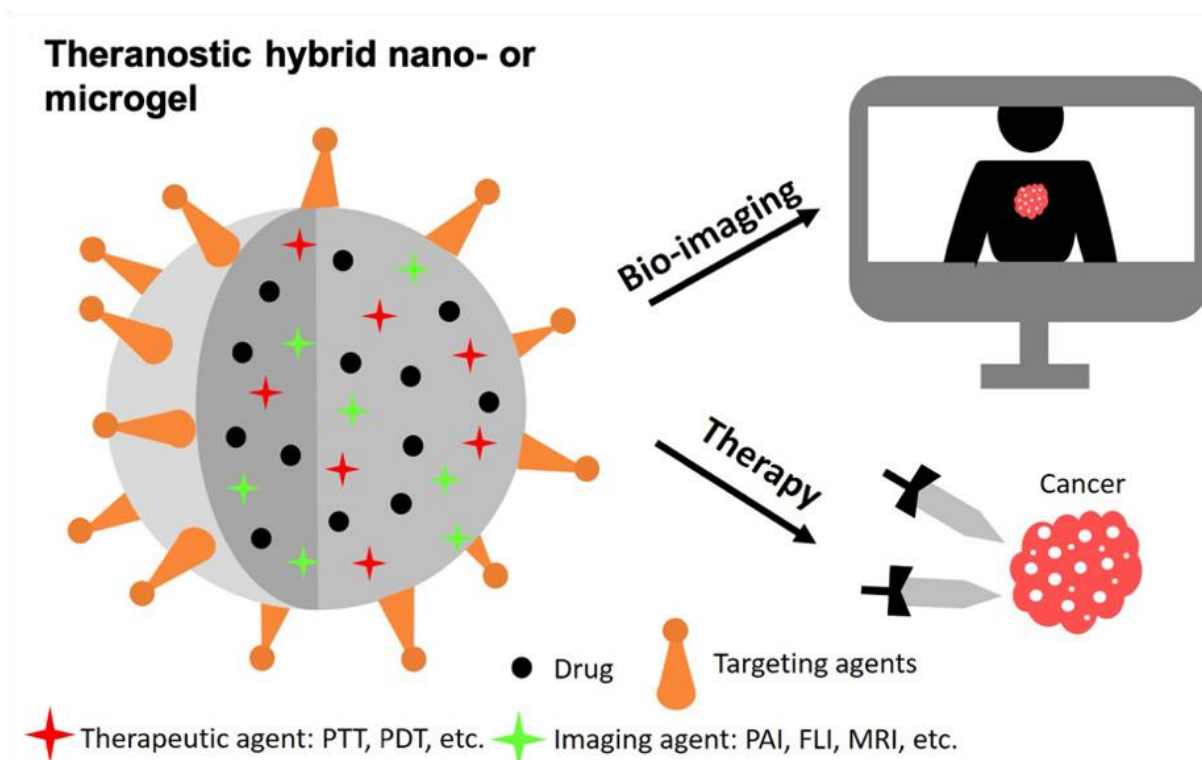


**Figure 1.1** Illustration of theranostic agent based on hybrid microgel encapsulating imaging and therapeutic agents for cancer diagnosis and therapy. PAI = photoacoustic imaging, PTT = photothermal therapy, PDT = photodynamic therapy, FLI = fluorescence imaging, MRI = magnetic resonance imaging.

In this chapter, we introduce the basic concepts for the design of hybrid microgels in the domain of PA imaging. The methods to synthesize hybrid assemblies are described and their applications in cancer related PAI and biomedicine are summarized focusing on two main orientations: i) multimodal cancer theranostics including PAI or/and synergistic therapy; and ii) cancer hallmark detection and microenvironment investigation using PAI.

## 1.2 Chemical nature of hybrid microgels for PA imaging

### 1.2.1 Polymer nano- and microgels

Various polymer nano- or microgels have been used to load contrast agents for PA imaging in oncology. They can be classified into 2 categories: i) biopolymers or ii) synthetic polymer particles, as listed in **Tables 1.1** and **1.2**. For example, engineered polypeptide (PC<sub>10A</sub>) expressed on *E. Coli* has been purified and loaded with PAI contrast agents<sup>17-19</sup>. Hyaluronic acid derivatives<sup>20</sup>, chitosan<sup>21</sup>, gelatin<sup>22</sup> and polyglutamic acid<sup>12, 23</sup> have been used for the design of multi-modal cancer theranostic platforms. Biopolymers exhibit excellent biodegradability, biocompatibility and low immunogenicity. However, some of them (ex. engineered polypeptide) require complex preparation and purification processes, with potential risk of batch to batch variation. Moreover, some natural polymers possess a few types of terminated functional groups, such as dextran, which has only -OH termini. This might limit the diversity of their possible post-functionalization or conjugation reactions. Alternatively, synthetic polymers based on polyethylenimine<sup>24</sup>, polyethylene glycol<sup>25-27</sup>, polypyrrole<sup>28</sup>, poly(acrylic acid)<sup>29-31</sup> and polyglycerol<sup>32</sup> have been reported as scaffolds for PAI contrast agent delivery. The advantages of synthetic polymers are their controllable physico-chemical (ex. size, shape, etc.) and surface properties (ex. surface charge, functional groups for conjugation, etc.), favoring the elaboration of multifunctional and multimodal system for bioimaging and therapy. Nevertheless, synthetic polymers might be non-biodegradable, as for example PHPMA (poly (N-(2-(hydroxypropyl) methacrylamide), even though it has been applied in prototype anti-cancer treatment<sup>33, 34</sup>. Therefore, one should carefully design and select proper synthetic polymers for drug delivery.

### 1.2.2 Synthesis of hybrid nano- and microgels for PAI

The elaboration of hybrid nano- and microgels for PAI can be achieved by three main approaches (cf. **Figure 1.2**): i) the *in situ* synthesis of contrast agents inside the hydrogel microparticle matrix; ii) the formation of gel particles from PA active monomers/initiators/crosslinkers; iii) the *ex situ* self-assembly of microgels and contrast agents. In the first method, the precursors are mixed with nano- or microgels, followed by contrast agent's generation process. For example, CuS NPs could be *in situ* synthesized in theranostic microgels by mixing Cu<sup>2+</sup> precursors with gels, followed by reaction with Na<sub>2</sub>S<sup>24</sup>. Another example is the *in situ* polymerization of polyaniline (PANI) in microgels from preloaded aniline monomers<sup>12</sup>. Besides, nanogels made of copper methacrylate

crosslinkers can act as precursors to generate *in situ* CuS NPs<sup>27</sup>. In the second approach, PA active monomers, such as pyrrole<sup>28</sup>, were used for the formation of microgels. Monomers could be also pre-functionalized by PA dye molecules, such as oxyphor G2<sup>35</sup>, for the *in situ* generation of gel matrix. In the third method, hybrid nano- and microgels can be prepared by the ex situ self-assembly of gel matrix and contrast agents, relying on attractive interactions, such as electrostatic forces,  $\pi$ - $\pi$  stacking, H-bonding or covalent grafting. For example, Ag<sub>2</sub>S NPs could be encapsulated into polypeptides<sup>18, 36</sup>. Methylene blue was loaded into cisplatin-modified gelatin nanogels<sup>22</sup>. Indocyanine was loaded to polydopamine coated PEGylated polypyrrole nanogels<sup>30</sup>. The first and second approaches described above are rapid and offer a simple way to generate hybrid gels. However, the morphology and properties of contrast agents (for the 1<sup>st</sup> method) and gel particles (for the 2<sup>nd</sup> method) are hard to control. Regarding the ex-situ generation approach (3<sup>rd</sup> method), it requires distinct stages to prepare separately the contrast agents and gels, and assemble them into hybrid particles, which can lead to longer procedures. Yet the size, shape and surface properties of each separate component can be defined and controlled more accurately.

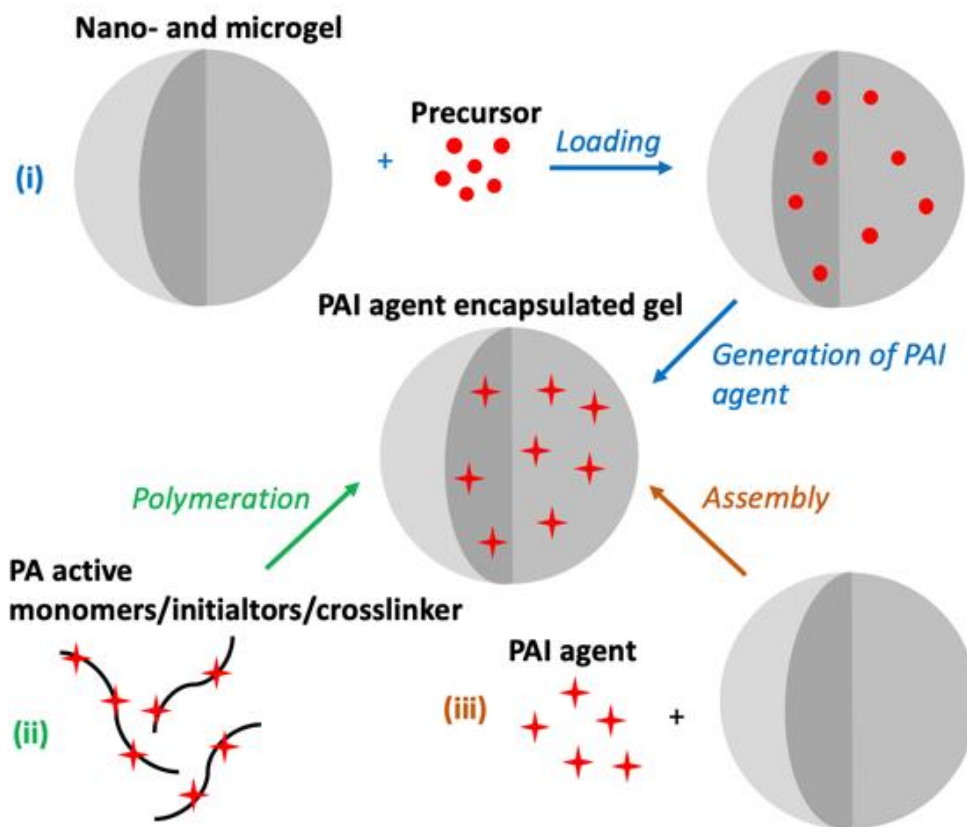


**Figure 1.2.** Illustration of the various elaboration strategies for designing hybrid nano- and microgels loaded with PAI contrast agents.

### 1.2.3 PAI contrast agents

Different types of PAI contrast agents have been loaded within polymer micro- or nanoparticles. They can be divided into three main categories (**Figure 1.3**): i) molecular dyes; ii) inorganic nanomaterials; iii) semiconducting polymers.

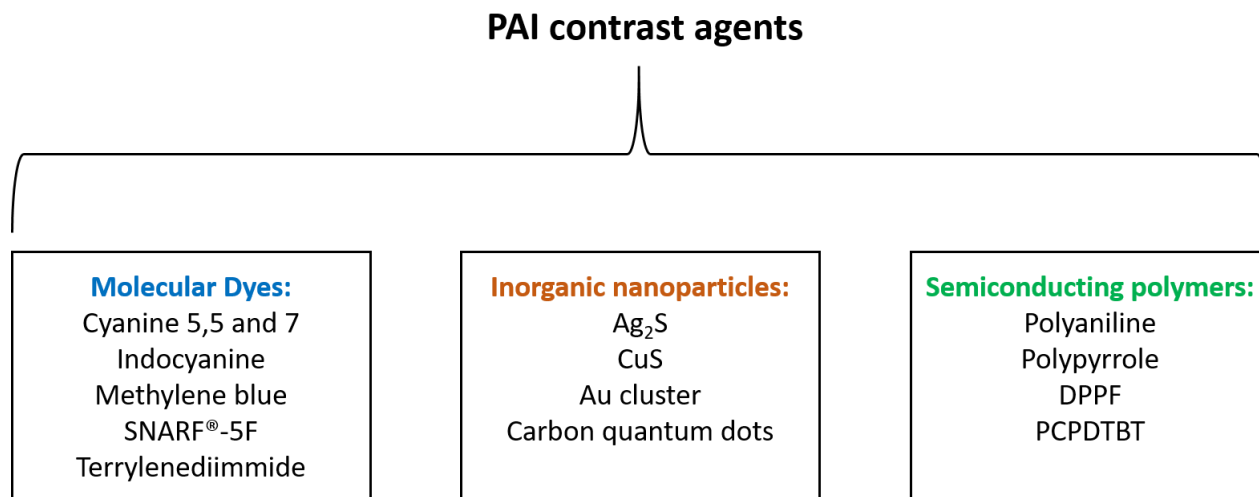


**Figure 1.3** PAI contrast agents for multi modal cancer theragnostic and cancer hallmark imaging. SNARF® = seminaphtharhodafluor; DPPF = Poly[3-(5-(9-hexyl-9-octyl-9H-fluoren-2-yl)thiophene-2-yl)-2,5-bis(2-hexyldecyl)-6-(thiophene-2-yl)pyrrolo[3,4-c]pyrrole-1,4(2H,5H)-dione]; PCPDTBT = poly[2,6-(4,4-bis(2-ethylhexyl)-4H-cyclopenta[2,1-b;3,4-b']dithiophene)-alt-4,7(2,1,3benzothiadiazole)].

**Molecular dyes** have been widely used in PA imaging due to their low toxicity and commercial availability. Commonly used dyes include cyanines, Alexa Fluor and azo derivatives, Black Hole Quencher 3 (BHQ3) and Atto dyes<sup>37-40</sup>. Nevertheless, major limitations hinder their application in clinics, such as their poor aqueous solubility, and short circulation time *in vivo*. To overcome these barriers, small molecular dyes were loaded within microgels, acting as carriers to increase the PAI contrast agent availability and improve targeting efficacy. For example, Zhai *et al.* designed multifunctional nanovesicles (MPV) based on cell membrane shells and gelatin nanogel cores to co-load methylene blue and cisplatin (Pt)<sup>22</sup>. Core-shell silica-polyethylene glycol NPs were doped with Cyanines 5.5 and 7 to provide fluorescent, photoacoustic and photothermal capabilities *in vitro* on MDA-MB-231 cancer cells<sup>26</sup>. Indocyanine functionalized polypyrrole NPs have been designed for PAI and PTT on HeLa tumor bearing nude mice<sup>30</sup>.

**Inorganic nanomaterials** based on plasmonic nanoparticles have also stimulated a wide interest for PAI due to their remarkable optical properties arising from localized surface plasmon (LSP). In particular, their optical absorption cross-sections are several order of magnitude larger than those of small molecular dyes<sup>41</sup>. Therefore, these NPs can release heat energy upon LSP excitation, resulting in light-to-heat conversion, which was exploited for PAI and photothermal therapy applications. However, it is still a great challenge to apply plasmonic colloids (e.g., Au NPs and Ag NPs) in clinics because the LSP resonance of simple spherical gold or silver nanoparticles can be only excited in the visible range (400-600 nm), where the strong absorbance of the hemoglobin limits the penetration depth to the mm-range. Fortunately, LSP properties can be adjusted by modifying NP morphology, structure and coupling to shift the excitation wavelength to the NIR region. For example, Chen *et al.* designed nanocomposites based on thermoresponsive poly(N-isopropylacrylamide) (PNIPAM) nanogels embedding gold nanorods (AuNR) and CuS NPs as nanoheaters<sup>42</sup>. In another example, sub-5nm Au NPs were encapsulated into reactive oxygen species (ROS) sensitive polyphosphazene nanogels for ROS imaging in cancer microenvironment<sup>43</sup>. NIR-absorbing Ag<sub>2</sub>S and CuS loaded gel matrix have been applied for cancer PAI and PTT<sup>18, 27</sup>. Besides, carbon-based nanomaterials, such as carbon quantum dots, carbon nanotubes and graphene, have been also reported for PAI<sup>21, 44-46</sup>. Although they exhibit lower molar extinction coefficients compared to plasmonic NPs, carbon-based nanomaterials offer valuable advantages for PAI, including ease of fabrication and surface functionalization.

**Semiconducting polymers** have emerged prominently in PA imaging due to their high absorption coefficient, strong photostability, adjustable optical properties and controllable size<sup>47, 48</sup>. This kind of contrast agent is mainly made of semiconducting polymers composed of biologically inert components, thus exhibiting good biocompatibility<sup>47</sup>. For example, polyaniline functionalized nanogels have been reported for PAI guided PTT of tumors<sup>12</sup>. Terrylenediimide-based polymeric NPs with high photothermal conversion effect have been studied in PAI and PTT<sup>29</sup>. Polypyrrole-loaded nanogels could enhanced PA intensity, favoring tumor photothermal ablation<sup>23</sup>.

## 1.3 Applications in theranostics and cancer hallmark imaging.

### 1.3.1 Multimodal cancer theranostics

Most PAI contrast agents exhibit photothermal effect, converting the absorbed light into heat. As a result, the surrounding temperature can be increased and cause cell death or/and tissue ablation. The treatment based on photothermal effect is called photothermal therapy or hyperthermia in clinical setting<sup>49</sup>. It is a minimally invasive way to treat cancer. The simultaneous use of PAI/PTT has attracted great interest for theranostics. Both inorganic and organic PAI contrast agents can be applied for PTT, as overviewed in recent reviews<sup>50, 51</sup>. For example, organic dyes (ex. methylene blue, indocyanine green)<sup>22, 52</sup> or polymers (ex. polyaniline and polypyrrole)<sup>53, 54</sup> have been reported as simultaneous PAI/PTT agents. Alternatively, inorganic materials, such as carbon nanomaterials (ex. carbon dots, graphene)<sup>44, 55</sup>, plasmonic (ex. Au)<sup>56-58</sup> and semiconducting NPs (ex. Ag<sub>2</sub>S, CuS)<sup>56, 59, 60</sup> have been used. Interestingly, the encapsulation of PAI/PTT theranostic agents within smart microgels offers unprecedented opportunities to control their delivery, release or/and biodistribution, favoring cancer diagnosis and therapy<sup>13</sup>. Therefore, such a multimodal system is receiving more and more attention. As summarized in Table 1.1, these multimodal theranostic systems can be obtained either by: i) loading simultaneously PAI and PTT agents in microgels with<sup>17, 18, 24</sup> or without<sup>12, 23, 26, 28-30</sup> tumor targeting agent on the surface or ii) by co-encapsulating PAI/PTT agents with chemo-therapeutic molecules, improving cancer treatment efficiency<sup>21, 22, 27, 30, 32, 36</sup>.

PAI agents based on organic dyes such as cyanine<sup>20, 26</sup> and methylene blue derivatives<sup>22</sup> or NPs, such as quantum dots, carbon dots<sup>21</sup> and Ag<sub>2</sub>S<sup>18</sup> have intense fluorescence emission, which could be applied for dual-mode PAI-fluorescence imaging. In addition, microgels are able to carry a secondary imaging agent (such as Gd<sup>3+</sup> complex for MRI) together with PAI agent, forming multimodal imaging system and boosting diagnostic accuracy<sup>24</sup>. Besides, it is possible to establish dual phototherapy, namely, PTT and photodynamic therapy (PDT), if the PAI agents release ROS under laser excitation. For example, a versatile theranostic system has been reported to encapsulate methylene blue and cisplatin in gelatin<sup>22</sup>. In this work, methylene blue is responsible for both imaging (e.g. PAI and fluorescence imaging) and phototherapy (e.g. PTT and PDT). Combined with anti-cancer drug (e.g. cisplatin), localized hyperthermia, PDT and chemotherapy, this multifunctional theranostic agent can efficiently kill 4T1 breast cancer cells leading to primary tumor regression and 97% inhibition of pulmonary metastasis.

**Table 1.1** Hybrid microgels for cancer photoacoustic imaging and theranostics.

Microgel scaffold	Imaging agent	Phototherapy agent	Targeting agent	Chemotherapeutic drug	Particle size	Administration mode	Ref.
<i>Biopolymer gel matrix</i>							
Polypeptides (PC <sub>10</sub> A)	Ag <sub>2</sub> S quantum dots for PAI and FLI	Ag <sub>2</sub> S quantum dots for PTT	Arginyl-glycyl-aspartic acid (RGD)	-	D <sub>h</sub> ≈ 160 nm	Intratumoral injection	<sup>18</sup>
Dextran-polypyrrole	Polypyrrole (PPY) for PAI	PPY for PTT	-	-	D <sub>h</sub> ≈ 93 nm	Intratumoral injection	<sup>28</sup>
γ-polyglutamic acid (γ-PGA)	Polyaniline (PANI) for PAI	PANI for PTT	-	-	D = 71.9 ± 15.8nm	Intratumoral injection	<sup>12</sup>
γ-PGA	PPY for PAI	PPY for PTT	-	-	D = 38.9 ± 8.6	Intratumoral injection	<sup>23</sup>
Gelatin	Methylene blue for PAI and FLI	Methylene blue for PTT and PDT	-	Cisplatin	D <sub>h</sub> = 146.3 ± 5.0 nm	Intravenous injection	<sup>22</sup>
Chitosan	Carbon quantum dots for PAI and FLI	Carbon quantum dots for PTT	-	Doxorubicin	D <sub>h</sub> = 78 nm D ≈ 65 nm	Intravenous injection	<sup>21</sup>

Janus-type hyaluronic acid derivatives	Indocyanine green for PAI and FLI	-	-	-	$D_h = 157 - 209$ nm	Intravenous injection	<sup>20</sup>
Polypeptides (PC <sub>10</sub> A)	Ag <sub>2</sub> S quantum dots for PAI for FLI	Ag <sub>2</sub> S quantum dots for PTT	-	Paclitaxel	$D = 85 \pm 15$ nm	Intratumoral injection	<sup>36</sup>
<b><i>Chemical polymer gel matrix</i></b>							
Polyethylenimine	CuS for PAI and Gd <sup>3+</sup> for MRI	CuS for PTT	Folic acid	-	$D_h = 150$ nm	Intravenous injection	<sup>24</sup>
PEGylated polypyrrole	Indocyanine green for PAI	Indocyanine green for PTT	-	-	$D = 65$ nm $D_h = 331.3 \pm 3.7$ nm	Intravenous injection	<sup>25</sup>
Terrylenediimide-poly (acrylic acid)	Terrylenediimide for PAI	Terrylenediimide for PTT	-	-	$D = 10 \pm 1.2$ nm $D_h = 12.6 \pm 2.3$ nm	Intravenous injection	<sup>29</sup>
Core-shell silica-polyethylene glycol	Cyanine 5.5 and 7 for PAI, FLI	Cyanine 5.5 and 7 for PTT	-	-	$D \approx 10$ nm $D_h \approx 30$ nm	-	<sup>26</sup>

Polystyrene-b-poly (N-isopropylacrylamide-co-acrylic acid)	Diketopyrrolo-pyrrole for PAI	Diketopyrrolo-pyrrole for PTT	-	Doxorubicin	$D_h = 75$ nm	Intravenous injection	<sup>30</sup>
Copolymers of polymethacrylic acid and poly (ethylene glycol) methacrylate	CuS for PAI	CuS for PTT	-	Doxorubicin	$D_h \approx 95$ nm	Intravenous injection	<sup>27</sup>
Polyglycerol	PPY for PAI	PPY for PTT	-	Methotrexate	$D_h = 176 - 244$ nm	Intravenous injection	<sup>32</sup>

PAI = photoacoustic imaging; FLI = fluorescence imaging; PTT = photothermal therapy; PDT = photodynamic therapy;  $D_h$  = mean hydrodynamic diameter, D = mean particle diameter determined from electronic microscopy

**Table 1.2** Hybrid microgels for cancer hallmark photoacoustic imaging.

Microgel scaffold	PAI agent	Method	Hallmark	Particle size	Administration	Ref.
Polyacrylamide (PAA)	SNARF <sup>□</sup> -5F	Ratiometric PA signal of pH-sensitive SNARF-5F at 600 and 565 nm	pH value changes	$D_h \approx 60$ nm	Intravenous injection	<sup>31</sup>
PAA	oxyphor G2 dye	PA life time of G2 dye related to surrounding O <sub>2</sub> concentration	Low oxygen concentration (hypoxia)	$D_h \approx 60$ nm	Intravenous injection	<sup>35</sup>

DPPF and PCPDTBT	DPPF, PCPDTB	PA sensing: signal increasing when probe binding to protein sulfonic acid.	Oxidative stress	$D_h \approx 18$ nm	Intravenous injection	<sup>61</sup>
PCCP and PPB	AuNPs	PA signal sensing: signal decreasing in case of reactive oxygen species	Reactive oxygen species	$D = 142.1 \pm 38.2$ nm	-	<sup>43</sup>
<p>PAA = Polyacrylamide; SNARF® = seminaphtharhodafluor; DPPF = Poly[3-(5-(9-hexyl-9-octyl-9H-fluoren-2-yl)thiophene-2-yl)-2,5-bis(2-hexyldecyl)-6-(thiophene-2-yl)pyrrolo[3,4-c]pyrrole-1,4(2H,5H)-dione]; PCPFTBT = poly[2,6-(4,4-bis(2-ethylhexyl)-4H-cyclopenta[2,1-b;3,4-b']dithiophene)-alt-4,7(2,1,3-benzothiadiazole)]; PCCP = poly[di(carboxylatophenoxy) phosphazene]; PPB = arylboronate polyphosphazene derivative; <math>D_h</math> = mean hydrodynamic diameter, <math>D</math> = mean particle diameter determined from electronic microscopy</p>						

### ***1.3.2 Applications in cancer hallmark imaging***

The hallmarks of cancer, first described by Hanahan and Weinberg<sup>62</sup>, constitute common traits and key mechanisms underpinning all cancers, including insensitivity to antigrowth signals, evasion of apoptosis, limitless replicative potential, sustained angiogenesis, tissue invasion and metastasis. Additional characteristic features of cancers are related to the tumor microenvironment<sup>63</sup>, such as reprogramming energy metabolism, evading immune response, extracellular matrix remodeling, aberrant vascularization, hypoxia and genome instability and mutation<sup>63,64</sup>. Imaging techniques offer unique opportunities to investigate most of these tumor-related characteristics and provide a noninvasive anatomic, physiologic, and molecular assessment of tumor biology for clinical practice and disease treatment. Therefore, great efforts have been devoted to the detection and imaging of cancer hallmarks. In this section, we will focus on the use of PAI for assessing cancer hallmarks, such as pH, oxygen changes, oxidative stress and ROS production (as summarized in **Table 1.2**). The detection of these traits are usually based on MRI<sup>65, 66</sup>, PET<sup>67, 68</sup> and fluorescent optical imaging<sup>69-71</sup>. However, MRI and PET are expensive techniques, and are not recommended for patients with pregnancy, breastfeeding, or with metal implants. In alternative, optical imaging and ultrasound techniques are non-invasive, low cost and easy to use. Nevertheless, fluorescence imaging measurements are not suitable for deep tissue analysis due to the strong optical scattering in tissue, limiting spatial resolution for *in vivo* imaging. As ultrasound scattering is 100 to 1000 times weaker than optical scattering, PAI allows improving spatial resolution deeply in tissue.

***pH value changes*** occur in tumor due to altered metabolic state, from aerobic glycolysis to anaerobic glycolysis<sup>72</sup>. This metabolic pathway produces excess lactic acid, leading to acidic microenvironment, which can be related to local recurrence, metastasis and failure of chemotherapy<sup>73-75</sup>. Therefore, it is very important to establish applicable clinical tools to obtain quantitative pH information in tumor. The use of PAI for pH sensing has been reported<sup>7, 76-78</sup> using molecular pH-indicators, exhibiting pH dependent absorption spectra in NIR. However, this approach does not allow accurate *in vivo* tumor pH imaging because the free molecular contrast agents may also interact with various biomolecules (ex. proteins, enzymes, etc...), that could modify their optical properties. Moreover, the strong presence of hemoglobin in biological tissues and its absorption spectra may prevent a simple amplitude-based discrimination of the contrast agent in the image, calling for the use of additional

spectral discrimination. Wang and co-workers reported the design of polyacrylamide (PAA) NPs encapsulating molecular contrast agents (*e.g.* SNARF<sup>□</sup>-5F) for PA pH imaging (**Figure 1.4a**)<sup>31</sup>. The PAA served as a matrix to load SNARF-5F, improving biocompatibility<sup>13</sup> and preventing interaction between biomolecules and dyes<sup>31</sup>. The NPs were also functionalized by tumor targeting F<sub>3</sub> peptides to target cancer cells. As shown in **Figure 1.4b**, the absorption band of SNARF-PAA NPs shifted in the visible range from 565 nm at pH = 6 to 600 nm at pH 8 ( $pK_a = 7.2^{79}$ ), providing an easy means to use the ratio of the PA absorption intensities at the two absorption wavelengths for pH measurement at mm-depths. Interestingly, a ratiometric method was proposed to discriminate the contributions of hemoglobin and the SNARF<sup>□</sup>-PAA NPs with as few as four excitation wavelengths.

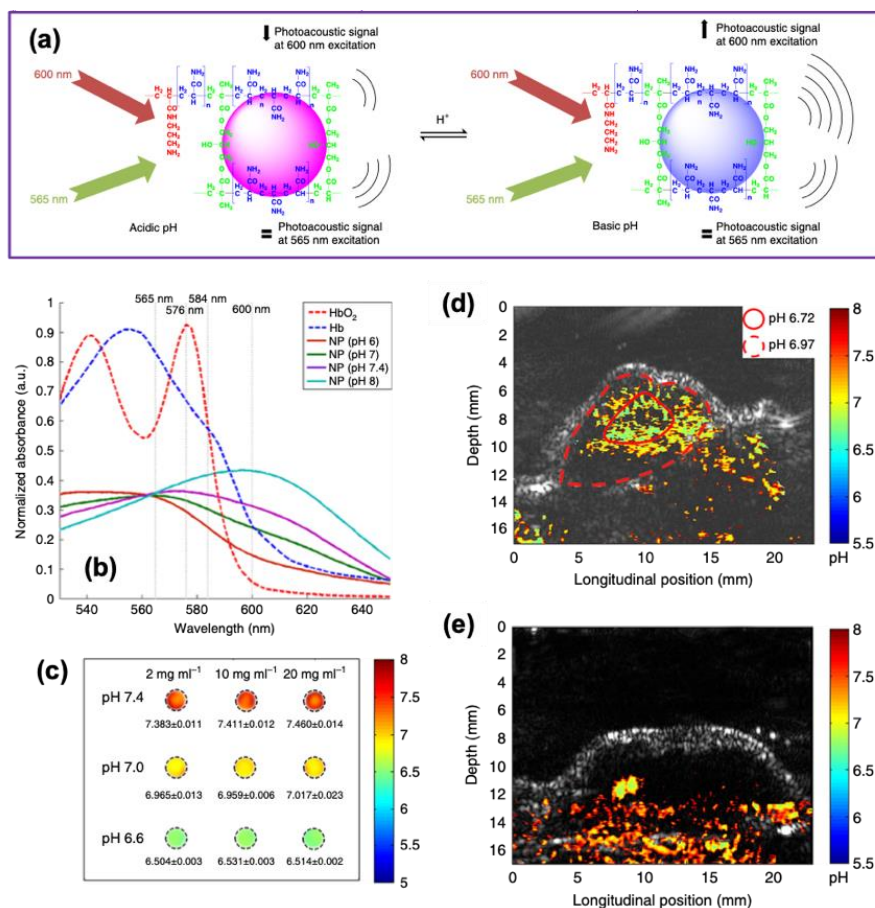


**Figure 1.4** (a) Illustration of the pH-sensing mechanism of SNARF-PAA NPs, based on PA signals. The PA signal intensity at 600 nm is pH-dependent whereas that at 565 nm is constant. The ratio of signal at 600 nm over that at 565 nm, chosen as an internal reference changes with pH variations. (b) UV-vis spectra of SNARF-PAA NPs, HbO<sub>2</sub> and Hb. (c) Results of the four-wavelength ratiometric pH imaging at pH = 6.6, 7.0 and 7.4, using 2, 10 and 20 mg mL<sup>-1</sup> of NPs in presence of 1% whole blood. *In vivo* pH imaging in mouse model 75 min after injection of SNARF-PAA (20 mg mL<sup>-1</sup>) for (d) tumor, and (e) normal tissue. Reprinted with permission from <sup>31</sup>.

From **Figure 1.4c**, PA signal can be clearly distinguished at different pH in the presence of 1% whole blood, regardless the concentration of SNARF<sup>□</sup>-PAA loading, in the concentration range of 2-20 mg mL<sup>-1</sup>. *In vivo* PA pH imaging performed 75 min after injection, showed that, the pH value was lower in tumor (**Figure 1.4d**) with respect to normal tissue (**Figure 1.4e**), evidencing a pH contrast between the center area (solid line) of the tumor and the peripheral part (dash line).

**Low oxygen concentration (hypoxia)** is also a characteristic of tumor microenvironment, associated with cancer pathologies<sup>80-82</sup>. PA oxygen imaging can firstly be based on endogenous hemoglobin, which absorption band changes upon binding/unbinding to oxygen<sup>83</sup>. However, hemoglobin gives only blood oxygen levels which provide an indirect information on the oxygen level in extravascular tumor tissues. Therefore, new PA contrast agents are desired to achieve direct tumor oxygen mapping. Recently, Kopleman and co-worked reported a PA life time (PALT) method for tumor oxygen imaging based on PAA nanogels doped with oxyphor G2 dye<sup>35</sup>, noted as G2-PAA NPs in **Figure 1.5a**. The hydrogels, functionalized by tumor-homing peptides, allowed the transport of the dye molecules to the target while protecting them from the interferences with biological species (such as proteins...). The phosphorescent G2 molecules act as light absorbers which absorbance decays over time with an exponential decay rate proportional to the oxygen concentration, after they have been excited with a pump laser pulse. The decay is evaluated with PAI by probe laser pulses at a different wavelength than the pump pulse. Varying delay times between pump and probe laser pulses (**Figure 1.5b and c**) allowed to assess the transient absorption and its decay rate and thereby the oxygen concentration. As shown in **Figure 1.5d**, the linear fit of the decay rate was similar for 2, 5 and 20 mg mL<sup>-1</sup> of G2-PAA NPs with/without human serum albumin (HSA), indicating that the oxygen concentration measurements is independent of NPs concentration and surrounding biological species. In mouse model, the PA images showed that NPs accumulate in the tumor region after 60 min of injection (**Figure 1.5e**). The PALT oxygen imaging showed low oxygen concentration in tumor (dashed cycle, **Figure 1.5f**) compared to normal tissue, as shown in **Figure 1.5g**.

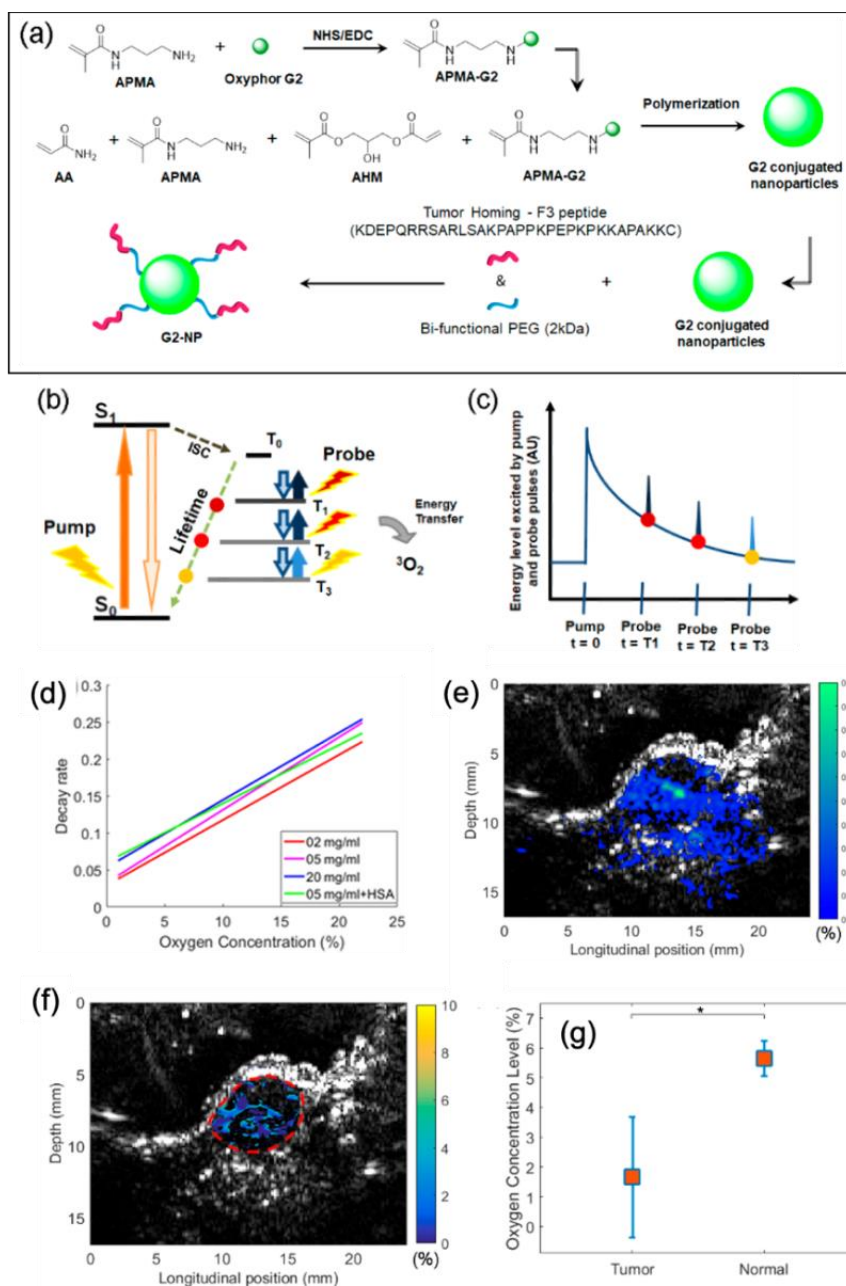


**Figure 1.5** (a) Representative scheme of the synthesis of G2-PAA NPs, conjugated to F3 peptide. Illustration of PALT method: (b) the dye molecule is excited by a pump pulse from  $S_0$  to  $S_1$  and the energy transferred to the triplet state  $T_0$ . Subsequently, probe pulses detect the energy transfer from  $T_0$  to ambient oxygen at different time points. (c) The phosphorescence decay curve can be established by varying the delay times between the pump and the probe pulses. (d) The decay rate is linearly correlated to oxygen concentration, as shown by the quantified decay rates as a function of the oxygen concentration. (e) PA imaging of G2-PAA NPs distribution and (f) PALT oxygen mapping in tumor area (dashed cycle). (f) Measured average oxygen concentration in tumor and normal (i.e. thigh) tissue (\* represents  $p < 0.01$ ). Reprinted with permission from <sup>35</sup>.

**Oxidative stress** is another hallmark of cancer<sup>84, 85</sup>, related to damaging effects caused by the production of ROS through disturbed redox state of cells. The formation of protein sulfonic acid (R-SOH), based on thiol oxidation in cell, is an indicator of damage caused by ROS. The detection of protein sulfonic acid is usually based on its interaction with a chemical probe, such as derivatives of dimedone (5,5-Dimethyl-1,3-cyclohexanedione), which can be monitored by fluorescence spectroscopy, for *in vitro* detection<sup>70, 86</sup>. *Pu et al* developed a PA method for the detection of R-SOH *in vivo*<sup>61</sup>. In this work, a core-shell nanocomposite (rSPN) was prepared using PA active polymers (SP2) cores coated by silica shells, functionalized by a chemical probe (Dyn-2, dimedone derivatives), which allow chemical binding to R-SOH, as shown in **Figure 1.6a**. The PA signal of rSPN2 (composite based on SP2 contrast agent) was maximal at 680 nm in the range 680 to 860 nm (**Figure 1.6b**). The absorption spectrum was in agreement with free SP2, indicating a good stability of SP2 within the composite. The PA intensity was not affected after mixing the composite with proteins while it increased upon bonding with BSA-SOH (bovine serum albumin with sulfenic acids), confirming efficient detection capacities of oxidative stress (**Figure 1.6c**). In xenografted HeLa tumor mouse model (**Figure 1.6d**), the PA signal of rSPN2 reach high intensity after 36h of injection, which is 1.3-fold higher than control (SPN2) and 2.2-fold higher than the PA background signal of tumor.

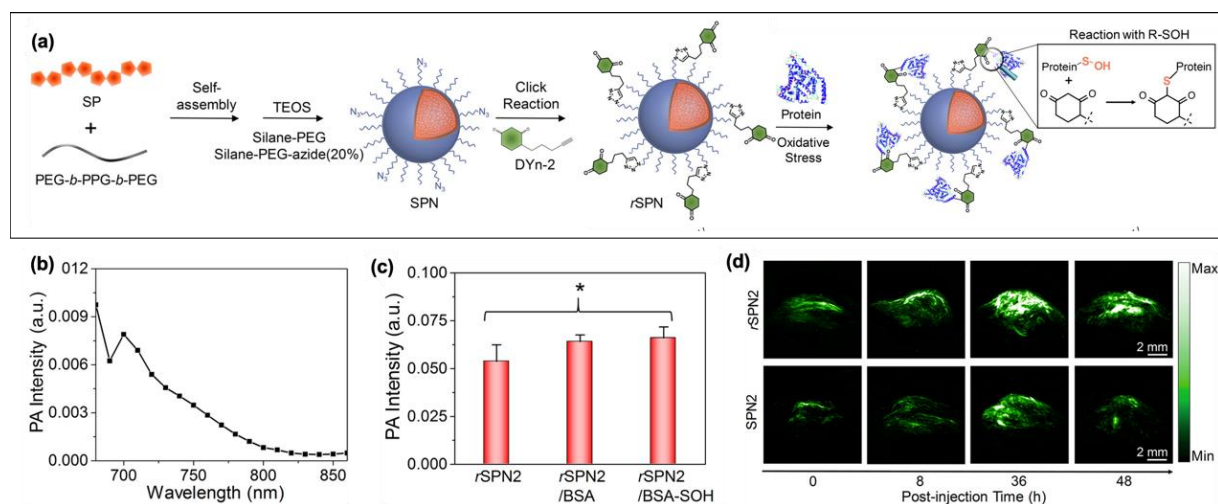


**Figure 1.6.** (a) Representative scheme of the synthesis of rSPN and mechanism of protein sulfonic acid detection. SP = SP2 = poly[2,6-(4,4-bis(2-ethylhexyl)-4H-cyclopenta[2,1-b;3,4-b]-dithiophene)-alt-4,7(2,1,3-benzothiadiazole)]; TEOS = tetraethyl orthosilicate, DYn-2 = 4-(pent-4-yn-1-yl)cyclohexane-1,3-dione, protein = BSA. (b) PA spectrum of rSPN2 (23 μg mL<sup>-1</sup> of SP2 contrast agent) in buffer solution at pH = 7.4. (c) PA intensity at 680 nm of rSPN2, rSPN2 with BSA and rSPN2 with BSA-SOH. (d) In vivo PA imaging of protein sulfonic acid in xenografted HeLa tumor mouse model after tail vein injection of rSPN2 and SPN2. Reprinted with permission from <sup>61</sup>.

**Reactive oxygen species (ROS)** production is another trait related to cancer. Cormode *et al* have recently reported the design of hybrid nanogels for ROS imaging<sup>43</sup>. As shown in **Figure 1.7a**, such a system is based on a ROS sensitive nanogel, formed by poly[di(carboxylatophenoxy) phosphazene] (PCPP) and arylboronate polyphosphazene derivative (PPB), loading densely packed ultra-small Au NPs (< 5nm). The scaffold exhibits ROS-triggered degradation, releasing Au NPs and thus resulting in a significant decrease of the PA signal due to plasmon band shifting out of the NIR region. By comparing the PA to CT signal, ratiometric ROS imaging could be established for in vitro model of inflammation of LPS-stimulated macrophages (**Figure 1.7b**).

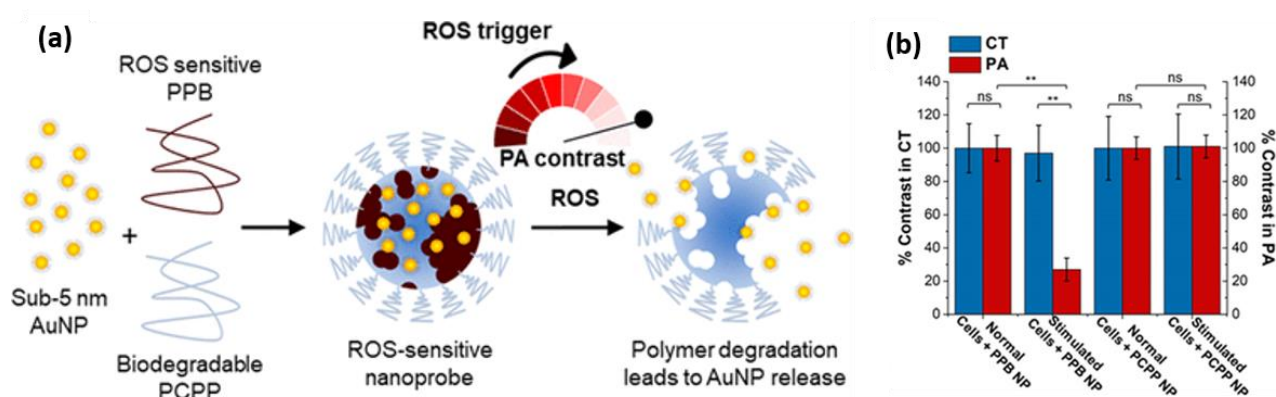


**Figure 1.7** (a) Illustration of ROS-sensitive hybrid nanogels. The degradation of the nanogels takes place with ROS, releasing ultra-small Au NPs and decreasing PA signal. (b) Comparison between PA and CT signals of normal and stimulated RAW264.7 cells incubated with PPB (ROS-sensitive hybrid nanogel) and PCPP NPs (PCPP nanogels encapsulated Au NPs). Reprinted with permission from <sup>43</sup>.

## 1.4 Conclusion on the design of microgels doped with PA contrast agents

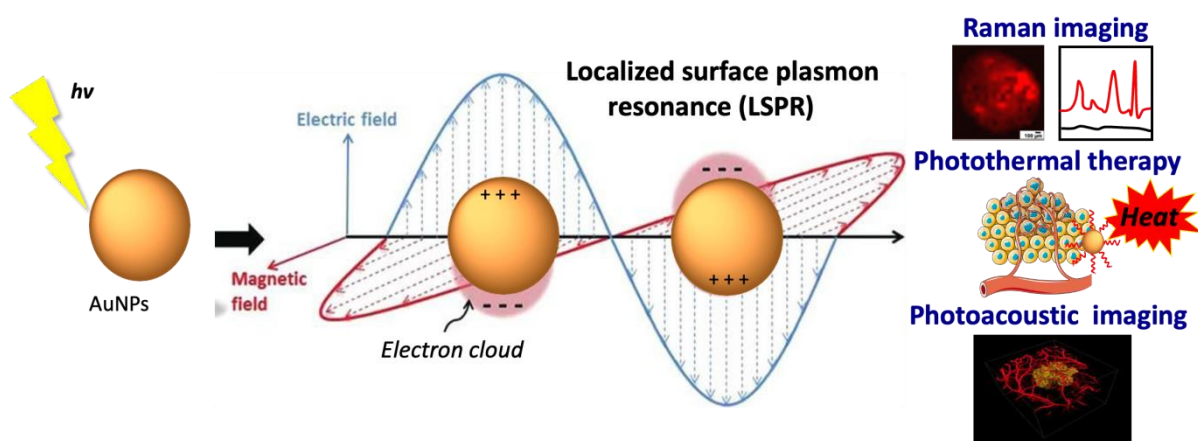
This chapter provides an up-to-date review on the development of nano- and microgels doped with PA contrast agents for photoacoustic imaging in cancer theranostics. Thanks to the loading of PA contrast agents, the hybrid microgels possess the capacity to convert NIR light to heat, a valuable feature for both PAI and phototherapy. In turn, the microgel network offers a protective matrix to improve the stability and biocompatibility of the trapped PA contrast agents. It also prevents their fast clearance by the reticuloendothelial system while fostering passive targeting of tumor by enhanced permeability and retention effect (EPR) or active targeting via conjugation to ligands. Moreover, the

stimuli-responsive properties of the hydrogel matrix offer unprecedented opportunities to achieve smart multifunctional platforms.

Nevertheless, this rapidly expanding research area is still in its infancy concerning clinical applications. There remain several challenges that need to be addressed before contrast agents based on hybrid microgels achieve their full potential for photoacoustic imaging. Particularly, from a chemical point of view, there is still much room for improvement to fully control i) the loading capacity of the microgel matrices, ii) their biodegradability and iii) the final properties of the hybrid network depending on the choice of the PA contrast agent.

## 1.5 Perspectives in the framework of this PhD

In this PhD project, we have focused on smart microgel matrix loaded with gold nanoparticles due to their outstanding optical properties, allowing their use for both surface enhanced Raman scattering (SERS), photoacoustic imaging (PAI) and photothermal therapy (PTT). As described previously, the optical properties of gold NPs arise from the ‘localized surface plasmon resonance’ (LSPR) phenomenon which is due to the oscillation of free conduction electrons at the particle surface upon light excitation, referred to as a plasmon. Interestingly, plasmons of gold nanoparticles could induce characteristic absorption in visible region and surface enhanced Raman scattering, which can be exploited for identification of chemical species and their localization. At the same time, plasmons convert a substantial part of the oscillation energy into heat, via a photothermal effect, which can be exploited both for photoacoustic imaging and photothermal therapy (Scheme 1). Gold nanoparticles can be divided into gold nanospheres (AuNPs), gold nanostars (AuNSs), gold nanorods (AuNRs), gold nanocages (AuNCs), gold nanovesicles (AuNVs) and so on according to their shapes. Plenty of research work have been done for the application of gold nanoparticles for SERS<sup>87, 88</sup>, PAI<sup>89</sup> and PTT<sup>90</sup> as these particles are relatively easy to be synthesized and functionalized. Gold nanoparticles with different shapes, sizes or aggregation states exhibit different surface and optical properties<sup>91, 92</sup>. Furong Tian *et al.* synthesized gold nanospheres, spherical aggregates, nanostars and investigated the dependence of SERS on the shape of those gold nanoparticles by using rhodamine 6G as a Raman tag<sup>93</sup>.



**Scheme 1.1.** Illustration of the optical properties of Au NPs and their applications in Raman imaging, photothermal therapy and photoacoustic imaging.

The authors concluded that the SERS effect can be optimized by increasing the number of hot spots. The plasmonic band of nanosphere aggregates shifted to 660 nm compared to single nanospheres (532 nm) due to electromagnetic coupling between Au NPs, causing a strong enhancement of the SERS signal of rhodamine 6G. In the biology field, near-infrared (NIR) SERS attracts more attention because absorption of endogenous molecules in our body is mostly in the visible range. Therefore, laser in NIR range can reduce the damage to normal cells. At the same time, NIR region corresponds to the "transparent window" of body, which is more suitable for biological applications such as photoacoustic imaging and photothermal therapy. Moreover, laser in the near-infrared region has a deeper penetration into the skin than in the visible region<sup>94</sup>, which will favor local tumor photothermal therapy while reducing damage to normal tissue. Based on this, researchers have preferentially selected gold nanorods and nanostars with plasmonic bands located in NIR-I (760 - 900 nm) or NIR-II (1000 - 1700 nm) window for bioimaging and cancer treatment. Jesse V. Jokerst *et al.* used gold nanorods as the agent for PAI and Raman imaging for the detection of ovarian cancer tumors *in vivo*<sup>95</sup>. Lu An *et al.* designed a macrophage-mediated delivery system with gold nanorods for photothermal therapy and tumor hypoxia photoacoustic (PA) imaging<sup>96</sup>. Thi Tuong Vy Phan *et al.* designed chitosan-based gold nanostars for photoacoustic imaging and photothermal therapy<sup>97</sup>.

Although the plasmonic band of nanorods and nanostars are in the NIR region, their biological toxicity cannot be ignored. The toxicity of gold nanorods and gold nanostars is mainly due to the addition of the toxic ligand cetyltrimethylammonium bromide (CTAB) during the synthesis process.

This issue has been overcome by replacing CTAB by other surface ligands such as mercaptoalkanoic acids<sup>98</sup> or polyethylene glycol (PEG)<sup>99</sup>. However, the question of biodegradability is also a crucial point. Gold nanoparticles are widely believed to remain intact in biological tissues. Although Alice Balfourier et al. reported that spherical gold nanoparticles of 4-22 nm can be degraded in cells<sup>100</sup>, there is no current report showing that gold nanostars and gold nanorods can be degraded in tissues.

To meet the requirements of both biocompatibility, biodegradability and optical properties extending in the NIR range, we have focused in this PhD work on smart microgels loaded with gold nanoparticle assemblies made of spherical nanoparticles, small enough (less than 5 nm), to be degraded by biological tissues. Moreover, when their particle size is less than 5 nm, such NPs can be eliminated by the kidneys<sup>101</sup>. To address the issue of NIR range excitation, the selected microgel platform displays stimuli-responsive properties allowing the pH- or temperature-induced shrinkage of the polymer matrix, resulting in plasmon coupling between individual NPs and efficient plasmon absorption at NIR wavelengths. Therefore, such gold nanosphere assemblies should be able to achieve a variety of biological applications, including Raman imaging<sup>102</sup>, photothermal therapy<sup>103</sup> and photoacoustic imaging<sup>2, 104</sup> while minimizing the toxicity of nanoparticles to the human body.

---

# *Chapter 2. Smart microgels loaded with fluorescent dyes and gold nanoparticles for biomedical applications*

---

## **2.1 Introduction**

The development of hybrid  $\mu$ Gels based on the integration of inorganic nanoparticles into polymeric particles has stimulated worldwide efforts in recent years due to their promising biomedical applications as smart therapeutic systems and bioimaging agents<sup>105, 106</sup>. These materials combine the unique properties of hydrogel particles, including softness, deformability, drug-loading capacity and stimuli-responsive behavior and the outstanding features of nanoparticles (NPs) with optical, magnetic, electronic or catalytic activities. Two main strategies have been explored to synthesize hybrid  $\mu$ Gels<sup>107</sup>: (i) the growth of NPs in situ in the presence of polymeric  $\mu$ Gels; (ii) the synthesis of inorganic NPs ex situ followed by their incorporation inside the polymer matrix. Although the first approach has stimulated a wide interest<sup>108, 109</sup> owing to its simplicity, it results in a poor control over the size and morphology of the inorganic NPs. In contrast, the second approach offers a unique opportunity to achieve a preliminary control of the colloidal characteristics (size, polydispersity, surface functionalities) of each separate building blocks ( $\mu$ Gels and inorganic NPs)<sup>110-112</sup>. However, it has received very little attention up to now due to the difficulties in obtaining large amounts of NPs trapped inside the microgel matrix while preventing their aggregation and leaching. Therefore, the development of a versatile strategy to achieve the self-assembly of separate preformed colloidal particles still remains challenging.

We propose here an innovative modular strategy to finely tune the loading density of inorganic NPs within the polymer matrix via successive incubation steps, from one to five times, leading to densely filled  $\mu$ Gels. As a proof of concept, a polymer matrix based on copolymers of oligo(ethylene glycol)

methyl ether methacrylate and methacrylic acid was chosen to provide a polyanionic building block with swelling/deswelling response, pH- and thermo-sensitive behavior, desirable colloidal stability and biodegradability<sup>110, 111</sup>. Besides, oligo(ethylene glycol) methacrylate based copolymers are interesting with respect to the criterion of biocompatibility<sup>113, 114</sup> and oligo(methacrylic acid) residues have been approved by the FDA (Food and Drug Administration) for drug delivery capsules. To impart fluorescence properties to the  $\mu$ Gels, three different dyes were loaded within the hydrogel matrix: rhodamine 6G (R6G), methylene blue (MB) and cyanine 7.5 (Cy), resulting in microparticles with optical emission extending from the visible to the NIR range. Gold NPs (Au NPs) coated with citrates were selected as the inorganic building blocks due to their outstanding optical properties<sup>115</sup>, based on the collective oscillations of free electrons at the particle surface, resulting in so-called localized surface plasmon resonances (LSPR). Upon light excitation of LSPR, a strong electromagnetic field enhancement is produced at the NP surface, leading to a wide range of applications in the fields of biology and chemistry, including surface enhanced Raman spectroscopy (SERS), bioimaging and sensing<sup>36</sup>. In addition, Au NPs are able to convert the absorbed light into heat through non-radiative energy dissipation, making them valuable light-to-heat plasmonic converters for biomedical hyperthermia and cancer treatments. Regarding nanotoxicity, sub-6 nm gold nanospheres are interesting candidates as they have been shown to undergo biodegradation and they can be excreted via the kidneys, which is a key parameter for clinical translation<sup>100, 101, 116</sup>. However, the plasmon resonance wavelength of gold nanospheres is located in the visible region, which limits their interest for in vivo applications. Although the optical resonances of anisotropic gold NPs such as nanostars or nanorods lie favorably in the NIR, their poor biodegradation and persistent accumulation in the body have raised some concerns about their potential long-term toxicity. Therefore, the combination of NIR optical absorption and bioelimination properties is still an important issue. It was addressed recently by designing dense assemblies of small spherical Au NPs with short double-strand DNA, resulting in plasmon coupling between individual NPs and efficient plasmon absorption at NIR wavelengths<sup>117</sup>.

The approach described herein offers a versatile alternative to obtain dense assemblies of small Au NPs within fluorescent multifunctional microparticles, which could be compared to the assembly of lego® bricks (see Figure 2.1). The first step consists in the loading of dyes within  $\mu$ Gels, while the second step is the uptake of Au NPs via diffusion, through successive incubation steps, promoting a

high loading density. The samples were experimentally characterized by UV-vis absorption, fluorescence spectroscopy, transmission electron microscopy (TEM), dynamic light scattering (DLS) and small angle X-ray scattering (SAXS). The potential of the final hybrid networks for biomedical science was then assessed through photothermal experiments, fluorescence microscopy, cell viability assays and photoacoustic spectroscopy. The fluorescent properties of the hybrid  $\mu$ Gels could be used to track their uptake by cells while they also exhibit high molar absorption coefficients at  $\lambda = 800$  nm, a key feature for PA imaging and photothermal therapy. Interestingly, pH and temperature stimuli could induce the shrinkage of the smart hybrid  $\mu$ Gels resulting in Au NPs aggregation, plasmon coupling and improved absorption in the NIR region. Therefore, the final hybrid networks not only combine the remarkable features of each component but also display synergetic properties that open promising prospects for a broad range of biomedical applications.

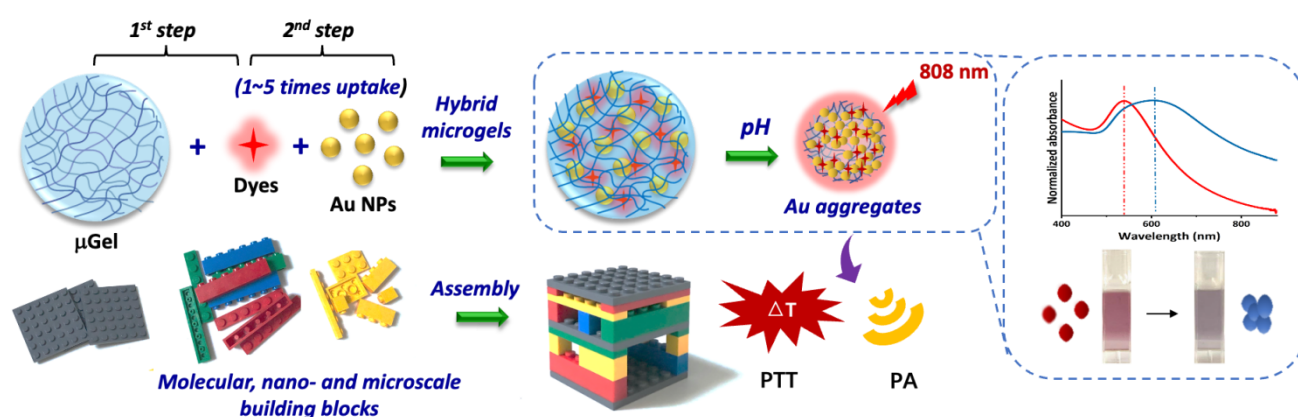


**Figure 2.1** Representative scheme of the combination and assembly of  $\mu$ Gels, fluorescent dyes and inorganic NPs (Au NPs). This approach provides a versatile toolbox to design a large variety of hybrid  $\mu$ Gels, which can be compared to the assembly of Lego® bricks, as illustrated at the bottom of the figure.

## 2.2 Results & Discussion

### 2.2.1 Synthesis of smart hybrid microgels

The  $\mu$ Gels were synthesized from oligo(ethylene glycol) methyl ether methacrylate monomers and methacrylic acid by surfactant-free precipitation polymerization in water solvent, as described by N. Griffete *et al.*<sup>111</sup> (see details in Materials & Method, section 2.3). Highly monodisperse spherical

$\mu$ Gels were obtained using this method (see TEM images in Fig. 2.2.a, b), with a mean hydrodynamic diameter  $D_h$  of 592 nm (polydispersity index = 0.1), measured from DLS at 20°C and pH 7.5.

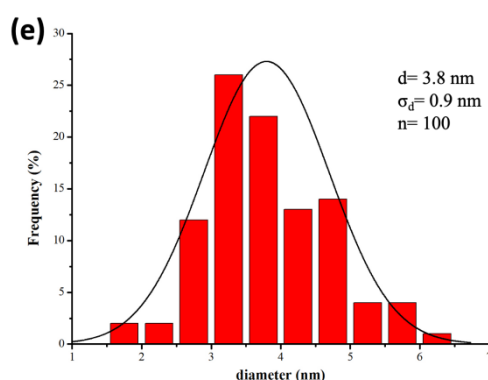
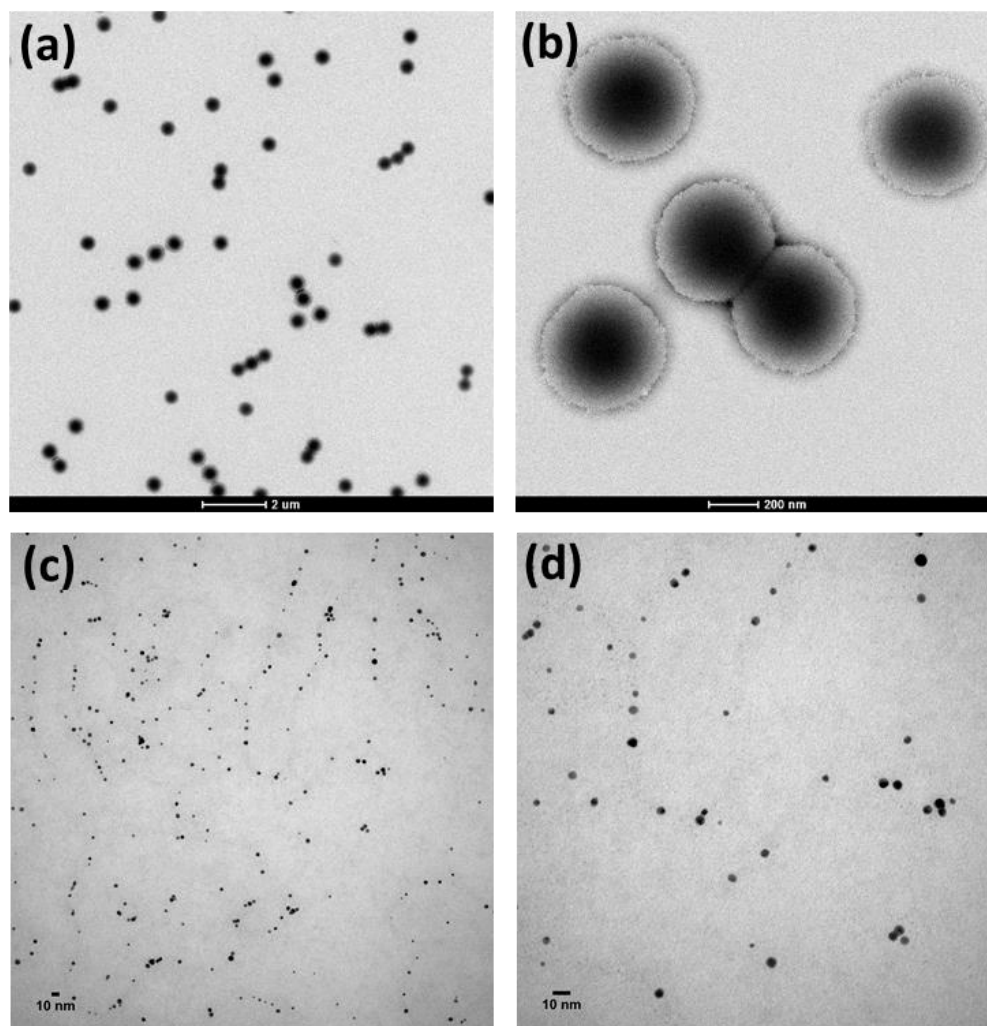


**Figure 2.2** TEM images of (a,b) bare  $\mu$ Gels and (c,d) Au NPs, at different magnifications. (e) histogram of Au NP diameter measured from TEM. The Au NP size was analyzed on 100 NPs using the software ImageJ.

They were negatively charged at physiological pH ( $\zeta$  potential = - 22 mV), due to the presence of carboxylic acid groups, which are deprotonated [ $pK_a \sim 4.8$ ]. The polyanionic  $\mu$ Gels could trap the fluorescent dyes (R6G, MB, Cy) after simple mixing of the microgel dispersion with dye solutions. As shown in Fig 2.3, the resulting fluorophore-loaded  $\mu$ Gels displayed the optical properties of each selected dye with absorption bands in the visible region and distinct fluorescence emission peaks at  $\lambda_{F[R6G]} = 560$  nm,  $\lambda_{F[MB]} = 686$  nm and  $\lambda_{F[Cy]} = 815$  nm. The excess of dyes (free dyes in solution) was removed by 1 cycle of centrifugation/redispersion and the supernatant was analyzed by UV-vis spectrophotometry to deduce the amount of dyes encapsulated within the  $\mu$ Gels  $Dye_{\text{uptake}}$  (eq. 1) and the loading efficiency (eq. 2).

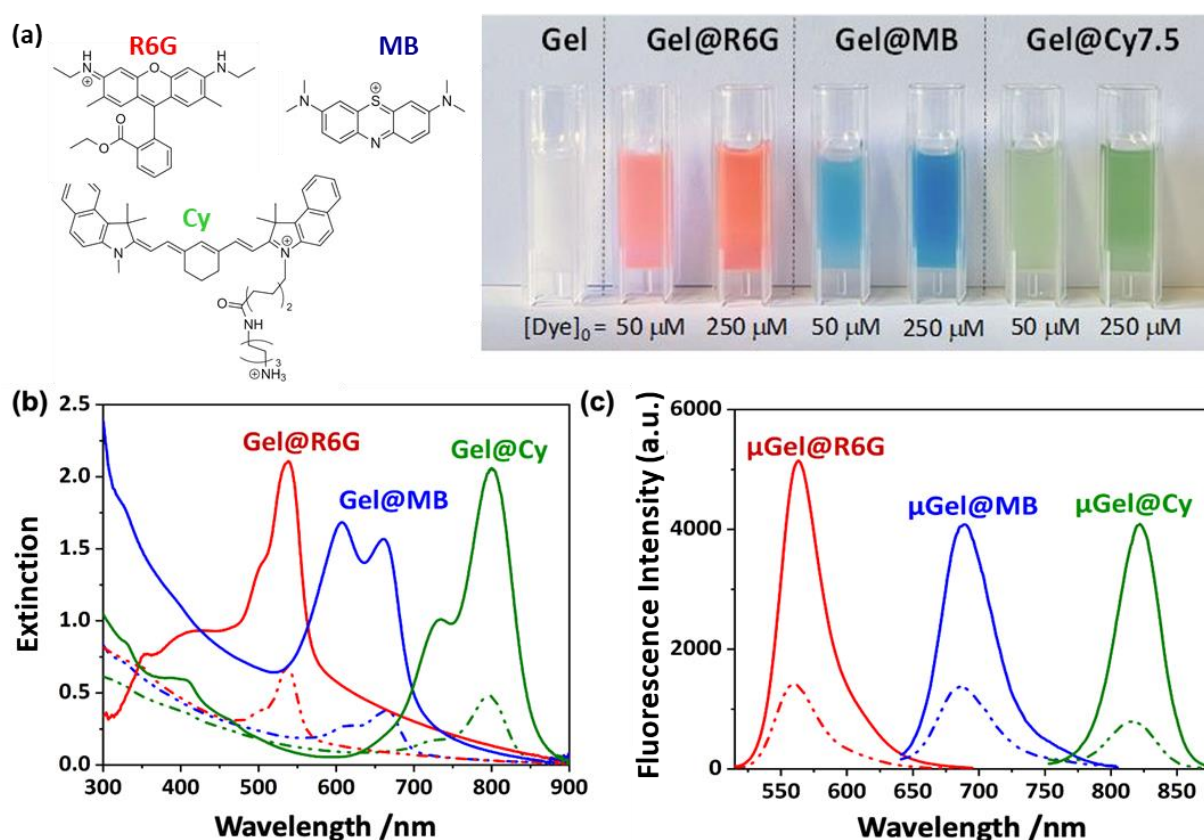


**Figure 2.3** (a) Chemical structure of the dyes and digital pictures of Gel@dye dispersions, prepared with initial dye concentrations  $[Dye]_0 = 50 \mu\text{M}$  or  $[Dye]_0 = 250 \mu\text{M}$ . (b) UV-vis spectra of the various Gel@dye samples at  $[Gel@dye] = 0.04 \text{ nM}$ , for an optical path length of 1 cm and (c) corresponding fluorescence spectra ( $\lambda_{\text{ex}[R6G]} = 490$  nm,  $\lambda_{\text{ex}[MB]} = 610$  nm,  $\lambda_{\text{ex}[Cy]} = 716$  nm). The dotted lines in (b) and (c) correspond to an initial dye concentration  $[Dye]_0$  of 50  $\mu\text{M}$ , while the continuous lines correspond to an initial dye concentration  $[Dye]_0$  of 250  $\mu\text{M}$ .

The dye loading efficiency reached *ca.* 94-100 % and the total amount of dyes loaded within the  $\mu$ Gels could be tailored from  $2.8 \pm 0.1$  to  $14.2 \pm 0.2$   $\mu\text{mol}$  of dyes per gram of  $\mu$ Gels, depending on the type of dyes and their initial concentration in the reaction mixture, as shown in Table 2.1.

$$Dye_{\text{uptake}} = \frac{\text{initial amount of dyes (mol)} - \text{excess amount of dyes (mol)}}{\text{mass of microgels (g)}} \quad (\text{eq. 1})$$

$$\text{Loading efficiency(\%)} = \frac{\text{initial amount of dyes (mol)} - \text{excess amount of dyes (mol)}}{\text{initial amount of dyes (mol)}} \times 100 \quad (\text{eq. 2})$$

The dye-loaded  $\mu$ Gels were then mixed with citrate-coated Au NPs (diameter  $3.8 \pm 0.9$  nm, Fig 2.2 c,d), yielding hybrid  $\mu$ Gels doped with both fluorescent molecules and plasmonic NPs (TEM images Fig 2.4).

**Table 2.1** Dye and Au NPs uptake ( $Dye_{\text{uptake}}$  and  $AuNPs_{\text{uptake}}$ ) and loading efficiency into  $\mu$ Gels.

Dye	$Dye_{\text{uptake}}$ ( $\mu\text{mol}$ of dyes per g of $\mu$ Gels) in Gel@Dye	$AuNPs_{\text{uptake}}$ (mg of Au NPs per g of $\mu$ Gels) in Gel@dye@Au(x)		
		x=1	x=3	x=5
<b>Loading efficiency in bracket</b>				
[R6G] <sub>0</sub> = 50 $\mu\text{M}$	$2.8 \pm 0.1$ (99%)	~ 50 (100%) <sup>b</sup>	~ 150 (100%) <sup>b</sup>	~ 250 (100%) <sup>b</sup>
[R6G] <sub>0</sub> = 250 $\mu\text{M}$	$14.2 \pm 0.2$ (96%)			
[MB] <sub>0</sub> = 50 $\mu\text{M}$	$2.8 \pm 0.1$ (99%)			
[MB] <sub>0</sub> = 250 $\mu\text{M}$	$13.9 \pm 0.3$ (96%)			
[Cy] <sub>0</sub> = 50 $\mu\text{M}$	2.9 <sup>a</sup> (100%)			
[Cy] <sub>0</sub> = 250 $\mu\text{M}$	$13.6 \pm 0.4$ (94%)			

<sup>a</sup>In the case of Gel@Cy, no absorption peak of cyanine could be detected in the supernatant after centrifugation, leading to an estimated dye loading efficiency of 100%. <sup>b</sup>The absorption peak of Au NPs in the supernatant after centrifugation was so weak for both  $[Dye]_0 = 50$  and  $250$   $\mu\text{M}$ , that the Au NPs loading efficiency was estimated to be approximately 100%.

Interestingly, the total amount of Au NPs uptaken by the  $\mu$ Gels could be finely tuned by performing several incubation experiments (number of incubation steps noted as x in Table 2.1 and Fig. 2.4), according to the following procedure: (i) mixing of Gel@dye with Au NPs solution ( $[Au \text{ NPs}] = 0.27$   $\mu\text{mol.L}^{-1}$ ); (ii) washing of the resulting  $\mu$ Gels *via* one cycle of centrifugation/redispersion; (iii) mixing of the Gel@dye@Au samples obtained in the previous step with fresh solutions of Au NPs. This three-steps process was repeated up to five times, leading to  $\mu$ Gels densely filled with Au NPs.

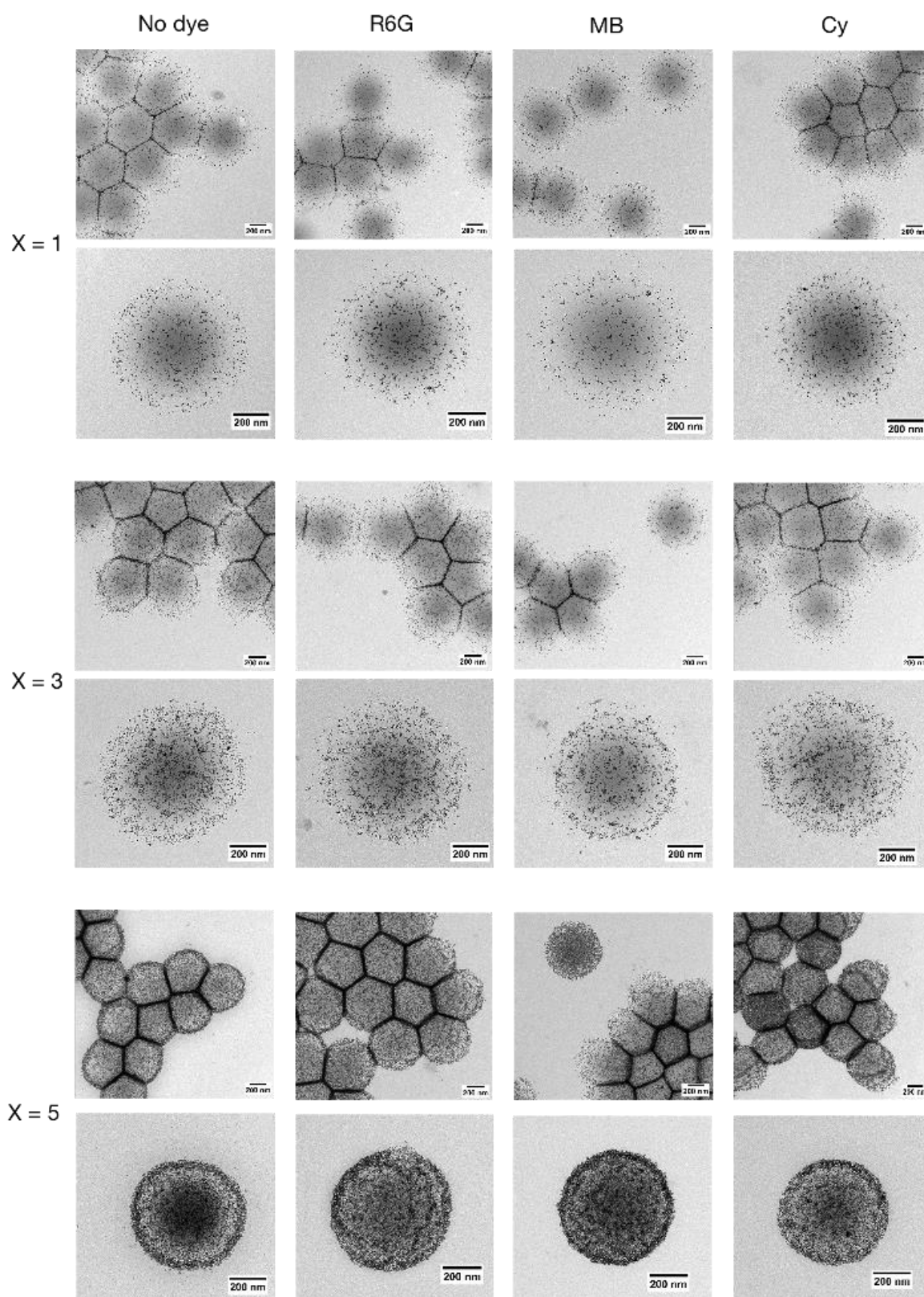


**Figure 2.4** Typical TEM images of hybrid  $\mu$ Gels obtained after incubation of bare (no dye) or Gel@dye particles with Au NPs. The number of incubation steps between the  $\mu$ Gels and the Au NPs is specified on the left by the values of  $x$ , varying from 1 to 5. All the Gel@dye particles were prepared from  $[Dye]_0 = 50 \mu M$  at pH 7.5 and RT while the concentration of Au NPs was  $[AuNPs] = 0.27 \mu mol.L^{-1}$ .

The excess of Au NPs (free Au NPs in solution) was removed by 1 cycle of centrifugation/redispersion in water and the supernatant was analyzed by UV-vis spectrophotometry to deduce the Au NPs uptake within the  $\mu$ Gels ( $\text{AuNPs}_{\text{uptake}}$ ) and loading efficiency (see Table 2.1). However, the  $\text{AuNPs}_{\text{uptake}}$  values may be slightly overestimated as some Au NPs were found adsorbed on the centrifuge tubes after centrifugation, thus artificially decreasing the amount of free Au NPs measured in the supernatant. It is noteworthy that even in the absence of dyes, the  $\mu$ Gels were able to load similar amounts of Au NPs (see Fig 2.4), showing that the presence of cationic dyes within the  $\mu$ Gels matrix is not responsible for the large Au NPs uptake. The encapsulation of Au NPs within the  $\mu$ Gels could rather be explained by a diffusion process driven by the concentration gradient of Au NPs from the solution to the core of the  $\mu$ Gels, as reported previously by E. Cazares-Cortes *et al.*<sup>112</sup> The hybrids obtained from the three different dyes were named Gel@dye@Au<sub>(x)</sub>, where *dye* stands for R6G, MB or Cy and x indicates the number of incubation steps between the  $\mu$ Gels and the Au NPs solution (x = 1, 3 or 5).

### 2.2.2 Optical properties

The optical properties of Gel@dye@Au<sub>(x)</sub> were analyzed using UV-vis spectroscopy (Fig 2.5). The plasmon band of Au NPs could be detected in the spectral range 510-560 nm while the presence of the dyes was revealed by absorption bands at 539 nm for R6G, 661 nm for MB and 808 nm for Cy.

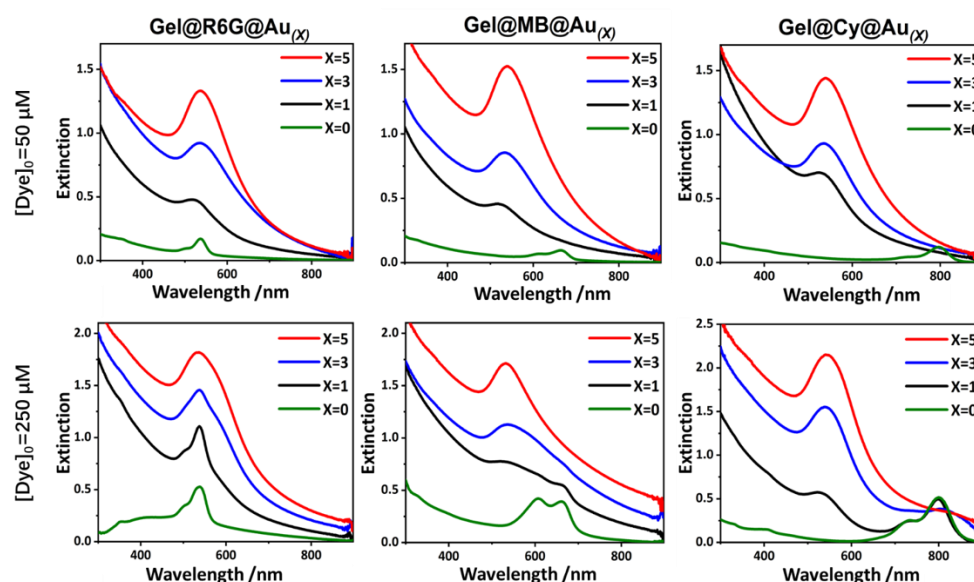


**Figure 2.5** UV-vis spectra of aqueous solutions (pH 7.5) of Gel@dye and Gel@dye@Au<sub>(x)</sub>, at 0.01 nM for an optical path length of 1 cm, with Dye = R6G, MB or Cy prepared from  $[\text{Dye}]_0 = 50 \mu\text{M}$  or  $250 \mu\text{M}$ . Spectra were obtained before incubation with Au NPs (green curves) or after 1 incubation (black curves), 3 incubation (blue curves) or 5 incubation cycles (red curves).

The uptake of Au NPs during the successive incubation steps with  $\mu$ Gels could be monitored by following the plasmon band intensity, which strongly increased after 1, 3 and 5 incubation cycles. Depending on the amount of dyes and Au NPs uptaken by the  $\mu$ Gels, the relative band intensities of each component appeared to vary strongly, revealing predominantly either the dye absorption bands (at high dye loading and low Au NPs uptake ( $x = 1$ )) or the plasmon peak (for high Au NPs uptake ( $x = 3$  or  $5$ )).

### 2.2.3 Stimuli-responsive properties

The stimuli-responsive properties of bare and hybrid  $\mu$ Gels were studied using DLS, by analyzing the swelling-deswelling behavior induced by temperature or pH changes. The pH was varied in steps of 0.5 over a range from 2 to 10 while the temperature was changed from 10°C to 70°C (Fig 2.6). For all samples,  $D_h$  was observed to decrease sharply as the temperature increases, emphasizing their thermoresponsive response. The inflection points observed in the curves of  $D_h$  vs temperature were used to estimate the volume phase transition temperature (VPTT). Below VPTT, interactions between the hydrophilic segments of the polymer network and water molecules are favored, with the formation of hydrogen bonds, resulting in the swelling of the  $\mu$ Gels. When the temperature increases above VPTT, water-polymer interactions are reduced due to hydrogen bond disruption while interactions between the hydrophobic portions of the polymer increase, leading to dehydration and self-aggregation of polymer chains, thus collapsing the microgel matrix and expelling water.

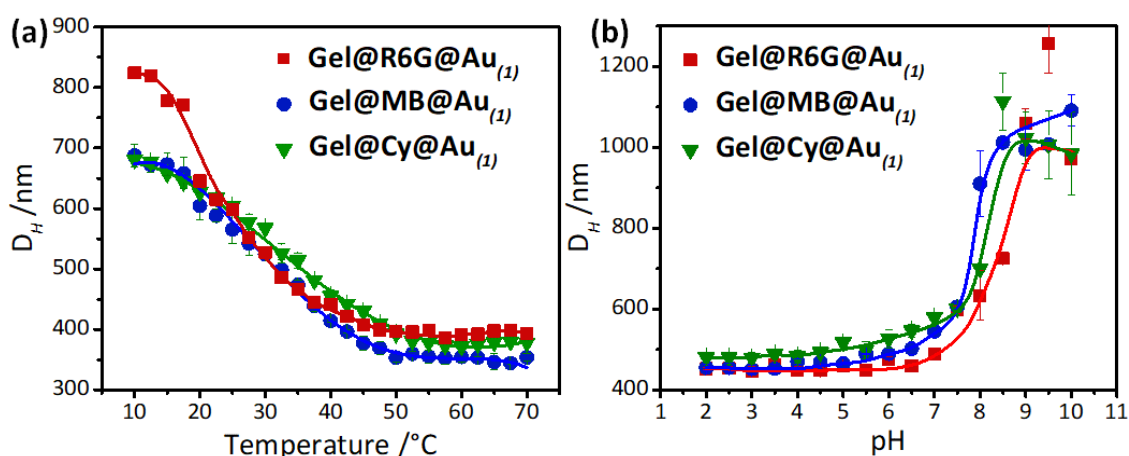


**Figure 2.6** Plots of  $D_H$  determined by DLS vs temperature (at pH 7) (a) and vs pH (at 25 °C) (b) for Gel@R6G@Au<sub>(1)</sub> (squares), Gel@MB@Au<sub>(1)</sub> (circles) and Gel@Cy@Au<sub>(1)</sub> (down triangles) hybrid  $\mu$ Gels. All Gel@dye@Au<sub>(1)</sub> samples were prepared from  $[Dye]_0 = 50 \mu\text{M}$ , after  $x = 1$  incubation cycle with Au NPs solution ( $[AuNPs] = 0.27 \mu\text{mol.L}^{-1}$ ). The lines were added for the sake of clarity but have no physical significance. (a) and (b) were measured with two different batches.

The VPTT was found to be  $\sim 30^\circ\text{C}$  for the hybrid particles, smaller than the VPTT of bare  $\mu\text{Gels}$  (*ca.*  $50^\circ\text{C}$ )<sup>6,7</sup>, indicating that the loading of dyes and Au NPs modifies the hydrophilic/hydrophobic balance of the hydrogel matrix. From the  $D_h$  values recorded at  $20^\circ\text{C}$  and  $60^\circ\text{C}$ , the maximum swelling ratio  $\alpha_{\text{max}}$  could be calculated, according to Eq. (3).

$$\alpha_{\text{max}} = \frac{V_{\text{swollen}}}{V_{\text{collapsed}}} = \frac{R_{h,\text{swollen}}^3}{R_{h,\text{collapsed}}^3} \quad (\text{eq. 3})$$

$\alpha_{\text{max}}$  characterizes the maximum amount of water that can be loaded and released by the  $\mu\text{Gels}$ . As shown in Table 2.2, a clear enhancement of the swelling/deswelling capacity of the hybrid networks is observed, compared to the pristine  $\mu\text{Gels}$ .

**Table 2.2** Characteristics of pristine and hybrid  $\mu\text{gels}$  at pH 7 determined from DLS and zeta potential measurements. All Gel@dye@Au(*l*) samples used for the Table below were prepared from  $[\text{Dye}]_0 = 50 \mu\text{M}$ , after  $x = 1$  incubation cycle with Au NPs solution ( $[\text{Au NPs}] = 0.27 \mu\text{mol.L}^{-1}$ ).

<i>Samples</i>	<i>D<sub>h</sub> at 20 °C nm (PDI)</i>	<i>D<sub>h</sub> at 60 °C nm (PDI)</i>	<i>ζ (mV)</i>	<i>α<sub>max</sub></i>
Bare $\mu\text{Gel}$	$592 \pm 11 (0.11)$	$396 \pm 4 (0.25)$	-21.7	3.3
Gel@R6G@Au( <i>l</i> )	$670 \pm 20 (0.20)$	$391 \pm 4 (0.18)$	-23.2	5.0
Gel@MB@Au( <i>l</i> )	$604 \pm 2 (0.20)$	$354 \pm 8 (0.16)$	-22.4	5.0
Gel@Cy@Au( <i>l</i> )	$627 \pm 2 (0.12)$	$372 \pm 6 (0.02)$	-20.8	4.8

The  $\mu\text{Gels}$  turned out to be concomitantly pH responsive. Indeed, raising the pH value from 2 to 10 resulted in a strong increase of  $D_h$  with a transition observed in the range 6-9 (see Fig 2.6 b). This pH-sensitive behavior can be explained on the basis of the Flory–Rehner theory<sup>118</sup>, in which the equilibrium swelling state of hydrogel networks is achieved when the total osmotic pressure  $\Pi_T$  tends towards 0.  $\Pi_T$  can be calculated by summing up the mixing ( $\Pi_{\text{mix}}$ ), elastic ( $\Pi_{\text{el}}$ ) and ionic ( $\Pi_{\text{ion}}$ ) contributions ( $\Pi_T = (\Pi_{\text{mix}} + \Pi_{\text{el}} + \Pi_{\text{ion}})$ )<sup>119</sup>. When the pH increases above the  $\text{pK}_a$  of carboxylic acid groups, their ionization rises the internal osmotic pressure due to electrostatic repulsions and free counterion motion, resulting in further swelling.

The UV-vis spectra of Gel@dye@Au(*x*) samples were recorded at two different temperatures ( $25$  and  $60^\circ\text{C}$ ) to reveal the influence of this stimulus upon the optical properties of the hybrid particles (Fig

2.7). As can be observed in Fig 2.7a, an increase in temperature, from 25 to 60 °C, had almost no effect on the shape of the plasmon band for the Gel@dye@Au<sub>(1)</sub> samples, reflecting the absence of plasmonic coupling between Au NPs within the  $\mu$ Gels matrix. This can be explained by the low density of Au NPs which are individually dispersed and isolated within the hydrogel matrix, even after temperature-induced particle shrinking. In contrast, as the uptake of Au NPs increases within Gel@dye@Au<sub>(3)</sub> and Gel@dye@Au<sub>(5)</sub>, their heating results in a broadening and a red shift of the plasmon band which is much more pronounced for the  $\mu$ Gels containing a high loading of Au NPs.

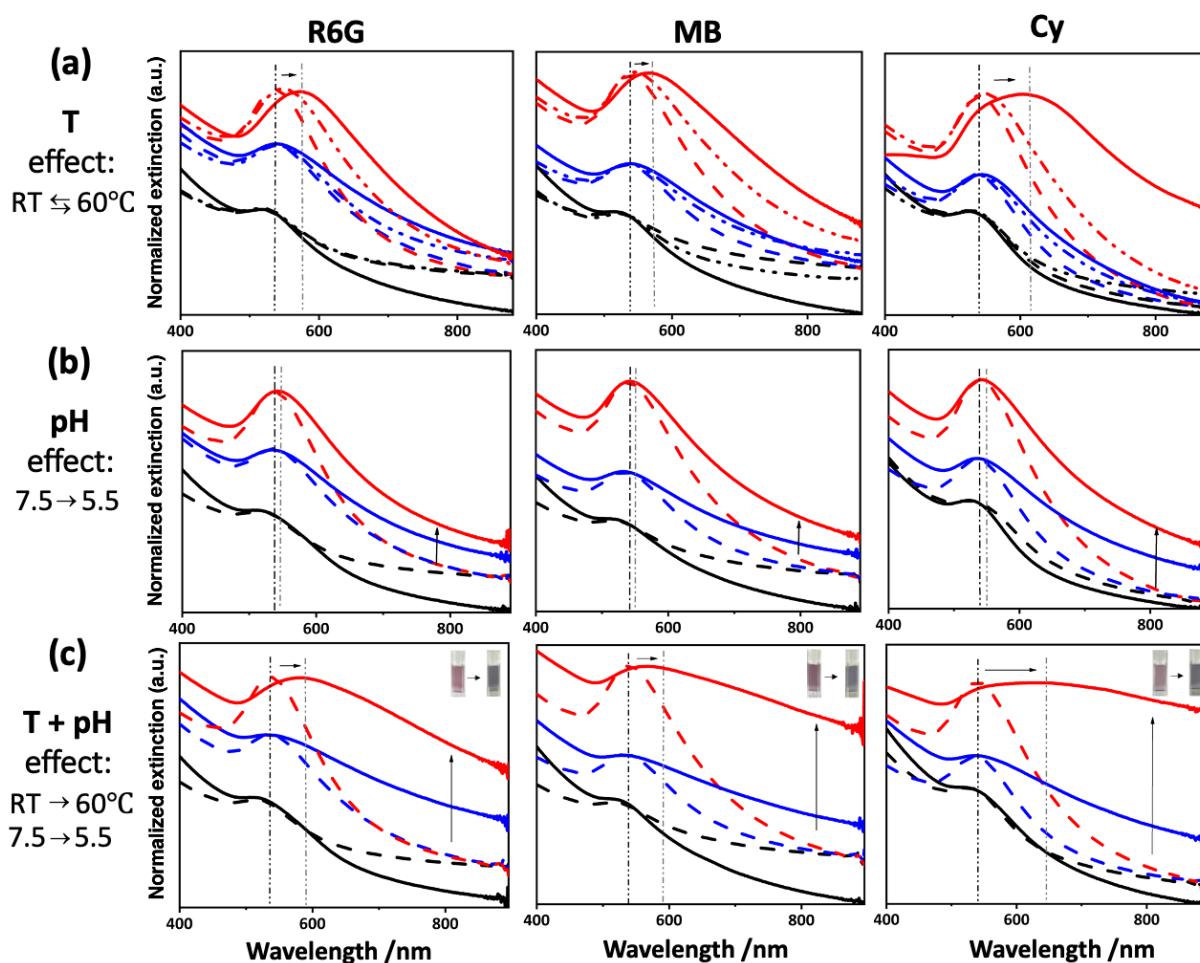


**Figure 2.7** Effect of temperature and pH stimuli upon the UV-vis spectra of Gel@dye@Au<sub>(x)</sub> samples at 0.01 nM, with dye = R6G, MB or Cy ([Dye]<sub>0</sub> = 50  $\mu$ M). The number of incubation steps between  $\mu$ Gels and Au NPs was varied from  $x = 1$  (black curves), to  $x = 3$  (blue curves) and  $x = 5$  (red curves). For each value of  $x$  (1-5), the spectra were normalized relative to the ones recorded at room temperature (RT) and pH 7.5 (dashed lines). (a) UV-vis spectra as a function of temperature: the full lines correspond to the spectra recorded at 60 °C and the dashed-dotted lines are the spectra after cooling down. (b) UV-vis spectra as a function of pH: the full lines correspond to the spectra recorded at pH 5.5. (c) Influence of both stimuli, *i.e.* temperature and pH: the full lines correspond to the spectra recorded at pH 5.5 at 60 °C. The insets display the optical pictures of the Gel@dye@Au<sub>(5)</sub> solutions before and after triggering the stimuli.

In this case, the huge density of Au NPs trapped inside the  $\mu$ Gels likely results in a short distance between them, which is even shorter once the  $\mu$ Gels have shrunk upon heating, leading to plasmonic coupling. These temperature-induced optical changes appear to be only partly reversible, which can be explained by the irreversible character of Au NP aggregation, due to strong van der Waals attraction between them. The effect of pH was also studied by recording the UV-vis spectra of the hybrid particles at pH 5.5 and 7.5. These pH values were selected to mimic both the physiological pH (7.4) and intracellular lysosomal pH (around 5.5). As observed in Fig 2.7b, the decrease in pH from 7.5 to 5.5 produced a broadening of the plasmon band, which can be explained by the presence of plasmonic coupling between NPs within the  $\mu$ Gels. This effect was much less pronounced than for the temperature stimulus, probably due to the choice of the pH range which lies at the bottom of the pH-induced volume-phase transition (see Fig 2.6b).

Nevertheless, a significant enhancement of the absorbance in the NIR region could be observed at pH 5.5 for Gel@dye@Au<sub>(3-5)</sub> samples, which is a key point for potential biomedical applications. Interestingly, the combination of the two stimuli (temperature and pH changes) appeared to further enhance the modifications of the plasmon band shape and wavelength, as observed in Fig 2.7c. These results thus show that the presence of dyes and Au NPs trapped within the microgels do not prevent the conformational changes of the copolymer network, which retain its stimuli-responsive properties.

The morphology changes of Gel@dye@Au<sub>(5)</sub> samples induced by pH and temperature stimuli were observed by TEM (see Fig 2.8). A temperature increase from RT to 60 °C appears to induce both (i) a  $\mu$ Gel shrinkage with an overall decrease in diameter and (ii) the aggregation of Au NPs within the polymer network. Regarding the pH stimulus, a decrease in pH from 7.5 to 5.5 has much less effect on the size of the  $\mu$ Gels, which is consistent with the DLS measurements but it induces a clear aggregation of the Au NPs. Interestingly, the combination of these two stimuli further amplifies these morphological modifications ( $\mu$ Gel collapse and Au NPs aggregation).

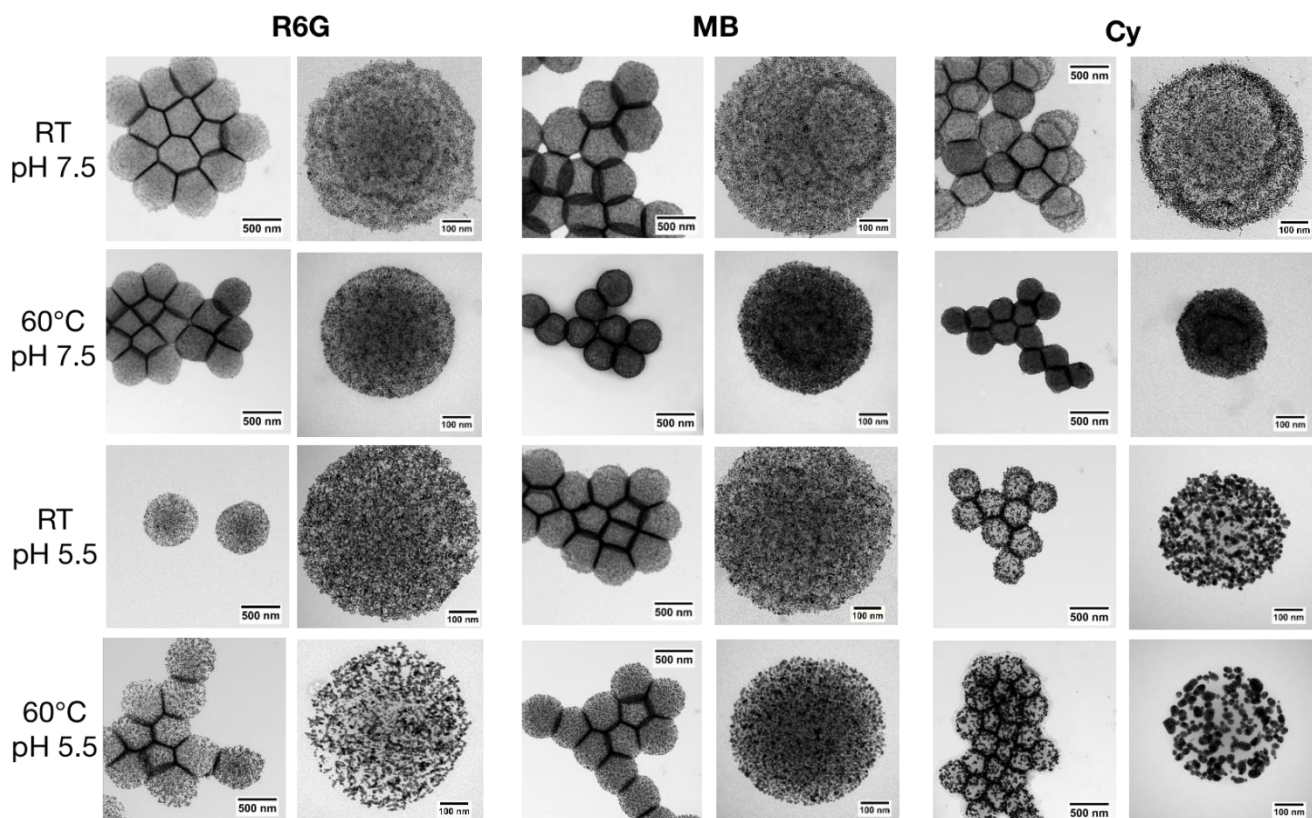


**Figure 2.8** TEM images at different magnifications of Gel@dye@Au<sub>(5)</sub> samples prepared from [Dye]<sub>0</sub> = 50 μM, recorded initially at room temperature (RT) and pH 7.5 and then submitted to different stimuli. The effect of temperature (T) corresponds to the heating of the colloidal dispersions to 60 °C, the effect of pH corresponds to the decrease of pH to 5.5 while the effect of temperature and pH indicates that the hybrid particles were subject to both stimuli simultaneously.

The structure of the μGels loaded with the different dyes (R6G, MB, Cy at [dye]<sub>0</sub> = 50 μM) and Au NPs (x = 1 or 5) has been studied by synchrotron small angle X-ray scattering (SAXS) on the SOLEIL/SWING beamline (Fig 2.9 and 2.10). This non-denaturing method allowed us to characterize the structure of the μGels and NPs on several length scales (*i.e.* 1-300 nm). We recall that the intensity scattered by an assembly of spheres of volume V depends on their average size through the sphere form factor P(q) and their organization through the average structure factor S(q) as follows (eq. 4):

$$I(q) = \Phi \cdot V \cdot (\Delta\rho)^2 \cdot P(q) \cdot S(q) \quad (\text{eq. 4})$$

where  $\Phi$  is the volume fraction of the particles, q is the norm of the scattering vector and  $\Delta\rho = \rho_{\text{sphere}} - \rho_{\text{water}}$  is the contrast of X-ray scattering length density ( $\rho$ ) between the spheres and water.

We first considered reference suspensions composed purely of  $\mu$ Gels or Au NPs. The scattering curve of  $\mu$ Gel suspension (*i.e.*  $x = 0$ , Figure 2.9a) exhibits oscillations at low  $q$  (*i.e.*  $q < 0.01 \text{ \AA}^{-1}$ ) which correspond fairly well to the form factor of non-interacting (*i.e.*  $S(q) = 1$ ) polydisperse spheres with a mean diameter  $D = 500 \text{ nm}$  and a log. normal size distribution (polydispersity:  $\sigma = 0.05$ ). This analysis agrees with the DLS result (*i.e.*  $D_h = 592 \text{ nm}$ ) considering that our SAXS measurement should underestimate the contribution of dangling chains on the surface of  $\mu$ Gels compared to DLS measurements. The scattering curve of Au NP suspension (Figure 2.9b) differs clearly from the  $\mu$ Gel curve by the absence of oscillations at small  $q$  and a decay at large  $q$  corresponding to the sphere form factor of polydisperse spheres with a mean diameter  $D \approx 3.3 \text{ nm}$  and log. normal polydispersity (*i.e.*  $\sigma = 0.4$ ). We then characterized the different types of  $\mu$ Gels loaded with dyes and Au NPs at two different pH (Figures 2.9c, 2.9e and 2.9g). Overall, all the scattering curves have the same shape. At low  $q$  (*i.e.*  $q < 0.01 \text{ \AA}^{-1}$ ), the scattered signal is dominated by the well-defined oscillation series corresponding to the contribution of the  $\mu$ Gel beads while at high  $q$  (*i.e.*  $q > 0.03 \text{ \AA}^{-1}$ ) the scattered signal is dominated by the contribution of the NPs.

As expected, the analysis of the high  $q$  domain shows that the size and polydispersity of Au NPs is the same in all cases and corresponds to the result obtained for a suspension of free Au NPs. Knowing the average size of Au NPs, one can exploit the fact of working in absolute units to calculate their concentration in the medium, using the following expression:  $c = \frac{I(q \rightarrow 0) \rho^2 N_A}{M_w (\widetilde{\rho}_P - \widetilde{\rho}_0)^2}$  with the gold volumic mass  $\rho \approx 19.3 \text{ g/cm}^3$ , the Avogadro number  $N_A \approx 6.022 \times 10^{23} \text{ mol}^{-1}$ , the molecular mass of Au NPs  $M_w \approx 200 \text{ kg/mol}$ , the difference of X-Ray scattering length density between Au NPs ( $\widetilde{\rho}_P$ ) and water ( $\widetilde{\rho}_0$ ):  $\widetilde{\rho}_P - \widetilde{\rho}_0 \approx (130 - 9.46) \times 10^{10} \text{ cm}^{-2}$ . It appears that the concentration increases on average by a factor of 5 when  $x$  (number of incubation steps between the  $\mu$ Gels and the Au NPs) increases from 1 to 5 (see Table 2.3), demonstrating the possibility to finely tune the amount of Au NPs loaded within the  $\mu$ Gels via the number of incubation steps. Another significant effect related to the increase of  $x$  concerns the local organization of Au NPs. This effect is highlighted by plotting the ratio between the total intensity scattered by the suspension of Gel@dye@Au ( $I_{\text{Tot.}}(q)$ ) and the intensity scattered by a suspension of Au NPs at the same concentration ( $I_{\text{AuNP}}(q)$ ) (Figure 2.9 d, f, h). At high  $q$  (*i.e.*  $q > 0.03 \text{ \AA}^{-1}$ ), this ratio corresponds to the structure factor  $S(q)$  of the NPs inside the

$\mu$ Gels. As shown on Figures 2.9d, f, h, the increase of  $x$  from 1 to 5 leads to the appearance of a structure peak revealing a correlation distance between Au NPs.

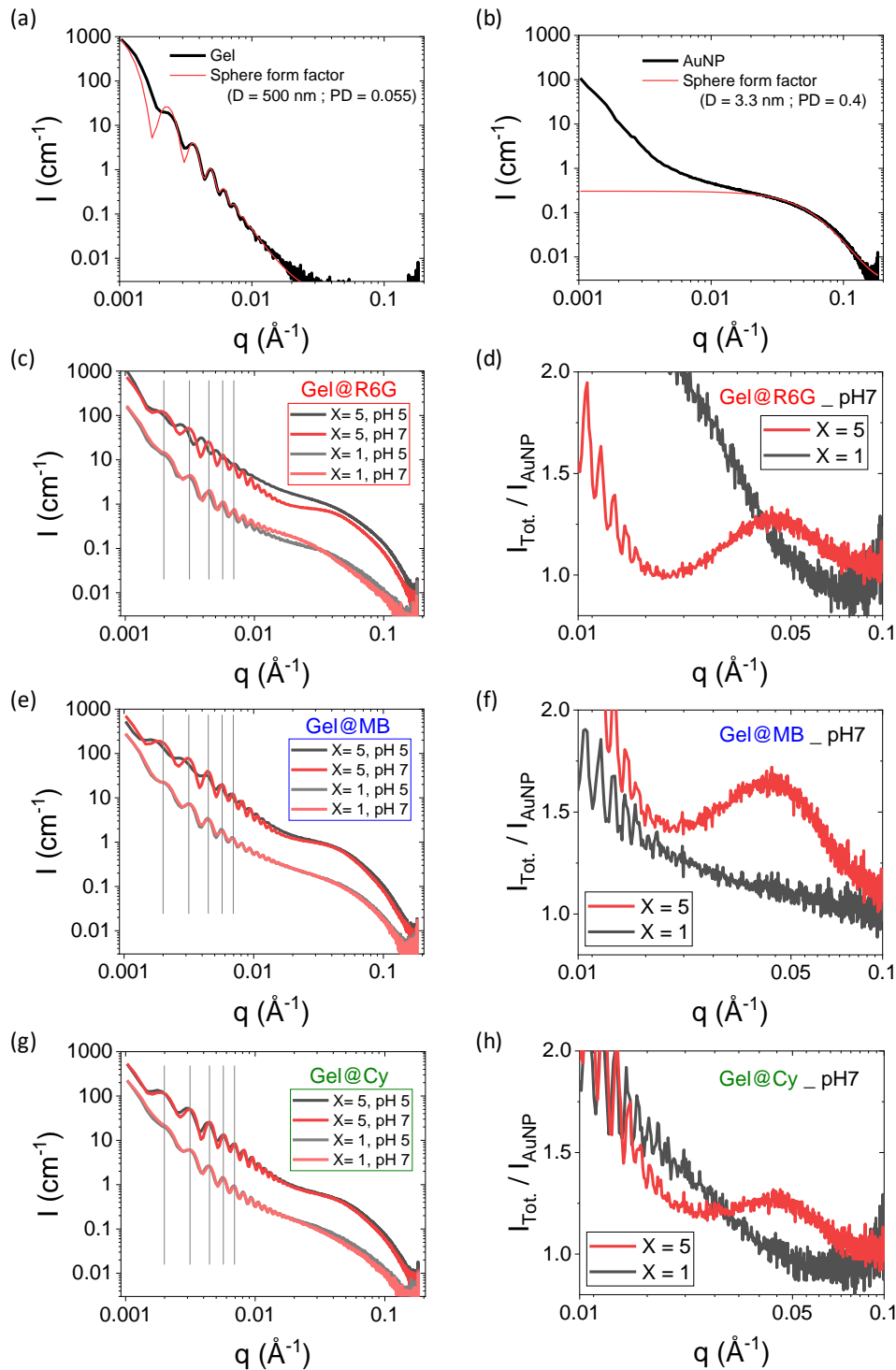


**Figure 2.9** Small angle X-ray scattering (SAXS) patterns of aqueous solutions (pH = 7 or 5) of (a)  $\mu$ Gels, (b) Au NPs and (c, e, g) Gel@dye@Au<sub>(x)</sub>, with dye = R6G, MB or Cy and  $x = 1$  or 5. All measurements were done at room temperature. Figures d, f and h represent the ratio between the total intensity ( $I_{\text{Tot.}}(q)$ ) scattered by the suspension of Gel@dye@Au<sub>(x)</sub> and the intensity scattered by a suspension of Au NPs at the same concentration ( $I_{\text{AuNP}}(q)$ ) as a function of  $q$  at pH 7. The curves corresponding to pH 5 are available in Fig S2.10.

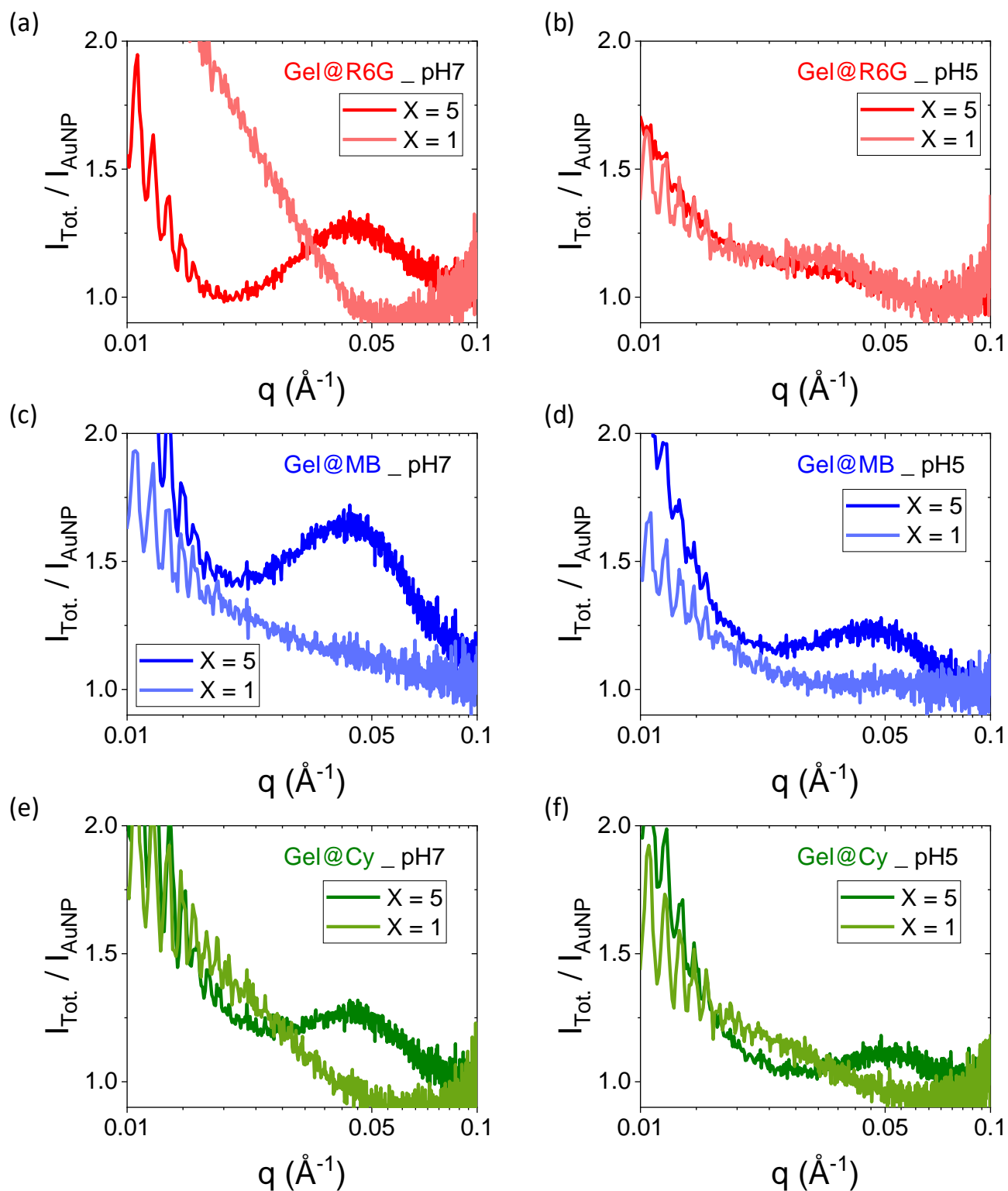


**Figure 2.10** Small angle X-ray scattering (SAXS) characterization of aqueous solutions (pH = 7 or 5) of Gel@dye@Au(x), with dye = R6G, MB or Cy and X = 1 or 5. All measurements were done at room temperature. Evolution of the ratio between the total intensity ( $I_{\text{Tot.}}(q)$ ) scattered by the suspension of Gel@dye@Au(x) and the intensity scattered by a suspension of AuNPs at the same concentration ( $I_{\text{AuNP}}(q)$ ) as a function of  $q$ .

Interestingly, this peak tends to widen and the position of the peak maximum ( $q^*$ ) shifts towards the large  $q$  as the pH decreases, such as:  $q^* \approx 0.035 \text{ \AA}^{-1}$  at pH 7 and  $q^* \approx 0.05 \text{ \AA}^{-1}$  at pH 5 (Fig. 2.10). This shift reflects a decrease in the average interparticle distance (edge-to-edge) from 14 nm to 9 nm, in qualitative agreement with the result of UV-Vis spectroscopy showing an amplification of the plasmonic coupling with a decrease of pH. Finally, we analyzed the low  $q$  domain to characterize the behavior of the  $\mu$ Gels in the different conditions. This analysis shows that the scattering curves are almost superposable in all cases (Figures 2.9c, 2.9e and 2.9g) with diameters around 560 nm. Thus the size variation detected by DLS and suggested by the evolution of the structure peak for  $x = 5$  does not appear significantly in our analysis. This counter intuitive result may be explained by the fact that the  $\mu$ Gel structure is heterogeneous and reorganizes with pH without apparent modification of the scattering curves at low  $q$ .

**Table 2.3** Au NP mass concentrations in Gel@dye@Au( $x = 1$  or  $5$ ) samples determined from the SAXS measurements shown in Figures 2.9 and 2.10.

Samples	pH = 5		pH = 7	
	x = 1	x = 5	x = 1	x = 5
Gel@R6G@Au( $x$ )	0.08 g.L <sup>-1</sup>	1.01 g.L <sup>-1</sup>	0.11 g.L <sup>-1</sup>	0.55 g.L <sup>-1</sup>
Gel@MB@Au( $x$ )	0.16 g.L <sup>-1</sup>	0.88 g.L <sup>-1</sup>	0.17 g.L <sup>-1</sup>	0.94 g.L <sup>-1</sup>
Gel@Cy@Au( $x$ )	0.10 g.L <sup>-1</sup>	0.56 g.L <sup>-1</sup>	0.09 g.L <sup>-1</sup>	0.50 g.L <sup>-1</sup>

#### 2.2.4 Photothermal properties

To assess the photothermal performances of Gel@dye@Au( $x=1$  or  $5$ ), the temperature changes of particle dispersions under illumination were recorded using a thermal imaging near infrared camera (Fig 2.11). The illumination was performed with an 808 nm laser at power densities of  $1.1 \text{ W.cm}^{-2}$  and the temperature was measured every 0.033 s for 300 s. The heating profiles were investigated on 100  $\mu$ L of particle dispersions at fixed  $\mu$ Gel ( $1.73 \text{ mg.mL}^{-1}$ ) and dye concentration (2.8-2.9  $\mu\text{mol}$  of dyes per g of  $\mu$ Gels, which corresponds to  $[\text{Dye}]_0 = 50 \text{ }\mu\text{M}$  in Table 2.1) but different Au NPs loading ( $x = 0, 1$  or  $5$ ). Illumination of the dye-loaded  $\mu$ Gels with no Au NPs trapped inside their matrix, did not result in any appreciable temperature variation, except for Gel@Cy which exhibits a small temperature increase ( $\Delta T = 2 \text{ }^\circ\text{C}$ ) within the first 25 s, likely due to Cy absorption at this laser excitation. This

slight temperature increase is followed by a fast decline that can be explained by the well-known photo-instability of Cy,<sup>120</sup> for which the main photobleaching pathway has been shown to be initiated by its triplet state that sensitizes oxygen resulting in the formation of singlet oxygen<sup>121</sup>. In the presence of Au NPs loaded within the gels, the suspensions showed a more significant time-dependent increase in temperature (Fig 2.11), due to the photothermal properties of Au NPs in dye-loaded  $\mu$ Gels, converting light into heat. As expected, the heat release appeared much higher for densely loaded  $\mu$ Gels (Gel@dye@Au<sub>(5)</sub>) with  $\Delta T$  values over 20 °C than for weakly doped  $\mu$ Gels (Gel@dye@Au<sub>(1)</sub>), showing  $\Delta T$  values of *ca.* 2-5 °C.

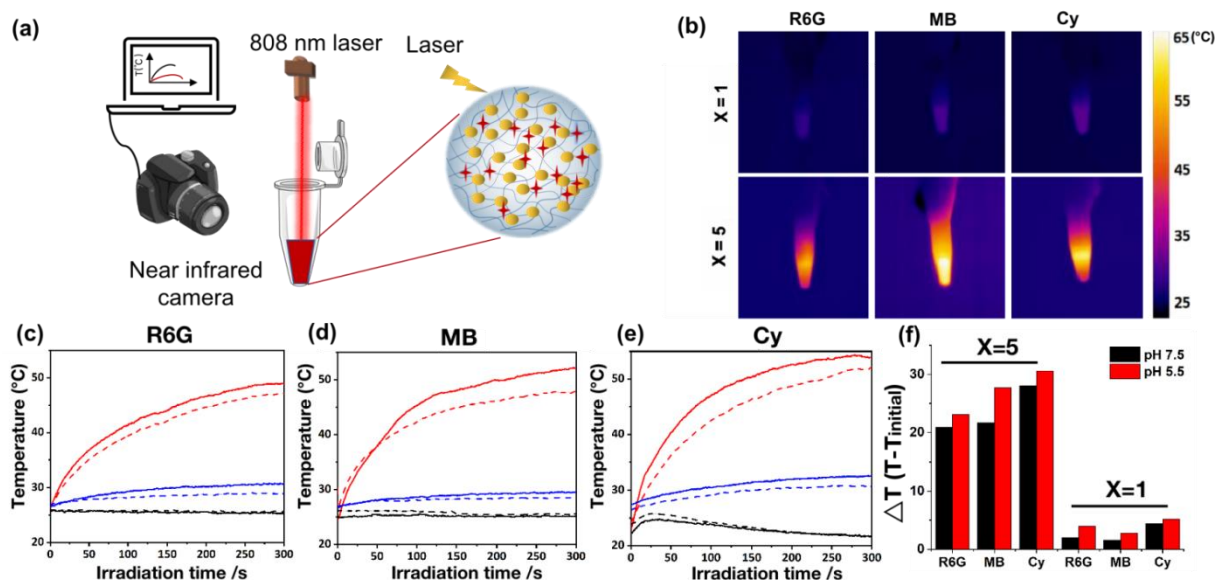


**Figure 2.11** Heating properties of Gel@dye@Au<sub>(x=0, 1 or 5)</sub> suspensions at 0.04 nM exposed to a 808 nm laser at 1.1W/cm<sup>2</sup>. (a) Illustration of the experimental setup, (b) Pictures of the suspensions exposed to the laser and monitoring of the heating by an infrared camera, (c-e) Heating profile of Gel@dye@Au<sub>(x)</sub> at different pH. The plain lines correspond to pH 5.5 while the dashed lines correspond to pH 7.5. The colors of the lines correspond to: x=0, *i.e.* no Au NPs (black lines), x=1 (blue lines), x=5 (red lines), (f) Temperature increment after irradiation for 300 s for the different Gel@dye@Au<sub>(x=1 or 5)</sub> at pH 5.5 and pH 7.5.

Interestingly, the enhancement of the heating capacities of Gel@dye@Au<sub>(5)</sub> compared to Gel@dye@Au<sub>(1)</sub> was higher than expected and could not be only related to the higher number of Au NPs within the microgel matrix. Indeed, the  $\Delta T$  values were 6 to 10 times higher for densely filled  $\mu$ Gels ( $x = 5$ ) while the amount of Au NPs was no more than 5 times higher. The superior heating capacities of Gel@dye@Au<sub>(5)</sub> could be explained by the presence of strong electromagnetic coupling between Au NPs at high loading, generating hot spots as suggested by the stronger interactions between Au NPs revealed by SAXS and observed on TEM pictures of  $\mu$ Gels as well as coupling

between the Cy dye and Au NPs. Additionally, the gradual shrinking of the  $\mu$ Gels with temperature enhances the optical attenuation. A further improvement of the heating capacities of Gel@dye@Au<sub>(5)</sub> was observed by lowering the pH from 7.5 to 5.5, probably due to enhanced plasmon coupling of Au NPs and of Au NPs and dye within the  $\mu$ Gels, consistent with the UV-vis spectra at pH 5.5 (cf. Fig 2.7).

### 2.2.5 Viability assay, cellular uptake, and phototoxicity in colon carcinoma cells

In order to assess the usability and behavior of such smart stimuable  $\mu$ Gel upon cellular internalization, we first investigated the effect of Gel@dye@Au<sub>(x)</sub> samples on the viability of CT26 colon carcinoma cell lines by measuring their metabolic activity using the Alamar Blue assay. Cells were incubated for 24 hours in a complete medium containing Gel@dye@Au<sub>(1,5)</sub> (see details of the Materials & Methods section). To compare the effect of the hybrid particles to that of the free dyes, cells were also incubated with the same dye concentrations as the one loaded within the  $\mu$ Gels (final dye concentrations in the cell culture medium of 5  $\mu$ M and 25  $\mu$ M, respectively, for the Gel@dye@Au<sub>(1,5)</sub> samples prepared from either [dye]<sub>0</sub> = 50  $\mu$ M or 250  $\mu$ M). As observed in Fig 2.12, at these concentrations, free R6G and MB exhibit a high cytotoxicity, with only 30% and 20 % of cell viability respectively, at 5  $\mu$ M and less than 10 % at 25  $\mu$ M.

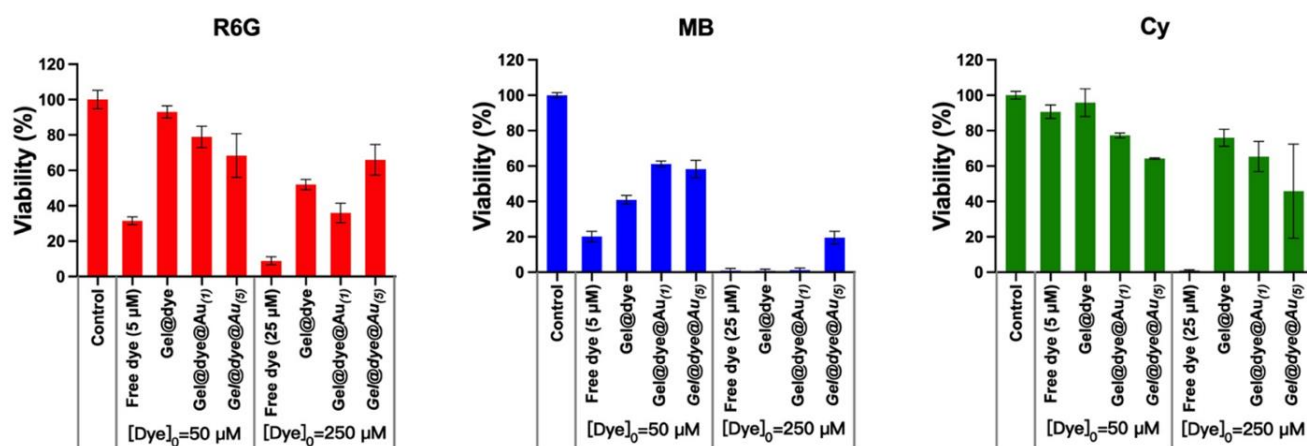


**Figure 2.12** Viability of CT 26 cells tested by Alamar Blue assay after 24 h of incubation with free dyes, Gel@dye or Gel@dye@Au samples prepared from [Dye]<sub>0</sub> = 50  $\mu$ M or 250  $\mu$ M with Dye = R6G, MB or Cy and Au NPs (x=1 and 5). For the Gel@dye@Au<sub>(1 or 5)</sub> samples prepared from either [dye]<sub>0</sub> = 50  $\mu$ M or 250  $\mu$ M, the final dye concentrations in the cell culture medium are 5  $\mu$ M and 25  $\mu$ M, respectively.

Cy appears toxic also but less than the other dyes at 5  $\mu\text{M}$  with 90 % viability while it falls to almost 0% at 25  $\mu\text{M}$ . Interestingly, after their uptake by the  $\mu\text{Gels}$ , the dyes displayed much lower toxicity than in the free state, at equivalent concentrations. Such lower toxicity might be due to different internalization pathway and intracellular release when the dyes are vectorized by the  $\mu\text{Gels}$ . To better understand the fate of the  $\mu\text{Gels}$  upon interactions with tumor cells, cell were observed by laser confocal microscopy at different incubation times with the  $\text{Gel@Dye@Au}_{(1)}$  and  $\text{Gel@Dye@Au}_{(5)}$  prepared from either  $[\text{dye}]_0 = 50 \mu\text{M}$  (Figure 2.13) or  $[\text{dye}]_0 = 250 \mu\text{M}$  (Figure 2.14). The characteristic fluorescence of each dyes could be observed in cells, with progressive increase of intracellular fluorescence. The dyes loaded in the  $\mu\text{Gels}$  clearly act as fluorescence tracers to visualize  $\mu\text{Gel}$  uptake.

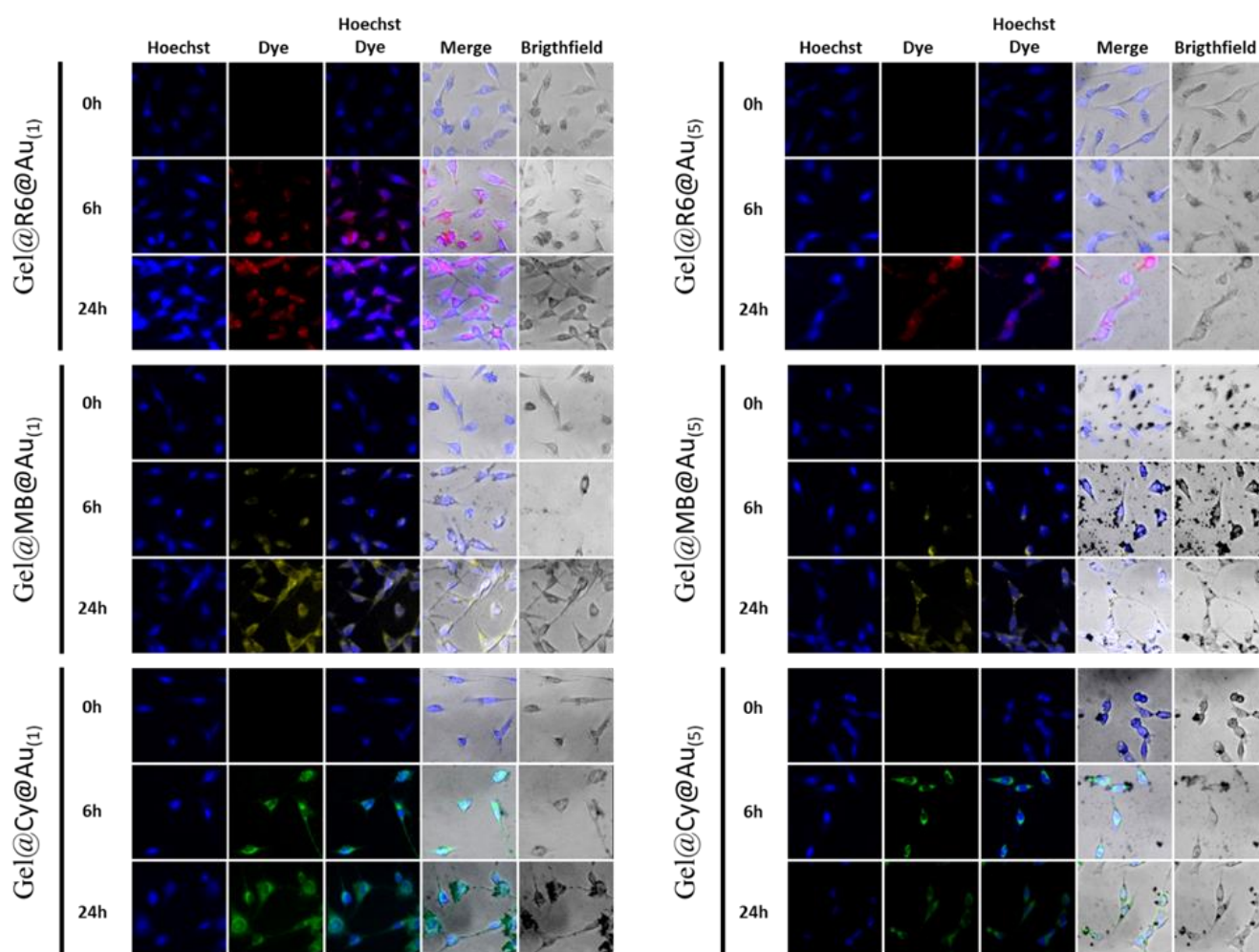


**Figure 2.13** Bright field and fluorescence microscopy of CT26 cells incubated for 24 h with  $\text{Gel@dye@Au}_{(1 \text{ or } 5)}$ , ( $[\text{Dye}]_0 = 50 \mu\text{M}$ ). After washing to remove exceeded  $\mu\text{Gels}$ , CT26 cells were further incubated for  $t=0, 6 \text{ h}$  and  $24 \text{ h}$  and observed by HCS CellInsight CX7.

After 5 min (0 h), no fluorescence is associated to cells. After 6 h of incubation, most of the cells show fluorescence with a cytoplasmic and perinuclear localization and the fluorescence intensity increases after 24H of incubation for R6G and MB, whereas it tends to saturate at 24 h for Cy. A similar behavior was observed with  $\mu$ Gels with the highest dye concentration (Figure 2.14). This suggests a time dependent uptake of  $\mu$ Gels consistent with the process of endocytosis of sub-micrometer hydrogels. Note that at  $x=5$ , the aggregation of Gel@dye@Au<sub>(5)</sub> can be observed on bright field images, featuring dark spots outside (at 6 h, particularly for MB) and inside the cells (particularly at 24 h) showing simultaneous gold nanoparticle uptake. The fluorescence of the dyes is not associated with the dark spots when they are located outside the cells, probably due to fluorescence quenching whereas it becomes apparent inside the cells, likely due to the release of the dyes from the hybrid  $\mu$ Gels or segregation of dye and Au NPs once inside the cells.

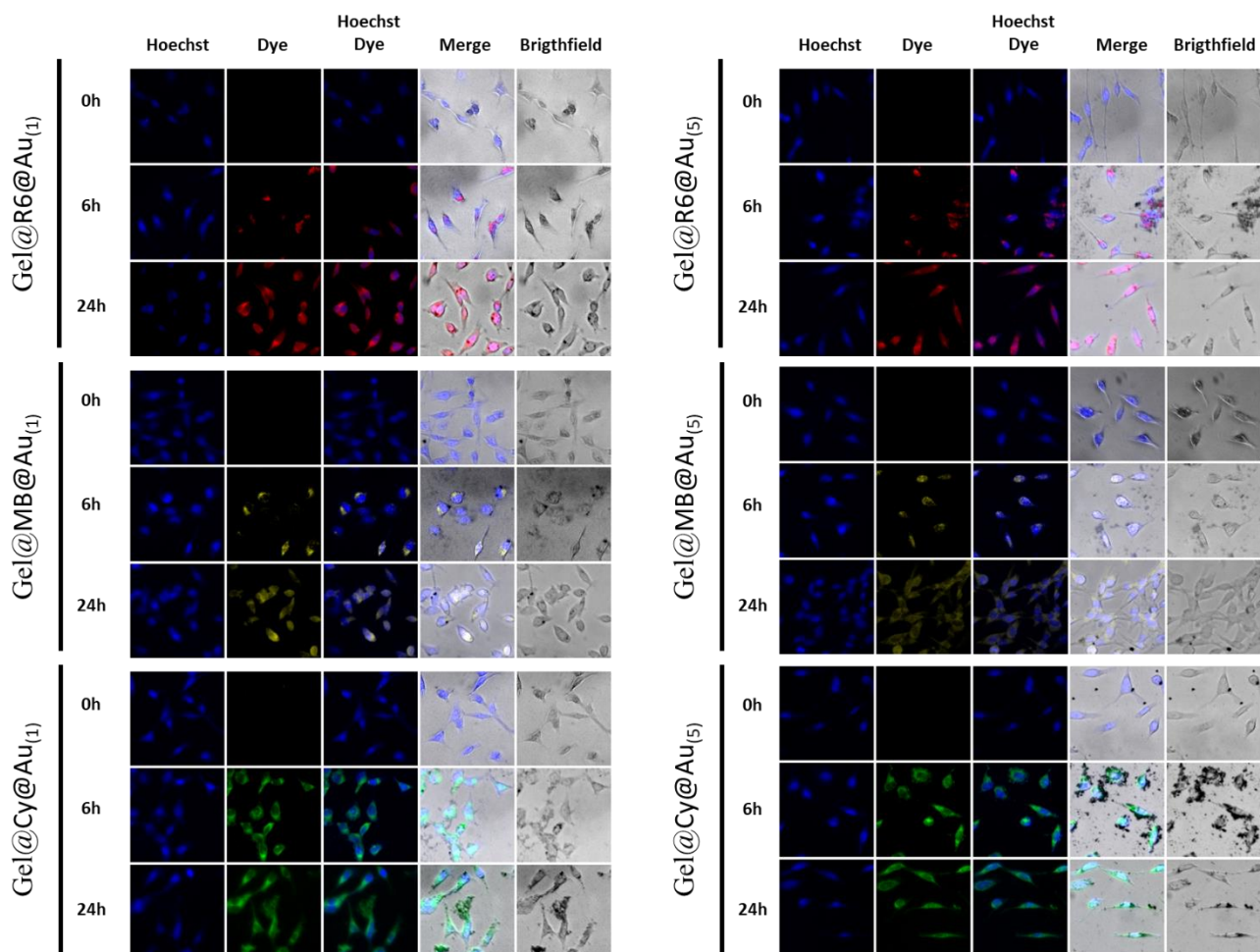


**Figure 2.14** Bright field and fluorescence microscopy of CT26 cells incubated for 24 h with Gel@dye@Au<sub>(1 or 5)</sub>, ([Dye]<sub>0</sub> = 250  $\mu$ M). After washing to remove exceeded  $\mu$ gels, CT26 cells were further incubated for  $t=0, 6$  h and 24 h and observed by HCS CellInsight CX7.

We further investigated the photothermal effect of Gel@dye@Au<sub>(x)</sub> on the viability of CT26 tumor cells. Due to the observed toxicity of samples loaded with high dye concentrations, we only focused in this study on the lowest dye concentrations for hydrogel loading ([dye]<sub>0</sub> = 50 μM). Monolayers of attached cells, previously incubated during 24 h with Gel@dye@Au<sub>(x)</sub> and rinsed, were irradiated for 10 min using 808 nm laser (power 1 and 2W/cm<sup>2</sup>). The control experiments were performed on CT26 tumor cells, without incubation with the μGel samples but irradiated with the same laser fluence. As shown in Figure 2.15, no cytotoxicity was observed with laser only.

In line with dark toxicity study, cell treatment with Gel@Dye@Au<sub>(x=1 or 5)</sub> (prepared from [dye]<sub>0</sub> = 50 μM) reduced cell viability to approximately 80% for x=1 and 70% for x=5 when no laser was applied (0 W/cm<sup>2</sup>). After irradiation, the cell viability decreased drastically. The phototoxicity is increased with laser power (1 and 2 W/cm<sup>2</sup>) and with Au NPs loading (x=1 or 5) in a dose dependant manner. Under optimal conditions (x=5, power of 2 W/cm<sup>2</sup>), cell viability is only 40% for R6G, 30% for MB and 15% for Cy.

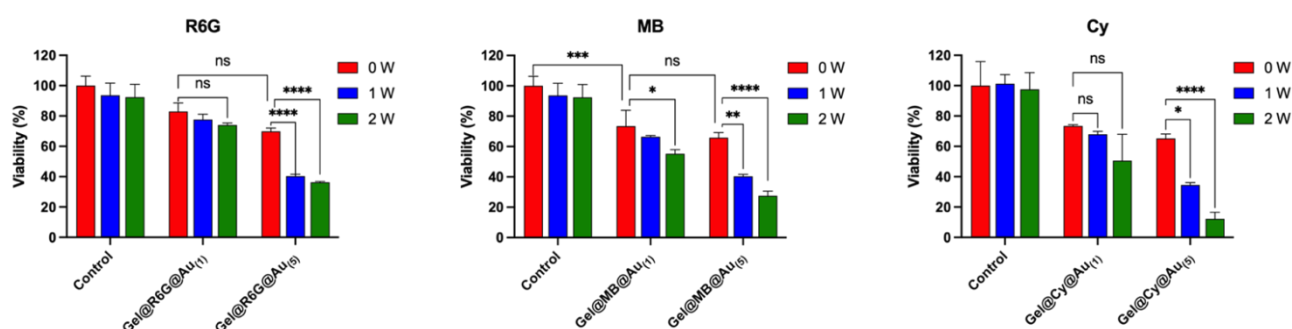


**Figure 2.15** Phototoxicity of Gel@dye@Au<sub>(1 or 5)</sub> measured by Alamar Blue assay on CT26 cells after 10 min irradiation at 808 nm laser at 1 and 2W/cm<sup>2</sup>. The results are shown as mean ± SEM (n=3). Two-way ANOVA for the analysis, \*\*\*\*p-value <0.0001, \*\*\*p-value <0.001, \*\*p-value<0.01, \*p-value<0.1 and ns represent no significant difference.

The fact that Gel@Cy@Au<sub>(5)</sub> produces the highest cell death after laser irradiation is consistent with their absorbance signal in the near infrared region, which combines the absorption of the cyanine and Au NPs. The absorbance is probably further increased by the effect of the low pH related to lysosomal uptake of the μGels and of the local increase of temperature. Interestingly the μGels with methylene blue induces an important cell death which might not be directly related to light-to-heat conversion at 808 nm. Dhaval Sanchala et al. explains the anticancer activity of methylene blue via the inhibition of

Heat Shock Protein 70 (HSP70)<sup>122</sup>. Such effect could participate to the high phototoxicity induced by Gel@MB@Au<sub>(1)</sub> irradiated with NIR laser since MB could diminish the HSP 70 cell defense mechanism against thermal stress.

An extensive study (going beyond the focus of the present paper) is underway to investigate the intracellular fate and optical properties of  $\mu$ Gels with tunable Au NPs load and plasmon coupling in cells: we expect the lysosomal acidic pH, on one part, and photothermal effect, on the other part, to transform the intracellular structures of  $\mu$ Gels and to result in interesting therapeutic and sensing applications. Here we have shown that the Gel@dye@Au<sub>(1 or 5)</sub> could induce massive cell death when irradiating cell monolayers (in absence of macroscopic global heating), which means that cytotoxic photo-activated intracellular hot spots are induced by Gel@dye@Au internalized in tumor cells.

### **2.2.6 Photoacoustic spectroscopy**

Photoacoustic (PA) imaging is a biomedical imaging modality able to map optical absorption at centimeter depth in tissues and in sub-millimeter resolution. PA imaging is based on the conversion of the optically absorbed energy in ultrasound waves and operates in the near infrared (NIR, typically between 680 nm and 980 nm) with nanosecond pulses. The optical absorption properties of the hybrid  $\mu$ Gels and their modulation with pH and temperature make them potential PA contrast agents. Because of the absorption of Cy in the NIR, we focused on  $\mu$ Gels loaded with Cy and performed an *in vitro* characterization at 25°C with a calibrated photoacoustic spectrometer<sup>123</sup> (see details of the experiments in section 2.3).

This study aims to provide (i) a characterization of the optical absorption of the hybrid  $\mu$ Gels while the UV-Vis spectra reported above are sensitive to the optical attenuation (or extinction) which is the added contribution of absorption and scattering, and (ii) an evaluation of the hybrid  $\mu$ Gels as smart photoacoustic contrast agents.

The  $\mu$ Gels with dyes and Au NPs are complex structures regarding the interactions with light as both the microgels and the plasmonic nanostructures scatter light and both the dyes and gold nanoparticles assembly absorb light. Moreover, gold nanostructures are both absorbing and scattering with potentially different absorption and scattering spectra<sup>124</sup>.

While UV-Vis spectrophotometry measures the attenuation coefficient that combines the scattering and the absorption coefficients, photoacoustic spectroscopy PA is insensitive to scattering and enables to probe only the optical absorption properties. The photoacoustic spectra of Gel@Cy@Au<sub>(x)</sub> with x= 0, 1 and 5 were measured and are presented in Figure 2.16. The photostability of the solutions was also evaluated by illuminating the samples with 900 successive laser pulses at the wavelength of 780 nm and monitoring the evolution of the PA coefficients with the number of pulses (Figure 2.17). The laser fluence on the tubes can be estimated to around 3.8 mJ.cm<sup>-2</sup>.

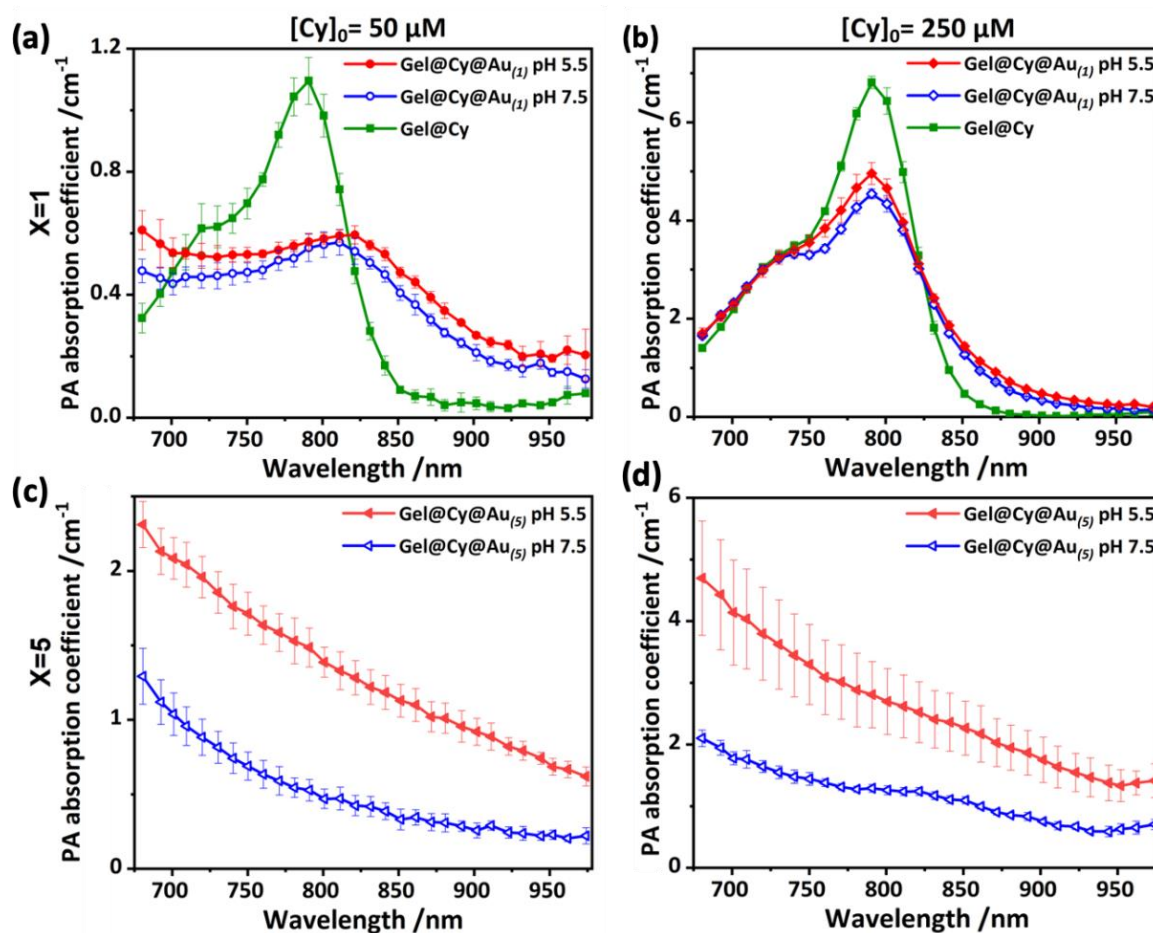


**Figure 2.16.** Photoacoustic spectra of Gel@Cy (green curves) and Gel@Cy@Au<sub>(x=1,5)</sub> at pH 7.5 (blue curves) and pH 5.5 (red curves) prepared from two different [Cy]<sub>0</sub> concentrations (50 μM and 250 μM). (a) PA spectra of Gel@Cy and Gel@Cy@Au<sub>(1)</sub> at 0.07 nM prepared from [Cy]<sub>0</sub> = 50 μM. (b) PA spectra of Gel@Cy and Gel@Cy@Au<sub>(1)</sub> at 0.07 nM prepared from [Cy]<sub>0</sub> = 250 μM. (c) PA spectra of Gel@Cy@Au<sub>(5)</sub> at 0.035 nM prepared from [Cy]<sub>0</sub> = 50 μM. (d) PA spectra of Gel@Cy@Au<sub>(5)</sub> at 0.035 nM prepared from [Cy]<sub>0</sub> = 250 μM. The amplitude of the PA spectra of all Gel@Cy@Au<sub>(5)</sub> samples have been multiplied two times for the sake of comparison with their Gel@Cy@Au<sub>(1)</sub> counterparts, which were concentrated twice for the PA experiments.

The general shape of the PA spectra of Gel@Cy (without Au NPs loading) recorded at pH= 7.5 is very similar to their UV-vis spectra (displayed in Figure 2.3, see spectral region 650-900 nm) with an absorption peak found around 790 nm. The ratio between the maximum amplitude for the initial dye concentrations  $[Dye]_0 = 50 \mu\text{M}$  and  $[Dye]_0 = 250 \mu\text{M}$  is around 6, consistent with a higher loading of dyes in the  $\mu\text{Gels}$ . Both Gel@Cy samples were found unstable under illumination pulses (Fig 2.17) with a progressive decrease of the PA amplitude, which can be explained by the photodegradation of the dye under laser excitation. After 1 cycle of incubation with Au NPs ( $x=1$ ), the PA spectra of Gel@Cy@Au<sub>(1)</sub> were significantly modified. Indeed, for  $[Dye]_0 = 50 \mu\text{M}$ , the PA spectrum of Gel@dye@Au<sub>(1)</sub> (Fig 2.16a) exhibits a peak in the range 750-850 nm that could be attributed to the cyanine, but it appears broader, with a lower amplitude and shifted from *ca.* 790 nm to around 810 nm, compared to Gel@Cy. It is noteworthy that this peak is revealed in the PA spectrum while it is hidden in the UV-vis attenuation spectrum (Fig 2.5).

Interestingly, an enhanced photostability is observed in Gel@dye@Au<sub>(1)</sub> prepared from  $[Dye]_0 = 50 \mu\text{M}$  (Fig 2.17). These modifications of the absorption spectra and the enhanced photostability suggest a coupling between the dye and the plasmonic nanoparticles inside the  $\mu\text{Gels}$ . In contrast, for  $[Dye]_0 = 250 \mu\text{M}$ , the absorption peak is still at 790 nm (Fig 2.16b) and the sample is not photostable, similarly to Gel@Cy, suggesting only a partial coupling between the dyes and Au NPs. This highlights the dominant contribution of the dye over the Au NPs in the absorption spectra of Gel@dye@Au<sub>(1)</sub> prepared with high dye concentration.

With a further encapsulation of Au NPs ( $x = 5$ ), the absorption associated with the dye vanishes for  $[Dye]_0 = 50 \mu\text{M}$  while it is very weak and hardly detectable for  $[Dye]_0 = 250 \mu\text{M}$ , in agreement with the UV-Vis spectra. However, the PA coefficient at 790 nm is about 2.4 times larger for  $[Dye]_0 = 250 \mu\text{M}$  than for  $[Dye]_0 = 50 \mu\text{M}$ , which shows indirectly that the increase in dye loading has an effect on the PA signal. Interestingly, the Gel@dye@Au<sub>(5)</sub> were found photostable and even an enhancement of the PA signal was observed that could be attributed to a local heating of the surrounding of the plasmonic NPs with the repetitive illuminations, that could enhance the Grüneisen coefficient compared to the initial conditions.

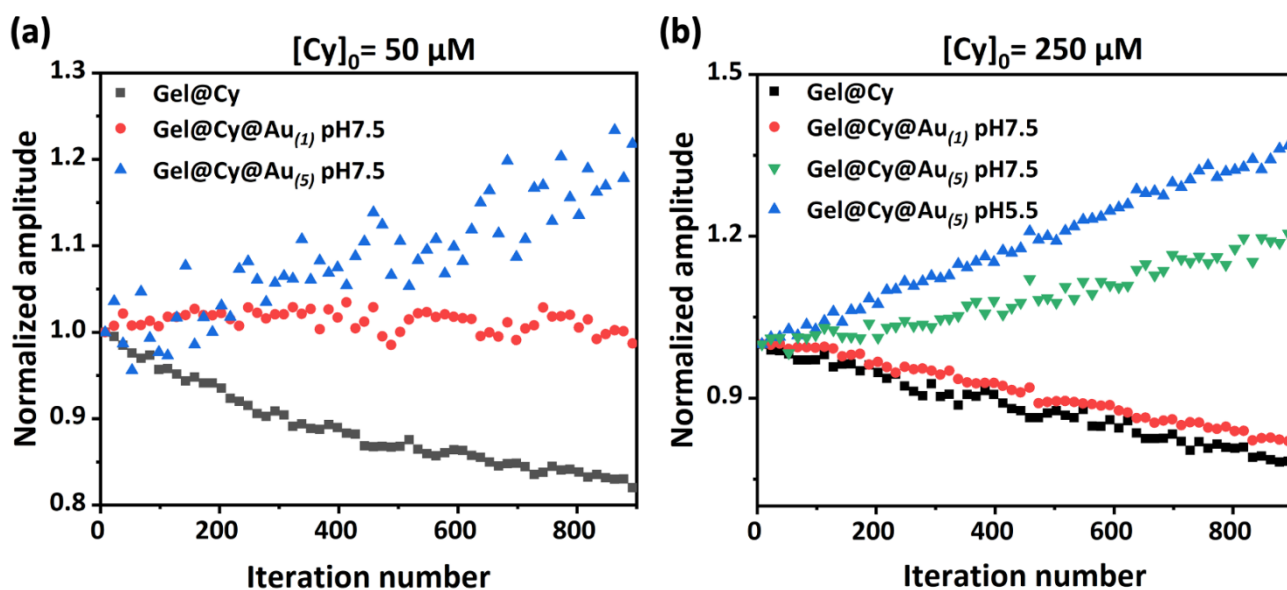


**Figure 2.17** Photostability of Gel@Cy and Gel@Cy@Au<sub>(1,5)</sub> samples prepared from (a) [Cy]<sub>0</sub>= 50 μM and (b) [Cy]<sub>0</sub>=250 μM. Each sample was illuminated 900 times at 780nm at 3.8 mJ.cm<sup>-2</sup>. The PA coefficients were averaged over 15 successive laser pulses and were normalized to the first value.

For Gel@dye@Au<sub>(1)</sub>, the PA spectra were only slightly affected by the pH change, in agreement with the UV-vis spectra shown in Figure 2.7. However, the spectral shape was modified for Gel@dye@Au<sub>(5)</sub> and a significant increase of the PA coefficient was observed when the pH decreased from pH 7.5 to 5.5. At 800 nm excitation, the PA coefficient increased by a factor of *ca.* 3 and 2 for [Cy]<sub>0</sub> = 50 μM and [Cy]<sub>0</sub> = 250 μM, respectively (Fig. 2.16). These results, which indicate a plasmon modification induced by the pH change in agreement with Figure 2.7 (UV-vis spectra), allow to quantify the influence of pH independently of the scattering modifications induced by the gel contraction. Interestingly, the photostability curve of Gel@dye@Au<sub>(5)</sub> at pH 5.5 (Fig. 2.17b) revealed a strong enhancement of the PA signal with the repetitive illuminations, higher than that observed at pH 7.5, suggesting that the pH-induced contraction of the μGels and the resulting plasmon coupling boosts the local increase in temperature.

The change in the spectral shape induced by the pH decrease may not be sufficient to discriminate the gels in acidic environment. However, the large increase in the PA signal could be used as a signature to detect that the environment of the contrast agents has become acidic. As slightly acidic microenvironments are observed in cancer tissues or inflamed area due to altered metabolic state<sup>125</sup>,

the pH sensitivity of the hybrid  $\mu$ Gels is an interesting feature for their use as stimuli-responsive photoacoustic contrast agents.

From the PA spectra, the molar absorption coefficients ( $\epsilon_{PA}$ ) at  $\lambda = 800$  nm were estimated, by dividing the PA absorption coefficients by the molar concentration of the hybrid  $\mu$ Gels. As shown in Table 2.4, the  $\epsilon_{PA}$  values of the hybrid  $\mu$ Gels range between 0.8 and  $6.6 \times 10^{10} \text{ M}^{-1}.\text{cm}^{-1}$ . These values are comparable to the extinction coefficients reported in the literature<sup>92</sup> for anisotropic gold nanostructures such as gold nanocubes ( $\epsilon = 2.19 \times 10^{10} \text{ M}^{-1}.\text{cm}^{-1}$  measured at  $\lambda = 808$  nm), gold nanocages ( $\epsilon = 1 \times 10^{10} \text{ M}^{-1}.\text{cm}^{-1}$ ,  $\lambda = 802$  nm) or poly(sodium 4-styrenesulfonate)-coated gold nanorods ( $\epsilon = 1.45 \times 10^{10} \text{ M}^{-1}.\text{cm}^{-1}$ ,  $\lambda = 785$  nm). However, they are far superior to that of isotropic gold nanospheres ( $\epsilon = 3.6 \times 10^6 \text{ M}^{-1}.\text{cm}^{-1}$  at  $\lambda = 506$  nm), which are similar to the NPs which were encapsulated in the  $\mu$ Gels. Therefore, although the spectral shapes of Gel@Cy@Au<sub>(1,5)</sub> samples do not exhibit a pronounced peak in the NIR, their high molar absorption coefficients at  $\lambda = 800$  nm and their pH-sensitivity are key assets for photoacoustic imaging<sup>126</sup>.

**Table 2.4** Molar absorption coefficients ( $\epsilon_{PA}$ ) of Gel@Cy and Gel@Cy@Au<sub>(x=1,5)</sub> samples at  $\lambda = 800$  nm, calculated by dividing the PA absorption coefficients by the molar concentration of the hybrid  $\mu$ Gels ( $7 \times 10^{-11} \text{ mol.L}^{-1}$ ) used for the PA experiments.

<i>Samples</i>	$\epsilon_{PA} (\text{M}^{-1}.\text{cm}^{-1})$ at pH 7.5	$\epsilon_{PA} (\text{M}^{-1}.\text{cm}^{-1})$ at pH 5.5
	<i>[Cy]<sub>0</sub> = 50 <math>\mu\text{M}</math></i>	
Gel@Cy	$1.4 \times 10^{10}$	-
Gel@Cy@Au <sub>(1)</sub>	$0.8 \times 10^{10}$	$0.8 \times 10^{10}$
Gel@Cy@Au <sub>(5)</sub>	$0.7 \times 10^{10}$	$2.0 \times 10^{10}$
<i>[Cy]<sub>0</sub> = 250 <math>\mu\text{M}</math></i>		
Gel@Cy	$9.1 \times 10^{10}$	-
Gel@Cy@Au <sub>(1)</sub>	$6.1 \times 10^{10}$	$6.6 \times 10^{10}$
Gel@Cy@Au <sub>(5)</sub>	$1.8 \times 10^{10}$	$3.8 \times 10^{10}$

## 2.3 Materials & Methods

### 2.3.1 Materials

Poly(ethylene glycol) diacrylate (OEGDA,  $M_n = 575 \text{ g}\cdot\text{mol}^{-1}$ ), Di(ethylene glycol) methyl ether methacrylate 95% (MEO<sub>2</sub>MA,  $M_n = 188.22 \text{ g}\cdot\text{mol}^{-1}$ ), Poly(ethylene glycol) methyl ether methacrylate (OEGMA,  $M_n = 300 \text{ g}\cdot\text{mol}^{-1}$ ), methacrylic acid (MAA,  $M_n = 86.09 \text{ g}\cdot\text{mol}^{-1}$ ) and potassium persulfate (KPS) were purchased from Sigma-Aldrich for the synthesis of microgels. Gold(III) chloride trihydrate ( $\text{HAuCl}_3 \cdot 3\text{H}_2\text{O}$ ), sodium tetrahydridoborate ( $\text{NaBH}_4$ ) and tri-sodium citrate dihydrate ( $\text{Na}_3\text{C}_6\text{H}_5\text{O}_7$ ) were purchased from Sigma-Aldrich for the synthesis of gold nanoparticles (Au NPs). Hydrochloric acid (37%, AnalaR NORMAPUR) and Sodium Hydroxide (NaOH) were purchased from VWR Chemicals and Sigma-Aldrich, respectively for adjusting the pH. Methylene blue (MB) and rhodamine 6G (R6G) were purchased from Sigma-Aldrich, Cyanine 7.5 amine was purchased from Lumiprobe. DMEM Medium (Glutamine-Max), Fetal Bovine Serum (FBS), 0.25% Trypsin-EDTA (1X), Dulbecco's Phosphate Buffered Saline [-]  $\text{CaCl}_2$ , [-]  $\text{MgCl}_2$  (DPBS), Penicillin Streptomycin 100 x (respectively 10,000 Units/mL and 10,000  $\mu\text{g}/\text{mL}$  Streptomycin (PS) and Alamar blue were purchased from ThermoFisher Scientific for *in vitro* studies.

### 2.3.2 Synthesis of gold nanoparticles (Au NPs)

Gold nanoparticles were synthesized using  $\text{NaBH}_4$  as a reducing agent, yielding Au NPs with an average diameter of  $3.8 \pm 0.9 \text{ nm}$ . Briefly, 3 mL of 0.1 M aqueous stock solution of sodium citrate, 0.3 mL of 0.1 M gold(III) chloride trihydrate solution and 55.5 mL of deionized water were added in a 100 mL flask equipped with a stir bar. The reaction solution was cooled down to 0 °C in ice bath under stirring (600 rpm). Next, 360  $\mu\text{L}$  of 0.1 M  $\text{NaBH}_4$  solution was added drop by drop until the resulting solution turned red.

### 2.3.3 Synthesis of oligo(ethylene glycol) methyl ether methacrylate-based microgels

The thermo- and pH-responsive  $\mu\text{Gels}$  were synthesized as described previously.<sup>13</sup> Briefly, 0.221 mmol MAA, 0.36 mmol OEGMA, 3.3 mmol MEO<sub>2</sub>MA and 0.14 mmol OEGDA cross-linker were dissolved in a round-bottom flask with 40 mL of distilled water and purged with Ar for 1 h. The

reaction solution was then stirred at 400 rpm and heated to 70°C. Then, 5 mg of KPS dissolved in 10 mL purged water were injected and the reaction solution was left to react for 5 h.

#### **2.3.4 Assembly process to yield hybrid microgels with fluorescent dyes and Au NPs**

1 mL of  $\mu$ Gels solution (17.3 g.L<sup>-1</sup>) was washed by 2 cycles of centrifugation at 7000 rpm for 15 min and redispersion in 1 mL of DI water. The pH of the  $\mu$ Gels dispersion was adjusted to 6.8-7.2 by adding NaOH. Various amounts of fluorescent dyes (methylene blue, rhodamine 6G and cyanine 7.5 amine) were added in the  $\mu$ Gels solution to prepare the stock Gel@dyes solution (final concentrations of each dye: 50  $\mu$ M or 250  $\mu$ M). After 48 hours, the dye-loaded  $\mu$ Gels were purified by one cycle of centrifugation and redispersion in 1 mL of DI water. Next, 900  $\mu$ L of the Au NPs solution ([Au<sub>atom</sub>]=0.5 mmol.L<sup>-1</sup>, [Au NPs] = 0.3  $\mu$ mol·L<sup>-1</sup>) were added into 100  $\mu$ L of dye-loaded  $\mu$ Gels solutions. The solution was left to react for 24 hours. The  $\mu$ Gels loaded with both Au NPs and dyes were then washed by 1 cycle of centrifugation at 7000 rpm for 15 min/redispersion in water to yield Gel@dye@Au. The self-assembly process between the dye-loaded  $\mu$ Gels and the Au NPs was controlled by varying the number of incubation steps, from 1 single step to 5 steps, as follows: (i) mixing of the Gel@dye with Au NPs solution ([Au NPs] = 0.27  $\mu$ mol.L<sup>-1</sup>); (ii) washing of the resulting  $\mu$ Gels *via* one cycle of centrifugation/redispersion; (iii) mixing of the Gel@dye@Au samples obtained in the previous step with fresh solutions of Au NPs (at [Au NPs] = 0.27  $\mu$ mol.L<sup>-1</sup>). This three-steps process was repeated up to five times, leading to  $\mu$ Gels densely filled with Au NPs.

#### **2.3.5 Characterization techniques**

The morphology of Gel@dye@Au samples was observed by Tecnai12 transmission electron microscope (FEI, The Netherlands). The hydrodynamic diameter was measured by dynamic light scattering (DLS, Malvern), as a function of pH and temperature. The UV-Vis absorption and fluorescence emission spectra were acquired using a UV-Vis spectrometer (Shimadzu 2700, Japan) and a cuvette with an optical path length of 1 cm and a fluorimeter (Hitachi F7000, Japan), respectively.

#### **2.3.6 Cell culture, dark cytotoxicity and Phototoxicity**

CT26 colon cancer cells were cultured in DMEM Medium (Glutamine-Max), FBS 10%, Penicillin Streptomycin 1x at 37°C and 5% CO<sub>2</sub>. Dark cytotoxicity of  $\mu$ Gels was assessed on CT26 colon cancer

cells. Cells were seeded at a density of 10,000 cells/well in 500  $\mu\text{L}$  of medium in 48 well plate and incubated overnight. Then, the medium was renewed with 350  $\mu\text{L}$  of fresh medium containing 5  $\mu\text{M}$  Gel@dye@Au<sub>(x)</sub> prepared from [Dye]<sub>0</sub>=50  $\mu\text{M}$  or 250  $\mu\text{M}$  and with different Au NPs loading ( $x=1$  and  $x=5$ ). After 24 h of incubation, the medium was removed and the excess of NPs was washed with 500  $\mu\text{L}$  of PBS once. Then, 200  $\mu\text{L}$  of DMEM without phenol red were added to each well. Cells were incubated for additional 18h and cytotoxicity was investigated by replacing the medium with fresh 200  $\mu\text{L}$  medium without FBS containing 10% alamar Blue. 200  $\mu\text{L}$  of each 48 wells were transferred to wells from a non-transparent 96 well plate and fluorescence intensity was measured in a plate reader (Ex 560 Em 590) (SpectraMax iD3, Molecular Devices, US).

Phototoxicity was measured in the same way as dark toxicity but a photothermal treatment was performed before the 18 h incubation. For this, each well was exposed for 10 minutes to an 808 nm laser at 1 or 2  $\text{W}/\text{cm}^2$  (CNI FC series Fiber Coupling Laser system).

### **2.3.7 Cell uptake of hybrid $\mu\text{Gels}$**

CT26-Luc cells were seeded in 6-well plates at a density of  $1.2 \times 10^6$  cells/well and cultured for 24 h. Then, the culture medium was replaced by 2 mL of medium containing the desired concentration of Gel@dye@Au<sub>(x)</sub> (prepared from [Dye]<sub>0</sub>=50  $\mu\text{M}$  and 250  $\mu\text{M}$ , with  $x=1$  and  $x=5$ ) and incubated with cells for 5 min at 4°C, 6 h and 24 h at 37°C. After incubation, cells were washed by PBS for three times and the nuclei were stained by hoechst 33342. Cellular imaging was performed with a Cell Insight™ CX7 HCS Platform (Thermofisher) (Hoechst: Ex. 405nm, Em. 446/37nm; R6G: Ex. 561nm, Em. 600/41nm; MB: Ex. 647nm, Em. 677/34nm; Cy7: Ex. 785nm, Em. 805nm).

### **2.3.8 Photothermal experiments**

Gel@dye@Au solutions with fixed  $\mu\text{Gel}$  ( $1.73 \text{ mg} \cdot \text{mL}^{-1}$ ) and dye concentration (with initial dye concentration [Dye]<sub>0</sub> = 50  $\mu\text{M}$ ) but with different Au NPs loading (from no Au NPs to 50  $\text{mg} \cdot \text{g}^{-1}$  for  $x=1$  and 250  $\text{mg} \cdot \text{g}^{-1}$  for  $x=5$ ) were exposed to a continuous wave CNI FC series Fiber Coupling Laser system with a wavelength of 808 nm and a density of 1.1  $\text{W}/\text{cm}^2$  for 300 s. The density was calculated by dividing the power after fiber, which is measured using a power meter PM400K5 thorlabs, with the surface of the laser beam. The temperature of samples was measured in Eppendorf micro centrifuge

tubes of 0.5 mL. Illumination from the laser was directed directly on the sample from the top, thanks to a fiber. The infrared camera FLIR t430sc recorded the temperature from the side. From the film thus obtained, we are able to delineate a Region of Interest (ROI) around the hot spot. The temperature obtained is the average temperature of each pixel located in this ROI.

### **2.3.9 Photoacoustic spectroscopy**

A calibrated photoacoustic (PA) spectrometer based on a conventional photoacoustic system was used. The system is detailed in Reference<sup>123</sup>. Only the main specifications are presented here. The sample solutions were injected in PTFE tubes of inner diameter 200 $\mu$ m, immersed in a water bath maintained at 25°C, and imaged successively at 30 optical wavelengths between 680 nm and 970 nm by steps of 10 nm. A tunable nanosecond laser with a pulse repetition frequency of 20Hz was used. The laser fluence at 780 nm was around 3.8 mJ.cm<sup>-2</sup>. 15 successive scans of the optical wavelengths were performed and the ultrasound data were averaged before the image formation. Blank datasets were acquired by filling the tubes with ultrapure water and were subtracted to the ultrasound signals for a baseline correction. Photoacoustic images were formed and the amplitude of the tube on the image was measured for each optical wavelength. A calibration was performed with a reference solution of pentahydrate copper (II) sulfate at 250 mM to convert this amplitude in a PA coefficient directly proportional to the decadic absorption coefficient of the solution. The proportionality factor between the PA coefficient and the decadic absorption coefficient is named photoacoustic generation efficiency (PGE) and is the product of the photothermal conversion efficiency (conversion efficiency of the absorbed optical energy to heat) and the Grüneisen coefficient relative to water (conversion of the heat energy to ultrasound waves). The PGE is equal to one for a sample for which the absorbed energy is fully converted into pressure in a medium with the Grüneisen coefficient of the water. The PA coefficient is expressed in cm<sup>-1</sup>, and is equal to the decadic absorption coefficient for a solution with a PGE equal to 1. The PGE of the microgels was not determined here. For each sample, the PA coefficient was measured eight times (two injections in four tubes). The PA spectra correspond to the median value and the error bars to the median absolute deviation with a scale factor 1.4826.

0.1 M HCl was used to adjust the pH of the hybrids for the Gel@Cy@Au samples studied at pH = 5.5. The decrease in pH from 7.5 to 5.5 was performed 30 min before the spectral measurements. To keep

the measurement range within the detection limit of PA setup, we concentrated the hybrid gels with low Au NPs loading (Gel@Cy@Au<sub>(1)</sub> with x=1) twice by D.I water for PA measuring. It is worth noting that due to the fact that the hybrid gels easily adhere to the wall of the centrifuge tubes during the preparation and transfer process, a certain degree of sample loss was observed. The photostability of the solutions was evaluated by illuminating the sample with 900 successive laser pulses at 780 nm with a laser fluence of 3.8 mJ.cm<sup>-2</sup>. The PA coefficient was assessed for each Laser pulse and the mean of 15 successive iterations was computed for a better signal to noise ratio.

## 2.4 Conclusion

In summary, we have proposed a straightforward strategy for the rational design of well-defined smart  $\mu$ Gels filled with dyes and Au NPs assemblies. Depending on the initial concentrations of the different building blocks during the assembly process and the number of incubation steps between the  $\mu$ Gels and Au NPs, the resulting hybrid materials exhibit various loading levels and well-defined internal organization of Au NPs inducing tunable plasmon coupling and unique optical properties.

Characterization of the samples using UV-vis extinction, fluorescence and photoacoustic spectroscopy, TEM, SAXS and DLS revealed that the final hybrid networks integrate the key features of each component, including the high loading capacity and stimuli-responsive behavior of the hydrogel matrix, the fluorescence of the dyes and the optical and photothermal response of plasmon-coupled Au NPs assemblies. Upon temperature or pH stimuli, the hybrid  $\mu$ Gels platforms were shown to shrink or swell, resulting in modifications of the organization and interactions of Au NPs trapped within the polymer matrix. In the case of  $\mu$ Gels densely filled with Au NPs, such as Gel@dye@Au<sub>(5)</sub>, the temperature or pH stimulation could be used to induce plasmon coupling between the aggregated Au NPs, which resulted in plasmon band broadening and red shift towards the near infrared region (NIR), a key feature for biomedical applications. Photothermal experiments showed that the Gel@dye@Au<sub>(5)</sub> samples display high heating capacities under NIR laser excitation, with an enhanced effect upon pH decrease, probably due to plasmon coupling. Interestingly, the dyes loaded within the  $\mu$ Gels could act as fluorescence tracers to visualize the  $\mu$ Gel uptake by colon tumor cells, while the dark cytotoxicity of the three different dyes was much lower in  $\mu$ Gels in comparison to the free dyes. Importantly, the

photoactivation of tumor cell monolayers exposed to the  $\mu$ Gels induced important cell death, that can be used for precision photothermal therapy. Moreover, as determined by photoacoustic spectroscopy, the hybrid  $\mu$ Gels exhibit high molar absorption coefficients at  $\lambda = 800$  nm, comparable to the ones of anisotropic gold nanostructures reported in the literature. Another important characteristic is the higher PA amplitude obtained at pH 5.5 compared to pH 7.5 and the enhanced photostability of the hybrid samples compared to free Cy or Gel@Cy. Therefore, although the synthesis methodology proposed herein relies on small, spherical Au NPs, with no particular signal in the NIR, the strategy which consists to assemble them within smart thermo- and pH-sensitive microgel platforms loaded with dyes offers unprecedented opportunities for better controlled photothermal therapy and bioimaging.

### ***Collaborators***

The results presented in this chapter have been obtained thanks to the joint efforts of several collaborators, described below:

- The members of the group Nanobiospectroscopy: Yun Luo, Delphine Onidas, Philippe Nizard and Claire Mangeney for the synthesis, characterization and cell uptake experiments and viability assays.
- The members of the group MSC Med: Florence Gazeau, Amanda Silva Brun, Alba Nicolas Boluda, Giulio Avveduto, Dmitri Ayollo etc... for the biological and PTT part.
- Jérôme Gateau and Théotim Lucas for the photoacoustic part experiment.
- Florent Carn for the SAXS experiments and for giving me access to the Zetasizer.

---

## ***Chapter 3. Insight into cellular uptake and intracellular degradation of hybrid microgels loaded with dyes and gold nanoparticle***

---

### **3.1 Introduction**

In the previous chapter, we have proposed an innovative approach to elaborate smart nanocomposites made of hydrogel particles loaded with dyes and gold nanoparticles and we have evaluated their potential for photothermal therapy and photoacoustic imaging. While most studies reported up till now on similar nanocomposite systems have been centered on their synthesis and characterization as well as on their uptake by cells and potential applications in nanomedicine, only few works have focused on the study of their fate within cells and intracellular transformation processes.

We fill this gap in the present chapter by performing an integrated study using complementary imaging techniques, *i.e.* TEM, Raman and fluorescence to investigate the biodegradation and transformation of the hybrid  $\mu$ Gels by monitoring their structural and optical properties as a function of time after their internalization within cells. In this study, we focused exclusively on the densely filled Gel@dye@Au<sub>(5)</sub> samples (prepared from initial dye concentrations  $[\text{dye}]_0 = 50 \mu\text{M}$  and with  $x = 5$  incubation steps with Au NPs), which exhibit tunable optical properties depending on pH and temperature.

### **3.2 Results & Discussion**

#### ***3.2.1 TEM analysis after pH and NIR light stimulation***

Prior to monitoring the transformation of the  $\mu$ Gel in cellular environment, we investigated in more detail the influence of acidic environment mimicking the lysosomal pH and NIR light stimulation on the structural properties of the  $\mu$ Gel. In acidic environment (pH 5.5) and after laser irradiation with 808 nm laser at  $2\text{W}/\text{cm}^2$ , the morphology of the Gel@dye@Au<sub>(5)</sub> samples changed, as observed in Fig.

3.1. Indeed, the  $\mu$ Gels shrunk and the Au NPs inside them aggregated and even fused to form bigger ones ( $\sim 5$ - $18$  nm, as calculated on more than 200 NPs using the software Image J), as indicated by the white arrows in the zoom of the TEM pictures.

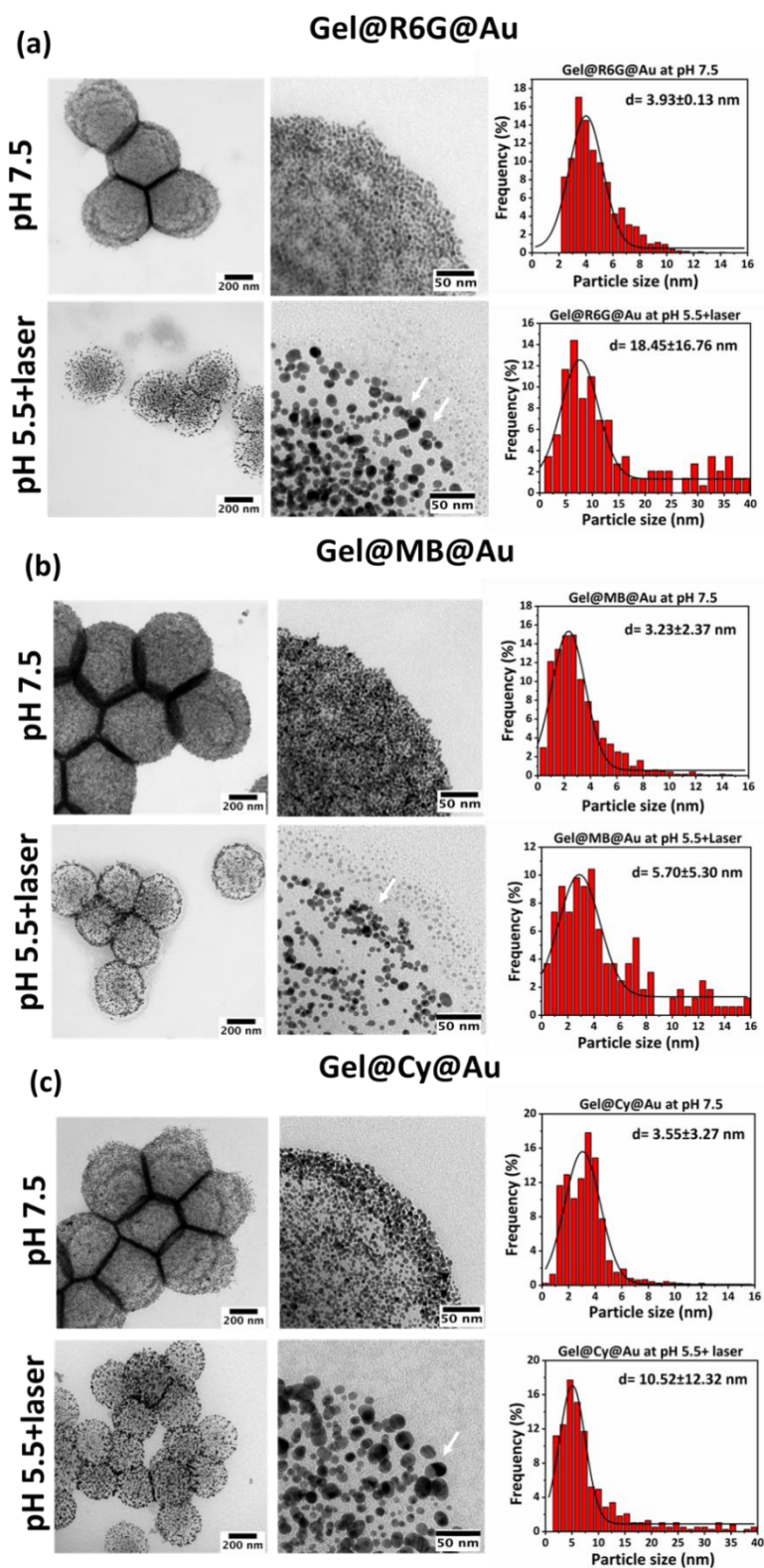


**Figure 3.1** (a) TEM images and size distribution of Gel@R6G@Au<sub>(5)</sub>, (b) Gel@MB@Au<sub>(5)</sub> and (c) Gel@Cy@Au<sub>(5)</sub>. The right side images correspond to a zoom of the TEM pictures in order to emphasize the

evolution of the aggregation state of the Au NPs within the  $\mu$ Gel matrix. The white arrows indicate NPs which seem to have fused together. The histograms correspond to the Au NPs size distribution inside the hybrid  $\mu$ Gels before and after pH and laser stimulation, as estimated using the software Image J ( $n > 200$ ). The samples were prepared from  $[Dye]_0 = 50 \mu M$  and  $x = 5$  (incubation steps).

### 3.2.2 SERS-fluorescent encoded particles as dual-mode optical probes

The introduction of dyes and Au NPs within the  $\mu$ Gels is expected to impart them dual properties based on fluorescence and SERS. To evaluate these dual properties, the fluorescence spectra were recorded in water (at 0.04 nM) while the SERS spectra were recorded on dried drops (1  $\mu$ L) deposited on glass plates. The presence of the dyes only in Gel@dye samples lead to intense fluorescence peaks (Fig. 3.2a) with emission at  $\lambda_{F[R6G]} = 560$  nm,  $\lambda_{F[MB]} = 686$  nm and  $\lambda_{F[Cy]} = 815$  nm. However, in the absence of Au NPs, no Raman signal could be detected (Fig. 3.2b) due to the low amount of dyes trapped within the  $\mu$ Gels and to the fact that Raman scattering is a weak effect. Typically, only about one in 10 million scattered photons are Raman scattered.

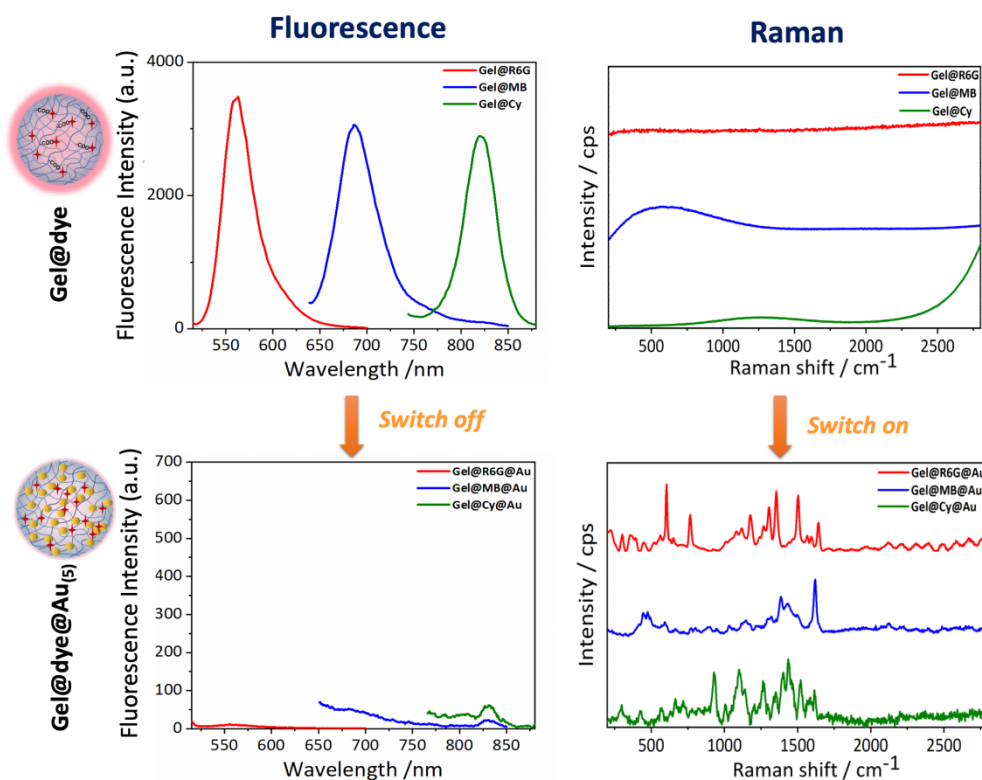


**Figure 3.2** Fluorescence and Raman spectra of the hybrid  $\mu$ Gels at 0.04 nM: (a) Fluorescence spectra of Gel@dye and (b) Raman spectra of Gel@dye. (c) Fluorescence spectra of Gel@dye@Au<sub>(5)</sub> and (d) Raman spectra of Gel@dye@Au<sub>(5)</sub>. The Gel@dye samples were prepared from  $[Dye]_0 = 50 \mu M$ . The fluorescence spectra were recorded in water while the SERS spectra were recorded on dried drops (1  $\mu$ L) deposited on glass plates.

Interestingly, the introduction of Au NPs inside the hydrogel network (in Gel@dye@Au samples) completely reverses these signal intensity contrasts between fluorescence and Raman. Indeed, the fluorescence of the dyes appear switched off (Fig. 3.2c), probably due to their quenching by the Au NPs while their Raman signals are clearly visible due to surface-enhanced Raman scattering provided by the proximity with Au NPs (Fig. 3.2d). The characteristic peaks of the dyes and their assignment, based on the literature, are detailed in Table 3.1. The loading of Au NPs thus offers an easy means to switch on the SERS spectra and off the fluorescence signal.

**Table 3.1** Assignment of Raman bands of R6G, MB and Cy in Gel@dye@Au<sub>(5)</sub>, based on a literature survey.

<i>Dyes</i>	<i>Raman shift (cm<sup>-1</sup>)</i>	<i>Assignment</i>	<i>Raman shift (cm<sup>-1</sup>)</i>	<i>Assignment</i>
R6G	1183	C-H in-plane bending <sup>127</sup>	1514	aromatic C-C stretching <sup>128</sup>
	1284	C-O-C antisym stretch	1619	aromatic C-C stretching <sup>128</sup>
	1365	aromatic C-C stretching <sup>128</sup>		
MB	922	C-H out-of-plane bending	1362	C-H in-plane ring deformation <sup>129</sup>
	1131	C-H in-plane bending	1441	N-C-H in-plane bending <sup>130</sup>
	1265	C-N stretching	1623	Stretching of C-C/C-N rings <sup>131</sup>
Cy	927	C-H out-of-plane bending	1431	C-N stretch (Amide III band)
	1132	C-H in-plane bending	1510	NH <sub>3</sub> <sup>+</sup> deformation
	1343	C-N stretching	1610	Benzene ring in aromatic compounds

The effect of the pH stimulus was investigated by decreasing the pH of the colloidal solution to 5.5 in order to simulate the lysosomal environment. The SERS spectra of the dried drops at pH 7.5 and pH 5.5 are compared in Figure 3.3. It appears that the pH decrease generates a strong increase of the Raman signals of about 5 -20 times. This observation can be explained by the plasmon coupling triggered by the aggregation of Au NPs upon pH-induced  $\mu$ Gel collapse, in agreement with the UV-vis extinction spectra and TEM images displayed in Chapter 2. These results demonstrate the potential of Gel@dye@Au<sub>(5)</sub> as pH-sensitive Raman/SERS probes.

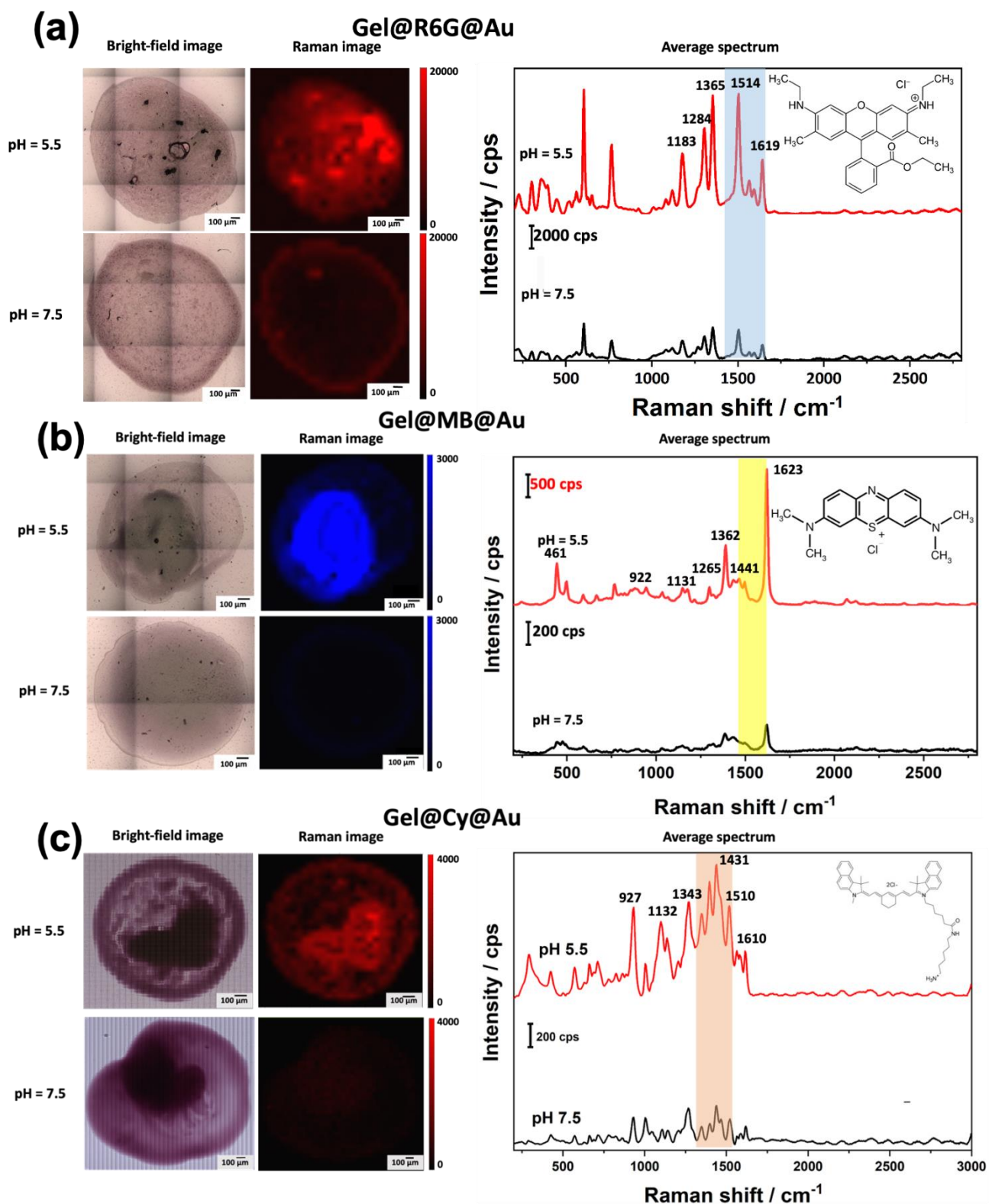


**Figure 3.3** Raman images and spectra of Gel@dye@Au<sub>(5)</sub> samples at pH 7.5 and pH 5.5, recorded on dried drops (1  $\mu\text{L}$ ) deposited on glass plates: (a) Gel@R6G@Au<sub>(5)</sub>, (b) Gel@MB@Au<sub>(5)</sub> and (c) Gel@Cy@Au<sub>(5)</sub>. The Raman images are on the left side and the SERS spectra are on the right side.

### 3.2.3 Surface enhanced Raman signal of the hybrids upon cellular uptake

To test the effect of cellular internalization of the hybrid  $\mu$ Gels, we incubated the Gel@MB@Au with fibroblasts for 24 h to investigate intracellular Raman signal. The specific Raman signal of dyes is detectable within fibroblasts and matches the Raman spectrum of dry drop at pH 5.5 rather than that at pH 7.5 (Fig. 3.4), suggesting internalization of hybrid gels in intracellular acidic compartments such as endo-lysosomes.



**Figure 3.4** Comparison of the Raman signals recorded in the intercellular environment and on dried drops of Gel@MB@Au<sub>(5)</sub>. The spectra of the dried drop are baseline-corrected and peak intensity normalized.

### 3.2.4 Comparison of the fluorescence and Raman intensity changes to investigate intracellular processing of hybrid $\mu$ Gels

Based on the unique properties of the hybrid  $\mu$ Gels, we used the dye molecules as both "Raman" and "fluorescence" probes to investigate the intracellular processing, biotransformation and degradation of hybrid materials in primary fibroblasts *in vitro* through dual-mode imaging. For that purpose, following a methodology proposed by our group in Balfourier et al.<sup>100</sup> in order to investigate long term transformation of nanomaterials in cells, we cultured the fibroblasts with low serum level (2%) to

inhibit massive cell division and subsequent dilution of the uptaken particles in cells. With such protocol, we can observe the fate of nanostructures upon their processing or metabolization by cells. We thus investigated both Raman and fluorescence signal of the hybrids upon their internalization in fibroblasts and intracellular ageing up to 7 days after exposure in fibroblasts. Overall our main observation is that cell internalization and intracellular ageing transform the optical signature of hybrids from a SERS ON / Fluorescence OFF state (when the AuNPs are still closed to each other and to the dye in  $\mu$ Gels inducing the presence of electromagnetic “hot spot” and SERS effect, while quenching the dye fluorescence) to a SERS OFF/Fluorescence ON behavior after few days in cells. Indeed, after uptaken by fibroblast cells for several days, the conformation of the hybrids can change modifying the Au NPs organization and the coupling between Au NPs and fluorescent dyes. Hence the change in dual SERS/Fluorescence properties of the hybrids witnesses their intracellular transformation. Below we describe in details the evolution of the hybrids optical properties before investigating their intracellular distribution and transformation with optical and electron microscopy.

### ***3.2.5 Intracellular evolution of Raman signature***

The average Raman spectra of fibroblasts exposed to three types of Gel@dye@Au<sub>(5)</sub> for 24h were taken by CLS analysis of Labspec 6 as shown in Figure 3.5. We compared the Raman intensity at different days after the initial exposure to the hybrids (1 day (soon after 24h incubation with the hybrids), 4 days and 7 days after exposure) by performing Raman imaging of individual cells and subtracting the experimental results from the baseline. The results showed that upon time in cells, the Raman signal specific to the hybrids gradually weakened or even disappeared. We see no signal for R6G on day 7 and no signal for Cy7.5 from day 4. This indicates that the structure of the hybrid  $\mu$ Gels has been transformed or even degraded from the 4th day, drastically diminishing the electromagnetic coupling between the dyes and the Au NPs.

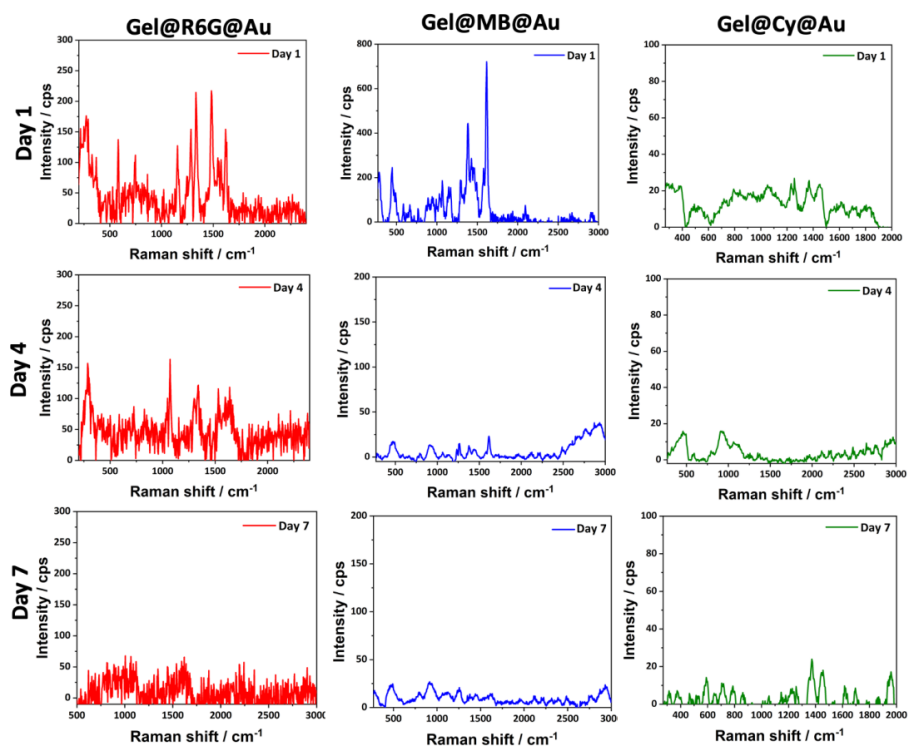


**Figure 3.5** Raman spectra of Gel@dye@Au<sub>(5)</sub> after cellular uptake by fibroblasts at day 1, day 4 and day 7.

Fibroblasts incubated with Gel@MB@Au<sub>(5)</sub> were also observed by Raman imaging and bright field microscopy at the different days post-exposure (Figure 3.6). The black spots on bright field which represent the  $\mu$ Gel composites are obviously uptaken around the nuclei of fibroblasts. From day 1 to day 7, there is no obvious change in cell morphology. The red channel refers to the signal of MB (peaks in the region of 360-1800  $\text{cm}^{-1}$ ) and the green channel corresponds to the signal of cells (lipid peaks at *ca.* 2800-3000  $\text{cm}^{-1}$ ). From the results of day 1, the merged image shows that the MB signal can be located into cells. Clearly, the distribution of red spots is limited in certain region, possible due to the formation of Au NP agglomerations in lysosomes, inducing SERS effect for MB and intracellular lipidic membranes. At day 4, the Raman image contrast (both red and green maps) becomes lower because of weaker signals detected with respect to day 1 suggesting degradation of the hybrid structure reducing the electromagnetic coupling between Au NPs and MB or between Au NPs and cellular lipids. In day 7, the red and green map are almost invisible because of the continuous decreasing of MB and lipid Raman signals. Actually, the MB signals nearly vanish, and only weak cell peak remains. All above results support the biodegradation of Gel@MB@Au<sub>(5)</sub> within 7 days.

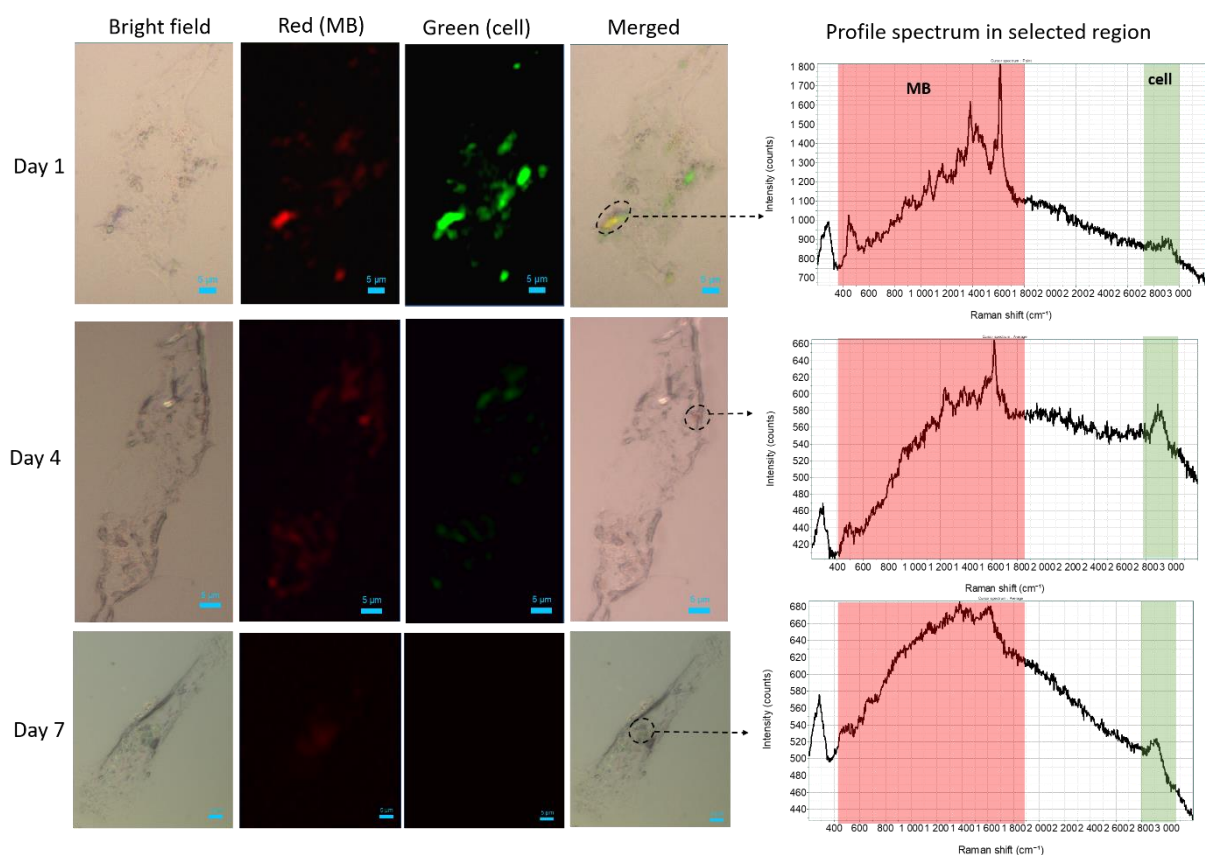


**Figure 3.6** Results of Raman imaging experiments to monitor intracellular transformation of hybrid  $\mu$ Gels in fibroblast cells incubated with Gel@MB@Au<sub>(5)</sub>. Raman red maps represent the MB signal (baseline corrected to avoid MB and cell autofluorescence) and are highlighted in the red region of the spectra; the green map corresponds to the cell signal without baseline correction (highlighted in green in the right hand side spectra) to take into account the cell autofluorescence. The merged images correspond to overlay of optical, red and green maps.

### 3.2.6 Intracellular evolution of fluorescence signal

In order to monitor the evolution of the fluorescence properties of Gel@MB@Au<sub>(5)</sub> in fibroblasts, we performed high content screening microscopy using Cell Insight CX7, comparing nuclear staining with Hoechst, MB fluorescence and bright field images of cells incubated with the  $\mu$ Gels for 2 h, 6 h and 24 h (day 1), or let for culture for 4 or 7 days after exposure to the  $\mu$ Gels (Figure 3.7). At short time-points of incubation, we can clearly see on bright field images the isolated or clustered  $\mu$ Gels outside the cells that appeared as black dots due to their high loading with Au NPs. Importantly they are not visible in the fluorescence channel of MB. Indeed, when Au NPs and MB are close to less than 5 nm, the MB fluorescence is quenched which seems to be the case in the extracellular  $\mu$ Gels. However, after the hybrid  $\mu$ Gels are taken up by cells (from day 1 in fibroblasts), the MB fluorescence appears, showing intracellular punctuated distribution that is *not* colocalized with the black microstructures.

Importantly the black dots (featuring the distribution of clustered AuNPs) are also found intracellular, probably accumulated in lysosomes. At day 4, the MB fluorescence becomes brighter with a more diffuse intracellular distribution suggesting intralysosomal and cytoplasmic release of the dye, independently of Au NPs. At day 7, both AuNPs and fluorescence signals are still intracellular with dimer intensities and with distinct localization. This suggests that hybrids undergo a process of disassembly once taken up by cells with distinct fate and relocation of Au NPs and MB dye. The hypothesis of the dye moving away from the gold nanoparticles is consistent with previous results showing that the hybrid's SERS signal gradually weakened over time in cells.

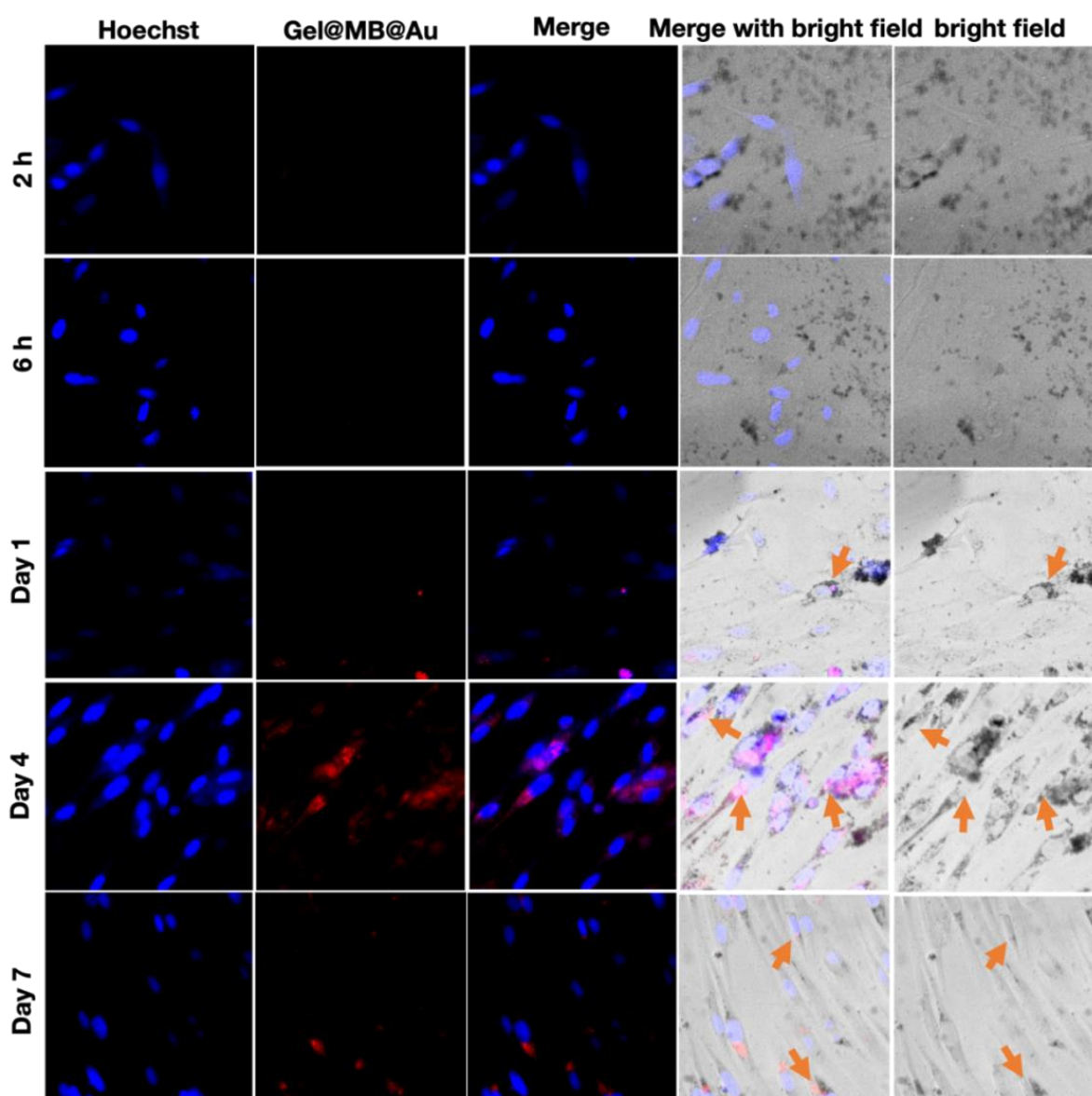


**Figure 3.7** Cellular uptake process of Gel@MB@Au<sub>5</sub> after incubation with fibroblasts for 2h, 6h, 1 day, 4 days and 7 days observed by Cell Insight CX7. The proximity of Gel@MB@Au<sub>5</sub> (black points) and methylene blue (red points) are marked by orange arrows.

### 3.2.7 Subcellular nanoscale transformations of the hybrid $\mu$ Gels inside fibroblasts

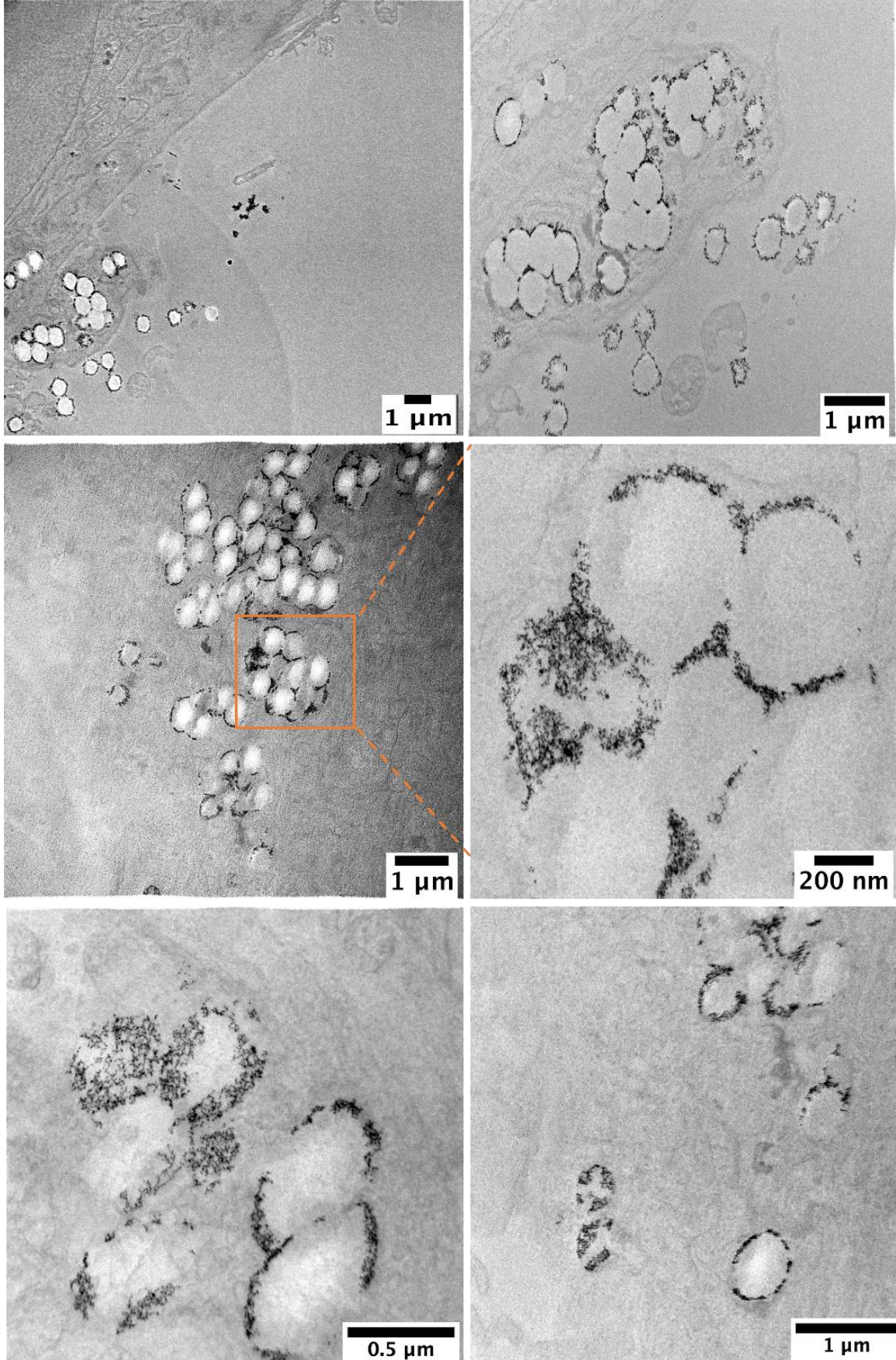
In order to investigate the subcellular localization and structural transformation of the hybrid  $\mu$ Gels at the nanoscale in cells, electron microscopy was performed on cells fixed at different time-points after exposure to the of Gel@MB@Au<sub>(5)</sub>. Figure 3.8a shows that the conformation of the hybrid  $\mu$ Gels has changed after being taken up by the fibroblasts for 24 h. In comparison to the TEM pictures in Fig 3.2, we observed that the  $\mu$ Gels keep their original spherical shape and size, but that the Au NPs are mostly segregated at the periphery of the  $\mu$ Gels.  $\mu$ Gels are seen as empty structures surrounded by a dense shell of Au NPs, mostly located and assembled within membrane bound intracellular structures. It suggests that the hybrid materials assembled by weak physical interactions (*i.e.* electrostatic, van der Waals forces and hydrogen bonds) are destabilized upon cell internalization and pH lowering with evident segregation of Au NPs on the periphery.

Nevertheless, we can suppose that the "gold nanorings" produced by the intracellular conformational changes can still support a SERS effect on MB or intracellular lipid membranes at day 1.

In contrast, from day 4, the Au NPs were partially degraded and aurosomes structures appeared as already observed by our group in fibroblasts after internalization of 4 nm Au NPs<sup>100</sup>. The aurosomes structure consists in curved self-assembly of sub 2.5 nm gold nanoparticles that results from the oxydative degradation of Au NPs by intracellularly produced reactive oxygen species and from recrystallisation process involving methallonioneins. Aurosomes are observed in the vicinity of intact original Au NPs. By day 7, we found more aurosomes inside the cells which indicate the further degradation of Au NPs.

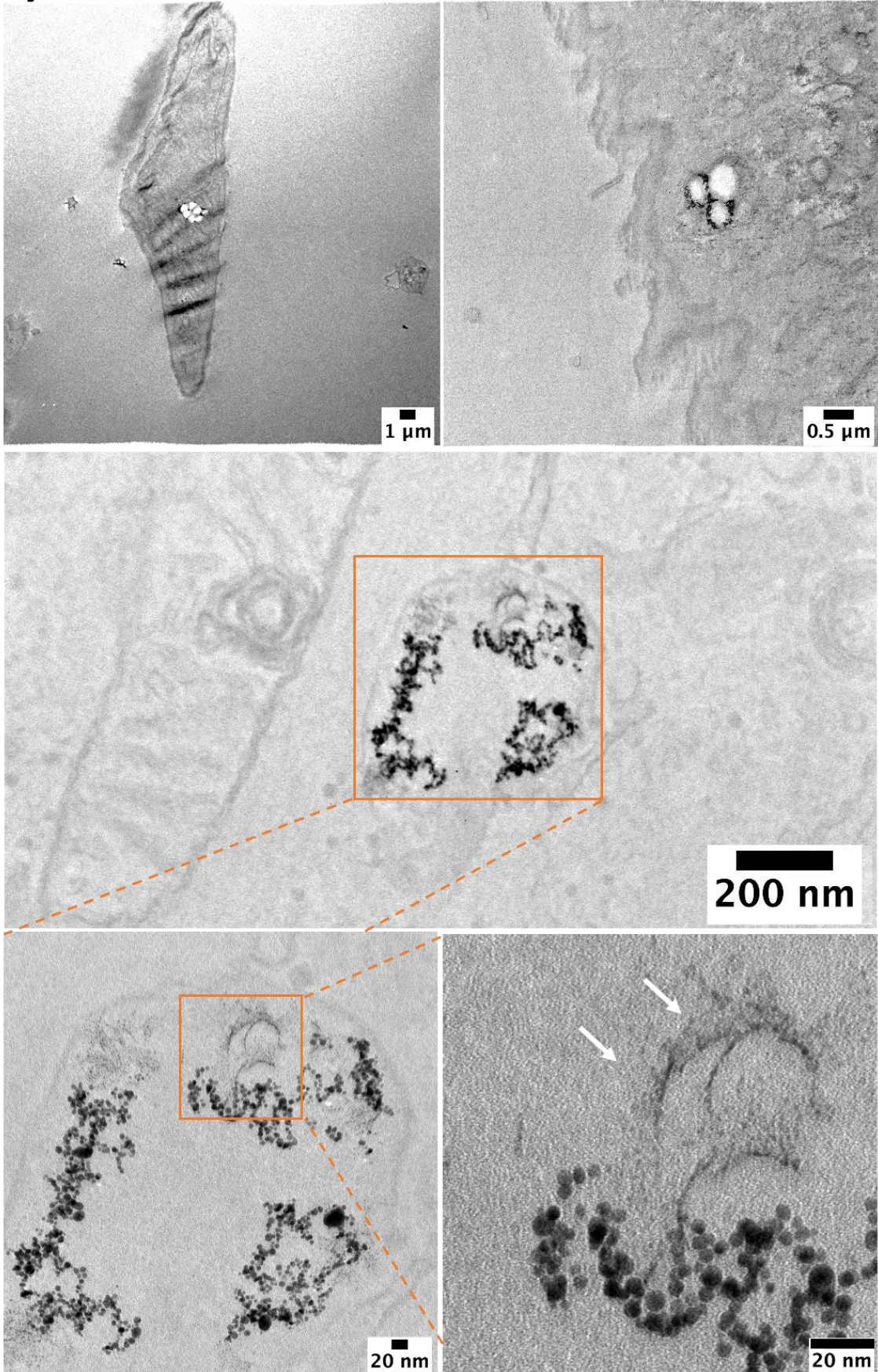
Although the  $\mu$ Gel empty structure is still observable at day 7, the Au NPs clearly changed their distribution with evident segregation and aurosomes formation. In view of such structural transformation of Au NPs, independent from the  $\mu$ Gel structure, we can hypothesize that the MB dye escapes from the direct vicinity of Au NPs (or aurosomes) loosing SERS amplification of the Raman signature and enhancing fluorescence.

**(a) Day 1**



**(b)**

**Day 4**



(c)

Day 7

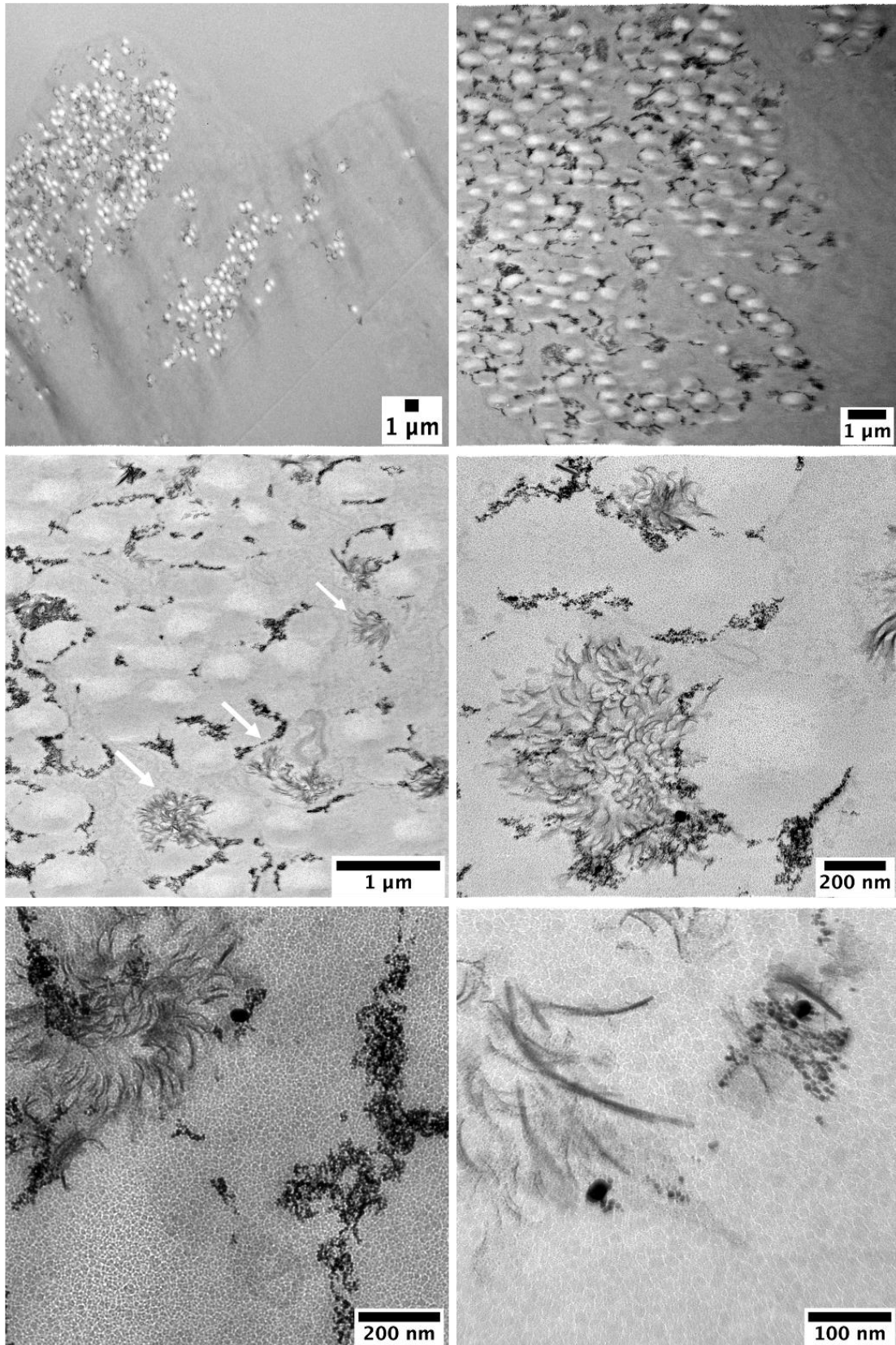


**Figure 3.8** Degradation of Gel@MB@Au<sub>(5)</sub> after incubation with fibroblasts for 1 day, 4 days and 7 days observed by TEM.

### 3.2.8 Photothermal therapy

We next investigated the photothermal toxicity of the hybrid gels by Alamar blue assay, after  $2 \text{ W/cm}^2$  808 nm laser irradiation on fibroblasts incubated with Gel@dye@Au<sub>(5)</sub> for 24 h and compared it to the cytotoxicity observed without irradiation (Figure 3.9).

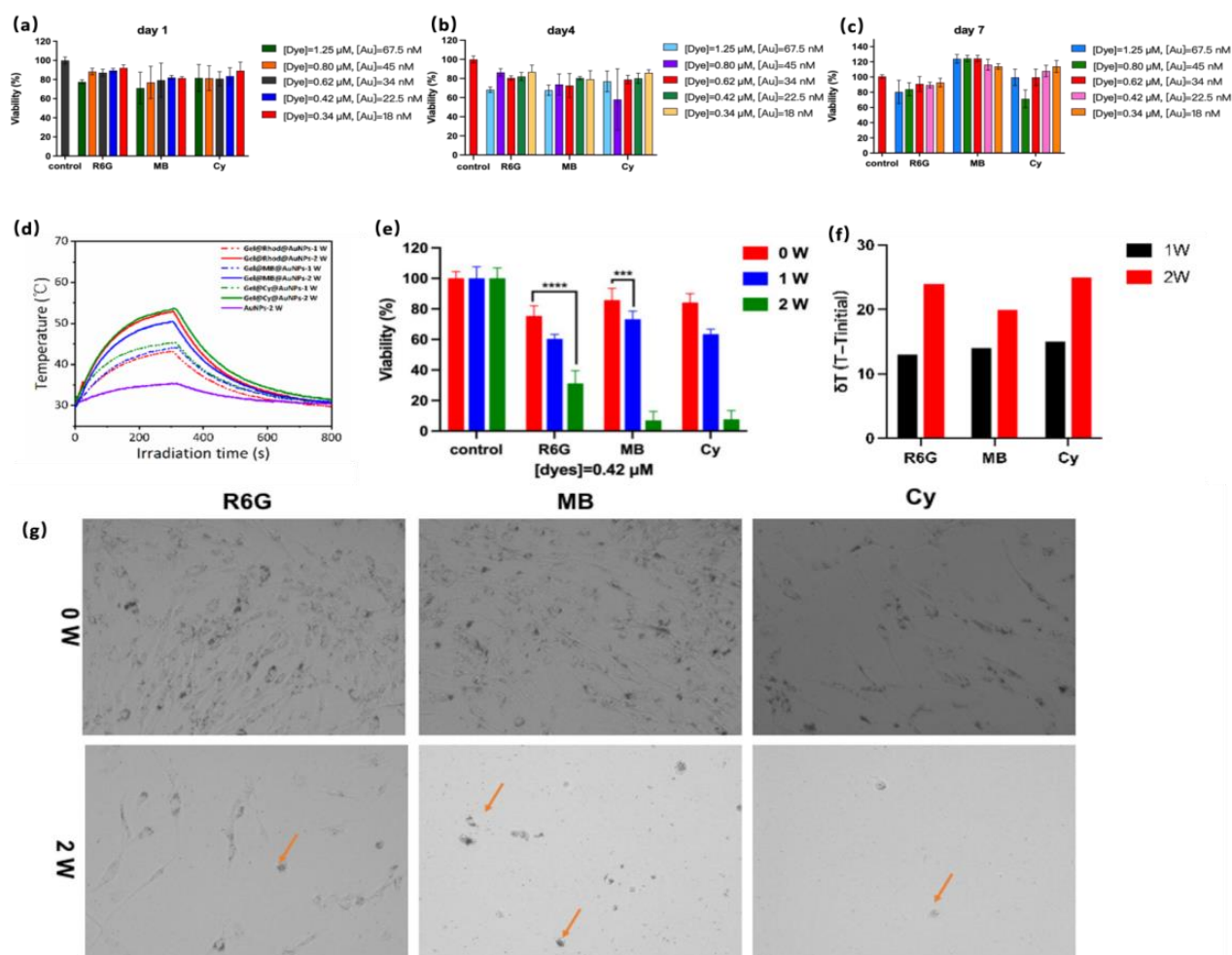


**Figure 3.9** Mid-term cytotoxicity test by alamar blue of Gel@R6G@Au<sub>(5)</sub>, Gel@MB@Au<sub>(5)</sub> and Gel@Cy@Au<sub>(5)</sub> on fibroblasts at day 1 (a), day 4 (b) and day 7 (c) after exposure. (d) Heating properties of fibroblast cell pellet incubated with Gel@dye@Au<sub>(5)</sub> and exposed to 808 nm laser. Cell pellets were collected in 100 µL DMEM without phenol red before irradiation. (e) Phototoxicity on treated fibroblast pellets at different laser irradiation powers (1W and 2W/cm<sup>2</sup>) with Gel@dye@Au<sub>(5)</sub> ([dye]=0.42 µM, [Au NPs]= 22.5 µM). (f) Temperature increase in treated fibroblast pellets with two laser irradiation powers. (g) Morphology of fibroblasts after exposure to 808 nm laser at 2W/cm<sup>2</sup> for 5 min and re-culture with complete medium overnight.

Fig 3.9 a,b,c shows the dark toxicity (without irradiation) of the Gel@dye@Au<sub>(5)</sub> at different concentrations and time after exposure. No significant toxicity is observed at low Gel@dye@Au<sub>(5)</sub> concentration, whereas the highest concentration, particularly for R6G and Cy shows a larger toxicity

at day 7, probably linked to the intracellular release of free dyes. After laser irradiation of cell pellet and re-culture with complete medium overnight, we observed that most of the cells were dead and the shape turned round after the irradiation (Fig 3.9g). Figure 3.9d shows the heating properties of fibroblast cell pellet previously incubated with Gel@dye@Au<sub>(5)</sub> and exposed to an 808 nm laser. The temperature of the pellet increased to 50-55 °C after exposition to the laser at 2W/cm<sup>2</sup> for 5 min, enough for inducing the apoptosis of cells. From Figure 3.9e, we could see the obvious phototoxicity of Gel@dye@Au<sub>(5)</sub>. Before irradiation, around 80% cells survived. However, after exposure to the laser, only 10%-30% cells were alive. This results suggest that Gel@dye@Au<sub>(5)</sub> are promising agents for photothermal therapy. It will be necessary to investigate the light to heat conversion and photothermal toxicity of the hybrids at later time points in fibroblasts to evidence the effects of hybrid biotransformations on their intracellular photothermal properties.

### **3.3 Materials&Methods**

#### ***3.3.1 Hybrid microgel preparation***

The hybrid microgels were prepared according to the protocol described in chapter 2. Briefly, 1 mL of bare microgel (17.3 mg. mL<sup>-1</sup>) and 5 µL of 10<sup>-2</sup> M fluorescent dyes (Rhodamine 6G (R6G), methylene blue (MB) or Cyanine 7.5 amine (Cy)) were mixed and incubated at 4°C. After 48 h, the free dyes were removed by 1 cycle of centrifugation/redispersion in water at 7000 rpm for 7 min. The protocol with 5 incubations steps described in Chapter 2 was then applied in order to get Gel@dyes@Au<sub>(5)</sub>.

#### ***3.3.2 Cell culture***

Deidentified human skin primary fibroblasts were cultured in DMEM Medium GlutaMax medium (Gibco) containing 10% fetal bovine serum (FBS) and 1% of a solution of Penicillin Streptomycin (respectively 10,000 Units/mL and 10,000 µg/mL) (Gibco) at 37°C in 5% CO<sub>2</sub> humidified atmosphere.

#### ***3.3.3 Mid-term cytotoxicity***

After the 24h uptake of µGels by cells, the medium was removed and exceeding nanoparticles were washed with 500 µL of PBS once. Then fresh 300 µL of medium without FBS and without phenol-red and containing 10% Alamar Blue were added to each well. 200 µL of each 48 wells were

transferred to wells from a non-transparent 96 wells plate and fluorescence intensity was measured in a plate reader (Ex 560 Em 590) (SpectraMax iD3, Molecular Devices, US).

### ***3.3.4 Phototoxicity***

Fibroblast seed in 6-well plate at density of 80 000 cells/well overnight. 6 mL of Gel@dye@Au<sub>(5)</sub> were incubated with fibroblasts for 24h (2 mL for each well and 3 wells for  $\mu$ Gels with one irradiation condition). After the 24h uptake of  $\mu$ Gels by cells, the medium was removed, and exceeding nanoparticles were washed with 2 mL of PBS once. Cell pellets were collected and dispersed into 100  $\mu$ L DMEM (without Phenol red) then irradiated with an 808 nm laser at light fluence of 1 or 2 W/cm<sup>2</sup> for 5 min, and re-cultured in 6 well plate with complete medium overnight. The cell viability was tested by replacing medium with fresh 2 mL of medium without FBS and without phenol red and containing 10% Alamar Blue and fluorescence intensity was measured in a plate reader (Ex 560 Em 590) (SpectraMax iD3, Molecular Devices, US)

### ***3.3.5 Transmission Electron Microscopy : characterization of hybrids***

200  $\mu$ L of Gel@dye@Au suspensions were irradiated with a 808 nm laser at 2W/cm<sup>2</sup> for 5 min. Then 3  $\mu$ L of the heated suspension was dropped onto a carbon grids. The drops deposited on the TEM carbon grids were heated for 1 min more with the 808 nm laser at 2W/cm<sup>2</sup> and then let to dry on the grids.

### ***3.3.6 TEM characterization of the hybrids inside cells in function of time***

After the 24h uptake of  $\mu$ Gels by cells, the medium was removed and exceeding nanoparticles were washed with 500  $\mu$ L of PBS once. Cells were further incubated for 4 days or 7 days in medium 2% FBS except for the condition day 1 where the cells were immediately fixed. Medium was removed and the cells were rinsed 3 times with 0.2M Cacodylate solution for 3 times. Then the cells were fixed with 0.1M sodium cacodylate buffer which contain 2% glutaraldehyde for 45 min at room temperature. The fixing solution was replaced with 0.2 M cacodylate buffer at 4 ° C and samples were incubated 1 h. The Buffer was then replaced with fresh 0.2 M Cacodylate buffer and the samples were kept at 4 ° C until inclusion. Samples were then contrasted with Oolong Tea Extract (0.5% in cacodylate buffer), osmium tetroxyde (1% in cacodylate buffer), and potassium cyanoferrate (1.5% in cacodylate buffer). They were then gradually dehydrated in ethanol (25 to 100%). The samples were then substituted

gradually in propylene oxide, a mix of propylene oxide and Epon, and finally, embedded in pure Epon (Delta microscopie, Labege, France). Thin sections (70 nm) of samples were collected on 200-mesh grids. Observations were performed on Tecnai 12 microscope (Platform Imago seine, Institut Jacques Monod, UMR7592, National Center for Scientific Research [France]/Universite Paris Diderot, Paris, France and operated at 80 kV.

### ***3.3.6 Raman imaging***

After the 24h uptake of hybrids by cells, the medium was removed and exceeding nanoparticles were washed with 500  $\mu$ L of PBS once. Cells were further incubated for 4 days or 7 days in medium 2%FBS except for the condition day 1 where the cells were immediately fixed. Cells were washed by ice DPBS 10 times to remove excess particles and were fixed with 4% PFA 20 min at room temperature and then washed 3 times with DI water for further analysis by Raman imaging (Laser 638 nm with power of 1%, Grating 300gr/mm, Objective 100x, Hole 100  $\mu$ m, Acq. Time 6s/pt).

### ***3.3.7 Fluorescence imaging***

After the 24h uptake of hybrid  $\mu$ Gels by cells, cells were washed by ice DPBS 10 times to remove excess particles and were fixed with 4% PFA 20 min at room temperature and then washed 3 times with DI water and stained by Hoechst 33342 (5  $\mu$ g.mL<sup>-1</sup>) for 5 min, and rinsed 3 times with DI water. Samples were kept at 4°C for further microscopy analysis.

## **3.4 Conclusion**

In this chapter, we have investigated the biotransformation process of Gel@dye@Au<sub>(5)</sub>. In this study, we took advantage of the optical properties of gold nanoparticles to monitor the de-assembly process and biotransformation of the hybrids  $\mu$ Gel through fluorescence/Raman imaging as well as TEM. The presence of gold nanoparticles provides an enhancement of the Raman signals of the dyes, which is further enhanced 5-20-fold when the pH decreases to pH5.5. The intracellular evolution of the Raman/Fluorescence signals of the hybrid  $\mu$ Gels as a function of time allowed to investigate their biodegradation process. The results show that the  $\mu$ Gels undergo a process of de-assembly from day 1 with Raman ON/fluorescence OFF to day 4 with Raman OFF/Fluorescence ON. Moreover, the study

of the subcellular nanoscale transformation of hybrids inside the fibroblasts reveals the biotransformation of hybrids from day1 (segregation of gold nanoparticles at the gel periphery) and the degradation of gold nanoparticles and formation of aurosome from day 4 to day 7, the later time-point investigated. Overall, this dual-modal imaging approach allows to track the processes from the degradation and disassembly of the hybrid  $\mu$ Gels and has the potential to be a useful tool for preliminary studies of the  $\mu$ Gel transformation and tracing in lysosomes.

### ***Collaborators***

The results presented in this chapter have been obtained thanks to the joint efforts of several collaborators, described below:

- The members of the group Nanobiospectroscopy: Yun Luo, Delphine Onidas, Philippe Nizard, Kartikey Pandey and Claire Mangeney for the characterization of Raman imaging and TEM.
- The members of the MSC Med group: Florence Gazeau, Kelly Aubertin, Giulio Avveduto, etc... for the biological part and TEM of cells.

---

## *Chapter 4. Raman reporters derived from aryl diazonium salts for SERS encoded-nanoparticles*

---

### Summary

#### Abstract

Surface-enhanced Raman scattering (SERS) tags are usually prepared by immobilizing Raman reporters on plasmonic nanoparticles (NPs) *via* thiol-based self-assembled monolayers. We describe here the first example of SERS tags obtained by combining gold NPs and aryl diazonium salts. This strategy results in robust Au–C covalent bonds between the Raman reporter and the NPs, thus ensuring a high stability of the nanohybrid interface.

#### Main objectives

- Elaboration of SERS tags obtained by the surface functionalization of gold NPs by aryl diazonium salts.
- Design of various SERS labels for cell Raman imaging, by changing the Raman reporter fingerprints (bearing -CN, -NO<sub>2</sub> or -COOH groups).

#### Methods

- Creation of multifunctional layers and conjugation with biomolecules.
- Synthesis of AuNPs and spontaneous grafting of aryl diazonium salts.
- Use of three different aryl diazonium salts (bearing either -NO<sub>2</sub>, -CN or -COOH end groups) and post-functionalization by adenosine monophosphate (AMP).
- Characterization of the hybrid particles by transmission electron microscopy (TEM), UV-vis absorption, X-ray photoelectron spectroscopy (XPS) and SERS.
- Raman imaging of EGI-1 cells and CT 26 cells after uptake of the modified NPs.

#### Reference of the publication

Y. Luo, Y. Xiao, D. Onidas, L. Iannazzo, M. Ethève-Quellejeu, A. Lamouri, N. Félidj, S. Mahouche-Chergui, T. Brulé, N. Gagey-Eilstein, F. Gazeau, C. Mangeney. Raman reporters derived from aryl diazonium salts for SERS encoded-nanoparticles. *Chem. Commun.*, **2020**, 56, 6822- 6825.

## 4.1 Introduction

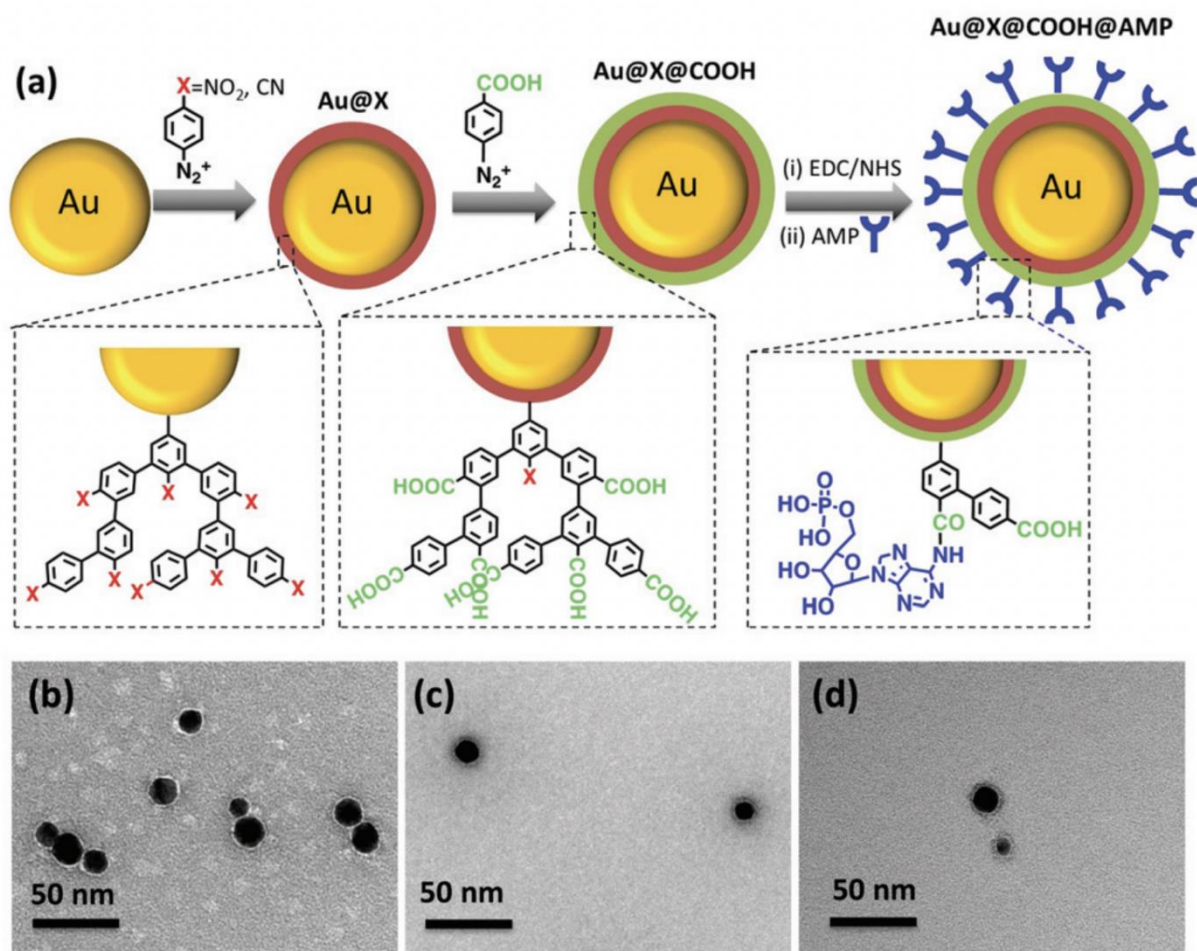
The popularity of surface-enhanced Raman scattering (SERS) tags has increased in recent decades, as an alternative to fluorescent probes, due to their attractive properties.<sup>132</sup> Indeed, unlike the broad spectral feature of fluorescence probes, SERS tags provide multiple sets of narrow peaks, resulting in low spectral overlap and high multiplexing ability. Besides, a single light source can be used to excite multiple Raman reporters, with negligible photobleaching, low background and a high sensitivity that competes with that of fluorescence. Moreover, their low toxicity, compared to quantum dots, has boosted their attractiveness for *in vitro* and *in vivo* biosensing.<sup>133</sup> SERS tags are based on several key elements:<sup>134</sup> a metal core providing the source of SERS enhancement,<sup>135, 136</sup> an adsorbed Raman reporter molecule giving the spectral fingerprints, a protective shell to enhance the stability of the adsorbed reporter molecule and a targeting entity to improve specificity. The stacking of all these elements into a single SERS tag is a multi-step process which is usually challenging.<sup>137</sup> In particular, reduction of the colloidal stability of plasmonic nanoparticles during the adsorption of Raman codes may lead to uncontrolled particle agglomeration. To solve this problem, the use of polymers or the co-adsorption of small Raman reporters and long-chain thiols was proposed, preserving colloidal stability all along the codification process.<sup>138, 139</sup> However, the chemical stability of thiolate self-assembled monolayers (SAMs) is a critical issue for applications in ambient and aqueous environments. Indeed, several studies have shown that SAMs desorb spontaneously from the surface in aqueous solutions after only few days<sup>140-142</sup> and degrade upon laser excitation.<sup>143</sup> Significant progress in stability have been obtained by using longer-chain thiols,<sup>144</sup> small amount of amphiphilic surfactant molecules<sup>141</sup> or multidentate sulfur-based adsorbates.<sup>145</sup>

Nevertheless, the development of alternative surface chemical approaches enabling robust covalent attachment of Raman reporters to plasmonic NPs can be expected to result in more significant improvements of interfacial stability. Aryl diazonium salts have emerged in recent years as a new generation of surface modifiers for plasmonic nanoparticles,<sup>146-150</sup> in alternative to thiol-based SAMs. These molecules present several advantages such as their ease of preparation, rapid grafting, large choice of reactive functional groups and robust metal–C interfacial bonds with the surface.

Their grafting on the surface of plasmonic NPs is a two-stage process:<sup>151,152</sup> (i) first, the spontaneous reduction of the diazonium salts generates an aryl radical that binds to the surface, and (ii) in a second step, due to their high reactivity, these radicals react with the first grafted layer to give nanometer to micrometer thick polyaryl layers. Aryl diazonium salts were used to modify plasmonic NPs in order to design NPs-coated electrodes,<sup>153</sup> colorimetric nanosensors,<sup>154</sup> antimicrobial agents<sup>155</sup> and functional lithographic arrays.<sup>156-158</sup> In the latter case, they were shown to result in regioselective grafting of organic patches located specifically in the regions of maximum near field enhancement around nanoparticles, *via* site-selective hot-electron mediated reduction of aryl diazonium salts. However, the application of these surface agents as Raman reporters for SERS encoded-nanoparticles has never been reported so far, although aryl layers derived from diazonium salts were shown to exhibit intense Raman signals.<sup>159,160</sup>

In this work, we explore the potential of aryl diazonium salts to provide a new class of Raman reporters with several advantages, such as: (i) the formation of strong interfacial bonds with the supporting NPs, (ii) the presence of intense SERS fingerprints, (iii) the possibility to create multilayers with various functions. The formation of multilayers will be exploited here to introduce straightforwardly (i) several SERS labels along the grafted polyaryl chains and (ii) post-functionalization moieties at their end. As a proof of concept, we selected three different aryl diazonium salts. Two of them, bearing either nitro groups (4-nitrobenzenediazonium tetrafluoroborate, noted D-NO<sub>2</sub>) or cyano groups (4-cyanobenzediazonium tetrafluoroborate, noted D-CN) were chosen to act as Raman reporters. The third one possesses carboxyl-terminated groups (4-carboxybenzene diazonium tetrafluoroborate, noted D-COOH) for post-functionalization with the nucleotide adenosine 5'-monophosphate (AMP) (see Fig. 4.1). Adenosine derivatives are important intermediary metabolites in cells, which have fundamental impacts on a wide range of cellular processes.<sup>161</sup> Particularly, AMP was identified recently to be a novel tumour-targeting ligand, guiding nanoparticles to cancer cells *via* adenosine A1 receptor, offering promising prospects for clinical diagnostic and therapeutic applications.<sup>162</sup> The functionalization of spherical gold NPs by the three aryl diazonium salts (–NO<sub>2</sub>, –CN, –COOH) and AMP was performed in water at room temperature, providing a simple method to create multifunctional SERS tags. The modified

NPs were characterized by transmission electron microscopy (TEM), UV-vis absorption, X-ray photoelectron spectroscopy (XPS) and SERS.



## 4.2 Results & Discussion

Spherical AuNPs with an average diameter of  $15 \pm 3$  nm (see typical TEM image Fig. 4.1a,b), were prepared through the well-known Turkevich method,<sup>163</sup> by citrate reduction of  $\text{HAuCl}_4$ . The procedure for grafting the Raman reporters on the AuNPs consisted of to add the corresponding diazonium salts ( $5 \times 10^{-5}$  M) to the AuNPs aqueous dispersions ( $[\text{AuNPs}] = 8 \times 10^{-9}$  M) and to let them react spontaneously during 60 min at room temperature. Multilayers were obtained by adding

the diazonium salts successively, one after the other in a controlled sequence. The functionalized AuNPs were then purified through 3 cycles of centrifugation/redispersion in water. Post-functionalization with AMP was performed by mixing an aqueous AMP solution ( $10^{-4}$  M) with the resulting NPs, and adding 1-ethyl-3-(3-dimethylaminopropyl)carbodiimide (EDC) and *N*-hydroxysuccinimide (NHS), in the presence of 0.001 wt% polyvinylpyrrolidone (PVP), as a stabilizer. After reaction at 4 °C overnight, the particles were washed through 3 cycles of centrifugation/redispersion in water. Details on the functionalization experiments are given in the Materials & Methods section. Transmission electron microscopy (TEM) images (see Fig. 4.1b–d and Fig. 4.2), show individually dispersed particles indicating that the reaction of the AuNPs with the diazonium salts does not disturb their colloidal stability.

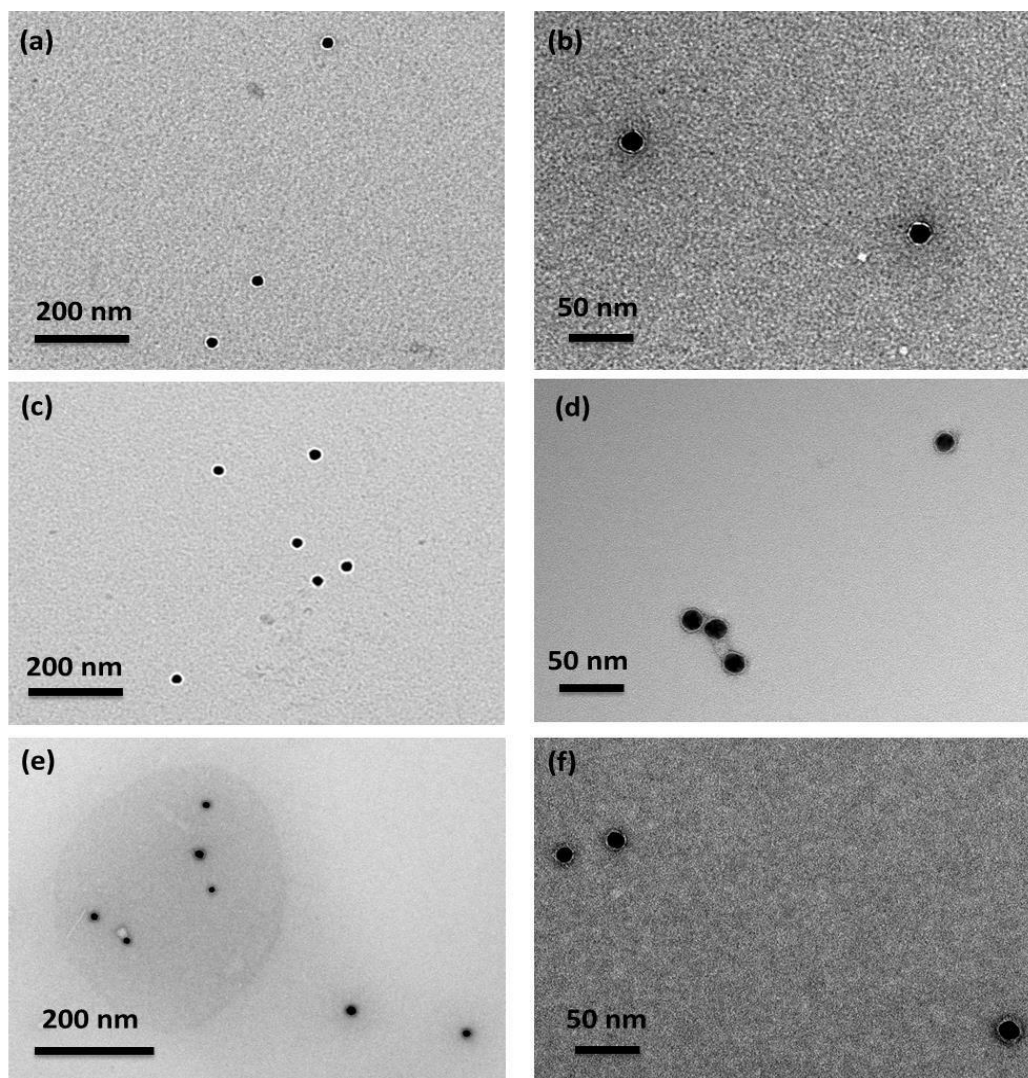


**Figure 4.2** TEM images of (a) and (b) AuNPs; (c) and (d) Au@NO<sub>2</sub>@COOH@AMP; (e) and (f) Au@CN@COOH@AMP.

TEM images (Fig. 4.2) show individually dispersed particles indicating that the reaction of the AuNPs with the diazonium salts does not disturb their colloidal stability. The AuNPs average diameter was estimated using 100 NPs from different TEM images. Interestingly, the overall NPs size appears to increase after surface functionalization (see Table 4.1) and the functionalization process leads to the appearance of a thin layer covering the NPs, likely due to the presence of the polyaryl layers and AMP.

**Table 4.1** Evolution of the average NPs diameter estimated by TEM for Au, Au@CN@COOH@AMP and Au@NO<sub>2</sub>@COOH@AMP.

Sample	NPs diameter (TEM) /nm
<b>Au</b>	15 ± 2
<b>Au@CN@COOH@AMP</b>	18 ± 2
<b>Au@NO<sub>2</sub>@COOH@AMP</b>	19 ± 2

Interestingly, it can be seen from TEM images that the functionalization process leads to the appearance of a thin layer covering the NPs, likely due to the presence of the polyaryl layers and AMP. An average thickness of the organic coating of *ca.* 3–4 nm was estimated using 100 NPs from different TEM images (see Table 4.1.).

The observation of polyaryl layers around the gold cores can be explained by the grafting reaction mechanism. Indeed, it is based on the formation of aryl radicals by spontaneous cleavage of diazohydroxides Ar–N=N–OH that form from aryl diazonium salts in neutral aqueous media, as described previously.<sup>164</sup> The formed aryl radicals bind to the AuNPs surface and to the first (and further) grafted aromatic groups *via* homolytic aromatic substitution, leading to polyaryl layers.

The extinction profile of the AuNPs (Fig. 4.3a and b) retained its original shape upon functionalization confirming that the colloidal stability was preserved. Nevertheless, a progressive red shift of the plasmon band was observed after each functionalization step (see zoom in Fig. 4.3 4.2a and b and  $\lambda_{\max}$  values in Table 4.2). This red shift increases with the number of grafted layers

and reaches *ca.* 10 nm for AMP-modified NPs, likely due to the modification of the local dielectric environment around the Au cores.

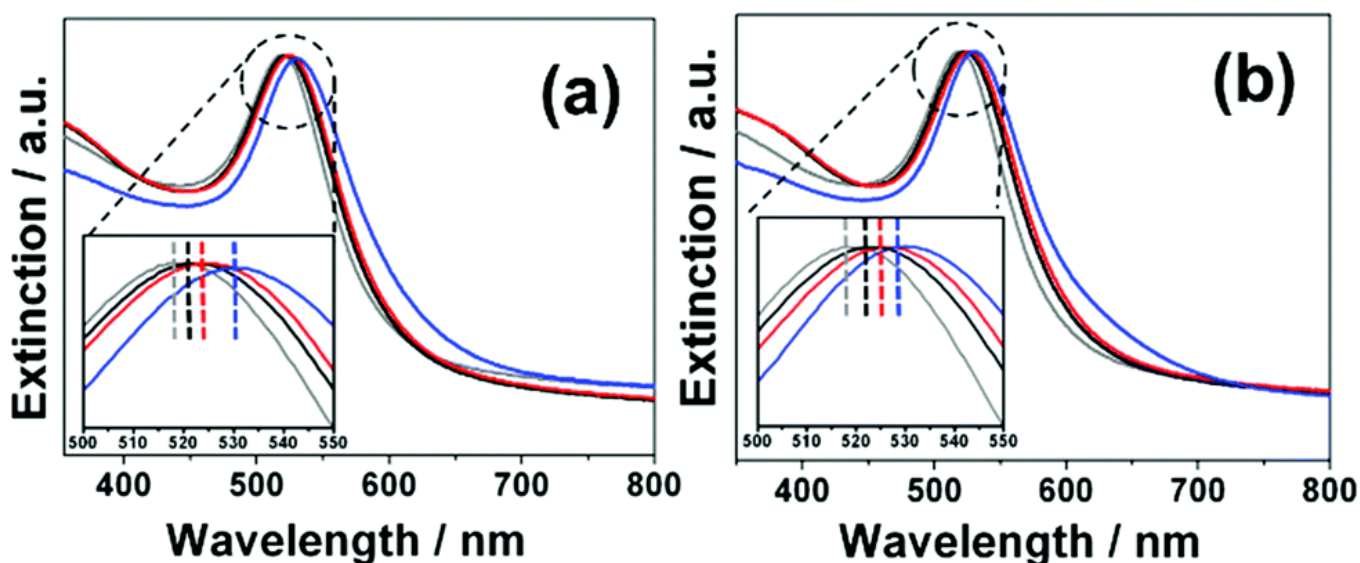


**Figure 4.3** (a) Normalized extinction spectra of AuNPs (grey), Au@CN (black), Au@CN@COOH (red) and Au@CN@COOH@AMP (blue); (b) normalized extinction spectra of AuNPs (grey), Au@NO<sub>2</sub> (black), Au@NO<sub>2</sub>@COOH (red) and Au@NO<sub>2</sub>@COOH@AMP (blue).

**Table 4.2** Wavelength of the plasmon band ( $\lambda_{max}$ ) observed in the extinction spectra of the different AuNP samples.

<i>Sample</i>	<i>Plasmon band <math>\lambda_{max}</math> (nm)</i>
Au	520
Au@CN	522
Au@CN@COOH	524
Au@CN@COOH@AMP	531
Au@NO <sub>2</sub>	523
Au@NO <sub>2</sub> @COOH	525
Au@NO <sub>2</sub> @COOH@AMP	530

It is noteworthy that the addition of a small amount of PVP (0.001 wt%) in the colloidal dispersion at the post-functionalization step was necessary in order to maintain a perfect colloidal stability, as described in the section Materials & Methods (see Fig. 4.4a). However, this parameter should be carefully controlled to ensure that the NP surface is still accessible for post-functionalization with AMP. Indeed, above a certain [PVP] value, the grafting of AMP is no more detected by SERS after the post-functionalization step (see Fig. 4.4 b). The SERS spectra, displayed in Fig. 4.4 (b) reveal that when the concentration of PVP is too high, the post-functionalization reaction cannot proceed, probably due to a poor access of the reactants to the surface. Indeed, the signal of AMP could not be detected on the SERS spectra when the PVP concentration reaches 1%. Finally, a good compromise between colloidal stability and post-functionalization capacity was found using a concentration of PVP of 0.001 wt%.

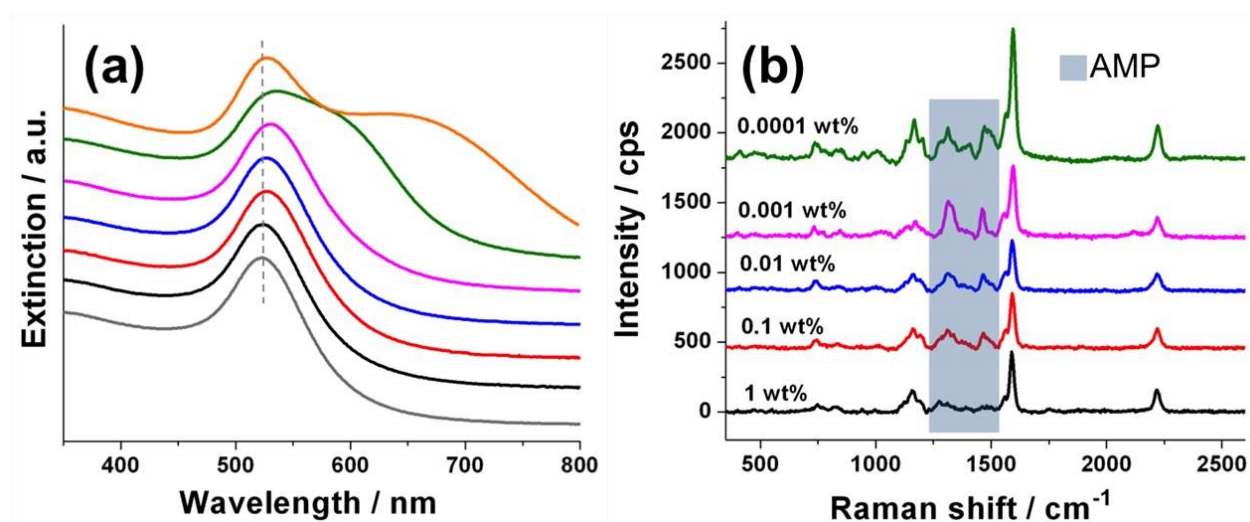


**Figure 4.4** (a) Normalized extinction spectra and (b) SERS spectra for AuNPs (grey), Au@CN@COOH@AMP prepared in 1 wt.% PVP (black), 0.1 wt.% PVP (red), 0.01 wt.% PVP (blue), 0.001 wt.% PVP (pink), 0.0001 wt.% PVP (green), and without (orange) PVP solution. The blue shadow highlights the SERS bands belonging to AMP.

The stability of the nanoprobe was evaluated in various media: aqueous solutions with a high ionic force, acid or basic solutions. No sign of aggregation could be detected, as shown in Fig. 4.5, regardless the medium to which the particles were exposed, demonstrating an extended colloidal stability.

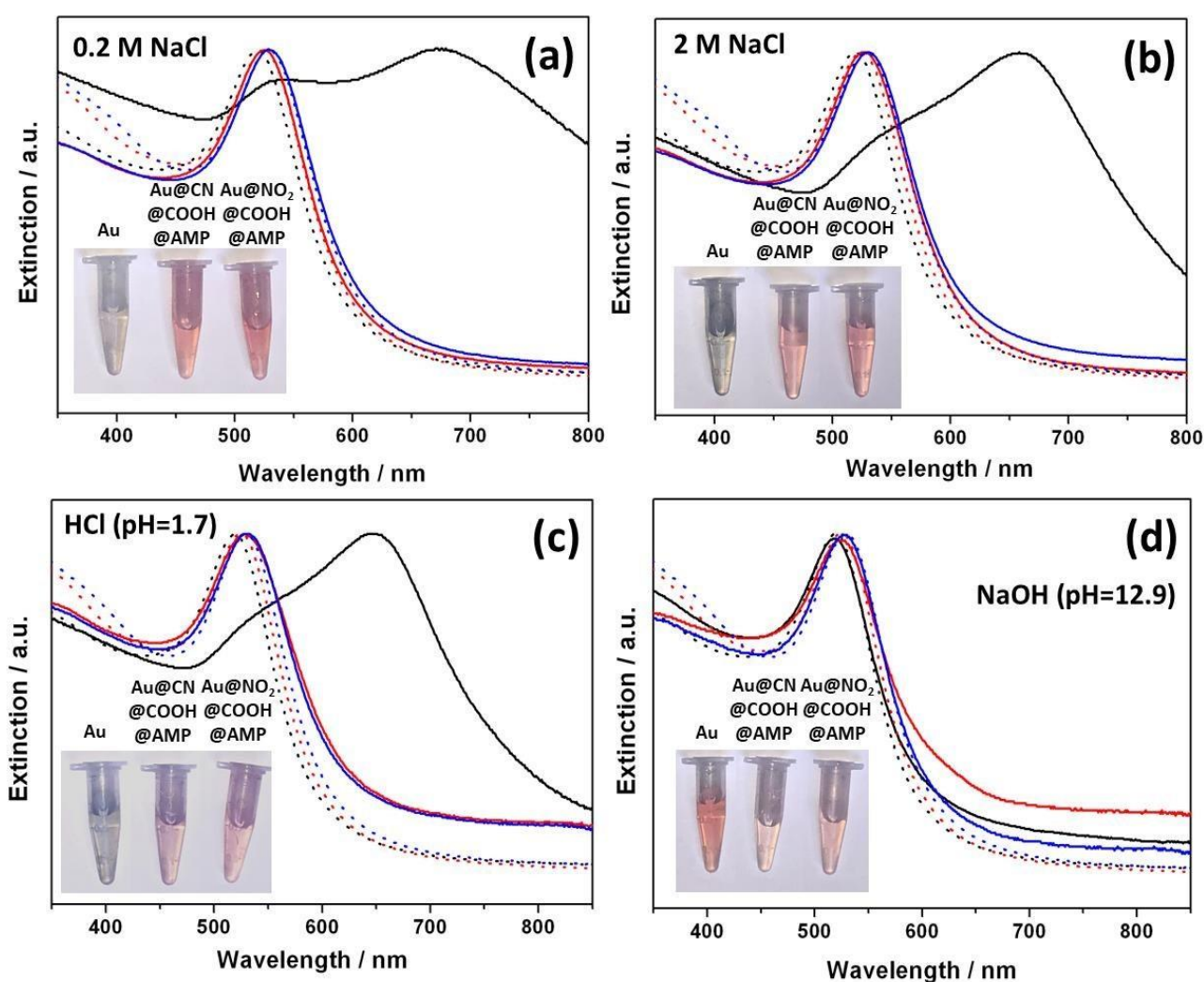


**Figure 4.5** Extinction spectra of AuNP samples dispersed in various aqueous media: (a) NaCl 0.2 M; (b) NaCl 2 M; (c) HCl at pH = 1.7 and (d) NaOH at pH = 12.9. The black solid line corresponds to the spectra of bare AuNPs, the red line to Au@CN@COOH@AMP and the blue spectra to Au@NO<sub>2</sub>@COOH@AMP. The spectra of the as-prepared AuNPs, Au@CN@COOH@AMP and Au@NO<sub>2</sub>@COOH@AMP were used as references (dotted lines). The insets show photos of the different samples in NaCl, HCl and NaOH containing aqueous media.

The surface chemical composition of the modified AuNPs was investigated by XPS (see Table 4.3 and Fig. 4.6). The XPS spectra revealed large modifications after functionalization. Particularly, the oxygen signal, very intense in the spectrum of the initial AuNPs due to the citrate capping layer, was strongly attenuated after reaction with the different diazonium salts due to the ligand exchange at the surface of the NPs.

**Table 4.3** Surface chemical composition (At %) of initial AuNPs, Au@CN, Au@CN@COOH@AMP, Au@NO<sub>2</sub>, Au@NO<sub>2</sub>@COOH@AMP.

Material <sup>[a]</sup>	Au	C	O	N	P
Citrate-capped AuNPs	4	59	36	1	-
Au@CN	27	50	19	4	-
Au@CN@COOH@AMP <sup>a</sup>	11	64	18	5	2
Au@NO <sub>2</sub>	21	54	21	4	-
Au@NO <sub>2</sub> @COOH@AMP	12	61	19	6	2

In the meanwhile, the intensity of the nitrogen signal increased markedly, in agreement with the presence of CN or NO<sub>2</sub> groups. After immobilization of AMP, the carbon content increased while a new peak assigned to phosphorus appeared. Peak fitting of the C1s signal, displayed in Fig. 4.6, further reflects the surface modifications introduced by the grafting of AMP, confirming the successful covering of the gold cores by the functional polyaryl layers and AMP.

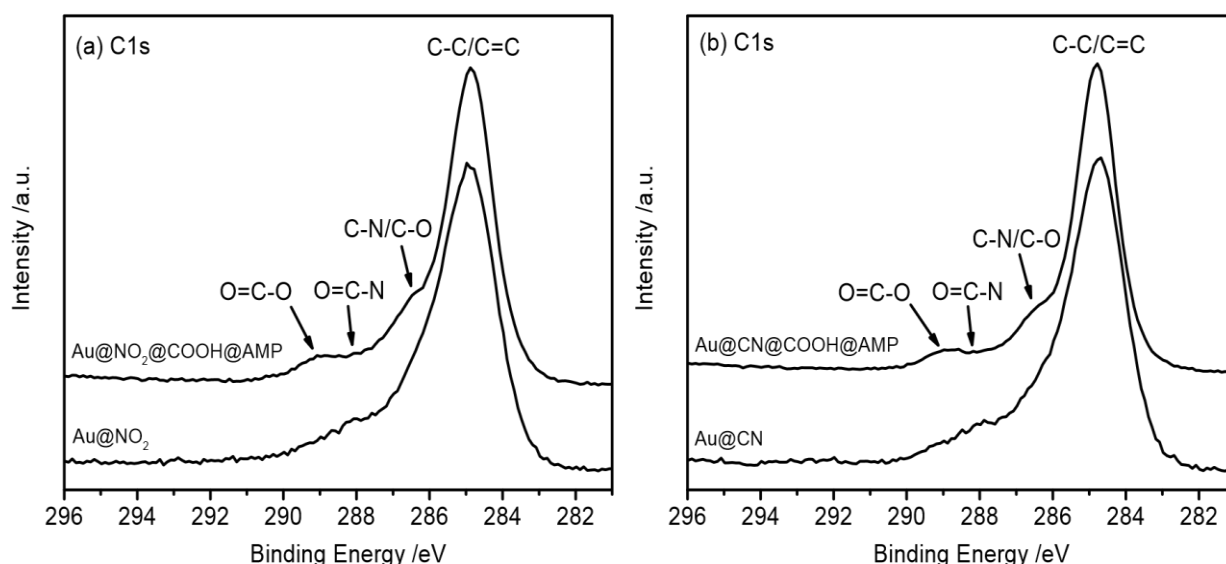


**Figure 4.6** XPS high resolution C1s spectra of the modified nanoparticles (a) Au@NO<sub>2</sub> and Au@NO<sub>2</sub>@COOH@AMP; (b) Au@CN and Au@CN@COOH@AMP.

The SERS properties of the encoded particles were studied at 633 nm laser excitation and compared to the Raman spectra of the free diazonium salts (Fig. 4.7).

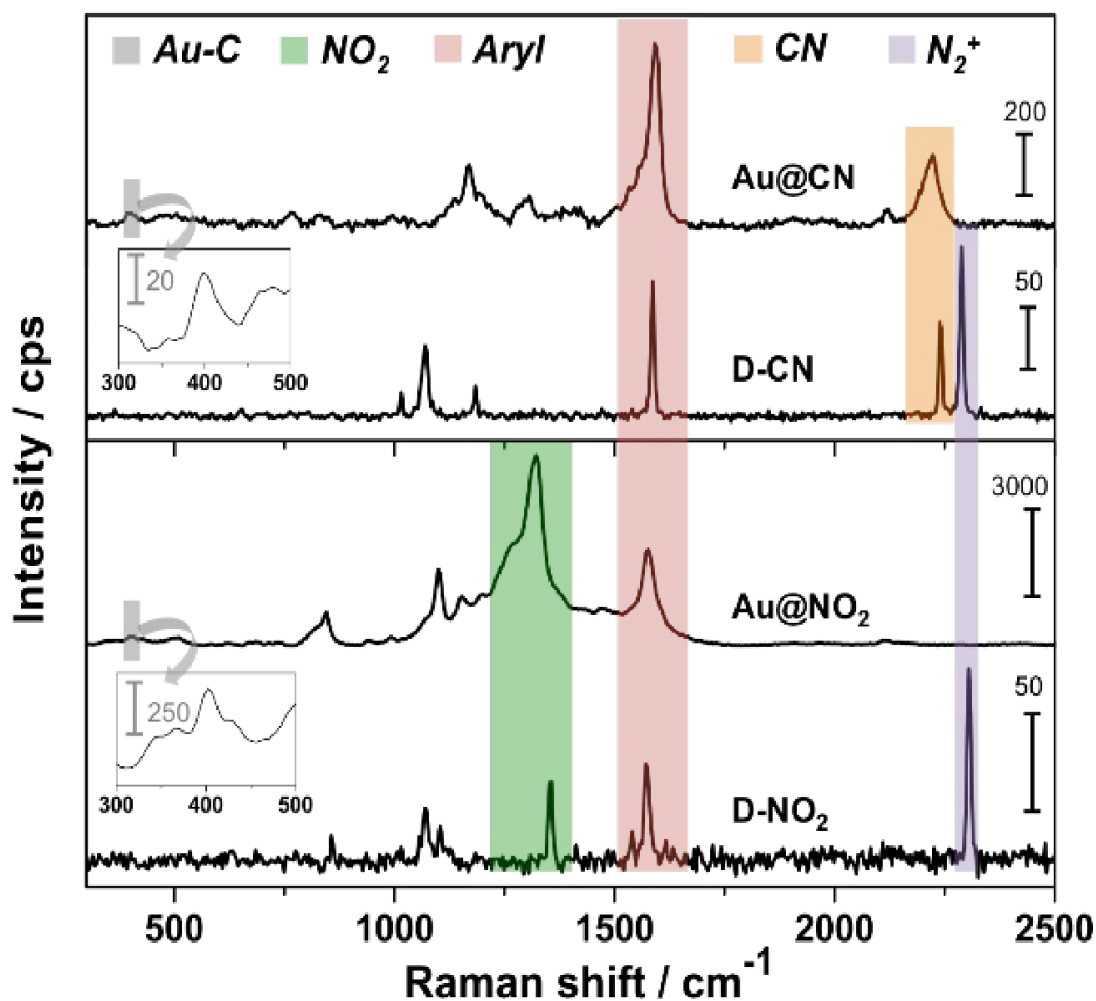


**Figure 4.7** Comparison between the SERS spectra of nanoprobcs Au@CN and Au@NO<sub>2</sub> and the Raman spectra of the corresponding diazonium salt powders, D-NO<sub>2</sub> and D-COOH. Inset: zoom in the spectral range 300-500  $\text{cm}^{-1}$ , revealing the presence of Au-C peak.

Several key features can be pointed out: first, the intense  $\text{N}\equiv\text{N}$  stretching peak, observed in the Raman spectra of the diazonium salt powders at ca. 2280–2300  $\text{cm}^{-1}$  disappears completely for all nanoprobcs, confirming the removal of the diazonium group during the grafting reaction. At the same time, one notices the appearance of a small peak at ca. 410–416  $\text{cm}^{-1}$ , assigned to the Au–C stretching vibration, evidencing the covalent grafting of the aryl layers. The SERS spectra display also the characteristic signature of phenyl-derivatives stemming from diazonium salts, particularly the aryl ring stretching peak at ca. 1580–1595  $\text{cm}^{-1}$ . For the nanoprobcs Au@NO<sub>2</sub> and Au@CN,

the characteristic NO<sub>2</sub> and CN stretching modes appear at 1330 cm<sup>-1</sup> and 2220 cm<sup>-1</sup>, respectively. Interestingly, thanks to the radical coupling mechanism in diazonium salt chemistry, different functional layers could be grafted one after another around the gold core, forming multifunctional layers with a wide variety of SERS signatures. For example, Fig. 4.8 compares the SERS spectra and the corresponding Raman images of Au@CN, Au@NO<sub>2</sub>, Au@NO<sub>2</sub>@CN and Au@CN@NO<sub>2</sub>, deposited as dried drops on a glass slide. Each type of NPs reveals distinct characteristic spectra, which can be associated to one particular color in Raman imaging. The spectra of Au@CN are associated here to the magenta color, Au@NO<sub>2</sub> to the blue, Au@NO<sub>2</sub>@CN to the green and Au@CN@NO<sub>2</sub> to the red. The blackline corresponds to the glass slide.

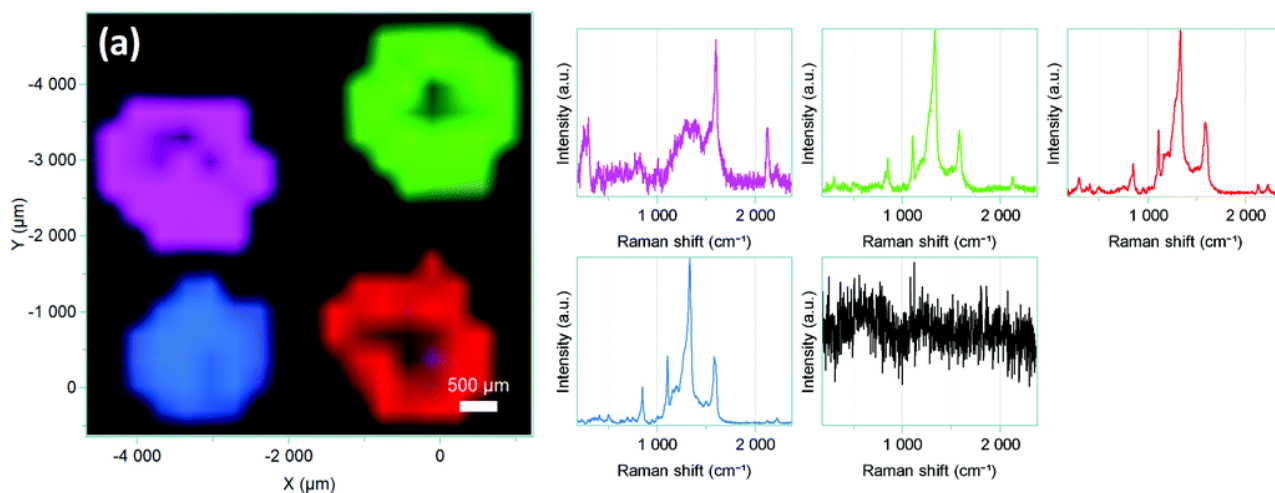


**Figure 4.8** Raman images and corresponding SERS spectra of Au@CN (magenta), Au@NO<sub>2</sub> (blue), Au@CN@NO<sub>2</sub> (green) and Au@NO<sub>2</sub>@CN (red), deposited as dried drops on a glass slide.

A layer of carboxyl-terminated functions was then added to the nanoconstructs to obtain a post-functionalizable platform. The successive grafting of the different layers for Au@CN@COOH and Au@NO<sub>2</sub>@COOH could be assessed by following the increase in intensity of the aryl ring stretching peak,  $I_{\text{aryl}}$  at 1580–1595 cm<sup>-1</sup> (see Fig. 4.9 and 4.10) and the evolution of  $I_{\text{CN}}/I_{\text{Au-C}}$ ,  $I_{\text{NO}_2}/I_{\text{Au-C}}$  and  $I_{\text{aryl}}/I_{\text{Au-C}}$  band intensity ratios (see Fig. 4.11). For this, D-NO<sub>2</sub> or D-CN (final concentration 5x10<sup>-5</sup> mol.L<sup>-1</sup>) were added in 1mL of AuNPs and an aliquot of the solution was taken out at various times after addition of the diazonium salts (5, 10, 15, 20 and 40 min). Each aliquot was washed by repeating 2 cycles of centrifugation/redispersion in water. After 60 min, D-COOH (final concentration 5x10<sup>-5</sup> mol.L<sup>-1</sup>) was added into the initial solution. New aliquots were then taken out at 60, 80, 100 and 120 min. The SERS spectra of each aliquot were recorded

by depositing a drop of the washed solutions on glass slides and let them dry at air (see Fig. 4.9 and 4.10). 5 spectra of each sample were recorded to obtain average band intensities.

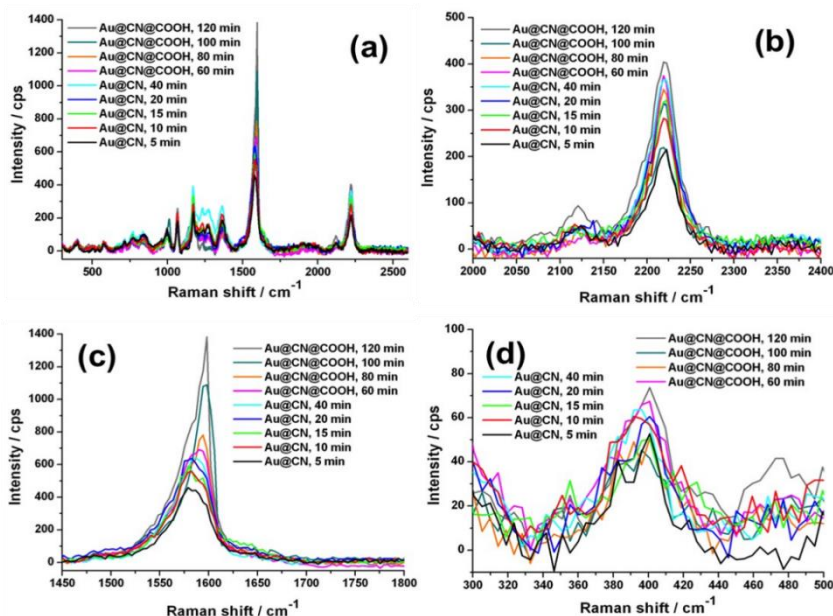


**Figure 4.9** SERS spectra of Au@CN and Au@CN@COOH recorded after different times of the functionalization reaction. (a) in the spectral range 300-2600 cm<sup>-1</sup>, (b) 2000-2400 cm<sup>-1</sup> (CN stretch), (c) 1450-1800 cm<sup>-1</sup> (aryl peak) and (d) 300-500 cm<sup>-1</sup> (Au-C stretch).

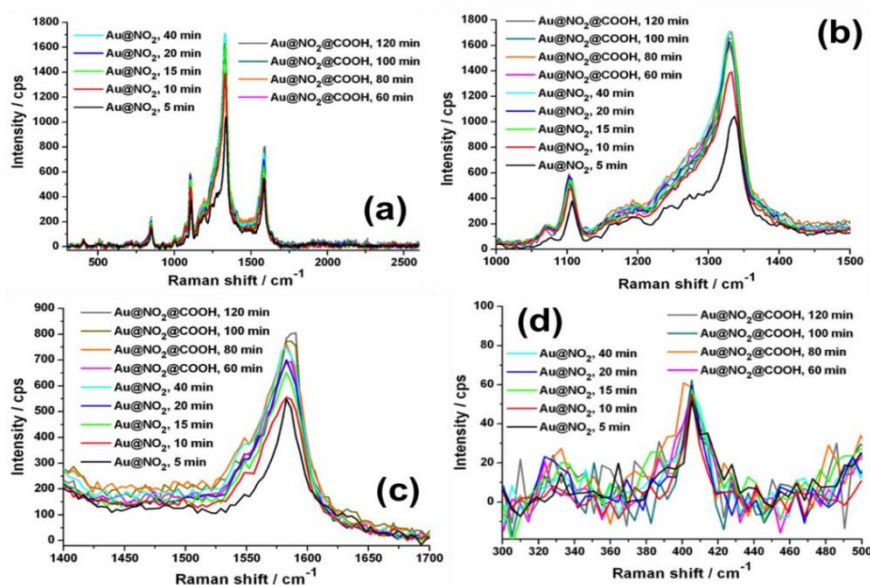


**Figure 4.10** SERS spectra of Au@NO<sub>2</sub> and Au@NO<sub>2</sub>@COOH recorded after different times of the functionalization reaction. (a) in the spectral range 300-2600 cm<sup>-1</sup>, (b) 1000-1500 cm<sup>-1</sup> (NO<sub>2</sub> peak), (c) 1400-1700 cm<sup>-1</sup> (aryl peak) and (d) 300-500 cm<sup>-1</sup> (Au-C stretch).

Figure 4.11 displays the evolution of band intensity ratios selected to monitor the successive grafting of the different layers for Au@CN@COOH and Au@NO<sub>2</sub>@COOH, as a function of reaction time with diazonium salts. The variations in relative intensity of the characteristic CN ( $I_{\text{CN}}$  at 2220 cm<sup>-1</sup>) and NO<sub>2</sub> peaks ( $I_{\text{NO}_2}$  at 1330 cm<sup>-1</sup>) were selected to measure the first layer growth, taking the Au-C peak intensity ( $I_{\text{Au-C}}$ ) as the reference. The intensity ratios

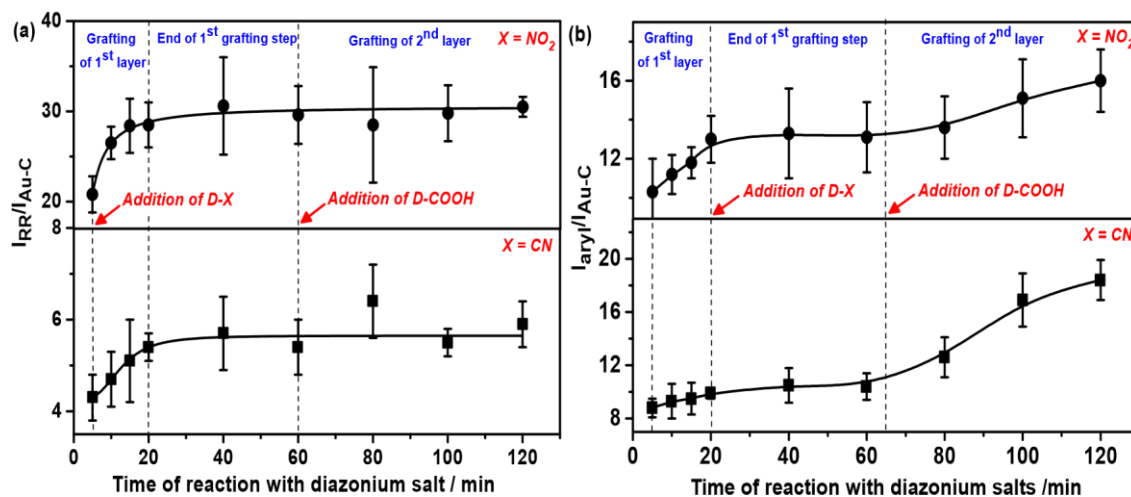


**Figure 4.11** SERS band intensity ratios vs time of reaction after the two-step addition of first, the Raman reporter diazonium salts (D-CN and D-NO<sub>2</sub>) and second, D-COOH: (a)  $I_{\text{NO}_2}/I_{\text{Au-C}}$  (circles) and  $I_{\text{CN}}/I_{\text{Au-C}}$  (squares); (b)  $I_{\text{aryl}}/I_{\text{Au-C}}$  for Au@NO<sub>2</sub>@COOH (circles) and Au@CN@COOH (squares).

$I_{\text{CN}}/I_{\text{Au-C}}$  and  $I_{\text{NO}_2}/I_{\text{Au-C}}$  were shown to increase during the first 20 minutes of reaction, revealing the grafting and polymerization of the first CN- or NO<sub>2</sub>-terminated polyaryl layer. After 20 min, the reaction seems to be complete as no more evolution of the SERS spectra is detectable. It is noteworthy that the introduction of D-COOH after 60 min does not bring any additional changes to  $I_{\text{CN}}/I_{\text{Au-C}}$  and  $I_{\text{NO}_2}/I_{\text{Au-C}}$  intensity ratios. To assess the growth of the second poly(aryl) layer derived from D-COOH, the intensity ratio  $I_{\text{aryl}}/I_{\text{Au-C}}$  was selected as the appropriate indicator. It was shown to increase at the beginning of the reaction, after addition of the Raman reporters, and then to remain constant after 20 min, thus following a similar trend than the intensity ratios  $I_{\text{NO}_2}/I_{\text{Au-C}}$  and  $I_{\text{CN}}/I_{\text{Au-C}}$ . However, after addition of DCOOH, the intensity ratio  $I_{\text{aryl}}/I_{\text{Au-C}}$  increased again, confirming the grafting of the second carboxyl-terminated polyaryl layer. The other peaks remain unchanged demonstrating the robustness of the grafted layers derived from diazonium salts at the surface of the nanoconstruct.

An activation step using EDC/NHS was necessary to activate the carboxyl groups for direct conjugation to the nucleotide AMP, *via* amide bonds. The presence of the grafted AMP generates new SERS characteristic peaks<sup>165</sup> (see Fig. 4.12) at  $\sim 733\text{ cm}^{-1}$  (in-plane ring breathing of adenine ring),  $\sim 1332\text{ cm}^{-1}$  (ring stretching mode) and  $\sim 1460\text{ cm}^{-1}$  (C–N stretching).

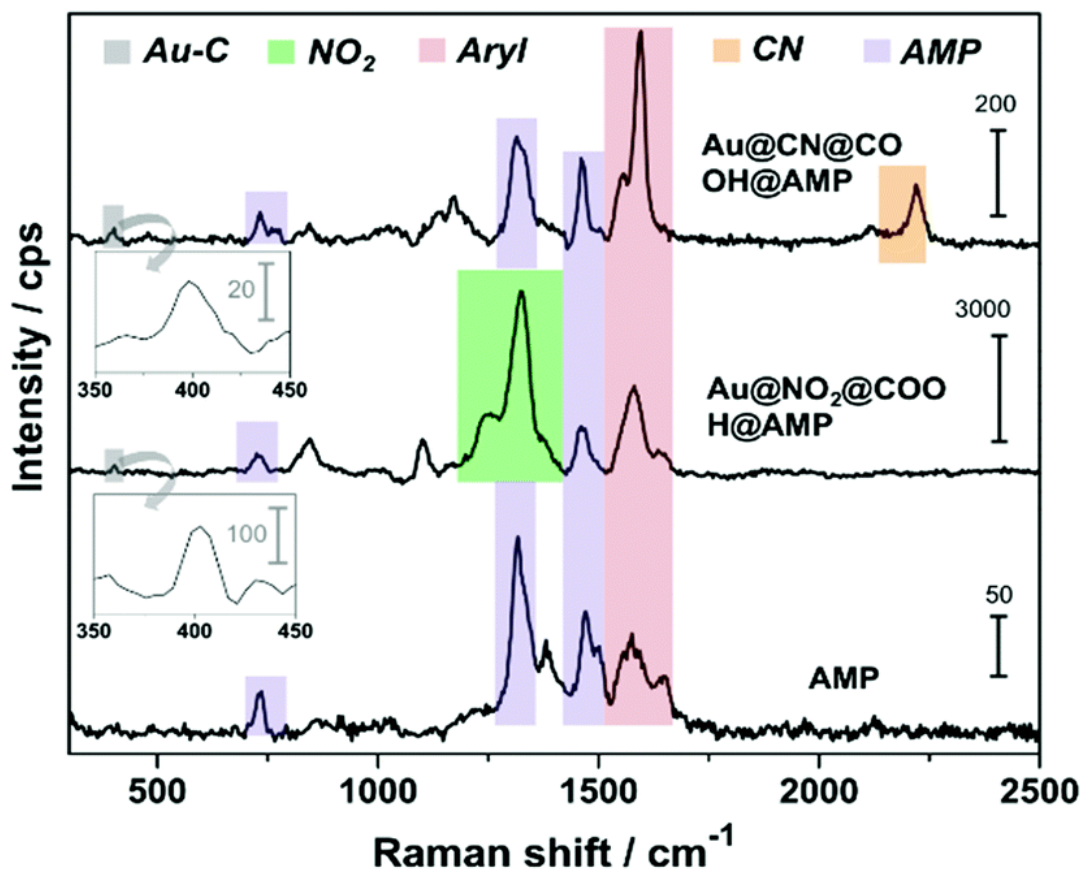


**Figure 4.12** SERS spectra of Au@CN@COOH@AMP and Au@NO<sub>2</sub>@COOH@AMP. The Raman spectrum of AMP is used as a reference. Inset: Zoom in the spectral range 350–450 cm<sup>-1</sup>, revealing the presence of n<sub>Au-C</sub> peak.

This new generation of SERS encoded NPs, based on AuNPs functionalized by aryl diazonium salts, was then evaluated as labels for Raman bioimaging inside cells. Proof of concept experiments consisted to expose different cell lines (EGI-1 and CT-26 cells) to Au@CN@COOH@AMP and Au@NO<sub>2</sub>@COOH@AMP (details of the experiments are given in ESI†). Fig. 4.13 shows that, when internalized inside cells, the SERS tags could be perfectly detected as bright spots, probably due to accumulation into endosomal compartments. These results demonstrate that this new generation of SERS labels offers promising prospects for multiplex SERS-based Raman imaging.

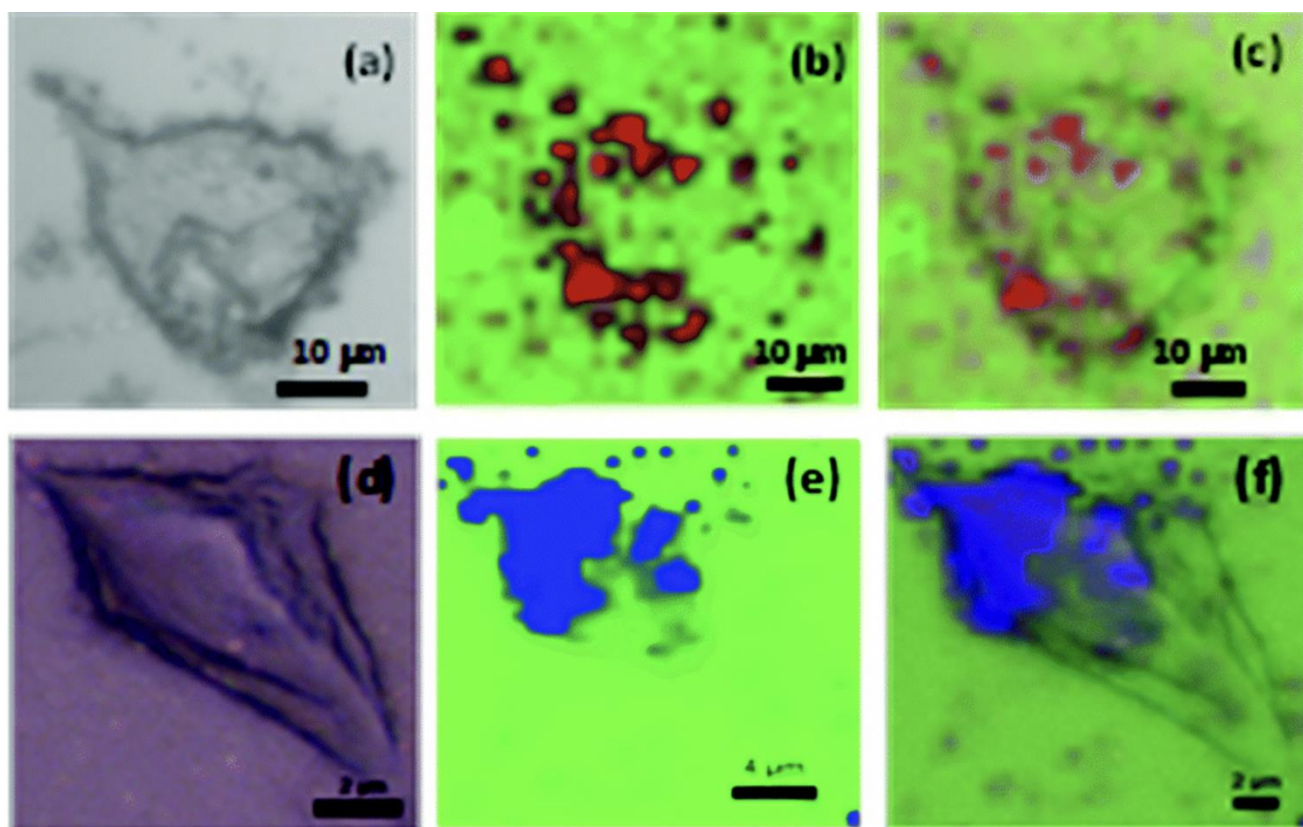


**Figure 4.13** (a and d) Bright-field optical images and (b and e) Raman images of EGI-1 cells after uptake of Au@CN@COOH@AMP, observed as red spots (b) and CT26 after uptake of Au@NO<sub>2</sub>@COOH@AMP, observed as blue spots (e). (c) Overlay images of (a) and (b); (f) overlay images of (d) and (e), revealing the intracellular distribution of the SERS tags inside cells. The excitation laser wavelength was 633 nm (1 mW, grating 300 g mm<sup>-1</sup>, objective 100× hole 50 μm, acq. time 2 s per pt, XY parameters: 10<sup>4</sup> × 10<sup>9</sup> 0.3 × 0.3 μm per pt).

## 4.3 Materials & Methods

### 4.3.1 Synthesis of aryl diazonium salts (D-COOH, D-CN and D-NO<sub>2</sub>)

The aryl diazonium salts were synthesized as described previously.<sup>166</sup> For the synthesis of DCOOH, 2 g of 4-aminobenzoic acid (≥99%, Sigma-Aldrich) was added into 12 mL of tetrafluoroboric acid solution (48% in H<sub>2</sub>O, Sigma-Aldrich) in a flask, followed by adding 10 mL of acetonitrile (≥99.9%, Sigma-Aldrich). The transparent solution was cooled down to *ca.* 2°C in ice/water bath under stirring. Then 2 mL of *tert*-butyl nitrite (90%, Sigma-Aldrich) was added dropwise into the flask. The solution was kept cooled under stirring for 30 min. The obtained diazonium salt was washed by diethyl ether (≥99.7%, Sigma-Aldrich) for 3 times, then dissolved in acetone (≥99.9%, Sigma-Aldrich) and dried at room temperature. The synthesis of D-CN and D-NO<sub>2</sub> followed the same

protocol, except using 4aminobenzonitrile (98%, Sigma-Aldrich) and 4-nitroaniline ( $\geq 99\%$ , Sigma-Aldrich) as precursors, respectively.

#### ***4.3.2 Synthesis of citrate-capped AuNPs***

50mL of gold(III) chloride trihydrate ( $\geq 99\%$ , Sigma-Aldrich) at a concentration of  $10^{-3}$  mol L<sup>-1</sup> was heated to boiling. Then 5mL of aqueous sodium citrate (anhydrous,  $\geq 99.5\%$ , SigmaAldrich) solution was injected into the boiling solution under vigorous stirring for 15 min. Soon, the solution turned to red. It was then cooled down to room temperature and stored at 4°C.

#### ***4.3.3 Spontaneous functionalization of AuNPs by aryl diazonium salts***

The functionalization reaction was performed in 1mL of citrate-capped AuNPs by mixing the colloidal solution obtained above, with 5 $\mu$ L of aqueous solutions of D-NO<sub>2</sub> or D-CN ( $10^{-2}$  mol.L<sup>-1</sup>) for 1h at room temperature. The solution was then centrifuged at 5000 rpm for 30 min. The supernatant was discarded and replaced by deionized water. The reaction was stopped by repeating 3 times of centrifugation/redispersion process, and the resulting samples were noted Au@CN and Au@NO<sub>2</sub>. For Au@CN@COOH and Au@NO<sub>2</sub>@COOH, the second layer was grafted by adding 5  $\mu$ L of D-COOH ( $10^{-2}$  mol L<sup>-1</sup>) into Au@CN and Au@NO<sub>2</sub> solutions and let the reaction proceed for 1h, followed by 3 times of centrifugation/redispersion process in water.

#### ***4.3.4 Post-functionalization by AMP***

The double-layer grafted AuNPs were stabilized by adding 0.0001-1 wt.% of polyvinylpyrrolidone (PVP, average mol. Wt. 10,000, Sigma-Aldrich). After 1h at room temperature, 10 $\mu$ L of an aqueous solution of adenosine 5'-monophosphate disodium salt (AMP,  $10^{-2}$  mol.L<sup>-1</sup>, from Sigma-Aldrich) was added in the stabilized AuNPs suspension, followed by the addition of 1  $\mu$ L of N-(3-Dimethylaminopropyl)-N'-ethylcarbodiimide hydrochloride (EDC, 50 g.L<sup>-1</sup>,  $\geq 99\%$ , Sigma-Aldrich) and 2  $\mu$ L of N-hydroxysuccinimide (NHS, 50 g.L<sup>-1</sup>, 98%, Sigma-Aldrich). The reaction was carried out at room temperature during 2h and then at 4°C overnight. After three cycles of centrifugation/redispersion in water, Au@CN@COOH@AMP and Au@NO<sub>2</sub>@COOH@AMP were obtained.

#### **4.3.5 Cellular uptake studies**

The cellular uptake study was performed by exposing Au@CN@COOH@AMP with cholangiocarcinoma EGI-1 cells and Au@NO<sub>2</sub>@COOH@AMP with CT-26 cells. EGI-1 and CT26 cells were seeded in 6-well plates with coverslips at a density of  $1.2 \times 10^6$  cells/well by using RPMI1640 (Gibco, Life Technologies Corporation, U.S.A) with 15% Fetal Bovine Serum (Gibco, Life Technologies Corporation, U.S.A) as the culture medium. The cells were cultured in an atmosphere of 5% CO<sub>2</sub> at 37°C for 24 h. The culture medium was then replaced by 2 mL of medium containing 1 nM NPs and incubated with cells for 24 h. After incubation, cells were washed with ice cold DPBS (Dulbecco's Phosphate Buffered Saline [-] CaCl<sub>2</sub>, [-] MgCl<sub>2</sub>, Gibco, Life Technologies Corporation, U.S.A) three times and then fixed with 1% PFA.

#### **4.3.6 Instrumentation**

The colloidal solutions were diluted 4 times for UV-vis spectroscopy. The extinction spectra were recorded on a Shimadzu 2700 UV-vis spectrometer, using 1x1cm quartz cuvettes. The SERS were recorded on a Horiba XploRA PLUS Raman microscope. All the measurements were performed on dried drops of the samples deposited on glass microscope slides, using a laser at 638 nm, an exposition time of 10s and an accumulation of 10 spectra. The SERS mappings (NPs and cells) were recorded on a Horiba LabRAM HR Evolution Raman microscope with an excitation wavelength of 633 nm. The exposition time for mappings was 0.8s per spectrum for the reference map and 2s per spectrum on the cell map. The XPS spectra were recorded using a Thermo Scientific K-Alpha spectrometer equipped with a monochromatic Al-K $\alpha$  X-ray source ( $h\nu = 1486$  eV). The spot size was of 400  $\mu$ m, while the pass energy of surveys and high-energy resolution were fixed at 200 and 50 eV, respectively. The charge compensation was performed by a combination of an electron flood gun with an argon ion gun. The TEM images were recorded with a Tecnai microscope (120 kV) and a 4kx4k Eagle camera (Thermofisher, USA), after depositing 4  $\mu$ L of each sample on carbon coated grids (primarily glow discharged).

## **4.4 Conclusion**

In summary, Raman reporters derived from aryl diazonium salts were grafted on gold NPs to design a new generation of SERS encoded-nanoparticles. AuNPs were modified by three different aryl

diazonium salts, bearing either nitro or cyano groups and carboxyl-terminated function. These nanoprobe were shown to combine unique SERS spectra and post-functionalization capacity for the immobilization of the nucleotide AMP. Unlike thiol-derived Raman reporters forming monolayers around plasmonic NPs, this approach enables the formation of strongly attached multilayers around the gold cores, with various chemical functions, providing a breakthrough strategy to create multifunctional SERS tags. It thus offers several advantages over conventional methods of SERS tag preparation, such as: (i) the formation of strong covalent bonds between the AuNP surface and the Raman labels and (ii) the growing of multifunctional layers around the gold cores, using a simple and straightforward process (in air, at room temperature). Therefore, this aryl diazonium salt-based approach will not only pave a new way for the functionalization of AuNPs by multilayers but also provide a general strategy to design SERS-encoded NPs.

## ***Aknowledgments***

The authors thank G. Pehau-Arnaudet (Institut Pasteur) for TEM analysis, Horiba for Raman imaging, L. Fouassier (Sorbonne Université) and A. Nicolas Boluda (Univ. de Paris) for providing cells.

## ***Collaborators***

The results presented in this chapter have been obtained thanks to the joint efforts of several collaborators, described below:

- The members of the group Nanobiospectroscopy: Yun Luo, Delphine Onidas, and Claire Mangeney for the synthesis, functionalization and characterization of Au NPs.
- The members of the group MSC-Med: Florence Gazeau and Alba Nicolas Boluda for the biological part.
- The members of the group Chemistry of RNAs, Nucleosides, Peptides and Heterocycles: Laura Iannazzo and Mélanie Ethève-Quellejeu for providing us the biomolecules, including AMP.
- The members of ITODYS: Aazdine Lamouri and Nordin Félidj for the synthesis of diazonium salts and the help for Raman spectroscopy.
- Our collaborator from Horiba: Thibault Brulé for the Raman imaging experiments.

---

## *Conclusions and perspectives*

---

**Conclusions.** In conclusion, we have designed innovative nanotools based on smart hybrids microgels loaded with fluorescent dyes and gold nanoparticles for nanomedicine applications.

In the first chapter, we have provided a state-of-the-art on the latest developments of photoacoustic active nano- and microgels for biomedical applications, particularly photoacoustic imaging. The chemical strategies for the synthesis of hydrogel particle-based photoacoustic contrast agents were described as well as their potential for cancer treatment and diagnosis.

In the second chapter, we have explored a new approach for the design of well-defined smart hybrid microgels ( $\mu$ Gels) doped with dyes (R6G, MB, Cy) and gold NPs, based on the assembly of the various building blocks. The step-by-step process used herein offers an easy means to tailor the loading level of gold NPs and dyes within the polymer network via successive incubation steps, from one to five times. The characterization of the formed hybrid particles by UV-vis absorption, fluorescence and photoacoustic spectroscopy, transmission electron microscopy and dynamic light scattering revealed that the concentration of dyes within the  $\mu$ Gels could be tuned by changing the initial dye concentration during the self-assembly process while the loading of Au NPs was tailored by the number of incubation steps, yielding densely filled  $\mu$ Gels after 5 incubations. Interestingly, the hybrid  $\mu$ Gels retained their pH- and thermo-responsive properties, even after the trapping of all these elements within their matrix. Thanks to the formation of dense assemblies of Au NPs in the  $\mu$ Gel platforms at high loading and the stimuli-induced aggregation of the NPs, plasmon coupling was observed, which resulted in plasmon band broadening and red shift towards the near infrared region (NIR), a critical point for bioimaging and phototherapy. Consequently, the hybrid  $\mu$ Gels achieved strong heating capacities and high molar absorption coefficients under NIR laser excitation. Moreover, the dyes loaded within the  $\mu$ Gels could act as fluorescence tracers to visualize the  $\mu$ Gel uptake by cells. Therefore, the strategy which consists to use small spherical Au NPs, with no particular signal in the NIR but with appropriate biocompatibility and biodegradability properties,

and to assemble them within smart microgel platforms loaded with dyes appears highly promising to obtain efficient nanotools for photothermal therapy and bioimaging.

In the third chapter, we exploited the fluorescence properties of the dyes and the enhancement of their Raman signals by the Au NPs trapped within the microgels to get new insights on the interaction of the nanocomposite microgels with cells, their biotransformation and their biodegradation in primary fibroblasts *in vitro* through dual-mode imaging. It appears that cell internalization and ageing results in strong modifications of the optical signature of the hybrid  $\mu$ Gels from a SERS ON/Fluorescence OFF state to a SERS OFF/Fluorescence ON behavior. Moreover, TEM images recorded as a function of incubation time confirmed the biodegradation process with the appearance of aurosomes structures after 4-7 days.

In the fourth chapter, we focused on the possible use of these nanotools as Raman imaging labels. We thus functionalized the Au NPs with Raman reporters derived from diazonium salts and performed proof-of-concept Raman imaging experiments on cell lines after NP uptake. This study highlighted the large potentials of diazonium salt chemistry to design Au NPs-based SERS labels for Raman bioimaging. However, due to a lack of time, these SERS tags could not be loaded within the microgels and this step therefore constitutes a perspective of the work described in this manuscript.

Finally, the studies conducted here highlight that the smart  $\mu$ Gel platforms are interesting tools to physically control the aggregation of Au NPs, with promising prospects for photothermal therapy and photoacoustic imaging and for monitoring the NPs fate inside cells through dual-mode fluorescence and Raman imaging.

**Perspectives.** However, there remains several limitations that should be addressed before considering clinical applications. First, due to the large size of the  $\mu$ Gels, they should be rapidly cleared by the reticuloendothelial system (RES) after entering the body, thereby limiting their capacity to target specific tissues. Therefore, for follow-up studies, it may be necessary to select smaller  $\mu$ Gels and to attach a targeting ligand on their surface to enhance their accumulation at the tumor site.

Secondly, the stability of the trapped dyes and Au NPs within the  $\mu$ Gel matrix deserve attention in order to avoid uncontrolled leakage before reaching the target tissue. The TEM results of cellular uptake showed that Au NPs could escape from the  $\mu$ Gels within 24 hours. It will be crucial to get new insights on the stability and biodegradation properties of the hybrid  $\mu$ Gels in vivo. Moreover, the capacity of the hybrid  $\mu$ Gels to load anticancer drugs and act as smart drug delivery carriers should be also studied.

Another important challenge is related to the optical properties of the hybrid microgels, usually settling across the first infrared window NIR-I (650 to 1000 nm). Designing nanocomposites with responsiveness in the NIR-II window (1000 to 1700 nm) will be the focus of future research, due to numerous advantages such as reduced optical absorption and tissue scattering together with deeper penetration depth.

From a practical perspective, there is still a long way to go from basic research to clinical applications. This will rely on the design of hybrid microgel theranostic agents with long-term stability in various environments and controlled pharmacodynamics, pharmacokinetics, and safety properties in vivo.

---

## *Annexes*

---

### **1. Dynamic light scattering (DLS)**

Dynamic Light Scattering, also known as Photon Correlation Spectroscopy or Quasi-Elastic Light Scattering, is a physical characterization method used to measure particle size distribution in solutions or suspensions, as well as complex fluids such as concentrated polymer solutions. This technique is based on the fact that suspended particles are subject to Brownian motion. Thus, the large particles will tend to move slowly while smaller particles will move faster. When the particles are excited by a laser, they will diffuse light randomly. The diffused light is recorded and detected at a certain angle. The presence of Brownian motion generates a fluctuation in the intensity of the scattered light which will be recorded. Then using a correlator, these fluctuations will be processed in order to obtain an autocorrelation function. The autocorrelation function gives access to the diffusion coefficient which itself is related to the hydrodynamic radius thanks to the Stokes-Einstein relation.

Dynamic light scattering is used to characterize the size of proteins, polymers, micelles, sugars and nanoparticles. If the system is monodisperse, the mean effective diameter of the particles can be found. Measures depend on particle's core, surface structure, particle concentration and ionic species in the medium. DLS can also be used for stability studies, by measuring the particle size distribution over time: as particles coagulate, the particles with larger sizes become more numerous. Similarly, DLS can also be used to analyze the effect of temperature on stability.

### **2. Raman spectroscopy**

Raman spectroscopy is a type of scattering spectroscopy: it is based on the Raman scattering effect discovered by Indian scientist CV Raman. Raman spectroscopy analyzes the scattering spectra with different frequencies from the incident light to obtain information on molecular vibration and rotation. It's an analytical method applied to the study of molecular structure.

When light irradiates a substance, elastic scattering and inelastic scattering occur. The scattered light of elastic scattering has the same wavelength as the wavelength of the excitation light. The scattered light of inelastic scattering has wavelengths lower and higher than the wavelength of the excitation light, which are collectively referred to as the Raman effect.

When a gas, liquid or transparent sample is irradiated with monochromatic light with a wavelength much smaller than the particle size of the sample, most of the light is transmitted in the original direction, while a small part is scattered at different angles, resulting in scattering light. When observed in the vertical direction, in addition to the Rayleigh scattering with the same frequency as the original incident light, there are also a series of symmetrically distributed Raman spectral lines that are very weakly shifted from the incident light frequency. This phenomenon is called Raman effect. Due to the number of Raman spectral lines and the magnitude of the displacement, the wavelength of the spectral lines is directly related to the vibrational or rotational energy level of the sample molecules. Therefore, as infrared absorption spectroscopy, Raman spectroscopy give information on molecular vibrations or rotations. Raman spectroscopic analysis technology has been widely used to identify substances and molecular structures.

The advantages of Raman spectroscopy are: i). it is a non-destructive and non-intrusive method, ii). the physical state of the sample is irrelevant : sample can be solid, liquid or gaseous, iii). it can be combined with other techniques, iv). it can be used *in situ* and under stress.

### **3. UV-Vis absorption spectroscopy**

The UV-Vis spectrophotometer is an analytical instrument based on the principle of UV-Vis absorption spectrophotometry, which uses the absorption of UV-Vis radiation by molecules to analyze samples. A UV-Vis spectrophotometer is mainly composed of light sources, monochromator, cuvette holder, detector, and signal processor. Light sources provide a stable, continuous and polychromatic beam of sufficient intensity. The ultraviolet radiation usually comes from a hydrogen lamp or a deuterium lamp whereas the visible radiation comes from a tungsten lamp or a halogen lamp. The function of the monochromator is to split the polychromatic beam emitted by the light source and to select the monochromatic light of the desired wavelength from it. A glass cuvette is used for measurements in the visible region, and a quartz absorption cuvette is

required for measurements in the UV. The function of the detector is to detect the intensity of the transmitted light through the photoelectric conversion element and to convert the optical signal into an electrical signal.

The UV-visible absorption spectrum of a molecule is due to electronic transitions of molecular groups absorbing UV-visible radiation. Since various substances contain different atoms and molecules with different molecular spatial structures, their absorption of light will not be the same. The level of absorbance at certain characteristic wavelengths on the spectrum is used to identify or determine the content of the substance, which is the basis of spectrophotometric qualitative and quantitative analysis.

Spectrophotometric analysis is an effective technique to study the composition, structure and interactions between substances according to the absorption spectrum of substances. According to Lambert's law, the absorption of light is proportional to the thickness of the absorption layer, and Lambert-Beer's law shows that the absorption of light is proportional to the concentration of the solution:  $A = \epsilon bc$  ( $A$  is the absorbance,  $\epsilon$  is the molar absorption coefficient,  $b$  is the thickness of the sample, and  $c$  is the solution concentration).

#### **4. Fluorescence spectroscopy**

Fluorescence spectrophotometer is an instrument used to scan the fluorescence photons emitted by fluorescent molecules of liquid samples. Fluorescence spectroscopy can provide various data such as excitation spectrum, emission spectrum, fluorescence intensity, fluorescence quantum yield, fluorescence lifetime, fluorescence polarization, etc.,. By recording such data, not only general quantitative analysis can be performed, but also conformational changes of molecules in various environments can be inferred, thereby clarifying the relationship between molecular structure and function. The excitation wavelength scanning range of the fluorescence spectrophotometer is generally 190-650 nm, and the emission wavelength scanning range is 200-800 nm.

Fluorescence follows UV-Vis excitation and corresponds to the emission of photons from excited electronic state. These molecules in the excited state are unstable, and in the process of returning to the ground state, part of the energy is returned to the form of light.

Different substances have different characteristics in the distribution of excited state energy levels due to different molecular structures. This characteristic is reflected in the fluorescence that various substances have their own characteristic fluorescence excitation and emission spectra. The difference in emission spectra can be used to qualitatively identify substances.

In solution, when the concentration of the fluorescent compound is low, fluorescence intensity and molecule concentration have usually a proportional relationship :  $IF=KC$ . Using this relationship, the quantitative analysis of fluorescent molecules can be carried out, which is consistent with UV-Vis spectroscopy.

## **5. Transmission electron microscopy (TEM)**

Transmission electron microscopy (TEM) is a method to study the structure and properties of the sample by using a transmission electron microscope. The working principle of TEM is the same as that of optical transmission microscope, except that the light beam is replaced by an electron beam, and the glass lens is replaced by a magnetically focused electron lens, and the electron image is displayed on a fluorescent screen. The electron beam is wavelike, and the accelerated electron beam has a wavelength of about 1/100,000 of the light wave and has strong penetrating power.

When electrons interact with a sample, they can be scattered, absorbed and transmitted. In the case of TEM, electrons subjected at high accelerating voltages (60 to 400 kW) are used to form an image.

## **6. Alamar blue test**

The main component of this reagent is a redox indicator, which is violet-blue and non-fluorescent in the oxidized state and converted into a reduction product with pink or red fluorescence in the reduced state, and its absorption peak is 530-560 nm. And the fluorescence peak is 590 nm.

During the process of cell proliferation, the ratios of NADPH/NADP, FADH/FAD, FMNH/FMN and NADH/NAD in the cells increase, and they are in a reducing environment. The dyes taken up into the cells are reduced by these metabolic intermediates and cytochromes, and then they are

released outside of the cells and dissolved in the medium, turning the medium from non-fluorescent indigo blue to fluorescent pink. Finally, the medium is analyzed by a UV-Vis spectrophotometer or a fluorescence photometer : absorbance and fluorescence intensity are proportional to the number of viable cells.

Compared to trypan blue, TTC, MTT, MTS and other analytical methods, Alamar-Blue has many advantages. Alamar-Blue uses a single reagent to detect continuously and rapidly the cells proliferation. Since Alamar-Blue is non-toxic and harmless to cells, and does not affect cell metabolism, cytokine secretion, antibody synthesis, etc., continuous observation and further experimental observation of the proliferation state of the same batch of cells can be performed. It is suitable for the detection of bacteria, yeast, insects, fish, mammals, and other cells, as well as adherent cells and non-adherent cells, and can be widely used for rapid detection and identification of cell proliferation, cytotoxicity and pathogenic microorganisms.

## **7. Photoacoustic Imaging (PAI)**

Photoacoustic Imaging (PAI) is a new non-invasive and non-ionizing biomedical imaging method developed in recent years. When biological tissue is irradiated by a pulsed laser (thermoacoustic imaging refers specifically to the irradiation by a radio frequency pulsed laser), light absorption by the tissue will generate an ultrasonic signal which is called photoacoustic signal. The photoacoustic signal generated by biological tissue carries the light absorption characteristic information of the tissue, and the light absorption distribution image in the tissue can be reconstructed by detecting the photoacoustic signal. Photoacoustic imaging combines the advantages of the high selectivity of pure optical tissue imaging and of the deep penetration in pure ultrasound tissue imaging, and thus allow to obtain high-resolution and high-contrast tissue images, avoiding the influence of light scattering, breaking through the high-resolution optical imaging depth "soft limit" (~1 mm) and enabling deep *in vivo* tissue imaging of 50 mm.

The principle of photoacoustic signal generation is when the absorber is irradiated with a short-pulse laser, some molecules of the absorber absorb photons and electronic transitions occurred

bringing molecules into excited electronic state. The electron in the excited state is extremely unstable, and when electron relaxes to a lower energy level, it releases energy in the form of photon or heat. In the application of photoacoustic imaging, a laser with a suitable wavelength is usually selected as the excitation source to maximize the efficiency of converting the energy of absorbed photons into thermal energy. The efficiency of converting light energy into thermal energy can reach more than 90%. The released heat causes a local temperature increase which induces thermal expansion generating pressure waves, which are photoacoustic signals. Therefore, the generation process of the photoacoustic signal is the conversion process of "light energy" - "heat energy" - "mechanical energy".

## **8. Photothermal therapy (PTT)**

Photothermal therapy (PTT) is to use materials with high photothermal conversion efficiency, to inject them into the human body, to use targeted recognition technology to gather them near tumor tissue, and to irradiate them with external light sources (usually near-infrared light). Thus it is a treatment method in which light energy is converted into heat energy to kill cancer cells.

Advantages of PTT:

- i). Reduce the pain experienced by the patient.
- ii). The treatment duration is short (about a few minutes), and the treatment effect is obvious.
- iii). The material is non-toxic and harmless, and has little side effect on the human body.

Disadvantages of PTT:

- i). People have not fully understood the treatment mechanism of this material, so it is difficult to achieve the best design effect.
- ii). Due to the limited transmission ability of the laser, it cannot be incident into the deep layers of the living body, resulting in the lack of strict measures for internal tumors.
- iii). When this material is used for treatment, its circulation in the human body has not been fully clarified, and there is no long-term experimental observation, so its potential toxicity is still unknown.

## 9. Résumé en français (long)

### 1. Nanoparticules d'or

Les nanoparticules (NPs) d'or ont été largement utilisées pour la Spectroscopie Raman exaltée de surface (SERS), l'imagerie photoacoustique (PAI) et la thérapie photothermique (PTT) en raison de leurs propriétés optiques particulières. Les propriétés optiques des NP d'or proviennent du phénomène de résonance plasmonique de surface localisée (LSPR) qui est dû à l'oscillation des électrons libres de conduction libre à la surface des particules lors d'une excitation lumineuse, appelée plasmon. Fait intéressant, les plasmons de NPs d'or peuvent induire une absorption caractéristique dans la région visible et une diffusion Raman exaltée à leur surface, qui peut être exploitée pour l'identification d'espèces chimiques et leur localisation. Dans le même temps, les plasmons convertissent une partie substantielle de l'énergie d'oscillation en chaleur, via un effet photothermique, qui peut être exploité à la fois pour l'imagerie photoacoustique et la thérapie photothermique (schéma 1).

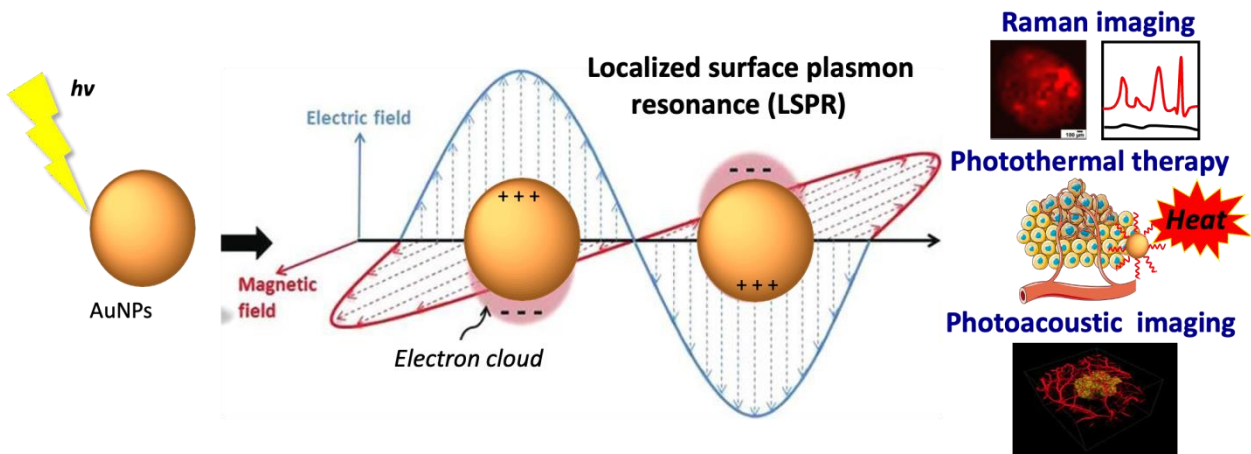


Schéma 1. Schéma d'illustration des propriétés optiques des AuNPs et de leur application pour l'imagerie raman, la thérapie photothermique et l'imagerie photoacoustique.

Les nanoparticules d'or peuvent être divisées en nanosphères d'or (AuNPs), nanoétoiles d'or, nanobâtonnets d'or, nanocages d'or, nanovésicules d'or et ainsi de suite selon leurs formes. De nombreux travaux de recherche ont été réalisés en utilisant des NPs d'or pour le SERS<sup>88, 167</sup>, PAI<sup>89</sup> et PTT<sup>90</sup> car, en plus de leurs synthèse et fonctionnalisation aisées, ces NPs possèdent un excellent

coefficient d'extinction molaire. Les nanoparticules d'or de formes, tailles et états d'agrégation différents ont des propriétés de surface et des coefficients d'extinction distincts<sup>91,92</sup>. Tian Rongfu et al. ont synthétisé des nanosphères d'or, des agrégats sphériques, des nanoétoiles et ont étudié la dépendance de SERS en fonction de la forme des nanoparticules d'or en utilisant la rhodamine 6G comme marqueur Raman<sup>93</sup>. Ils ont conclu que l'effet SERS peut être optimisé en augmentant le nombre de points chauds du champ local. La bande plasmonique des agrégats de nanosphères passe à 660 nm par rapport à la nanosphère unique (532 nm), et provoque, en raison du "point chaud" du plasmon de surface, une augmentation significative du signal SERS de la rhodamine 6G sous excitation à 785 nm. Dans le domaine de la biologie, le SERS dans le proche infrarouge (NIR) attire d'avantage l'attention des chercheurs car les molécules endogènes du corps humain absorbent principalement la lumière visible : l'utilisation d'un laser NIR peut réduire efficacement les dommages aux cellules normales. De plus, la région NIR correspond à la "fenêtre transparente" du corps, qui convient mieux aux applications biologiques telles que l'imagerie photoacoustique et la thérapie photothermique. Et le rayonnement NIR a une pénétration plus profonde dans la peau que le rayonnement visible<sup>94</sup>, ce qui sera plus propice à la thérapie photothermique tumorale locale tout en réduisant les dommages aux tissus normaux. Sur cette base, les chercheurs ont choisi les NPs d'or telles les nanobâtonnets d'or et les points quantiques d'Ag<sub>2</sub>S dont la bande plasmonique est située dans la fenêtre NIR-I (760 -900 nm) ou NIR-II (1000 -1700 nm) pour la bioimagerie et le traitement du cancer. Jesse V. Jokerst et al. ont utilisé des nanobâtonnets d'or comme agent pour l'imagerie PAI et Raman pour la détection des tumeurs cancéreuses de l'ovaire *in vivo*<sup>95</sup>. Lu An et al. ont conçu un système d'administration médié par les macrophages avec des nanobâtonnets d'or pour la thérapie photothermique et l'imagerie photoacoustique de l'hypoxie tumorale<sup>96</sup>. Thi Tuong Vy Phan et al. ont synthétisé des nanoétoiles d'or à base de chitosane pour l'imagerie photoacoustique et la thérapie photothermique<sup>97</sup>.

Bien que la bande plasmonique des nanobâtonnets et des nanoétoiles se situe dans la région NIR, leur toxicité biologique ne peut être ignorée. La toxicité de ces deux types de NPs d'or est principalement due à l'ajout du ligand toxique bromure de cétyltriméthylammonium au cours du processus de synthèse. Dans le même temps, en termes de biodégradabilité des nanoparticules dans les tissus biologiques, les nanobâtonnets et les nanoétoiles d'or sont plus difficiles à dégrader que

les nanosphères. On pense généralement que les nanoparticules d'or restent intactes dans les tissus biologiques. Cependant, Alice Balfourier et al. ont rapporté que des nanoparticules d'or sphériques de 4 à 22 nm de diamètre peuvent être dégradées dans les cellules<sup>100</sup>, mais aucun rapport actuel ne montre que les nanoétoiles d'or et les nanobâtonnets d'or peuvent être dégradés dans les tissus.

Pour relever le défi de la toxicité et des propriétés fortement dégradables des nanoparticules d'or, des agrégats sphériques de nanoparticules d'or ont été utilisés par des chercheurs pour des applications biodiagnostiques et thérapeutiques. Comme mentionné précédemment, la bande plasmonique de ces agrégats peut être déplacée vers la région NIR d'environ 120 nm par rapport à celle d'une sphère individuelle, grâce à la génération de "points chauds" de surface, ce qui est bénéfique pour les applications en bioimagerie. Si les nanoparticules sphériques sont suffisamment petites (moins de 22 nm), elles peuvent être dégradées par les tissus biologiques et lorsque leur granulométrie est inférieure à 5 nm, elles peuvent être éliminées par les reins<sup>101</sup>. Ainsi, les agrégats de nanosphères d'or peuvent être utilisés pour des applications biologiques tout en minimisant la toxicité des NPs pour le corps humain. De nombreuses études ont montré le fort potentiel des agrégats de nanosphères d'or pour l'imagerie Raman<sup>102</sup>, la thérapie photothermique<sup>103</sup> et l'imagerie photoacoustique<sup>2, 104</sup> : pour cela la surface des AuNPs a été modifiée chimiquement pour permettre l'agrégation des NPs en réponse à un stimulus tel que le microenvironnement acide des tumeurs.

Pour optimiser et étendre les possibilités d'application multifonctionnelles des nanoagrégats, telles que l'administration de cibles ou l'encapsulation de médicaments anticancéreux, etc., le nanogel intelligent sera un support "inclusif" et modulable, qui peut transporter et libérer des médicaments ou reconnaître des molécules cibles tout en permettant l'agrégation des AuNPs après stimuli.

## **2. Nanocomposites hybrides intelligents**

Les nanocomposites hybrides intelligents constitués de particules d'hydrogel dopées avec des nanoparticules inorganiques ont suscité un énorme intérêt en tant que matériaux multifonctionnels uniques pour les applications en nanomédecine, notamment l'administration de médicaments, la thérapie et l'imagerie. Les microgels ( $\mu$ Gels) nanocomposites se sont révélés particulièrement

prometteurs en tant qu'agents de contraste pour l'imagerie photoacoustique (PAI), qui est une technique émergente de bioimagerie non invasive et peu coûteuse, avec des perspectives prometteuses pour le théranostic du cancer. Les nano- et microgels hybrides peuvent agir comme supports protecteurs pour incorporer des agents de contraste d'imagerie photoacoustique en raison de leur capacité de charge élevée, de leur biocompatibilité et de leurs propriétés de réponse aux stimuli. Bien que divers types d'agents de contraste PAI aient été explorés, les NPs plasmoniques se sont révélées être des candidats prometteurs pour le PAI en raison de leurs propriétés optiques exceptionnelles basées sur le plasmon de surface localisé (LSP). Ces nanoparticules présentent des sections efficaces d'absorption optique élevées, supérieures de plusieurs ordres de grandeur à celles des colorants de petite taille moléculaire. Lors de l'excitation du LSP, ces NPs assurent la conversion de la lumière en chaleur et se comportent ainsi comme des nanosources de chaleur. Remarquablement, l'absorption d'impulsions lumineuses nanosecondes par ces NPS produit une dilatation thermique localisée du milieu environnant, entraînant la génération d'ondes ultrasonores. Cela ouvre de nouvelles opportunités, car, grâce à la détection des ondes ultrasonores, la PAI peut cartographier la distribution des nanoéléments chauffants avec une résolution spatiale inférieure au mm dans les tissus profonds. En raison de ces caractéristiques attractives, plusieurs approches chimiques ont été proposées pour élaborer des  $\mu$ Gels nanocomposites incorporant des NP plasmoniques. Elles reposent principalement sur la synthèse *in situ* des nanoparticules inorganiques au sein des particules polymères préformées ou sur la synthèse *ex situ* des deux composants suivie de leur assemblage. Cependant, les méthodes de synthèse développées jusqu'à présent présentent des limitations importantes, telles que la difficulté de contrôler la quantité de chargement de nanoparticules plasmoniques dans la matrice d'hydrogel. Par conséquent, le développement d'une stratégie polyvalente pour parvenir à l'élaboration de microgels nanocomposites avec des paramètres contrôlés (taille des particules, efficacité de chargement) reste toujours une tâche difficile.

### **3. Projet de thèse**

Afin de relever ce défi, ce travail de thèse explore une stratégie innovante basée sur l'assemblage étape par étape des différents éléments ( $\mu$ Gels, colorants, NPs plasmoniques) des nanocomposites,

et sur l'optimisation du taux de chargement des nanoparticules dans la matrice polymère via des étapes successives d'incubation. Comme preuve de concept, nous nous sommes concentrés ici sur les éléments suivants (schéma 2):

- (i) Pour le composant  $\mu$ Gel, une matrice polymère pH et thermosensible composée de copolymères d'oligo(éthylène glycol) méthyl éther méthacrylate et d'acide méthacrylique a été choisie.
- (ii) Pour les colorants, la rhodamine 6G (R6G), le bleu de méthylène (MB) et la cyanine 7,5 (Cy) ont été sélectionnés.
- (iii) En ce qui concerne les nanoparticules inorganiques, des nanoparticules d'or recouvertes de citrate (Au NPs) ont été choisies.

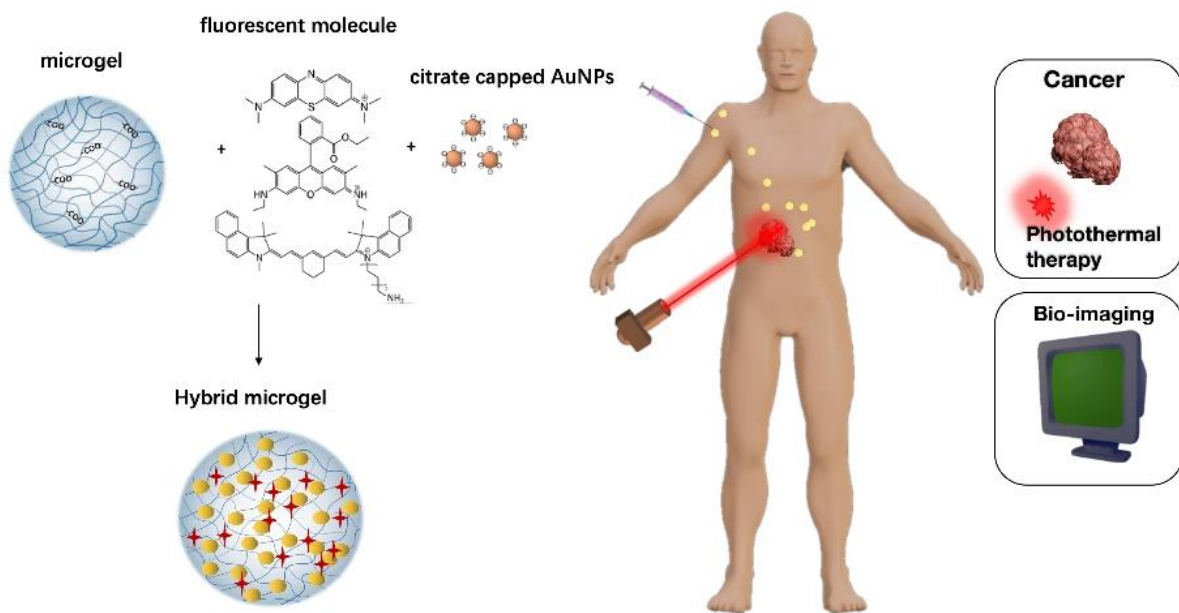


Schéma 2. Illustration du processus d'assemblage d'un agent théranostique basé sur un microgel hybride encapsulant des sondes fluorescentes pour l'imagerie et des agents thérapeutiques pour le diagnostic et le traitement du cancer.

Chaque composant des  $\mu$ Gels nanocomposites finaux devrait apporter des propriétés spécifiques précieuses pour la nanomédecine théranostique, comme suit :

- Les nanoparticules d'or et leur assemblage au sein des microgels vont 1/ produire localement de la chaleur par effet photothermique, 2/ servir d'agents de contraste pour l'imagerie photoacoustique (PAI) et 3/ amplifier les spectres Raman des colorants pour l'imagerie Raman.
- Les microgels pH et thermosensibles agiront comme 1/ un réseau de polymères pour incorporer et transporter les AuNPs, 2/ une matrice rétractable lors du chauffage ou de la diminution du pH,

induisant le couplage des nanoparticules d'or chargées dans le  $\mu$ Gel, générant une amélioration de leurs propriétés optiques.

- Les colorants (rhodamine 6G, bleu de méthylène et cyanine 7.5) assureront une émission de fluorescence allant du visible au NIR.

Dans le premier chapitre de ce manuscrit, nous introduisons les principes de base pour la conception de microgels hybrides à visée théranostique et nous présentons l'état de l'art de l'imagerie basée sur les agents de contraste photoacoustiques pour la détection des cancers. Puis nous donnons un aperçu des principales méthodes chimiques pour l'élaboration de matrices hybrides, en décrivant les différents types de gels et d'agents de contraste PAI et en soulignant leurs avantages et potentiel pour le diagnostic et le traitement du cancer.

Dans le deuxième chapitre, nous nous concentrons sur la conception de nos microgels hybrides en utilisant une approche étape par étape offrant la possibilité d'ajuster finement le taux d'incorporation des NP d'or dans la matrice polymère via des étapes d'incubation successives, de une à cinq incubations. Les  $\mu$ Gels hybrides finaux ont été entièrement caractérisés à l'aide de plusieurs techniques complémentaires, telles que la spectroscopie d'absorption UV-vis, la fluorescence, la spectroscopie et l'imagerie Raman, l'imagerie photoacoustique, la microscopie électronique à transmission et la diffusion dynamique de la lumière. Grâce à ces techniques, nous avons pu étudier le comportement pH et thermo-sensible des microgels vierges (sans colorants ni AuNPs) et hybrides, leurs propriétés photoluminescentes en fonction des colorants incorporés dans la matrice polymère et leurs propriétés optiques dues à la présence nanoparticules d'or. Une fois les plateformes nanocomposites entièrement caractérisées, leur potentiel pour des applications biomédicales a été évalué en menant des expériences photothermiques, d'imagerie photoacoustique et Raman ainsi que des tests de viabilité cellulaire.

Dans le troisième chapitre, nous avons exploité les propriétés de fluorescence des colorants et l'amplification de leur signal Raman grâce aux AuNPs incorporées dans les microgels pour obtenir de nouvelles informations sur l'interaction des microgels nanocomposites avec les cellules et sur leur processus de biodégradation.

Les nanoparticules plasmoniques, sous excitation LSPR, pouvant agir à la fois comme agents de contraste pour l'imagerie PAI et Raman, nos microgels nanocomposites pourraient servir de doubles marqueurs pour ces deux techniques. Dans le quatrième chapitre, nous nous concentrons spécifiquement sur le potentiel des petites NP d'or sphériques pour le greffage de marqueurs Raman pour la bioimagerie SERS. Pour cela, nous avons exploré une nouvelle approche pour la fixation de marqueurs Raman à la surface des AuNPs, grâce aux sels d'aryle de diazonium. Nous montrons que l'utilisation de la chimie des sels d'aryle de diazonium fournit un moyen facile d'obtenir des liaisons covalentes Au-C robustes entre les étiquettes Raman et les NPs, assurant une grande stabilité de l'interface nanohybride. Cette approche permet la formation de multicouches à la surface des NPs, donnant accès à de nouvelles signatures SERS spectralement distinguables, élargissant ainsi la bibliothèque de marqueurs Raman disponibles. Des expériences d'imagerie Raman, preuves de concept, ont été réalisées sur des lignées cellulaires après incubation en présence de NPs greffées avec des marqueurs Raman : elles mettent en évidence le fort potentiel de la chimie des sels de diazonium pour concevoir des étiquettes SERS à base de NPs métalliques pour la bioimagerie Raman. L'incorporation des marqueurs SERS au sein des microgels étudiés dans les chapitres précédents n'a pas pu être étudié dans le cadre de cette thèse, faute de temps, mais elle constitue une des perspectives principales de ce travail.

Dans la dernière partie du manuscrit, nous concluons et proposons plusieurs perspectives concernant le développement d'agents de contraste ciblés plus efficaces et plus biodégradables pour l'imagerie PAI et Raman. En raison de la petite taille, de la biodégradabilité et de la faible toxicité des nanoparticules d'or utilisées dans ce travail ainsi que de la biocompatibilité des matrices polymères, les nanocomposites intelligents devraient avoir un excellent potentiel de traduction clinique et d'applications en tant qu'agents PAI/Raman et système d'administration de médicaments pour le traitement du cancer.

Durant mon travail de thèse, j'ai réalisé sur (i) la conception des microgels hybrides ; (ii) la caractérisation de leurs propriétés chimiques et l'évaluation de ces propriétés en fonction de plusieurs stimuli ; (iii) l'étude de l'effet PA des hybrides intelligents sous stimulus et de l'efficacité du PTT *in vitro* ; (iv) leur étude de cytotoxicité à court terme et leur devenir à l'intérieur des cellules

via des expériences complémentaires d'imagerie Raman, d'imagerie de fluorescence et de microscopie électronique à transmission (MET).

Les résultats obtenus en MET montrent que le processus d'assemblage des nanohybrides est très efficace avec un dopage ajustable en AuNPs. Les spectres UV-vis et les images MET prouvent que l'agrégation des AuNPs est induite par la contraction des particules des  $\mu$ Gels sous stimuli (pH et de la température); agrégation qui permet le déplacement de la bande plasmonique amélioré vers la région NIR. Sous irradiation laser à 808 nm, les  $\mu$ Gels hybrides ont chauffé jusqu'à 55 °C et présentent une grande phototoxicité au sein de cellules CT 26 avec seulement 16% à 30% de cellules vivantes après exposition. L'agrégation des AuNPs, causée par la variation de pH, crée les "points chauds" qui permettent l'augmentation d'un facteur 5 à 10 des signaux SERS des colorants situés proches de la surface des AuNPs. Les  $\mu$ Gels hybrides et les fibroblastes sont incubés pendant différentes périodes pour étudier le devenir des nanocomposites au sein des cellules. Au cours de la dégradation et du désassemblage des  $\mu$ Gels, les molécules fluorescentes s'éloignent progressivement de la surface métallique et l'état de fluorescence passe de "quenched" à "on". Dans le même temps, le signal Raman passe de "on" à "off". Les images MET des cellules révèle le processus de dégradation et de désassemblage.

Pour conclure, les études menées lors de ma thèse soulignent que les microgels hybrides conçus sont des outils efficaces pour contrôler physiquement l'agrégation des nanoparticules d'or et sont prometteurs pour la thérapie photothermique du cancer ainsi que pour le suivi du devenir des nanoparticules à l'intérieur des cellules par multi-imagerie.

Mots clés : Nanoparticule d'or, microgel sensible au pH et à la température, colorants fluorescents, imagerie photoacoustique, thérapie photothermique, spectroscopie Raman exaltée de surface, diagnostic du cancer et thérapie.

---

## Bibliography

---

1. Bell, A. G., The Production of Sound by Radiant Energy. *Science* **1881**, 2 (49), 242.
2. Song, J.; Kim, J.; Hwang, S.; Jeon, M.; Jeong, S.; Kim, C.; Kim, S., "Smart" gold nanoparticles for photoacoustic imaging: an imaging contrast agent responsive to the cancer microenvironment and signal amplification via pH-induced aggregation. *Chemical Communications* **2016**, 52 (53), 8287-8290.
3. Huang, K.; Zhang, Y.; Lin, J.; Huang, P., Nanomaterials for photoacoustic imaging in the second near-infrared window. *Biomaterials Science* **2019**, 7 (2), 472-479.
4. Jiang, S.; Huang, K.; Qu, J.; Lin, J.; Huang, P., Cancer nanotheranostics in the second near-infrared window. *View* **2021**, 2 (1), 20200075.
5. Lin, L.; Hu, P.; Shi, J.; Appleton, C. M.; Maslov, K.; Li, L.; Zhang, R.; Wang, L. V., Single-breath-hold photoacoustic computed tomography of the breast. *Nat. Comm.* **2018**, 9 (1), 2352.
6. Wang, L. V.; Hu, S., Photoacoustic Tomography: In Vivo Imaging from Organelles to Organs. *Science* **2012**, 335 (6075), 1458.
7. Ray, A.; Yoon, H. K.; Koo Lee, Y. E.; Kopelman, R.; Wang, X., Sonophoric nanoprobe aided pH measurement in vivo using photoacoustic spectroscopy. *Analyst* **2013**, 138 (11), 3126-3130.
8. Beard, P., Biomedical photoacoustic imaging. *Interface Focus* **2011**, 1 (4), 602-31.
9. Schwarz, M.; Buehler, A.; Aguirre, J.; Ntziachristos, V., Three-dimensional multispectral optoacoustic mesoscopy reveals melanin and blood oxygenation in human skin in vivo. *J. Biophotonics* **2016**, 9 (1-2), 55-60.
10. Stoffels, I.; Morscher, S.; Helfrich, I.; Hillen, U.; Leyh, J.; Burton, N. C.; Sardella, T. C.; Claussen, J.; Poeppel, T. D.; Bachmann, H. S.; Roesch, A.; Griewank, K.; Schadendorf, D.; Gunzer, M.; Klode, J., Metastatic status of sentinel lymph nodes in melanoma determined noninvasively with multispectral optoacoustic imaging. *Sci. Transl. Med.* **2015**, 7 (317), 317ra199.
11. Yang, X.; Stein, E. W.; Ashkenazi, S.; Wang, L. V., Nanoparticles for photoacoustic imaging. *Wiley Interdiscip. Rev. Nanomed. Nanobiotechnol.* **2009**, 1 (4), 360-8.
12. Zhou, Y.; Hu, Y.; Sun, W.; Zhou, B.; Zhu, J.; Peng, C.; Shen, M.; Shi, X., Polyaniline-loaded  $\gamma$ -polyglutamic acid nanogels as a platform for photoacoustic imaging-guided tumor photothermal therapy. *Nanoscale* **2017**, 9 (34), 12746-12754.
13. Zhang, C.; Shi, X., Hybrid nanogels for photoacoustic imaging and photothermal therapy. In *Photonanotechnology for Therapeutics and Imaging*, Choi, S. K., Ed. Elsevier: 2020; p 23.
14. Jiang, L.; Zhou, Q.; Mu, K.; Xie, H.; Zhu, Y.; Zhu, W.; Zhao, Y.; Xu, H.; Yang, X., pH/temperature sensitive magnetic nanogels conjugated with Cy5.5-labeled lactoferrin for MR and fluorescence imaging of glioma in rats. *Biomaterials* **2013**, 34 (30), 7418-7428.
15. Peng, S.; Ouyang, B.; Xin, Y.; Zhao, W.; Shen, S.; Zhan, M.; Lu, L., Hypoxia-degradable and long-circulating zwitterionic phosphorylcholine-based nanogel for enhanced tumor drug delivery. *Acta Pharmaceutica Sinica B* **2021**, 11 (2), 560-571.

16. Kong, L.; Campbell, F.; Kros, A., DePEGylation strategies to increase cancer nanomedicine efficacy. *Nanoscale Horizons* **2019**, *4* (2), 378-387.
17. Jin, R.-M.; Yao, M.-H.; Yang, J.; Zhao, D.-H.; Zhao, Y.-D.; Liu, B., One-step in situ synthesis of polypeptide–gold nanoparticles hybrid nanogels and their application in targeted photoacoustic imaging. *ACS Sustain. Chem. Eng.* **2017**, *5* (11), 9841-9847.
18. Zhao, D.-H.; Yang, J.; Xia, R.-X.; Yao, M.-H.; Jin, R.-M.; Zhao, Y.-D.; Liu, B., High quantum yield Ag<sub>2</sub>S quantum dot@ polypeptide-engineered hybrid nanogels for targeted second near-infrared fluorescence/photoacoustic imaging and photothermal therapy. *Chem. Comm.* **2018**, *54* (5), 527-530.
19. Jin, R.; Yang, X.; Zhao, D.; Hou, X.; Li, C.; Song, X.; Chen, W.; Wang, Q.; Zhao, Y.; Liu, B., An injectable hybrid hydrogel based on a genetically engineered polypeptide for second near-infrared fluorescence/photoacoustic imaging-monitored sustained chemo-photothermal therapy. *Nanoscale* **2019**, *11* (34), 16080-16091.
20. Miki, K.; Inoue, T.; Kobayashi, Y.; Nakano, K.; Matsuoka, H.; Yamauchi, F.; Yano, T.; Ohe, K., Near-infrared dye-conjugated amphiphilic hyaluronic acid derivatives as a dual contrast agent for in vivo optical and photoacoustic tumor imaging. *Biomacromolecules* **2015**, *16* (1), 219-227.
21. Wang, H.; Mukherjee, S.; Yi, J.; Banerjee, P.; Chen, Q.; Zhou, S., Biocompatible Chitosan-Carbon Dot Hybrid Nanogels for NIR-Imaging-Guided Synergistic Photothermal-Chemo Therapy. *ACS Appl. Mater. Interfaces* **2017**, *9* (22), 18639-18649.
22. Zhai, Y.; Ran, W.; Su, J.; Lang, T.; Meng, J.; Wang, G.; Zhang, P.; Li, Y., Traceable Bioinspired Nanoparticle for the Treatment of Metastatic Breast Cancer via NIR-Triggered Intracellular Delivery of Methylene Blue and Cisplatin. *Adv. Mater.* **2018**, *30* (34), 1802378.
23. Zhou, Y.; Hu, Y.; Sun, W.; Lu, S.; Cai, C.; Peng, C.; Yu, J.; Popovtzer, R.; Shen, M.; Shi, X., Radiotherapy-sensitized tumor photothermal ablation using  $\gamma$ -polyglutamic acid nanogels loaded with polypyrrole. *Biomacromolecules* **2018**, *19* (6), 2034-2042.
24. Zhang, C.; Sun, W.; Wang, Y.; Xu, F.; Qu, J.; Xia, J.; Shen, M.; Shi, X., Gd/CuS-Loaded Functional Nanogels for MR/PA Imaging-Guided Tumor-Targeted Photothermal Therapy. *ACS Appl. Mater. Interfaces* **2020**, *12* (8), 9107-9117.
25. Li, W.; Wang, X.; Wang, J.; Guo, Y.; Lu, S. Y.; Li, C. M.; Kang, Y.; Wang, Z. G.; Ran, H. T.; Cao, Y.; Liu, H., Enhanced Photoacoustic and Photothermal Effect of Functionalized Polypyrrole Nanoparticles for Near-Infrared Theranostic Treatment of Tumor. *Biomacromolecules* **2019**, *20* (1), 401-411.
26. Biffi, S.; Petrizza, L.; Garrovo, C.; Rampazzo, E.; Andolfi, L.; Giustetto, P.; Nikolov, I.; Kurdi, G.; Danailov, M. B.; Zauli, G.; Secchiero, P.; Prodi, L., Multimodal near-infrared-emitting PluS Silica nanoparticles with fluorescent, photoacoustic, and photothermal capabilities. *Int. J. Nanomedicine* **2016**, *11*, 4865-4874.
27. Zhang, Z.; Zhang, X.; Ding, Y.; Long, P.; Guo, J.; Wang, C., NIR-Induced Disintegration of CuS-Loaded Nanogels for Improved Tumor Penetration and Enhanced Anticancer Therapy. *Macromol. Biosci.* **2019**, *19* (4), 1800416.
28. Huang, W.; Leng, T.; Gao, M.; Hu, Q.; Liu, L.; Dou, H., Scalable dextran-polypyrrole nano-assemblies with photothermal/photoacoustic dual capabilities and enhanced biocompatibility. *Carbohydr. Polym.* **2020**, *241*, 116224.

29. Zhang, S.; Guo, W.; Wei, J.; Li, C.; Liang, X. J.; Yin, M., Terrylenediimide-Based Intrinsic Theranostic Nanomedicines with High Photothermal Conversion Efficiency for Photoacoustic Imaging-Guided Cancer Therapy. *ACS Nano* **2017**, *11* (4), 3797-3805.
30. Xu, Y.; Chen, J.; Tong, L.; Su, P.; Liu, Y.; Gu, B.; Bao, B.; Wang, L., pH/NIR-responsive semiconducting polymer nanoparticles for highly effective photoacoustic image guided chemo-photothermal synergistic therapy. *J. Control. Release* **2019**, *293*, 94-103.
31. Jo, J.; Lee, C. H.; Kopelman, R.; Wang, X., In vivo quantitative imaging of tumor pH by nanosonophore assisted multispectral photoacoustic imaging. *Nat. Comm.* **2017**, *8* (1), 471.
32. Theune, L. E.; Buchmann, J.; Wedepohl, S.; Molina, M.; Laufer, J.; Calderón, M. J. J. o. C. R., NIR-and thermo-responsive semi-interpenetrated polypyrrole nanogels for imaging guided combinational photothermal and chemotherapy. *J. Control. Release* **2019**, *311*, 147-161.
33. Vasey, P. A.; Kaye, S. B.; Morrison, R.; Twelves, C.; Wilson, P.; Duncan, R.; Thomson, A. H.; Murray, L. S.; Hilditch, T. E.; Murray, T.; Burtles, S.; Fraier, D.; Frigerio, E.; Cassidy, J., Phase I Clinical and Pharmacokinetic Study of PK1 [2-(2-Hydroxypropyl)methacrylamide Copolymer Doxorubicin]: First Member of a New Class of Chemotherapeutic Agents—Drug-Polymer Conjugates. *Clinical Cancer Research* **1999**, *5* (1), 83.
34. MaHam, A.; Tang, Z.; Wu, H.; Wang, J.; Lin, Y., Protein-Based Nanomedicine Platforms for Drug Delivery. *Small* **2009**, *5* (15), 1706-1721.
35. Jo, J.; Lee, C. H.; Folz, J.; Tan, J. W. Y.; Wang, X.; Kopelman, R., In Vivo Photoacoustic Lifetime Based Oxygen Imaging with Tumor Targeted G2 Polyacrylamide Nanosonophores. *ACS Nano* **2019**, *13* (12), 14024-14032.
36. Jeong, H.-H.; Choi, E.; Ellis, E.; Lee, T.-C., Recent advances in gold nanoparticles for biomedical applications: from hybrid structures to multi-functionality. *Journal of Materials Chemistry B* **2019**, *7* (22), 3480-3496.
37. Sano, K.; Ohashi, M.; Kanazaki, K.; Ding, N.; Deguchi, J.; Kanada, Y.; Ono, M.; Saji, H., In vivo photoacoustic imaging of cancer using indocyanine green-labeled monoclonal antibody targeting the epidermal growth factor receptor. *Biochem. Biophys. Res. Commun.* **2015**, *464* (3), 820-825.
38. Tsunoi, Y.; Sato, S.; Kawauchi, S.; Ashida, H.; Saitoh, D.; Terakawa, M., In vivo photoacoustic molecular imaging of the distribution of serum albumin in rat burned skin. *Burns* **2013**, *39* (7), 1403-8.
39. Jeon, M.; Song, W.; Huynh, E.; Kim, J.; Kim, J.; Helfield, B. L.; Leung, B. Y.; Geortz, D. E.; Zheng, G.; Oh, J., Methylene blue microbubbles as a model dual-modality contrast agent for ultrasound and activatable photoacoustic imaging. *J. Biomed. Opt.* **2014**, *19* (1), 016005.
40. Park, S.; Kim, J.; Jeon, M.; Song, J.; Kim, C., In vivo photoacoustic and fluorescence cystography using clinically relevant dual modal indocyanine green. *Sensors* **2014**, *14* (10), 19660-19668.
41. Weber, J.; Beard, P. C.; Bohndiek, S. E., Contrast agents for molecular photoacoustic imaging. *Nat. Methods* **2016**, *13* (8), 639-650.
42. Chen, Y.-S.; Yoon, S. J.; Frey, W.; Dockery, M.; Emelianov, S., Dynamic contrast-enhanced photoacoustic imaging using photothermal stimuli-responsive composite nanomodulators. *Nat. Comm.* **2017**, *8* (1), 15782.

43. Bouche, M.; Puhlinger, M.; Iturmendi, A.; Amirshaghghi, A.; Tsourkas, A.; Teasdale, I.; Cormode, D. P., Activatable Hybrid Polyphosphazene-AuNP Nanoprobe for ROS Detection by Bimodal PA/CT Imaging. *ACS Appl. Mater. Interfaces* **2019**, *11* (32), 28648-28656.
44. Ge, J.; Jia, Q.; Liu, W.; Guo, L.; Liu, Q.; Lan, M.; Zhang, H.; Meng, X.; Wang, P., Red-Emissive Carbon Dots for Fluorescent, Photoacoustic, and Thermal Theranostics in Living Mice. *Adv. Mater.* **2015**, *27* (28), 4169-77.
45. Zerda, A. d. I.; Liu, Z.; Bodapati, S.; Teed, R.; Vaithilingam, S.; Khuri-Yakub, B. T.; Chen, X.; Dai, H.; Gambhir, S. S., Ultrahigh Sensitivity Carbon Nanotube Agents for Photoacoustic Molecular Imaging in Living Mice. *Nano Lett.* **2010**, *10* (6), 2168-2172.
46. Sheng, Z.; Song, L.; Zheng, J.; Hu, D.; He, M.; Zheng, M.; Gao, G.; Gong, P.; Zhang, P.; Ma, Y.; Cai, L., Protein-assisted fabrication of nano-reduced graphene oxide for combined in vivo photoacoustic imaging and photothermal therapy. *Biomaterials* **2013**, *34* (21), 5236-5243.
47. Feng, L.; Zhu, C.; Yuan, H.; Liu, L.; Lv, F.; Wang, S., Conjugated polymer nanoparticles: preparation, properties, functionalization and biological applications. *Chem. Soc. Rev.* **2013**, *42* (16), 6620-33.
48. Pu, K.; Chattopadhyay, N.; Rao, J., Recent advances of semiconducting polymer nanoparticles in in vivo molecular imaging. *J. Control. Release* **2016**, *240*, 312-322.
49. Eskiizmir, G.; Ermertcan, A. T.; Yapici, K., Chapter 17 - Nanomaterials: promising structures for the management of oral cancer. In *Nanostructures for Oral Medicine*, Andronesco, E.; Grumezescu, A. M., Eds. Elsevier: 2017; pp 511-544.
50. Liu, Y.; Bhattarai, P.; Dai, Z.; Chen, X., Photothermal therapy and photoacoustic imaging via nanotheranostics in fighting cancer. *Chem. Soc. Rev.* **2019**, *48* (7), 2053-2108.
51. Lyu, Y.; Li, J.; Pu, K., Second Near-Infrared Absorbing Agents for Photoacoustic Imaging and Photothermal Therapy. *Small Methods* **2019**, *3* (11), 1900553.
52. Wang, G.; Zhang, F.; Tian, R.; Zhang, L.; Fu, G.; Yang, L.; Zhu, L., Nanotubes-Embedded Indocyanine Green-Hyaluronic Acid Nanoparticles for Photoacoustic-Imaging-Guided Phototherapy. *ACS Appl. Mater. Interfaces* **2016**, *8* (8), 5608-5617.
53. Liang, X.; Li, Y.; Li, X.; Jing, L.; Deng, Z.; Yue, X.; Li, C.; Dai, Z., PEGylated polypyrrole nanoparticles conjugating gadolinium chelates for dual - modal MRI/photoacoustic imaging guided photothermal therapy of cancer. *Adv. Funct. Mater.* **2015**, *25* (9), 1451-1462.
54. Tian, Q.; Li, Y.; Jiang, S.; An, L.; Lin, J.; Wu, H.; Huang, P.; Yang, S., Tumor pH-Responsive Albumin/Polyaniline Assemblies for Amplified Photoacoustic Imaging and Augmented Photothermal Therapy. *Small* **2019**, *15* (42), 1902926.
55. Lalwani, G.; Cai, X.; Nie, L.; Wang, L. V.; Sitharaman, B., Graphene-based contrast agents for photoacoustic and thermoacoustic tomography. *Photoacoustics* **2013**, *1* (3), 62-67.
56. Chen, G.; Ma, B.; Wang, Y.; Xie, R.; Li, C.; Dou, K.; Gong, S., CuS-Based Theranostic Micelles for NIR-Controlled Combination Chemotherapy and Photothermal Therapy and Photoacoustic Imaging. *ACS Appl. Mater. Interfaces* **2017**, *9* (48), 41700-41711.
57. Lu, S.; Li, X.; Zhang, J.; Peng, C.; Shen, M.; Shi, X., Dendrimer-Stabilized Gold Nanoflowers Embedded with Ultrasmall Iron Oxide Nanoparticles for Multimode Imaging-Guided Combination Therapy of Tumors. *Adv. Sci.* **2018**, *5* (12), 1801612.
58. Cai, C.; Li, X.; Wang, Y.; Liu, M.; Shi, X.; Xia, J.; Shen, M., Polydopamine-coated gold core/hollow mesoporous silica shell particles as a nanoplatform for multimode imaging and photothermal therapy of tumors. *Chem. Eng. J.* **2019**, *362*, 842-850.

59. Yang, T.; Tang, Y.; Liu, L.; Lv, X.; Wang, Q.; Ke, H.; Deng, Y.; Yang, H.; Yang, X.; Liu, G.; Zhao, Y.; Chen, H., Size-Dependent Ag<sub>2</sub>S Nanodots for Second Near-Infrared Fluorescence/Photoacoustics Imaging and Simultaneous Photothermal Therapy. *ACS Nano* **2017**, *11* (2), 1848-1857.
60. Ouyang, Z.; Li, D.; Xiong, Z.; Song, C.; Gao, Y.; Liu, R.; Shen, M.; Shi, X., Antifouling Dendrimer-Entrapped Copper Sulfide Nanoparticles Enable Photoacoustic Imaging-Guided Targeted Combination Therapy of Tumors and Tumor Metastasis. *ACS Appl. Mater. Interfaces* **2021**, *13* (5), 6069-6080.
61. Lyu, Y.; Zhen, X.; Miao, Y.; Pu, K., Reaction-Based Semiconducting Polymer Nanoprobes for Photoacoustic Imaging of Protein Sulfenic Acids. *ACS Nano* **2017**, *11* (1), 358-367.
62. Hanahan, D.; Weinberg, R. A., The hallmarks of cancer. *Cell* **2000**, *100* (1), 57-70.
63. Hanahan, D.; Weinberg, R. A., Hallmarks of cancer: the next generation. *Cell* **2011**, *144* (5), 646-74.
64. Jafari, M.; Hasanzadeh, M., Cell-specific frequency as a new hallmark to early detection of cancer and efficient therapy: Recording of cancer voice as a new horizon. *Biomed. Pharmacother.* **2020**, *122*, 109770.
65. Gallagher, F. A.; Kettunen, M. I.; Day, S. E.; Hu, D.-E.; Ardenkjær-Larsen, J. H.; Jensen, P. R.; Karlsson, M.; Golman, K.; Lerche, M. H.; Brindle, K. M., Magnetic resonance imaging of pH in vivo using hyperpolarized <sup>13</sup>C-labelled bicarbonate. *Nature* **2008**, *453* (7197), 940-943.
66. Dewhirst, M. W.; Birer, S. R., Oxygen-enhanced MRI is a major advance in tumor hypoxia imaging. *Cancer Res.* **2016**, *76* (4), 769-772.
67. Frackowiak, R. S.; Lenzi, G. L.; Jones, T.; Heather, J. D., Quantitative measurement of regional cerebral blood flow and oxygen metabolism in man using <sup>15</sup>O and positron emission tomography: theory, procedure, and normal values. *J. Comput. Assist. Tomogr.* **1980**, *4* (6), 727-736.
68. Vävere, A. L.; Biddlecombe, G. B.; Spees, W. M.; Garbow, J. R.; Wijesinghe, D.; Andreev, O. A.; Engelman, D. M.; Reshetnyak, Y. K.; Lewis, J. S., A Novel Technology for the Imaging of Acidic Prostate Tumors by Positron Emission Tomography. *Cancer Res.* **2009**, *69* (10), 4510.
69. Wang, X. D.; Wolfbeis, O. S., Optical methods for sensing and imaging oxygen: materials, spectroscopies and applications. *Chem. Soc. Rev.* **2014**, *43* (10), 3666-761.
70. Seo, Y. H.; Carroll, K. S. J. P. o. t. N. A. o. S., Profiling protein thiol oxidation in tumor cells using sulfenic acid-specific antibodies. *Proc. Natl. Acad. Sci. U.S.A.* **2009**, *106* (38), 16163-16168.
71. Berezin, Mikhail Y.; Guo, K.; Akers, W.; Northdurft, Ralph E.; Culver, Joseph P.; Teng, B.; Vasalatiy, O.; Barbacow, K.; Gandjbakhche, A.; Griffiths, Gary L.; Achilefu, S., Near-Infrared Fluorescence Lifetime pH-Sensitive Probes. *Biophys. J.* **2011**, *100* (8), 2063-2072.
72. Hockel, M.; Vaupel, P., Tumor hypoxia: definitions and current clinical, biologic, and molecular aspects. *J. Natl. Cancer Inst.* **2001**, *93* (4), 266-76.
73. Kato, Y.; Ozawa, S.; Miyamoto, C.; Maehata, Y.; Suzuki, A.; Maeda, T.; Baba, Y., Acidic extracellular microenvironment and cancer. *Cancer Cell Int.* **2013**, *13* (1), 89.
74. Raghunand, N.; He, X.; Sluis, R. v.; Mahoney, B.; Baggett, B.; Taylor, C. W.; Paine-Murrieta, G.; Roe, D.; Bhujwalla, Z. M.; Gillies, R. J., Enhancement of chemotherapy by manipulation of tumour pH. *Br. J. Cancer* **1999**, *80* (7), 1005-1011.

75. Trédan, O.; Galmarini, C. M.; Patel, K.; Tannock, I. F., Drug Resistance and the Solid Tumor Microenvironment. *J. Natl Cancer. Inst.* **2007**, *99* (19), 1441-1454.
76. Chen, Q.; Liu, X.; Chen, J.; Zeng, J.; Cheng, Z.; Liu, Z., A Self-Assembled Albumin-Based Nanoprobe for In Vivo Ratiometric Photoacoustic pH Imaging. *Adv. Mater.* **2015**, *27* (43), 6820-7.
77. Guha, S.; Shaw, G. K.; Mitcham, T. M.; Bouchard, R. R.; Smith, B. D., Croconaine rotaxane for acid activated photothermal heating and ratiometric photoacoustic imaging of acidic pH. *Chem. Comm.* **2016**, *52* (1), 120-3.
78. Kimbrough, C. W.; Khanal, A.; Zeiderman, M.; Khanal, B. R.; Burton, N. C.; McMasters, K. M.; Vickers, S. M.; Grizzle, W. E.; McNally, L. R., Targeting Acidity in Pancreatic Adenocarcinoma: Multispectral Optoacoustic Tomography Detects pH-Low Insertion Peptide Probes In Vivo. *Clin. Cancer Res.* **2015**, *21* (20), 4576-85.
79. Han, J.; Burgess, K., Fluorescent Indicators for Intracellular pH. *Chem. Rev.* **2010**, *110* (5), 2709-2728.
80. Petrova, V.; Annicchiarico-Petruzzelli, M.; Melino, G.; Amelio, I., The hypoxic tumour microenvironment. *Oncogenesis* **2018**, *7* (1), 10.
81. Zhong, H.; De Marzo, A. M.; Laughner, E.; Lim, M.; Hilton, D. A.; Zagzag, D.; Buechler, P.; Isaacs, W. B.; Semenza, G. L.; Simons, J. W., Overexpression of Hypoxia-inducible Factor 1 $\alpha$  in Common Human Cancers and Their Metastases. *Cancer Res.* **1999**, *59* (22), 5830.
82. Maxwell, P. H.; Wiesener, M. S.; Chang, G.-W.; Clifford, S. C.; Vaux, E. C.; Cockman, M. E.; Wykoff, C. C.; Pugh, C. W.; Maher, E. R.; Ratcliffe, P. J., The tumour suppressor protein VHL targets hypoxia-inducible factors for oxygen-dependent proteolysis. *Nature* **1999**, *399* (6733), 271-275.
83. Tzoumas, S.; Nunes, A.; Olefir, I.; Stangl, S.; Symvoulidis, P.; Glasl, S.; Bayer, C.; Multhoff, G.; Ntziachristos, V., Eigenspectra optoacoustic tomography achieves quantitative blood oxygenation imaging deep in tissues. *Nat. Comm.* **2016**, *7* (1), 12121.
84. Fiaschi, T.; Chiarugi, P., Oxidative stress, tumor microenvironment, and metabolic reprogramming: a diabolic liaison. *Int. J. Cell Biol.* **2012**, *2012*, 762825.
85. Raj, L.; Ide, T.; Gurkar, A. U.; Foley, M.; Schenone, M.; Li, X.; Tolliday, N. J.; Golub, T. R.; Carr, S. A.; Shamji, A. F.; Stern, A. M.; Mandinova, A.; Schreiber, S. L.; Lee, S. W., Selective killing of cancer cells by a small molecule targeting the stress response to ROS. *Nature* **2011**, *475* (7355), 231-4.
86. Rudyk, O.; Eaton, P., Biochemical methods for monitoring protein thiol redox states in biological systems. *Redox Biol.* **2014**, *2*, 803-13.
87. Szekeres, G. P.; Kneipp, J., SERS probing of proteins in gold nanoparticle agglomerates. *Frontiers in chemistry* **2019**, *7*, 30.
88. Ando, J.; Fujita, K.; Smith, N. I.; Kawata, S., Dynamic SERS imaging of cellular transport pathways with endocytosed gold nanoparticles. *Nano letters* **2011**, *11* (12), 5344-5348.
89. Agarwal, A.; Huang, S.; O'donnell, M.; Day, K.; Day, M.; Kotov, N.; Ashkenazi, S., Targeted gold nanorod contrast agent for prostate cancer detection by photoacoustic imaging. *Journal of applied physics* **2007**, *102* (6), 064701.
90. Zhang, Y.; Zhan, X.; Xiong, J.; Peng, S.; Huang, W.; Joshi, R.; Cai, Y.; Liu, Y.; Li, R.; Yuan, K., Temperature-dependent cell death patterns induced by functionalized gold nanoparticle photothermal therapy in melanoma cells. *Scientific reports* **2018**, *8* (1), 1-9.

91. Liu, X.; Atwater, M.; Wang, J.; Huo, Q., Extinction coefficient of gold nanoparticles with different sizes and different capping ligands. *Colloids and Surfaces B: Biointerfaces* **2007**, *58* (1), 3-7.
92. Weber, J.; Beard, P. C.; Bohndiek, S. E., Contrast agents for molecular photoacoustic imaging. *Nature methods* **2016**, *13* (8), 639-650.
93. Tian, F.; Bonnier, F.; Casey, A.; Shanahan, A. E.; Byrne, H. J., Surface enhanced Raman scattering with gold nanoparticles: effect of particle shape. *Analytical Methods* **2014**, *6* (22), 9116-9123.
94. Ash, C.; Dubec, M.; Donne, K.; Bashford, T., Effect of wavelength and beam width on penetration in light-tissue interaction using computational methods. *Lasers in medical science* **2017**, *32* (8), 1909-1918.
95. Jokerst, J. V.; Cole, A. J.; Van de Sompel, D.; Gambhir, S. S., Gold nanorods for ovarian cancer detection with photoacoustic imaging and resection guidance via Raman imaging in living mice. *ACS nano* **2012**, *6* (11), 10366-10377.
96. An, L.; Wang, Y.; Lin, J.; Tian, Q.; Xie, Y.; Hu, J.; Yang, S., Macrophages-mediated delivery of small gold nanorods for tumor hypoxia photoacoustic imaging and enhanced photothermal therapy. *ACS applied materials & interfaces* **2019**, *11* (17), 15251-15261.
97. Phan, T. T. V.; Ahn, S.-H.; Oh, J., Chitosan-mediated facile green synthesis of size-controllable gold nanostars for effective photothermal therapy and photoacoustic imaging. *European Polymer Journal* **2019**, *118*, 492-501.
98. Del Cano, R.; Gisbert-Gonzalez, J. M.; Gonzalez-Rodriguez, J.; Sanchez-Obrero, G.; Madueno, R.; Blazquez, M.; Pineda, T., Effective replacement of cetyltrimethylammonium bromide (CTAB) by mercaptoalkanoic acids on gold nanorod (AuNR) surfaces in aqueous solutions. *Nanoscale* **2020**, *12* (2), 658-668.
99. Liu, K.; Zheng, Y.; Lu, X.; Thai, T.; Lee, N. A.; Bach, U.; Gooding, J. J., Biocompatible gold nanorods: One-step surface functionalization, highly colloidal stability, and low cytotoxicity. *Langmuir* **2015**, *31* (17), 4973-4980.
100. Balfourier, A.; Luciani, N.; Wang, G.; Lelong, G.; Ersen, O.; Khelfa, A.; Alloyeau, D.; Gazeau, F.; Carn, F., Unexpected intracellular biodegradation and recrystallization of gold nanoparticles. *Proceedings of the National Academy of Sciences* **2020**, *117* (1), 103-113.
101. Yu, M.; Xu, J.; Zheng, J., Renal clearable luminescent gold nanoparticles: from the bench to the clinic. *Angewandte Chemie International Edition* **2019**, *58* (13), 4112-4128.
102. Jung, S.; Nam, J.; Hwang, S.; Park, J.; Hur, J.; Im, K.; Park, N.; Kim, S., Theragnostic pH-sensitive gold nanoparticles for the selective surface enhanced Raman scattering and photothermal cancer therapy. *Analytical chemistry* **2013**, *85* (16), 7674-7681.
103. Cheng, X.; Sun, R.; Yin, L.; Chai, Z.; Shi, H.; Gao, M., Light - triggered assembly of gold nanoparticles for photothermal therapy and photoacoustic imaging of tumors in vivo. *Advanced Materials* **2017**, *29* (6), 1604894.
104. Sun, M.; Liu, F.; Zhu, Y.; Wang, W.; Hu, J.; Liu, J.; Dai, Z.; Wang, K.; Wei, Y.; Bai, J., Salt-induced aggregation of gold nanoparticles for photoacoustic imaging and photothermal therapy of cancer. *Nanoscale* **2016**, *8* (8), 4452-4457.
105. Zhao, N.; Yan, L.; Zhao, X.; Chen, X.; Li, A.; Zheng, D.; Zhou, X.; Dai, X.; Xu, F.-J., Versatile types of organic/inorganic nanohybrids: from strategic design to biomedical applications. *Chemical reviews* **2018**, *119* (3), 1666-1762.

106. Park, W.; Shin, H.; Choi, B.; Rhim, W.-K.; Na, K.; Han, D. K., Advanced hybrid nanomaterials for biomedical applications. *Progress in Materials Science* **2020**, 100686.
107. Hood, M. A.; Mari, M.; Muñoz-Espí, R., Synthetic strategies in the preparation of polymer/inorganic hybrid nanoparticles. *Materials* **2014**, 7 (5), 4057-4087.
108. Seyfoori, A.; Seyyed Ebrahimi, S.; Samiei, E.; Akbari, M., Multifunctional Hybrid Magnetic Microgel Synthesis for Immune-Based Isolation and Post-Isolation Culture of Tumor Cells. *ACS applied materials & interfaces* **2019**, 11 (28), 24945-24958.
109. Bhol, P.; Mohanty, P. S., Smart microgel-metal hybrid particles of PNIPAM-co-PAA@AgAu: synthesis, characterizations and modulated catalytic activity. *Journal of Physics: Condensed Matter* **2020**, 33 (8), 084002.
110. Boularas, M.; Deniau-Lejeune, E.; Alard, V.; Tranchant, J.-F.; Billon, L.; Save, M., Dual stimuli-responsive oligo (ethylene glycol)-based microgels: insight into the role of internal structure in volume phase transitions and loading of magnetic nanoparticles to design stable thermoresponsive hybrid microgels. *Polymer Chemistry* **2016**, 7 (2), 350-363.
111. Cazares-Cortes, E.; Espinosa, A.; Guigner, J.-M.; Michel, A.; Griffete, N.; Wilhelm, C.; Ménager, C., Doxorubicin intracellular remote release from biocompatible oligo (ethylene glycol) methyl ether methacrylate-based magnetic nanogels triggered by magnetic hyperthermia. *ACS applied materials & interfaces* **2017**, 9 (31), 25775-25788.
112. Cazares-Cortes, E.; Wilhelm, C.; Perez, J. E.; Espinosa, A.; Casale, S.; Michel, A.; Abou-Hassan, A.; Ménager, C., Tuning the load of gold and magnetic nanoparticles in nanogels through their design for enhanced dual magneto-photo-thermia. *Chemical Communications* **2021**.
113. Lutz, J.-F.; Stiller, S.; Hoth, A.; Kaufner, L.; Pison, U.; Cartier, R., One-pot synthesis of PEGylated ultrasmall iron-oxide nanoparticles and their in vivo evaluation as magnetic resonance imaging contrast agents. *Biomacromolecules* **2006**, 7 (11), 3132-3138.
114. Ulasan, M.; Yavuz, E.; Bagriacik, E. U.; Cengeloglu, Y.; Yavuz, M. S., Biocompatible thermoresponsive PEGMA nanoparticles crosslinked with cleavable disulfide - based crosslinker for dual drug release. *Journal of Biomedical Materials Research Part A* **2015**, 103 (1), 243-251.
115. Kuppe, C.; Rusimova, K. R.; Ohnoutek, L.; Slavov, D.; Valev, V. K., "Hot" in Plasmonics: Temperature - Related Concepts and Applications of Metal Nanostructures. *Advanced Optical Materials* **2020**, 8 (1), 1901166.
116. Cheheltani, R.; Ezzibdeh, R. M.; Chhour, P.; Pulaparthi, K.; Kim, J.; Jurcova, M.; Hsu, J. C.; Blundell, C.; Litt, H. I.; Ferrari, V. A., Tunable, biodegradable gold nanoparticles as contrast agents for computed tomography and photoacoustic imaging. *Biomaterials* **2016**, 102, 87-97.
117. Kim, S.-E.; Lee, B.-R.; Lee, H.; Jo, S. D.; Kim, H.; Won, Y.-Y.; Lee, J., Near-infrared plasmonic assemblies of gold nanoparticles with multimodal function for targeted cancer theragnosis. *Scientific reports* **2017**, 7 (1), 1-10.
118. **!!! INVALID CITATION !!! 118, 119.**
119. Quesada-Pérez, M.; Maroto-Centeno, J. A.; Forcada, J.; Hidalgo-Alvarez, R., Gel swelling theories: the classical formalism and recent approaches. *Soft Matter* **2011**, 7 (22), 10536-10547.
120. Cooper, D.; Uhm, H.; Tauzin, L. J.; Poddar, N.; Landes, C. F., Photobleaching Lifetimes of Cyanine Fluorophores Used for Single Molecule Förster Resonance Energy Transfer

in the Presence of Various Photoprotection Systems. *Chembiochem: a European journal of chemical biology* **2013**, *14* (9).

121. Bera, A.; Bagchi, D.; Pal, S. K., Improvement of Photostability and NIR Activity of Cyanine Dye through Nanohybrid Formation: Key Information from Ultrafast Dynamical Studies. *The Journal of Physical Chemistry A* **2019**, *123* (35), 7550-7557.

122. Sanchala, D.; Bhatt, L. K.; Pethe, P.; Shelat, R.; Kulkarni, Y. A., Anticancer activity of methylene blue via inhibition of heat shock protein 70. *Biomedicine & Pharmacotherapy* **2018**, *107*, 1037-1045.

123. Sarkar, M.; Lucas, T.; Atlas, Y.; Renault, G.; Gazeau, F.; Gateau, J., Calibrated photoacoustic spectrometer for in vitro characterization of contrast agents based on a standard imaging system. 2021.

124. Jain, P. K.; Lee, K. S.; El-Sayed, I. H.; El-Sayed, M. A., Calculated absorption and scattering properties of gold nanoparticles of different size, shape, and composition: applications in biological imaging and biomedicine. *The journal of physical chemistry B* **2006**, *110* (14), 7238-7248.

125. Chen, Q.; Liu, X.; Chen, J.; Zeng, J.; Cheng, Z.; Liu, Z., A self - assembled albumin - based nanoprobe for in vivo ratiometric photoacoustic pH imaging. *Advanced Materials* **2015**, *27* (43), 6820-6827.

126. Nguyen, V. P.; Qian, W.; Li, Y.; Liu, B.; Aaberg, M.; Henry, J.; Zhang, W.; Wang, X.; Paulus, Y. M., Chain-like gold nanoparticle clusters for multimodal photoacoustic microscopy and optical coherence tomography enhanced molecular imaging. *Nature Communications* **2021**, *12* (1), 34.

127. Huang, D.; Cui, J.; Chen, X., A morpholinium surfactant crystallization induced formation of Au nanoparticle sheet-like assemblies with uniform SERS activity. *Colloids and Surfaces A: Physicochemical and Engineering Aspects* **2014**, *456*, 100-107.

128. Wang, T.-J.; Chang, H.-W.; Chen, J.-S.; Chiang, H.-P., Nanotip-assisted photoreduction of silver nanostructures on chemically patterned ferroelectric crystals for surface enhanced Raman scattering. *Scientific reports* **2019**, *9* (1), 1-10.

129. Zamora-Peredo, L.; García-Ramírez, J. I.; García-Velasco, A. C.; Hernández-Torres, J.; García-González, L.; Bizarro, M.; Báez-Rodríguez, A., Influence of Ag Photodeposition Conditions over SERS Intensity of Ag/ZnO Microspheres for Nanomolar Detection of Methylene Blue. *Nanomaterials* **2021**, *11* (12), 3414.

130. Nithiyantham, U.; Ede, S. R.; Kundu, S., Self-assembled wire-like and honeycomb-like osmium nanoclusters (NCs) in DNA with pronounced catalytic and SERS activities. *Journal of Materials Chemistry C* **2014**, *2* (19), 3782-3794.

131. Shattique, M. R.; Stepanova, M., Surface Plasmon-Driven Reversible Transformation of DNA-Bound Methylene Blue Detected In Situ by SERS. *Plasmonics* **2020**, *15* (2), 427-434.

132. Fabris, L., SERS tags: the next promising tool for personalized cancer detection? *ChemNanoMat* **2016**, *2* (4), 249-258.

133. Wang, Y.; Yan, B.; Chen, L., SERS tags: novel optical nanoprobe for bioanalysis. *Chemical reviews* **2013**, *113* (3), 1391-1428.

134. Alvarez - Puebla, R. A.; Liz - Marzán, L. M., SERS - based diagnosis and biodetection. *Small* **2010**, *6* (5), 604-610.

135. Tabatabaei, M.; McRae, D.; Lagugné-Labarhet, F., Recent advances of plasmon-enhanced spectroscopy at bio-Interfaces. In *Frontiers of Plasmon Enhanced Spectroscopy Volume 2*, ACS Publications: 2016; pp 183-207.
136. Rus, Y. B.; Galmiche, L.; Audebert, P.; Courty, A.; Maisonhaute, E.; Miomandre, F., Electrodeposition of Silver Nanoparticles on Reduced Graphene Functionalized by Pyridine - Pyridazine Units: Application to Surface - Enhanced Raman Spectroscopy and Electrocatalysis. *ChemistrySelect* **2019**, *4* (4), 1298-1305.
137. Lane, L. A.; Qian, X.; Nie, S., SERS nanoparticles in medicine: from label-free detection to spectroscopic tagging. *Chemical reviews* **2015**, *115* (19), 10489-10529.
138. Mahato, K.; Nagpal, S.; Shah, M. A.; Srivastava, A.; Maurya, P. K.; Roy, S.; Jaiswal, A.; Singh, R.; Chandra, P., Gold nanoparticle surface engineering strategies and their applications in biomedicine and diagnostics. *3 Biotech* **2019**, *9* (2), 57-57.
139. Mir-Simon, B.; Reche-Perez, I.; Guerrini, L.; Pazos-Perez, N.; Alvarez-Puebla, R. A., Universal one-pot and scalable synthesis of SERS encoded nanoparticles. *Chemistry of Materials* **2015**, *27* (3), 950-958.
140. Bhatt, N.; Huang, P.-J. J.; Dave, N.; Liu, J., Dissociation and degradation of thiol-modified DNA on gold nanoparticles in aqueous and organic solvents. *Langmuir* **2011**, *27* (10), 6132-6137.
141. Yang, G.; Amro, N. A.; Starkewolfe, Z. B.; Liu, G.-y., Molecular-level approach to inhibit degradations of alkanethiol self-assembled monolayers in aqueous media. *Langmuir* **2004**, *20* (10), 3995-4003.
142. Vericat, C.; Vela, M.; Benitez, G.; Carro, P.; Salvarezza, R., Self-assembled monolayers of thiols and dithiols on gold: new challenges for a well-known system. *Chemical Society Reviews* **2010**, *39* (5), 1805-1834.
143. Walia, J.; Guay, J.-M.; Krupin, O.; Variola, F.; Berini, P.; Weck, A., Visible light driven plasmonic photochemistry on nano-textured silver. *Physical Chemistry Chemical Physics* **2018**, *20* (1), 238-246.
144. Tam-Chang, S.-W.; Biebuyck, H. A.; Whitesides, G. M.; Jeon, N.; Nuzzo, R. G., Self-assembled monolayers on gold generated from alkanethiols with the structure RNHCOCH<sub>2</sub>SH. *Langmuir* **1995**, *11* (11), 4371-4382.
145. Chinwangso, P.; Jamison, A. C.; Lee, T. R., Multidentate adsorbates for self-assembled monolayer films. *Accounts of chemical research* **2011**, *44* (7), 511-519.
146. Laurentius, L.; Stoyanov, S. R.; Gusarov, S.; Kovalenko, A.; Du, R.; Lopinski, G. P.; McDermott, M. T., Diazonium-derived aryl films on gold nanoparticles: Evidence for a carbon-gold covalent bond. *ACS nano* **2011**, *5* (5), 4219-4227.
147. Mirkhalaf, F.; Paprotny, J.; Schiffrin, D. J., Synthesis of metal nanoparticles stabilized by metal-carbon bonds. *Journal of the American Chemical Society* **2006**, *128* (23), 7400-7401.
148. Ahmad, R.; Félidj, N.; Boubekour-Lecaque, L.; Lau-Truong, S.; Gam-Derouich, S.; Decorse, P.; Lamouri, A.; Mangeney, C., Water-soluble plasmonic nanosensors with synthetic receptors for label-free detection of folic acid. *Chemical Communications* **2015**, *51* (47), 9678-9681.
149. Troian-Gautier, L.; Valkenier, H.; Mattiuzzi, A.; Jabin, I.; Van den Brande, N.; Van Mele, B.; Hubert, J.; Reniers, F.; Bruylants, G.; Lagrost, C., Extremely robust and post-functionalizable gold nanoparticles coated with calix [4] arenes via metal-carbon bonds. *Chemical communications* **2016**, *52* (69), 10493-10496.

150. Bouriga, M.; Chehimi, M. M.; Combellas, C.; Decorse, P.; Kanoufi, F. d. r.; Deronzier, A.; Pinson, J., Sensitized Photografting of Diazonium Salts by Visible Light. *Chemistry of Materials* **2013**, *25* (1), 90-97.
151. Pinson, J.; Podvorica, F., Attachment of organic layers to conductive or semiconductive surfaces by reduction of diazonium salts. *Chemical Society Reviews* **2005**, *34* (5), 429-439.
152. Berisha, A.; Chehimi, M. M.; Pinson, J.; Podvorica, F., Electrode surface modification using diazonium salts. *Electroanalytical Chemistry, CRC Press* **2015**, 115-224.
153. Gervais, E.; Aceta, Y.; Gros, P.; Evrard, D., Study of an AuNPs functionalized electrode using different diazonium salts for the ultra-fast detection of Hg (II) traces in water. *Electrochimica Acta* **2018**, *261*, 346-355.
154. Du, J.; Du, H.; Li, X.; Fan, J.; Peng, X., In-situ colorimetric recognition of arylamine based on chemodosimeter-functionalized gold nanoparticle. *Sensors and Actuators B: Chemical* **2017**, *248*, 318-323.
155. Kalachyova, Y.; Olshtrem, A.; Gusebnikova, O. A.; Postnikov, P. S.; Elashnikov, R.; Ulbrich, P.; Rimpelova, S.; Švorčík, V.; Lyutakov, O., Synthesis, Characterization, and Antimicrobial Activity of Near - IR Photoactive Functionalized Gold Multibranched Nanoparticles. *ChemistryOpen* **2017**, *6* (2), 254-260.
156. Nguyen, M.; Kherbouche, I.; Gam-Derouich, S.; Ragheb, I.; Lau-Truong, S.; Lamouri, A.; Lévi, G.; Aubard, J.; Decorse, P.; Félidj, N., Regioselective surface functionalization of lithographically designed gold nanorods by plasmon-mediated reduction of aryl diazonium salts. *Chemical Communications* **2017**, *53* (82), 11364-11367.
157. Nguyen, M.; Lamouri, A.; Salameh, C.; Lévi, G.; Grand, J.; Boubekeur-Lecaque, L.; Mangeney, C.; Félidj, N., Plasmon-mediated chemical surface functionalization at the nanoscale. *Nanoscale* **2016**, *8* (16), 8633-8640.
158. Nguyen, V.-Q.; Ai, Y.; Martin, P.; Lacroix, J.-C., Plasmon-induced nanolocalized reduction of diazonium salts. *ACS omega* **2017**, *2* (5), 1947-1955.
159. Tijunelyte, I.; Kherbouche, I.; Gam-Derouich, S.; Nguyen, M.; Lidgi-Guigui, N.; de la Chapelle, M. L.; Lamouri, A.; Lévi, G.; Aubard, J.; Chevillot-Biraud, A., Multi-functionalization of lithographically designed gold nanodisks by plasmon-mediated reduction of aryl diazonium salts. *Nanoscale Horizons* **2018**, *3* (1), 53-57.
160. Supur, M.; Smith, S. R.; McCreery, R. L., Characterization of growth patterns of nanoscale organic films on carbon electrodes by surface enhanced raman spectroscopy. *Analytical chemistry* **2017**, *89* (12), 6463-6471.
161. Antonioli, L.; Blandizzi, C.; Pacher, P.; Haskó, G., Immunity, inflammation and cancer: a leading role for adenosine. *Nature Reviews Cancer* **2013**, *13* (12), 842-857.
162. Dai, T.; Li, N.; Han, F.; Zhang, H.; Zhang, Y.; Liu, Q., AMP-guided tumour-specific nanoparticle delivery via adenosine A1 receptor. *Biomaterials* **2016**, *83*, 37-50.
163. Turkevich, J.; Stevenson, P. C.; Hillier, J., A study of the nucleation and growth processes in the synthesis of colloidal gold. *Discussions of the Faraday Society* **1951**, *11*, 55-75.
164. Berisha, A.; Combellas, C.; Kanoufi, F.; Decorse, P.; Oturan, N.; Médard, J.; Seydou, M.; Maurel, F.; Pinson, J., Some theoretical and experimental insights on the mechanistic routes leading to the spontaneous grafting of gold surfaces by diazonium salts. *Langmuir* **2017**, *33* (35), 8730-8738.
165. Kundu, J.; Neumann, O.; Janesko, B.; Zhang, D.; Lal, S.; Barhoumi, A.; Scuseria, G.; Halas, N., Adenine- and adenosine monophosphate (AMP)- gold binding

interactions studied by surface-enhanced Raman and infrared spectroscopies. *The Journal of Physical Chemistry C* **2009**, *113* (32), 14390-14397.

166. Doppelt, P.; Hallais, G.; Pinson, J.; Podvorica, F.; Verneyre, S., Surface modification of conducting substrates. Existence of azo bonds in the structure of organic layers obtained from diazonium salts. *Chemistry of Materials* **2007**, *19* (18), 4570-4575.

167. Szekeres, G. P.; Kneipp, J., SERS probing of proteins in gold nanoparticle agglomerates. *Frontiers in Chemistry* **2019**, 30.